Annual Report for

Contract DE-FG36-08GO18192

Stanford Geothermal Program

September 2010 – September 2011

Table of Contents

1. FRACTURE CHARACTERIZATION USING PRODUCTION DATA 1

1.1 SUMMARY 1

1.2 INTRODUCTION 2

1.3 SUMMARY OF REGRESSION MODELING METHODS 3

1.4 ADVECTION-DISPERSION EQUATION WITH TIME VARYING COEFFICIENTS 10

1.5 INTERPRETATION METHODS FOR PRESSURE AND FLOW RATE DATA 18

1.6 KERNEL ESTIMATION 23

1.7 OPTIMIZATION OF REINJECTION SCHEDULING 39

1.8 CONCLUSIONS 60

2. FRACTURE CHARACTERIZATION OF ENHANCED GEOTHERMAL SYSTEMS USING NANOPARTICLES 63

2.1 SUMMARY 63

2.2 INTRODUCTION 65

2.3 CHARACTERIZATION OF POROUS AND FRACTURED MEDIA 66

2.4 NANOPARTICLE AND MICROPARTICLE INJECTION EXPERIMENTS 78

2.5 SYNTHESIS, CHARACTERIZATION, AND CENTRIFUGATION OF TIN-BISMUTH NANOPARTICLES 91

2.6 EXPERIMENTAL INVESTIGATION OF MAGNETIC COLLECTION OF NANOSENSORS 97

2.7 ANALYSIS OF TRACER RETURN CURVES TO ESTIMATE MEASUREMENT GEOLOCATION 101

2.8 RESULTS 107

2.9 FUTURE WORK 132

3. FRACTURE CHARACTERIZATION USING RESISTIVITY 133

3.1 SUMMARY 133

3.2 INTRODUCTION 133

3.3 WATER FLOW ANALOGY OF ELECTRICAL FLOW 135

3.4 RESULTS 137

4. REFERENCES **145**

1. FRACTURE CHARACTERIZATION USING PRODUCTION DATA

This research project is being conducted by Research Assistant Egill Juliusson, Senior Research Engineer Kewen Li and Professor Roland Horne. The objective of this project is to investigate ways to characterize fractures in geothermal reservoirs using production data.

1.1 SUMMARY

In this annual report we highlight the results of our research on fracture characterization using production data from summer 2010 through spring 2011. The overall progress over this past year has culminated in a method that can be used to construct a reservoir model designed to optimize injection scheduling in strongly fracture dominated enhanced geothermal systems (EGS).

The report begins by a brief overview of the various types of regression methods that have been used in this project to interpret production data. In the discussion we attempt to show the similarities and differences between the methods which range from multiple linear regression to nonlinear nonparametric multiple regression methods. It is worthwhile to review these methods, along with the main assumptions required to allow greater flexibility in capturing complex time series. This also shows that care must be taken in choosing not too complex a model, since that can lead to models with poor predictive capacity.

Next a solution to the one-dimensional advection-dispersion equation for transient flow rate and dispersion is developed. This solution may be of interest on its own, since it is a general and compact analytical solution to a commonly encountered partial differential equation, which has not been reported in the literature to the best of our knowledge. The key idea is to transform the time variable into cumulative injection. This transformation is applicable to many known solutions of the advection-dispersion equation, even in two or three dimensions. Moreover, this solution brings the possibility of lifting the steady-state flow condition which can often be problematic when interpreting and modeling tracer returns.

Much of our previous work has focused on tracer transport. To broaden the horizon we have looked into pressure and flow rate data. A brief literature survey of methods for interpreting pressure and rate signals between wells is presented here. This field seems to have been well addressed by researchers in the petroleum industry and a couple of promising methods were identified. Some of the key components of the methods were also implemented to enhance our understanding of how they work. Some of these methods can also provide important input parameters for multiwell tracer and thermal transport problems.

The solution to the advection-dispersion equation given in Chapter 1.4 opened up the possibility for interpretation of tracer tests under variable flow rate conditions. Our findings indicate that if the flow paths between well pairs are strongly constrained by the fracture network, then this method works very well and a convolution relationship exists between the injected and produced tracer concentration. The method also shows promise in cases with more complex fracture patterns. The key discovery is that the convolution is in terms of cumulative flow between each well pair (as opposed to time) and that the mixing between well-to-well flow streams can (and should) be accounted for.

The interwell connectivity is represented by a linear flow rate transformation and tracer kernel function, which can be estimated via deconvolution. Application of a nonparametric kernel estimation method is illustrated by deconvolving synthetic data generated from flow simulations. The results are verified using both cross-validation and by comparison to known solutions.

Lastly we present a method for optimizing injection rate scheduling based on tracer and flow rate data, and theoretical models for thermal transport and specific power output for a binary power plant. The objective is to maximize the net present value of the operation over a given period. The method is tested on a very simple reservoir model with two injectors, two producers and three fractures. Another application example is given for a four injector, three producer model with a relatively complex fracture network.

1.2 INTRODUCTION

Much of the work done previously in this research project has culminated in a method for optimizing injection rate in geothermal reservoirs. Determining how to allocate water to injection wells in geothermal fields is an important and challenging task. Conceptually, the objective of the injection scheduling problem is to delay thermal breakthrough as long as possible, while maintaining as much pressure support for the production wells as possible. With more advanced models it is possible to aim towards maximizing thermal recovery from the geothermal resource, or the net present value of production from the reservoir. The same requirement applies to both EGS and conventional hydrothermal resources.

Lovekin and Horne (1989) discussed methods for optimizing injection schedules in geothermal reservoirs based on tracer return data. They posed the problem as either, a linear program where only the injection rates were adjusted, or a quadratic program where both injection and production rates were adjusted. The objective functions depended on interwell connectivity (IWC) parameters (or arc costs) that were inferred from tracer test. The IWC parameters were computed in an empirical manner and their value was independent of the injection and production rates.

Whether tracer returns vary much with injection and production rates has been debated. In cases where the flow rates being circulated by the power plant are small in comparison to a large ground water current flowing through the reservoir, it seems reasonable to assume that the tracer returns would be insensitive to the particular injection and production rates. In hot dry rock systems, on the other hand, the natural ground water current should be negligible and thus the tracer returns would vary more significantly with the injection and production rates. This observation led our research efforts towards defining methods to predict tracer returns under variable flow rate conditions.

In this report we introduce a method for extracting tracer transfer kernels from tracer data gathered in fractured geothermal systems under variable flow rate conditions. One of the key additions to previous tracer models was that the tracer kernels were defined as functions of cumulative flow from well to well. These tracer kernels could be used to predict the response to an arbitrary input of tracer via convolution. The method works particularly well in fractured reservoirs, where the fractures limit the variability in the streamlines between wells as the injection and production rates change.

The main novelty of this work has been to bring the advantages of the tracer kernel method to the injection scheduling problem. An efficient objective function is suggested and the results verified by comparison to results from numerical simulation. Besides presenting a practical method for optimizing field management, working through the problem revealed the challenges involved in solving the problem effectively. This helps focus further research on ways to overcome those particular challenges.

1.3 SUMMARY OF REGRESSION MODELING METHODS

In this section we give an overview of the regression methods that have been used in this research project to infer interwell connectivity. We will try to keep the equations general in terms of notation, and give examples through references to other papers. In general we will refer to x as the input or predictor variable, and y as the output or response variable. We will also attempt to give graphical representations of each method to enhance understanding and shed light on the similarities and differences between each method.

1.3.1 Multiple input linear regression

Multiple linear regression is a model that relates a linear combination of multiple inputs, x_j, to a single output, y. In most cases there are multiple measurements in time so we have $x(t)$ and $y(t)$.

$$y(t) = \sum_{j=1}^{N_j} a_j x_j\,(t) \tag{2.1}$$

Where N_j is the number of inputs, and the parameters a_j are the unknowns. Since there are usually more time measurements than unknowns, there will be more relations of the type (2.1) than unknowns and the a_j can be determined uniquely. A time lag, τ_j, could also be considered by modifying (2.1) to read:

$$y(t) = \sum_{j=1}^{N_j} a_j x_j\left(t - \tau_j\right) \tag{2.2}$$

The slopes, a_j, are generally assumed to be independent and can take any value. The multiple input linear regression model represented by (2.2) is shown graphically in Figure 1.1.

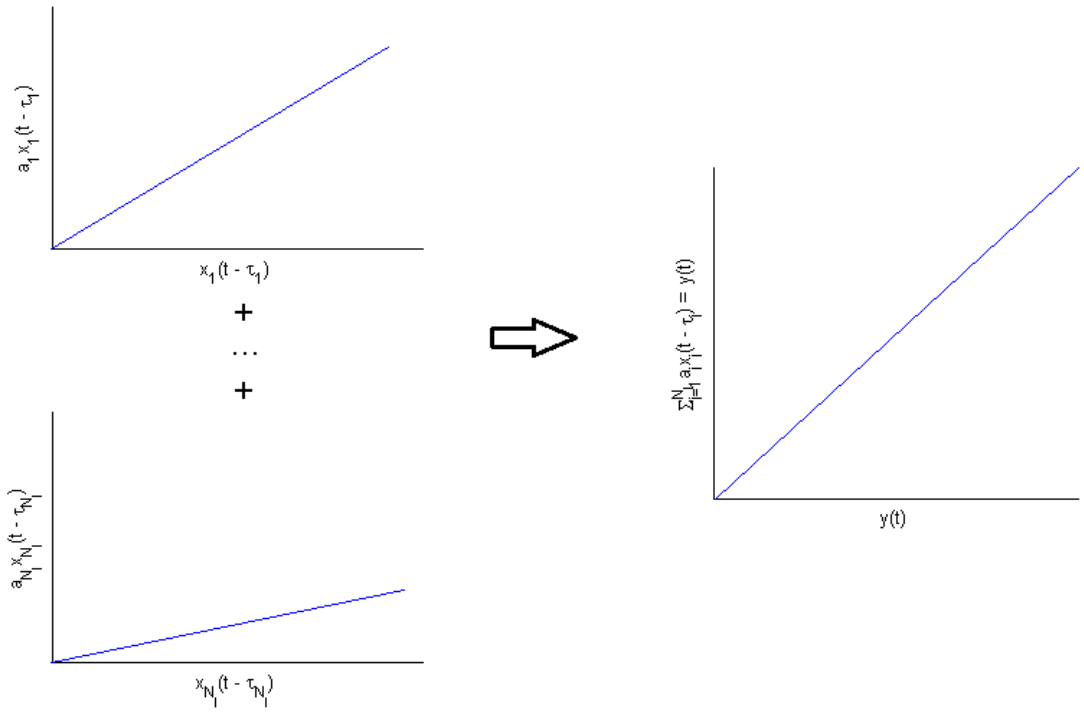

Figure 1.1: Linear regression model with multiple inputs and possible time lags

The work of Urbino and Horne (1991) and Sullera and Horne (2001), relied mostly on regression models of this type, without the inclusion of time lags. The inclusion of time lags was presented earlier in this research project, in the quarterly report for winter 2009. The M-ARX model applied by Lee et al. (2010) can also be seen as a multiple input linear regression model, where some of the inputs, were the same as the output, but with a constant time lag.

1.3.2 Single input convolution

The single input convolution model in continuous form is:

$$y(t) = \int_0^t x(t-\tau) f(\tau) d\tau \tag{2.3}$$

In discrete from this can be written as:

$$y(t_k) = \sum_{i=1}^{n(k)} a_i x(t_k - \tau_i) \tag{2.4}$$

Where k is a counter of time measurements, $n(k)$ denotes a number dependent on k, $a_i = f(\tau_i)\Delta\tau_i$, and $\Delta\tau_i$ is determined by the discretization used to approximate the integral. In equation (2.4) the function f is represented as a series of scalars, rather than a specific function of some undetermined parameters. That is why this is called a nonparametric model. Equation (2.4) clearly defines a linear regression system, much like Equation (2.2). The difference is that in the convolution model there are inputs from only one source, but with multiple time lags. Figure 1.2 shows the convolution model.

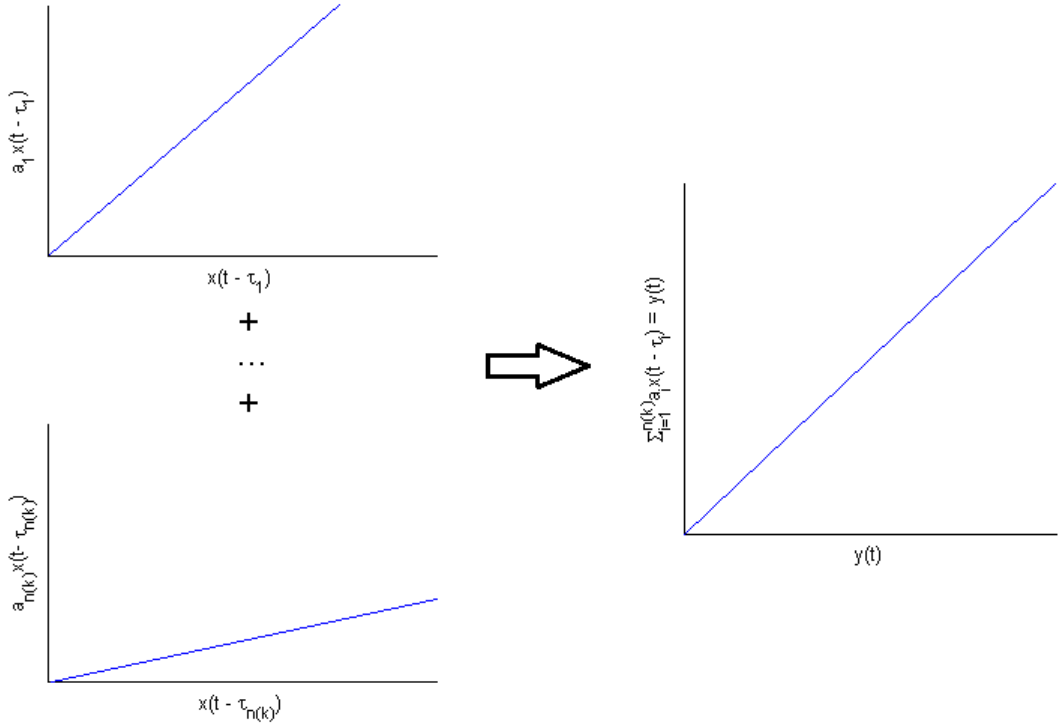

Figure 1.2: Convolution model. The slopes, a_i, associated with consecutive time lags are positively correlated. This is usually imposed by introducing a penalty for large variances between consecutive slopes a_i.

Again the output is a combination of linear functions, each of which can be defined by a single parameter, a_i. The factor a_i weights the influence that the input τ_i time units ago, has on the output at the current time, t.

In terms of the deconvolution problem it should be noted that there is one unknown (a_i) for each time lag, i.e. each predictor. If the discretization for τ coincides with the measurement times, there will be N_k equations and $n(k) = N_k$ unknowns. The unknowns associated with the small time lags (a_i for small i) will appear in more of the equations than those associated with large time lags, and therefore the a_i for small i can be determined with more confidence. For real data sets with associated noise, the system will often be close to singular. A simple way to fix that is to reduce the number of discretization points, i.e. time lags considered. Moreover, from the

physics of the problem, one can usually deduce that $f(t)$ should be continuous. Thus, there should be a positive correlation between consecutive values of a_i. This is can be enforced by adding a regularization term to the solution method, as was done e.g. by Schroeter (2004), and Nomura and Horne (2009).

1.3.3 Multiple input convolution

The convolution model with N_j inputs affecting a single output, in continuous form, is:

$$y(t) = \sum_{j=1}^{N_j} \int_0^t x_j(t-\tau) f_j(\tau) d\tau \tag{2.5}$$

The discrete analog is:

$$y(t_k) = \sum_{j=1}^{N_j} \sum_{i=1}^{n(k,j)} a_{ij} x_j(t_k - \tau_{ij}) \tag{2.6}$$

The coefficients, $a_{ij} = f_j(\tau_{ij})\Delta\tau_{ij}$, are analogous to what was seen for single well deconvolution. In terms of deconvolving (2.6), note that if there are N_k time measurements and the discretization of τ coincides with t, the number of equations is N_k but the number of unknowns is $N_j N_k$. This means that the system is highly underdetermined. To make up for this, the system is usually solved with a smaller number of discretization points and added regularization terms for consecutive a_{ij} in terms of i. Essentially, as the number of inputs, N_j, increases, the number of discretization points, $n(k,j)$, must decrease, and the reconstruction of $f_j(t)$ will be coarser. A graphical representation of multiple input convolution is given in Figure 1.3.

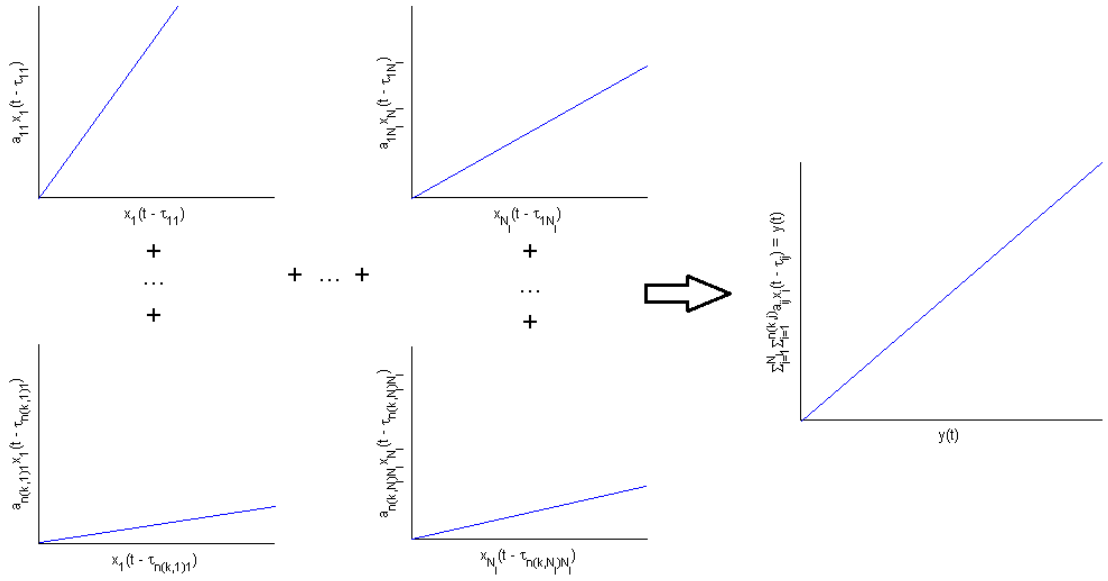

Figure 1.3: Multiple input convolution model. Generally the slopes, a_{ij}, associated with consecutive time lags are positively correlated, i.e. there is a positive correlation between the slopes going from top to bottom in the left part of the figure.

Multiple input deconvolution was applied for example by Lee et al. (2009) and in previous quarterly reports (summer 2009).

1.3.4 Alternating conditional expectation

The models that have been discussed so far can all be seen as linear regression models. That is, the output is a linear combination of multiple inputs, coming from different sources and with variable time lags. The alternating conditional expectation (ACE) model (Breiman and Friedman, 1985) is a more general model, in that it allows the functions of both the predictors and the responses to be nonlinear and nonparametric. The ACE model is as follows:

$$f\big(y(t)\big) = \sum_{j=1}^{N_j} g_j\left(x_j\big(t-\tau_j\big)\right) \tag{2.7}$$

The main restrictions on f and g_j are, that they must be smooth. This allows for great flexibility in fitting data, but the solutions will be highly susceptible to noise. This flexibility is perhaps more clear when viewing the discrete form:

$$f\big(y(t_k)\big) = \sum_{j=1}^{N_j} g_j\left(x_j\big(t_k-\tau_j\big)\right) \tag{2.8}$$

Note that $f(y(t_k))$ and $g_j\left(x_j(t_k-\tau_j)\right)$ are simply scalars which are only restricted to have a positive correlation with nearby scalars in terms of k. The cost of this increased flexibility is that the predictive power of the ACE model will often be poor. Figure 1.4 illustrates the ACE model graphically.

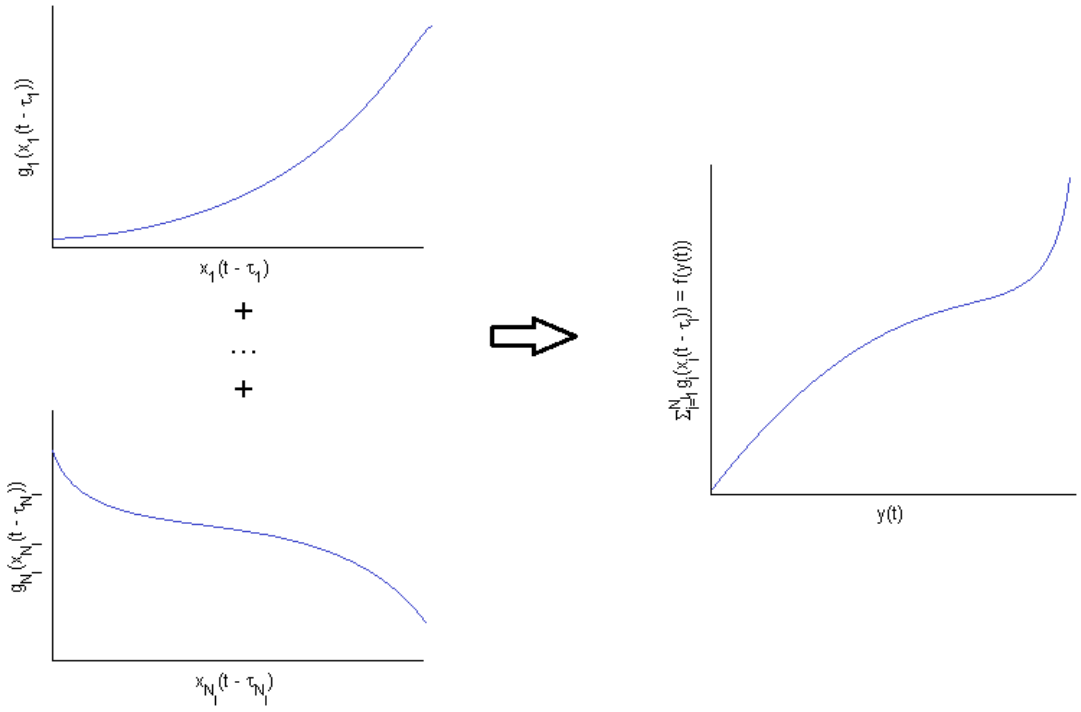

Figure 1.4: A graphical representation of the ACE model with inputs from multiple sources sampled with a possible time lag

The ACE model shown in (2.7) can be compared to the multiple input linear regression model (2.2). Note that simple straight lines which can be defined by a single parameter, have been replaced by a continuous sequences of N_k points. Thus the number of unknown variables for the model in (2.8) is $N_j N_k$. The ACE model was applied in the winter 2009 quarterly report and by Horne and Schutz (2008). The ACE algorithm could also be used in an autoregressive manner, much like the M-ARX model. We experimented with this approach, but found that it had stability issues, and poor predictive power.

One of the drawbacks of using ACE in the way described by Equation (2.7) is that this model assumes that the output is dependent on each source with a unique time lag for each source. However, the physics of a problem sometimes indicate that the response is a function of each source with multiple time lags. The ACE model could easily be used to take in data with multiple time lags as predictors, i.e.:

$$f\big(y(t)\big) = \sum_{j=1}^{N_j} \sum_{i=1}^{n} g_{ij}\left(x_j\big(t-\tau_{ij}\big)\right) \tag{2.9}$$

where n denotes the number of time lags taken into account. The graphical representation is shown in Figure 1.5.

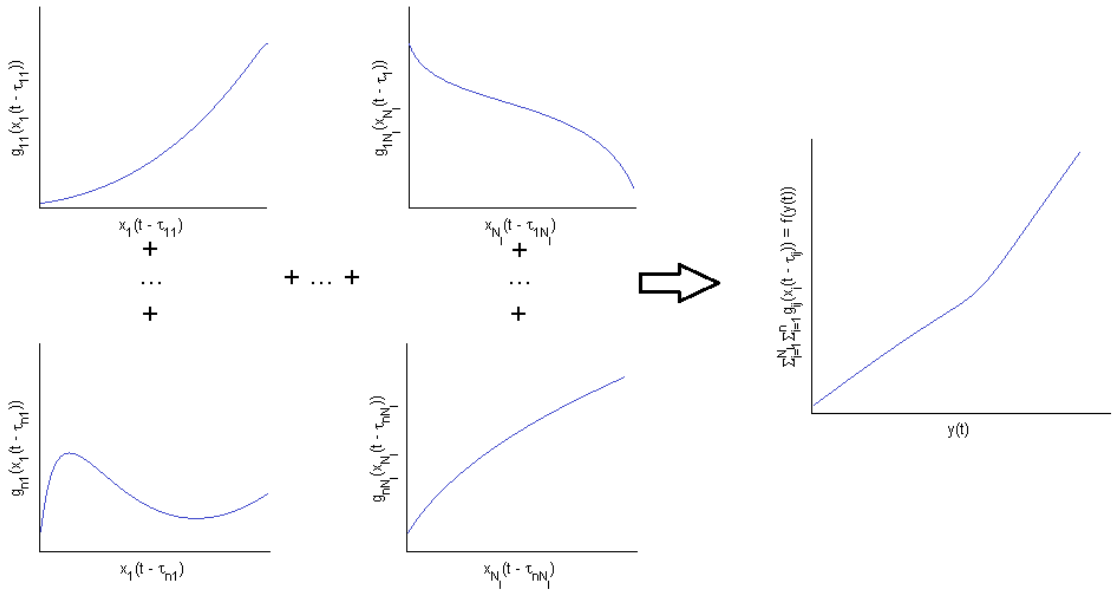

Figure 1.5: A graphical representation of the ACE model with inputs from multiple sources sampled with multiple time lag

Although this model would be exceptionally robust in fitting data, its predictive power would most likely be very poor. The number of equations in this case would be N_k and the number of unknowns nN_jN_k. Additional constraints might be applicable to the model, e.g. by requiring there to be some sort of continuity between consecutive functions g_{ij} in terms of i. The details of how to impose such a continuity constraint are not clear at this point. It might also be possible to use an alternative predictor, e.g. cumulative flow rate, to make the predictions of ACE more unique and meaningful.

When using such a flexible regression method, the nature of the problem at hand should be carefully examined, since the nonuniqueness of the solution may lead to deceptively good data fits with poor representation of the physics of the problem. This may in some cases be avoided by choosing the predictors and responses carefully (e.g. based on physical intuition), and using a more restrictive regression model.

1.4 ADVECTION-DISPERSION EQUATION WITH TIME VARYING COEFFICIENTS

An important step forward was made in the interpretation and application of tracer transport data with the development of an analytical solution for tracer transport under transient flow conditions (transient flow rate and dispersion). In this case, the advection dispersion equation would be:

$$\frac{\partial c}{\partial t} + u(t)\frac{\partial c}{\partial x} - D(t)\frac{\partial^2 c}{\partial t^2} = 0 \tag{2.10}$$

Here we will show the development of a solution to this equation, using the known solution for the impulse response on an infinite x-domain, assuming constant velocity, u_0, and dispersivity, D_0. This solution, for a tracer slug (impulse) of mass m released at $x = 0$, at time t_0 is:

$$c(x,t|t_0,u_0,D_0) = \frac{m}{A\sqrt{4\pi D_0(t-t_0)}} e^{-\frac{(u_0(t-t_0)-x)^2}{4D_0(t-t_0)}} \quad t > t_0 \tag{2.11}$$

This (which is applicable under resident fluid conditions (Kreft and Zuber, 1978)) essentially describes a normal distribution in x, with a linearly increasing mean, $u_0(t-t_0)$, and variance, $2D_0(t-t_0)$. The state of the tracer concentration as a function of x at a time t_1 is shown in Figure 1.6, along with the observed concentration at a location ξ, at times $t_0 < t < t_1$.

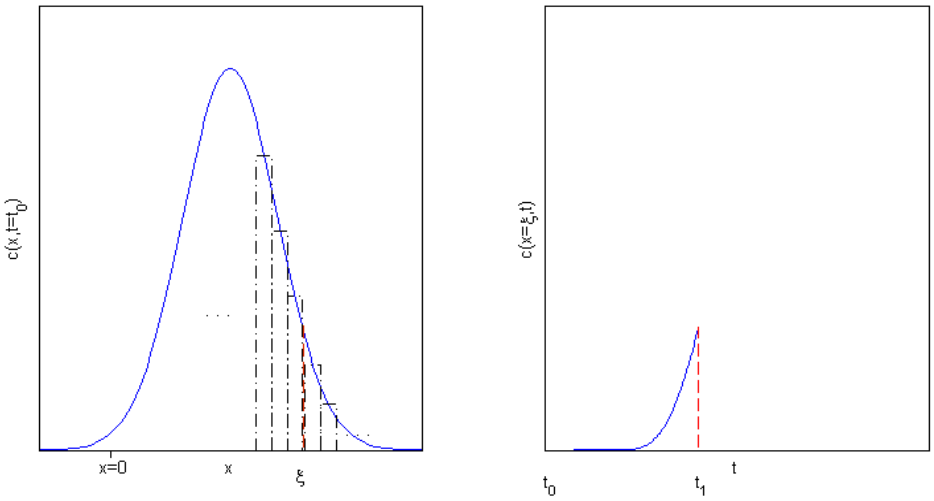

Figure 1.6: Tracer slug as a function of x (on the left) and as seen at location ξ, up until time t_1.

Now, say that at time, t_1, the injection rate changes such that the flow velocity and dispersion become u_1 and D_1. The observed returns at ξ after t_1 can be computed by identifying that the response at ξ is a combination of impulse responses coming from small impulses released at incremental locations along x (dashed boxes in Figure 1.6), each with associated mass:

$$dm(x,t_1) = c(x,t_1|t_0,u_0,D_0)Adx = \frac{m\,dx}{\sqrt{4\pi D_0(t_1-t_0)}}e^{-\frac{(u_0(t_1-t_0)-x)^2}{4D_0(t_1-t_0)}} \tag{2.12}$$

Thus, the concentration function becomes:

$$c\big(x,t|t_0,u_0,D_{0,}t_1,u_1,D_1\big) = \begin{cases} c(x,t|t_0,u_0,D_0) & t_0 < t < t_1 \\ \int_{-\infty}^{\infty} \frac{c(x-\xi,t|t_1,u_1,D_1)}{m}\,dm(\xi,t_1) & t_1 > t \end{cases} \tag{2.13}$$

or:

$$c\big(x,t|t_0,u_0,D_{0,}t_1,u_1,D_1\big) = \begin{cases} c(x,t|t_0,u_0,D_0) & t_0 < t < t_1 \\ \frac{A}{m}\int_{-\infty}^{\infty} c(x-\xi,t|t_1,u_1,D_1)c(\xi,t_1|t_0,u_0,D_0)\,d\xi & t_1 > t \end{cases} \tag{2.14}$$

Note that after time t_1 we have a convolution of two impulse responses, in terms of x. Remembering that the impulse response can be viewed as a normal probability distribution, scaled by m/A, we obtain:

$$c(x,t|t_0,u_0,D_0) = \frac{m}{A}\frac{1}{\sqrt{4\pi D_0(t-t_0)}}e^{-\frac{(u_0(t-t_0)-x)^2}{4D_0(t-t_0)}} = \frac{m}{A}f_{\mathcal{N}}(x|u_0(t-t_0),2D_0(t-t_0)) \quad t > t_0 \tag{2.15}$$

where $f_{\mathcal{N}}(x|u_0(t-t_0),2D_0(t-t_0))$ denotes the probability density function (pdf) for a normally distributed variable with mean $u_0(t-t_0)$ and variance $2D_0(t-t_0)$. The first key observation here is that the sum, Y, of two normally distributed random variables, say X_1 and X_2, will have a mean equal to the sum of the means of X_1 and X_2. Similarly the variance of Y will be the sum of the variances of X_1 and X_2. Secondly it is important to observe, that the pdf of Y, is the convolution of the pdf's of X_1 and X_2, which is precisely what was seen in (2.14). Thus,

$$
\begin{aligned}
&c\big(x,t|t_0,u_0,D_{0,}t_1,u_1,D_1\big)\\
&=\begin{cases} c(x,t|t_0,u_0,D_0) & t_0<t<t_1\\ \dfrac{m}{A}\displaystyle\int_{-\infty}^{\infty} f_{\mathcal{N}}(x-\xi|u_1(t-t_1),2D_1(t-t_1))f_{\mathcal{N}}\big(\xi\big|u_0(t_1-t_0),2D_0(t_1-t_0)\big)\,d\xi & t_1>t \end{cases}\\
&=\begin{cases} \dfrac{m}{A}f_{\mathcal{N}}\big(x\big|u_0(t-t_0),2D_0(t-t_0)\big) & t_0<t<t_1\\ \dfrac{m}{A}f_{\mathcal{N}}(x|u_0(t_1-t_0)+u_1(t-t_1),2D_0(t_1-t_0)+2D_1(t-t_1)) & t_1>t \end{cases}
\end{aligned}
\tag{2.16}
$$

From this point it is straight forward to infer that if the flow rate is changed again, with a corresponding change in u and D, these changes can be incorporated into the mean and variance of $f_{\mathcal{N}}$. For example after k changes in injection:

$$
\begin{aligned}
&c\big(x,t|t_0,u_0,D_{0,}\dots,t_k,u_k,D_k\big)\\
&=\frac{m}{A}f_{\mathcal{N}}\big(x\big|u_0(t_1-t_0)+\cdots+u_k(t-t_k),2D_0(t_1-t_0)+\cdots+2D_k(t-t_k)\big)\quad t_k>t
\end{aligned}
\tag{2.17}
$$

Letting the changes in time, $\Delta t=t_{i+1}-t_i$, become incrementally small leads to the solution of (2.10), given a tracer slug of mass m released at $x=0$, at time t_0:

$$
\begin{aligned}
c(x,t|u(t),D(t)) &= \frac{m}{A}f_{\mathcal{N}}\left(x\left|\int_{t_0}^{t}u(\tau)d\tau,2\int_{t_0}^{t}D(\tau)d\tau\right.\right)\quad u(t),D(t)\geq 0\\
&=\frac{m}{A\sqrt{4\pi\int_{t_0}^{t}D(\tau)d\tau}}e^{-\frac{\left(\int_{t_0}^{t}u(\tau)d\tau-x\right)^2}{4\int_{t_0}^{t}D(\tau)d\tau}}\quad u(t),D(t)\geq 0
\end{aligned}
\tag{2.18}
$$

A discrete (albeit slightly convoluted) version of this formulation was derived by Carlier (2008). Carlier also listed three other impulse response solutions, derived for different boundary conditions. The solution given for a constant flux concentration boundary on a semiinfinite domain for constant u and D is (Kref and Zuber, 1978):

$$
c(x,t|t_0,u_0,D_0)=\frac{mx}{Au_0(t-t_0)\sqrt{4\pi D_0(t-t_0)}}e^{-\frac{(u_0(t-t_0)-x)^2}{4D_0(t-t_0)}}\quad t>t_0,x>0 \tag{2.19}
$$

Carlier generalized this solution for a discrete number of flow periods. If we let these discrete periods become incrementally small the solution generalizes to an expression similar to Equation (2.18):

$$c(x,t|u(t),D(t)) = \frac{mx}{A\int_{t_0}^{t} u(\tau)d\tau \sqrt{4\pi \int_{t_0}^{t} D(\tau)d\tau}} e^{-\frac{\left(\int_{t_0}^{t} u(\tau)d\tau - x\right)^2}{4\int_{t_0}^{t} D(\tau)d\tau}} \quad u(t), D(t), x \geq 0 \quad (2.20)$$

Here it has been shown that two impulse response solutions which were derived for constant u and D, can be generalized to solutions with time varying coefficients by replacing ut with $\int_{t_0}^{t} u(\tau)d\tau$ and Dt with $\int_{t_0}^{t} D(\tau)d\tau$. Other versions of impulse response solutions to the advection dispersion equation could be generalized in the same manner, e.g. Equations (7), (8), (26) and (27) in Carlier (2008).

Figure 1.7 shows the semiinfinite and infinite impulse responses to a sinusoidal flow rate and a step-wise varying flow rate (in this case we let $q(t) = u(t) = D(t)$).

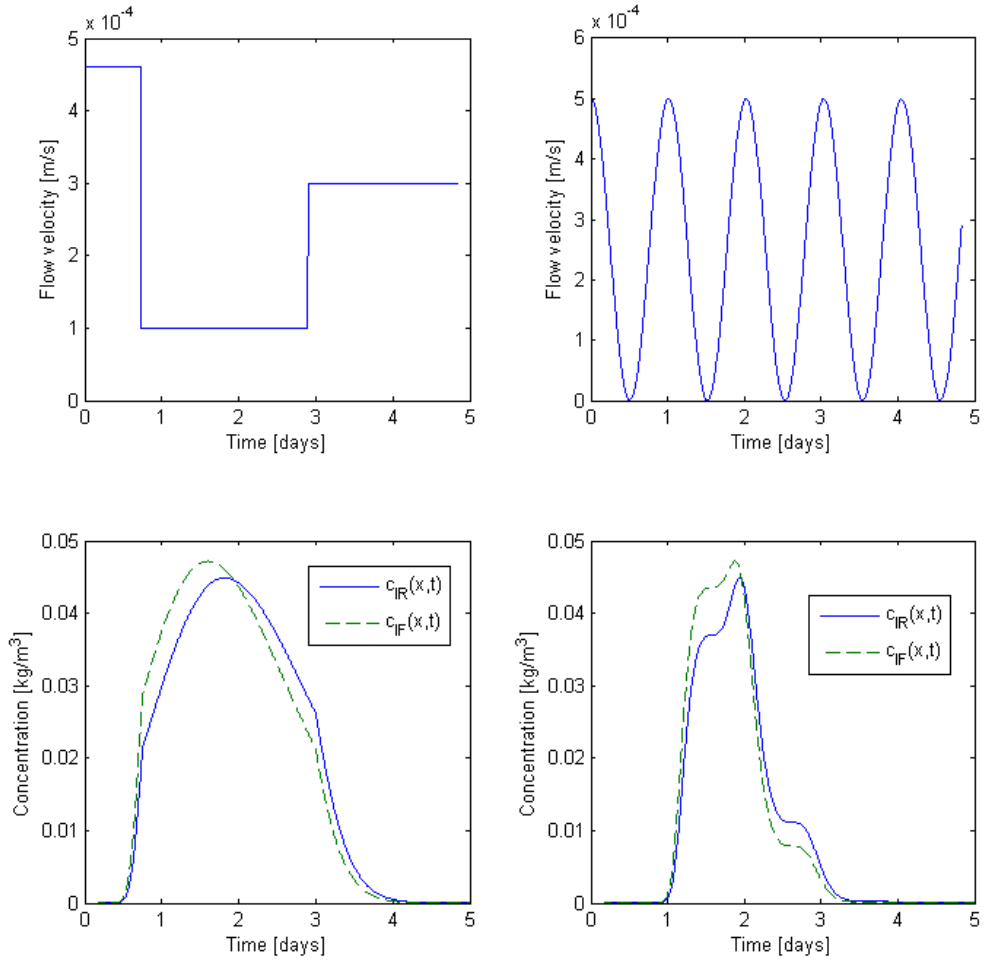

Figure 1.7: Impulse responses to the advection-dispersion equation with varying flow velocity and dispersion. The time varying flow velocities are above the corresponding impulse responses for an infinite medium (c_{IR}) and a semiinfinite medium (c_{IF}). Here $m = 1kg$, $A = 1m^2, x = 40m$, and $D(t) = u(t)$.

The impulse response can be used to find the response for any transient input of the tracer concentration. To see this, imagine a series of impulses, released from point $x = 0$ at times t'. Each impulse has mass:

$$dm(t') = c(x = 0, t')u(t')Adt' = c_0(t')u(t')Adt' \tag{2.21}$$

where $c_0(t)$ is a time varying concentration introduced to the flow stream at $x = 0$. Replacing m in (2.18) with $dm(t')$, and integrating with respect to t' over all times from 0 to t, leads to the concentration for any time varying concentration injected.

$$c(x,t|u(t),D(t),c_0(t)) = \int_0^t \frac{dm(t')}{A\sqrt{4\pi\int_{t'}^t D(\tau)d\tau}} e^{-\frac{\left(\int_{t'}^t u(\tau)d\tau - x\right)^2}{4\int_{t'}^t D(\tau)d\tau}}$$
$$= \int_0^t \frac{c_0(t')u(t')}{\sqrt{4\pi\int_{t'}^t D(\tau)d\tau}} e^{-\frac{\left(\int_{t'}^t u(\tau)d\tau - x\right)^2}{4\int_{t'}^t D(\tau)d\tau}} dt' \quad (2.22)$$

Similarly, for the semiinfinite case, replacing m in Equation (2.20) with $dm(t')$ leads to:

$$c(x,t|u(t),D(t),c_0(t)) = \int_0^t \frac{c_0(t')u(t')x}{\int_{t'}^t u(\tau)d\tau\sqrt{4\pi\int_{t'}^t D(\tau)d\tau}} e^{-\frac{\left(\int_{t'}^t u(\tau)d\tau - x\right)^2}{4\int_{t'}^t D(\tau)d\tau}} dt' \quad (2.23)$$

Tracer responses for the same situation as presented in Figure 1.7, except with a linearly increasing concentration, are shown in Figure 1.8.

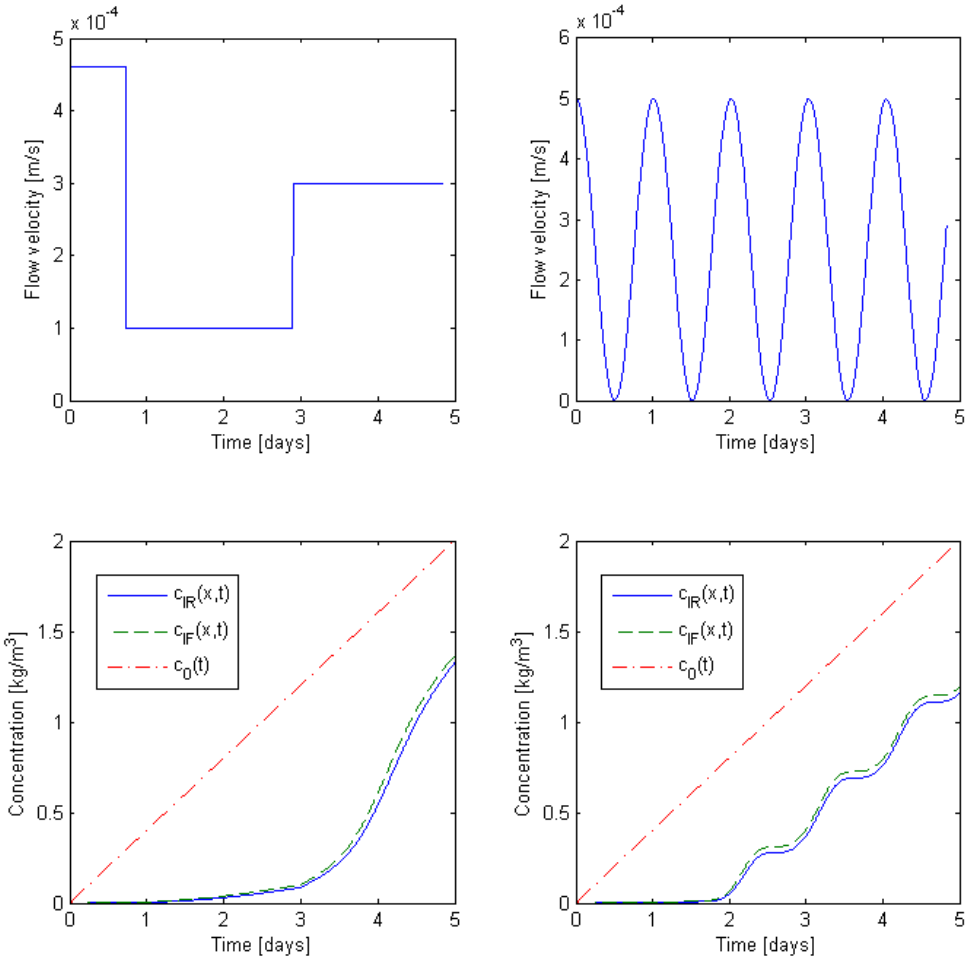

Figure 1.8: Responses to the advection-dispersion equation with a linearly increasing injection concentration (c_0) and varying flow velocity and dispersion. The time varying flow velocities, $u(t)$, are above the corresponding responses for an infinite medium (c_{IR}) and a semiinfinite medium (c_{IF}). Here $m = 1kg$, $A = 1m^2, x = 40m$, and $D(t) = u(t)$.

1.4.1 Cumulative injection model for multiwell tracer tests

Although the models presented in Equations (2.22) and (2.23) lack some essential properties, e.g. matrix diffusion (Jensen, 1983), they give some insight into which predictors might be appropriate for finding a unique transfer function between injector and producer. Take Equation (2.22) for example. Assuming that dispersion depends on velocity as $D(t) = \alpha u(t)$ and letting $q(t) = Au(t)$, Equation (2.22) can be rewritten as:

$$c(x,t|q(t),c_0(t)) = \int_0^t \frac{c_0(t')q(t')}{\sqrt{4\pi A\alpha \int_{t'}^t q(\tau)d\tau}} e^{-\frac{\left(\int_{t'}^t q(\tau)d\tau - Ax\right)^2}{4A\alpha \int_{t'}^t q(\tau)d\tau}} dt' \tag{2.24}$$

Noting that:

$$\int_{t'}^t q(\tau)d\tau = \int_0^t q(\tau)d\tau - \int_0^{t'} q(\tau)d\tau = Q_0(t) - Q_0(t')$$
$$dQ_0(t') = q(t')dt' \tag{2.25}$$

Substituting into (2.24) gives:

$$\begin{aligned} c\big(x,t\big|Q_0(t),c_0(t)\big) &= \int_0^{Q_0(t)} \frac{c_0\big(Q_0(t')\big)}{\sqrt{4\pi A\alpha\big(Q_0(t)-Q_0(t')\big)}} e^{-\frac{\left(Q_0(t)-Q_0(t')-Ax\right)^2}{4A\alpha\left(Q_0(t)-Q_0(t')\right)}} dQ_0(t') \\ &= \int_0^{Q_0(t)} c_0\big(Q_0(t')\big)\kappa\big(Q_0(t)-Q_0(t')\big)dQ_0(t') \end{aligned} \tag{2.26}$$

Equation (2.26) is a convolution equation in terms of cumulative injection. To be able to use it the concentration needs to be represented as a function of cumulative injection, and the transfer function, κ, will also be a function of cumulative injection. This transfer function, however, is representative of the connectivity between the wells, independent of what the current injection rate is. Therefore, it can be applied to predict tracer breakthrough at any injection rate, and it can be compared to other such transfer functions without the bias caused by variable injection rates. Moreover, this type of model might work well in conjunction with a pressure or rate based model, since the signals generated by varying both injection rate and concentration at the same time could be interpreted by these methods. For example, a nonparametric deconvolution approach, similar to that introduced in the quarterly report from summer 2009 would probably work well in cases where the flow rates are strongly governed by simple fracture networks.

Equation (2.26) was derived by an alternative method in the quarterly report from fall 2010 where the advection-dispersion equation was written as:

$$\frac{\partial C}{\partial Q} = V_\alpha \frac{\partial^2 C}{\partial V_x^2} - \frac{\partial C}{\partial V_x} \tag{2.27}$$

The following change of variables had been made:

$$Q(t) = A\int_0^t u(\tau)d\tau \tag{2.28}$$

$$V_x = Ax \tag{2.29}$$

$$V_\alpha = A\alpha \tag{2.30}$$

An important result of deriving Equation (2.26) by these two methods was that if the injection and detection of the tracer is in resident mode, i.e. the infinite media formulation, then the dispersion coefficient, $D(t)$ can be any function of time and Equation (2.26) will still hold. For all other tracer injection and detection modes, i.e. models with semi-infinite media boundary conditions, it must be assumed that $D(t) = \alpha u(t)$, for Equation (2.26) to apply.

1.5 INTERPRETATION METHODS FOR PRESSURE AND FLOW RATE DATA

The interpretation of pressure signals has been a long standing research topic in both the ground water hydrology and the petroleum sciences. A multitude of regression methods, analytical models and numerical models have been documented. This section provides a brief overview of a few notable methods, relating rate-pressure, pressure-pressure and rate-rate interactions between wells. Nonparametric models based on the pressure equation, will in generally involve solutions of the deconvolution problem, because pressure disturbances in the reservoir are superposable. The pressure and rate in a well are often linearly related, which makes it possible to find a unique transfer function between pressure, or rate, in one well and pressure, or rate, in another well.

1.5.1 Rate-pressure models

Rate-pressure transfer functions are commonly used in well tests and interference tests. A multitude of analytical solutions for these types of models are in the literature, some of which are given in Lee (1982). Some very interesting generalizations of the analytical well test models for fractal dimensions can be found in the paper by Barker (1988).

If an analytical rate-pressure model is not assumed, one can still assert (based on the superposition principle) that a change in production rate at $\boldsymbol{x} = 0$ will induce a pressure change at $\boldsymbol{x}$ according to the convolution equation:

$$p(\boldsymbol{x}, t) = p_0(\boldsymbol{x}) - \int_0^t q(\mathbf{0}, t-\tau)g(\boldsymbol{x}, \tau)d\tau \tag{2.31}$$

Discusssions of the validity of this assumption can be found in Deng and Horne (1993) and Schroeter and Gringarten (2007), which conclude that if wellbore storage and skin effects are negligible, it should hold (and in many other cases as well). In other words, if q and p are representative for measurements within the formation, then Equation (2.31) should hold.

The unknown in Equation (2.31) is the pressure impulse response, g, which is the time derivative of the rate normalized pressure, $p_u(\boldsymbol{x}, t)$. This is the characteristic rate-pressure transfer function

between the two wells in question, and it is determined by the physics of the reservoir. It is related to the diagnostic pressure derivative in well testing as follows:

$$dp_u(\boldsymbol{x},t)/dln(t) = t\,dp_u(\boldsymbol{x},t)/dt = tg(\boldsymbol{x},t) \tag{2.32}$$

Schroeter et al. (2004) developed a widely used nonparametric single well deconvolution method for obtaining $tg(\boldsymbol{x},t)$ and $q(\mathbf{0},t)$ simultaneously. Some aspects of this method were improved by Levitan (2005) and Pimonov et al. (2009), but the basic method in the 2004 publication is still the industry standard. The crux of the method is to transform the problem to a logarithmic time scale. This makes the problem nonlinear, which is not good, but it also makes it easier to capture important parts of pressure transient with relatively few unknown parameters. A number of alternative deconvolution methods have been proposed e.g. by Nomura and Horne (2009) and many others which are referred to in Schroeter et al (2004).

Levitan (2006) also extended the work of Schroeter et al. (2004) to include the effects of multiple wells. The multiwell convolution equation is:

$$p(\boldsymbol{x_i},t) = p_0(\boldsymbol{x_i}) - \sum_{j=1}^{N_w}\int_0^t q\big(\boldsymbol{x_j},t-\tau\big)g\big(\Delta\boldsymbol{x_{ij}},\tau\big)d\tau \tag{2.33}$$

where i and j refer to each of the N_w wells in the reservoir. Levitan (2006) asserts that only pressure build-up data can be used for the deconvolution method, because variable skin effects, which are often seen between drawdown and build-up, would violate the deconvolution principle. He also stresses that it is impractical to extract information about the interwell transfer functions between wells i and j when both wells are active. The reason is that the pressure signal from the active well on itself (p_{ii}) will overshadow the interwell pressure signal (p_{ij}). Finally he mentions that the multiwell rate-pressure convolution problem could benefit from work on optimal production-injection signals, that would provide transients that are well suited for deconvolution.

It is clear from this summary that researchers of well-to-well interaction in terms of rate-pressure data have worked on problems similar to those that have been found for well-to-well tracer interactions in this research project. Schroeter et al. (2004) solved the problem of finding an appropriate time scale by a logarithmic transformation of the time scales. In the quarterly report from summer 2009 we faced a similar problem of time scales that were hard to quantify, which was solved using a set of heuristic search algorithms. In the this report we are suggesting a transformation of the time variable into cumulative injection. Finally, we dealt with the problem of designing injection schedules that provide highly informative tracer transients, which is similar to the pressure transient topic mentioned by Levitan (2006).

To highlight some of the differences between the pressure and tracer problem, we note that the pressure transport is governed by the diffusion equation, and the response is generally a linear function of the pressure change that caused the disturbance. Moreover, most of the pressure response is usually seen within a very short time frame, as compared to the tracer response. A

pressure pulse is usually much easier to send and measure than is a tracer pulse. The tracer response is governed by the advection-dispersion equation. This means the tracer response is a linear function of the injected tracer concentration (which caused the disturbance), but a nonlinear function of the flow rate. Therefore, the well-to-well transfer functions (κ_{ij}) that were found by deconvolution in the summer 2009 quarterly report were specific to a single set of steady-state injection and production rates. In cases where fractures constrain the streamlines between wells this problem can sometimes be solved by viewing the transfer function in terms of cumulative injection.

1.5.2 Pressure-pressure models

Pressure-pressure deconvolution studies are less abundant in the literature. In fact we only reviewed a single study of pressure-pressure deconvolution, i.e. that of Onur et al. (2009). The work of Onur et al. utilized the deconvolution algorithm of Schroeter et al. (2004) with the extensions from Pimonov et al. (2009). It is shown that the pressure-pressure relationship can be modeled by the convolution equation:

$$p(\boldsymbol{x},t) = p_0(\boldsymbol{x}) - \int_0^t p(0,t-\tau)G(\boldsymbol{x},\tau)d\tau \tag{2.34}$$

where $G(\boldsymbol{x},t)$ is the pressure-pressure impulse response that is to be determined. After comparing Equations (2.34) and (2.31), it should not be surprising that the same deconvolution methods are applicable.

Much of the discussion in Onur et al. is on the diagnostic interpretation of tG, which is similar to that of the diagnostic derivative, tg, for rate-pressure responses. The main advantages mentioned for pressure-pressure deconvolution are that pressure signals are often less susceptible to noise and that G is independent of wellbore storage. It is stated that G is a unique function of the skin factor and the hydraulic diffusivity. This also means that problems are encountered in the presence of variable skin, and that permeability and porosity cannot be estimated individually.

1.5.3 Rate-rate models

Rate-rate models seem to have captured the attention of a slightly different group of researchers within the petroleum industry. The methods of characterizing the transfer functions in rate-rate modeling have been less focused on capturing the details of the transients, and more focused on multiwell applications and the long term effects that controlled injection has on production rates. Much work has been done on the so called capacitor-resistor models (CRM), which draw upon an analogy between the well-to-well connections and electronic circuitry. Several variations of the CRM model have been suggested, e.g. by Yousef et al. (2005), Sayarpour et al. (2006) and Lee et al. (2009, 2010). The governing differential equation used for the development of the CRM, assuming constant bottomhole pressure at the producer, is:

$$\frac{dq_P(t)}{dt} + \frac{1}{\mathrm{T}}q_P(t) = \frac{1}{\mathrm{T}}q_I(t) \tag{2.35}$$

Here the subscripts P and I refer to production and injection, and T is a time constant representative of the drainage volume between the injector and producer. This equation has the solution:

$$q_P(t) = q_P(0)e^{-\frac{t}{\mathrm{T}}} + \int_0^t q_I(t-\tau)\frac{e^{-\frac{\tau}{\mathrm{T}}}}{\mathrm{T}}d\tau \tag{2.36}$$

It is clear by contemplating this solution that the long term production rate will tend to follow the injection rate, and the time lag will be defined by the time constant T. Note also that the second term on the right is a convolution integral, similar to that shown in Equations (2.31) and (2.34). In this case, however, an analytical transfer function is assumed to be known, and only the time constant, T, is what needs to be determined.

A multiwell analog of equation (2.36) was also derived by Yousef et al. (2006) (here assuming constant bottomhole pressure at the producer):

$$q_{Pi}(t) = \lambda_{Pi}q_{Pi}(0)e^{-\frac{t}{\mathrm{T_{Pi}}}} + \sum_{j=1}^{N_I}\int_0^t q_{Ij}(t-\tau)\lambda_{PiIj}\frac{e^{-\frac{\tau}{\mathrm{T_{PiIj}}}}}{\mathrm{T_{PiIj}}}d\tau \tag{2.37}$$

In this case, the indexes i and j refer to specific producers and injectors, respectively. The factor λ_{Pi} should ideally be 1, but was included to allow more flexibility in fitting the model at late times. Note here that given constant injection rates, the late time production rate will be the weighted sum of the injection rates, with λ_{PiIj} defining the weights. Thus, λ_{PiIj} can be viewed as the long term contribution of injection in injector j to the production in producer i.

The CRM model is essentially a parametric model, where the unknowns are the parameters λ and T. An alternative approach, more in the line with what this research project has focused on, and the work of Schroeter et al. (2004), is to model the transfer function nonparametrically. Since the analytical solution of the rate-rate model is based on the convolution integral, a deconvolution approach is well suited to find the nonparametric transfer function. This approach was carried out by Lee et al. (2009), where he proposed a model of the form:

$$q_{Pi}(t) = q_{Pi}(0)e^{-\frac{t}{\mathrm{T_{Pi}}}} + \sum_{j=1}^{N_I}\int_0^t q_{Ij}(t-\tau)h_{ij}(\tau)d\tau \tag{2.38}$$

in which h denotes the nonparametric function to be determined. Lee et al. solved this equation using a deconvolution algorithm, similar to the one we proposed in the quarterly report from summer 2009. They did not, however, adjust the time scales dynamically and therefore the estimates for h were rather coarse. We suspect that the main reason for the method working as well as reported is that the test examples were based on data where the flow rates would stabilize

quickly and thus the model was mostly being fitted to steady-state data points. This may very well applicable in practice, especially with incompressible (or slightly compressible) flows, where the time constant should be very small.

In Lee et al. (2010) the development of the rate-rate model was based on a set of coupled differential equations similar to Equation (2.35), where for each of the N_P producers there was an equation of the form:

$$\frac{dq_{Pi}(t)}{dt} + \sum_{k=1}^{N_P} \frac{\alpha_{ik}}{\mathrm{T_i}} q_{Pk}(t) = \sum_{j=1}^{N_I} \frac{\beta_{ij}}{\mathrm{T_i}} q_{Ij}(t) \tag{2.39}$$

This set of equations can be represented in matrix form as:

$$\frac{d\boldsymbol{q_P}(t)}{dt} + A_c \boldsymbol{q_P}(t) = B_c \boldsymbol{q_I}(t) \tag{2.40}$$

where:

$$A_c = \begin{bmatrix} \mathrm{T}_1 & \cdots & 0 \\ \vdots & \ddots & \vdots \\ 0 & \cdots & \mathrm{T}_{N_P} \end{bmatrix}^{-1} \begin{bmatrix} \alpha_{11} & \cdots & \alpha_{1N_P} \\ \vdots & \ddots & \vdots \\ \alpha_{N_P1} & \cdots & \alpha_{N_PN_P} \end{bmatrix} \tag{2.41}$$

and:

$$B_c = \begin{bmatrix} \mathrm{T}_1 & \cdots & 0 \\ \vdots & \ddots & \vdots \\ 0 & \cdots & \mathrm{T}_{N_P} \end{bmatrix}^{-1} \begin{bmatrix} \beta_{11} & \cdots & \beta_{1N_P} \\ \vdots & \ddots & \vdots \\ \beta_{N_I1} & \cdots & \beta_{N_IN_P} \end{bmatrix} \tag{2.42}$$

The solution to (2.40) is quite similar to equations (2.36) and (2.37), i.e.:

$$\boldsymbol{q_P}(t) = \boldsymbol{q_P}(0) e^{-A_c t} + \int_0^t \boldsymbol{q_I}(t-\tau) B_c e^{-A_c \tau} d\tau \tag{2.43}$$

The main additional development in this solution is that the producer-producer interactions are now also taken into account, in addition to the injector-producer interactions. For practical applications it is more convenient to deal with the discrete form of Equation (2.40). This was done by Lee et al. (2010), which presented the discrete counterpart of (2.40) as:

$$\boldsymbol{q_P}(n+1) = -A\boldsymbol{q_P}(n) + B\boldsymbol{q_I}(n) \tag{2.44}$$

where n is a time-like discrete variable, and A and B are the discrete counterparts of A_c and B_c, respectively. Equation (2.44) defines a multivariate autoregressive model for determining $\boldsymbol{q_I}$ with exogenous inputs, $\boldsymbol{q_I}$. It is referred to as the M-ARX model. A set of $N+1$ measurements yields N equations which can be solved together to find the elements of A and B.

$$[\boldsymbol{q_P}(2) \dots \boldsymbol{q_P}(N+1)] = [-A+B]\begin{bmatrix} \boldsymbol{q_P}(1) & \dots & \boldsymbol{q_P}(N) \\ \boldsymbol{q_I}(1) & \dots & \boldsymbol{q_I}(N) \end{bmatrix} \tag{2.45}$$

To ensure that the solution is stable, it is important to add the constraint that $A \preccurlyeq 1$ (element-wise), or that $(I+A)^{-1}B \preccurlyeq 1$. It can be shown via the z-transform (discrete analog of Laplace transform) that if the injection rates are kept constant, the production will stabilize at:

$$\boldsymbol{q_P} = (I+A)^{-1}B\boldsymbol{q_I} = F\boldsymbol{q_I} \tag{2.46}$$

The matrix $F = (I+A)^{-1}B$ then defines the interwell connectivity for each of the injector-producer pairs in terms of flow rate.

If the total compressibility is small, the flow rates stabilize relatively quickly, i.e. within a few hours. This would likely be the case for production from enhanced geothermal systems, and thus the M-ARX model would be ideal, e.g. for reinjection scheduling.

1.6 KERNEL ESTIMATION

1.6.1 Kernel estimation in a single injector, single producer system

In this section we illustrate how to obtain an estimate of the kernel or transfer function, κ, that is representative of a single fracture connecting an injector and a producer. To illustrate the concept we created data with the reservoir simulator FEFLOW using variable flow rate and concentration conditions. The two-dimensional FEFLOW model, with a one-dimensional fracture, is illustrated in Figure 1.9.

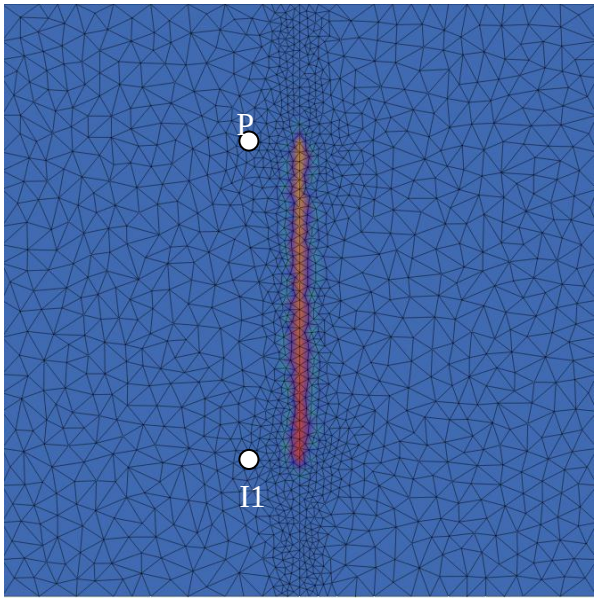

Figure 1.9: Two-dimensional FEFLOW model of tracer travelling along a single fracture. The injector and producer are labeled I1 and P1, respectively.

The injected flow rate was varied in steps as shown in Figure 1.10. Since the simulation involved single-phase liquid flow, the production rate was very similar to the injection rate.

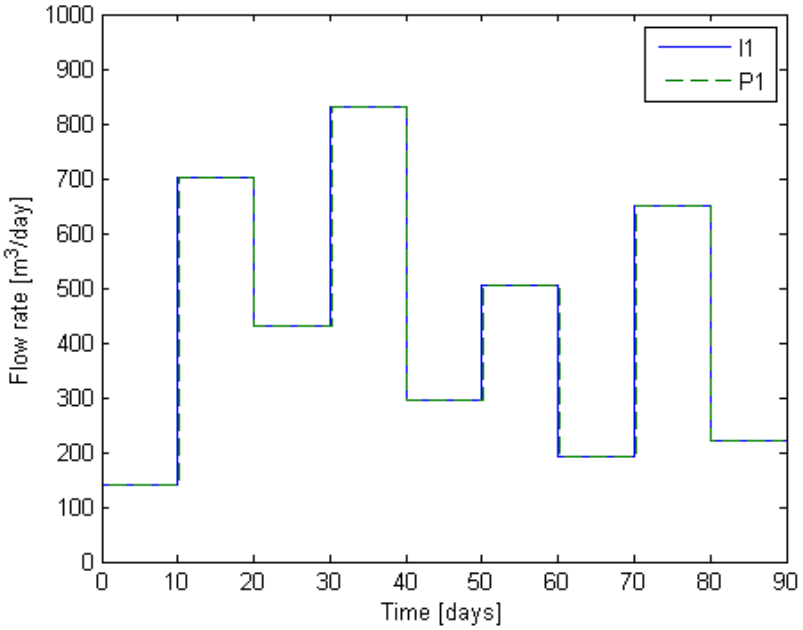

Figure 1.10: Injection and production rate for the single fracture case shown in Figure 1.9.

The injected tracer concentration was increased linearly with time, which led to the variation in produced concentration shown in Figure 1.11.

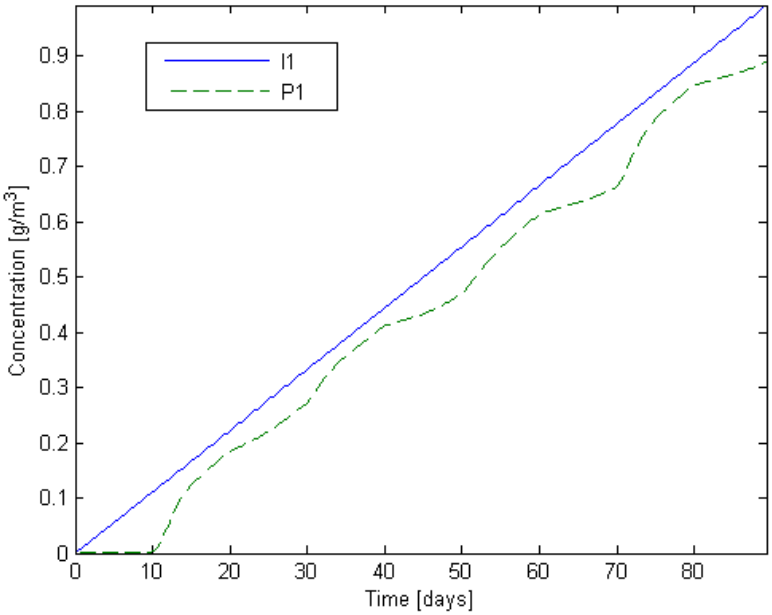

Figure 1.11: Injected and produced tracer concentration as a function of time.

To be able to find a unique mapping from the injected to the produced concentration, the variations in flow rate needed to be taken into account. This was done by viewing the concentrations as functions of the cumulative flow (we used the production rate, but the injection rate would clearly have given similar results). The injected and produced concentrations are shown in Figure 1.12, as functions of cumulative flow.

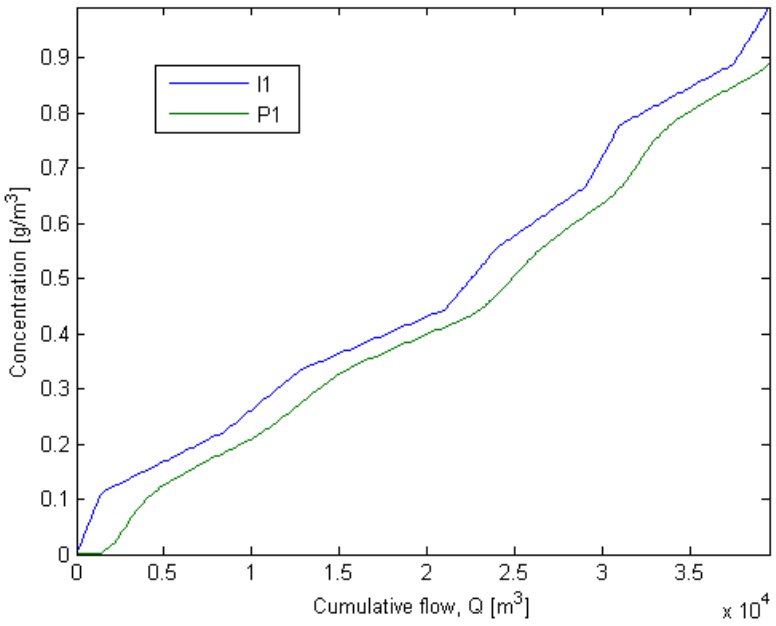

Figure 1.12: Injected and produced tracer concentration as functions of cumulative flow.

The kernel relating the two tracer concentration curves was the analog of Equation (2.36). The goal was to determine this kernel using a nonparametric deconvolution method similar to that described in Juliusson and Horne (2010).

For the production of tracer at a given point, V_x, the convolution integral analogous to Equation (2.34) can be approximated as:

$$\begin{aligned} C_{P1}(Q \mid V_x) &= \int_0^Q C_{I1}(Q-\tilde{Q})\kappa(\tilde{Q})d\tilde{Q} \approx C_{I1}(Q-\tilde{Q}_1)\kappa(\tilde{Q}_1)\frac{\tilde{Q}_1+\tilde{Q}_2}{2} \\ &+ \sum_{j=2}^{k} C_{I1}(Q-\tilde{Q}_j)\kappa(\tilde{Q}_j)\frac{\tilde{Q}_{j+1}+\tilde{Q}_{j-1}}{2} + C_{I1}(Q-\tilde{Q}_{k+1})\kappa(\tilde{Q}_{k+1})\left(t-\frac{\tilde{Q}_k+\tilde{Q}_{k+1}}{2}\right) \end{aligned} \tag{2.47}$$

where k was defined as $k = \left\{ j \mid \frac{\tilde{Q}_j+\tilde{Q}_{j+1}}{2} < Q \le \frac{\tilde{Q}_{j+1}+\tilde{Q}_{j+2}}{2} \right\}$. For the special case when $Q < \frac{\tilde{Q}_1+\tilde{Q}_2}{2}$ we took $C_{P1}(Q \mid V_x) \approx C_{I1}(Q-\tilde{Q}_1)\kappa(\tilde{Q}_1)Q$; and when $Q-\tilde{Q}_j < 0$ we used $C_{I1}(Q-\tilde{Q}_j) = C_{I1}(\tilde{Q}_1)$. Thus, the convolution could be written as the vector-matrix multiplication:

$$\vec{C}_{P1} = \mathbf{H}\vec{\kappa} \tag{2.48}$$

where the vector $\vec{C}_{P1}$ has the same number of elements as there are data points, and $\vec{\kappa}$ has one element for each discretization point. The matrix **H** holds the time-shifted reinjection terms, $C_{I1}(Q-\tilde{Q}_j)$, and the interval terms, $d\tilde{Q}$.

To determine $\vec{\kappa}$, the problem was formulated as a regularized least squares minimization problem:

$$\min_{\vec{\kappa}} \underbrace{\frac{1}{2}\left(\vec{C}_{P1}-\mathbf{H}\vec{\kappa}\right)^T\left(\vec{C}_{P1}-\mathbf{H}\vec{\kappa}\right)}_{data\,misfit}+\underbrace{\frac{1}{2}\vec{\kappa}^T R\vec{\kappa}}_{roughness\,penalty} \tag{2.49}$$

The roughness penalty (or regularization) term was formulated as:

$$\frac{1}{2}\vec{\kappa}^T R\vec{\kappa}=\sum_{i=2}^{m-1}\frac{\sigma_i}{2}\left(\kappa_{i-1}-2\kappa_i+\kappa_{i+1}\right)^2 \tag{2.50}$$

where *m* denotes the number of discretization points and σ_i are weighting parameters that had to be tuned to determine how much weight to place on the roughness penalty terms.

One final challenge that was faced in determining the kernel was to determine the range of the discretization terms, $\tilde{Q}$. This was solved by using an even discretization from zero to $\tilde{Q}_{\max}$, where the final value was found by global search algorithms (a Genetic Algorithm followed by a Pattern Search). Clearly this would not give a unique optimal value for $\tilde{Q}_{\max}$, but it helped to focus the estimation on the transient parts of the kernel (as opposed to late time parts which were essentially zero).

The kernel representing the fracture shown in Figure 1.9 was estimated from the data shown in Figure 1.12. In Figure 1.13, the estimate is compared to an analytical solution representing the fracture.

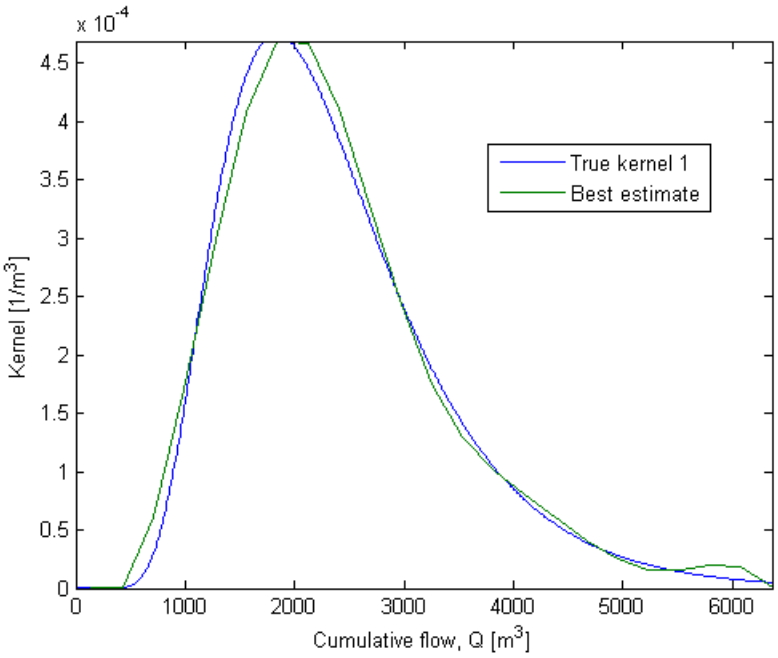

Figure 1.13: Estimation of kernel based on the deconvolution approach.

Clearly, the kernel estimate was obtained with considerable accuracy in this case, and the data misfit was very small as illustrated in Figure 1.14.

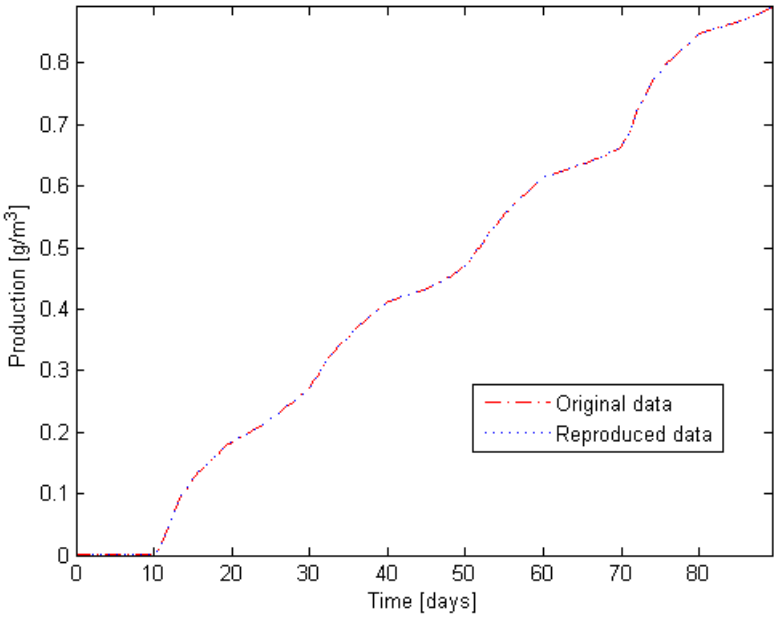

Figure 1.14: The data misfit after determining the kernel shown in Figure 1.13. The two lines are almost indistinguishable.

1.6.2 Kernel estimation in multiwell systems

In practice there are usually more than one injector and one producer, and the connectivity between each injector-producer pair is sought. Revealing these relationships based on fluctuations in production data becomes more challenging as the number of connections grows. Thus it is practical to start by analyzing a simple scenario where there are only two injectors and two producers, and no fracture intersections other than at the wells.

1.6.2.2 Simple fracture pattern

In a manner similar to that discussed in the previous section, an example flow model with discrete fractures was created (Figure 1.15). The example was configured with three fractures of equal properties in all but the fracture length, which was 60 m for the *I1-P1* and *I2-P2* fractures, but 75 m for the *I1-P2* fracture. The fractures only intersected at the wells, which was advantageous because that allowed accurate estimation of flow rates in each fracture based only on the flow rate data. This also meant that a unique kernel should be obtainable for each injector-producer combination.

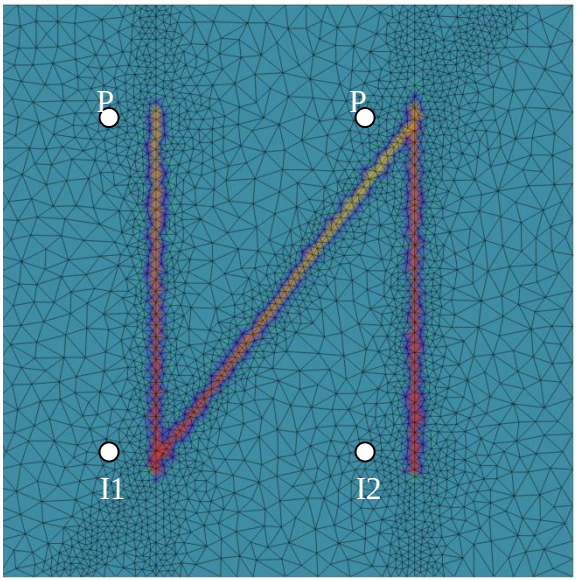

Figure 1.15: Two-dimensional FEFLOW model with two injectors and two producers. Discrete fractures connect each injector-producer pair, with the exception of I2-P1.

Flow simulations were run under variable flow rate conditions with linearly increasing concentration, as shown in Figure 1.16. At the end of 90 days, the injected tracer concentration was dropped to zero. This fluctuation was added to illustrate that the model could be used to predict large scale changes in concentration.

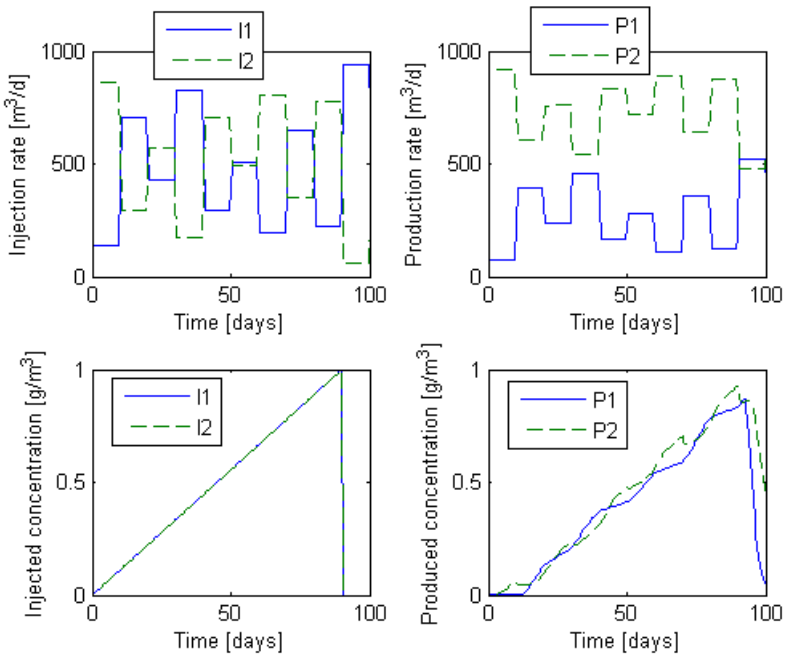

Figure 1.16: Injected and produced flow rates and concentrations for the scenario illustrated in Figure 1.15.

The single fracture model was extended to the multiple fracture case by the following formulation:

$$C_{Pj}(t) = \sum_{k=1}^{N_I} w_{jk}(t) \int_0^{Q_{jk}} C_{Ik}(Q_{jk} - \tilde{Q}_{jk}) \kappa_{jk}(\tilde{Q}_{jk}) d\tilde{Q}_{jk} \tag{2.51}$$

where N_I denotes the number of injectors and Q_{jk} refers to the cumulative flow between injector *Ik* and producer *Pj*. The weighting factor $w_{jk}(t)$ was added to account for the fact that the inflowing concentration from each injector would contribute to the concentration at *Pj* in proportion to the volumetric flow rate coming in. Thus, when the flow rates, q, were changed abruptly, the concentration balance would follow, albeit with a slight delay because of diffusion processes in the mixing fluids. To capture this delay we used a simple exponential kernel. Thus, the weighting factor was modeled as:

$$w_{jk}(t) = \int_0^t \frac{q_{PjIk}(t-\tau)}{q_{Pj}(t-\tau)} \frac{\exp(-\tau/T)}{T} d\tau \tag{2.52}$$

The exponential kernel was found initially by trial-and-error, but it was later seen to fit the description of a mixing cell process, with a time constant, T (Bear 1972). The flow rate q_{Pj} is the volumetric fluid production rate and q_{PjIk} is the estimated flow rate going from injector *Ik* to producer *Pj*.

The M-ARX linear regression method (Lee et al., 2010), was used to estimate q_{PjIk}. Using this method the production rates are modeled as a linear combination of the injection and production rates at the previous time.

$$\vec{q}_P(n+1) = -\mathbf{A}\vec{q}_P(n) + \mathbf{B}\vec{q}_I(n) \tag{2.53}$$

Here n is a time like variable which was taken to represent time in increments of 0.5 days. The flow rate vectors are defined as $\vec{q}_P = [q_{P1}...q_{PN_P}]^T$ and $\vec{q}_I = [q_{I1}...q_{IN_I}]^T$. The unknowns are the elements of the matrices **A** and **B**. Compiling the observed flow rates over all n_{max} time steps gives the matrix-matrix equation:

$$[\vec{q}_P(2)...\vec{q}_P(n_{\max})] = [-\mathbf{A}\ \mathbf{B}]\begin{bmatrix}\vec{q}_P(1)...\vec{q}_P(n_{\max}-1)\\ \vec{q}_I(1)...\vec{q}_I(n_{\max}-1)\end{bmatrix} \tag{2.54}$$

Solving this equation under the constraint of $\mathbf{A} \succ 0$ (element-wise), yields the interwell connectivity matrix for flow rates:

$$\mathbf{F} = \left(\mathbf{I} + \mathbf{A}\right)^{-1}\mathbf{B} \tag{2.55}$$

This matrix relates the flow rates as follows:

$$\vec{q}_P = \mathbf{F}\vec{q}_I \tag{2.56}$$

Therefore the flow rate between each injector-producer pair was evaluated as:

$$\vec{q}_{Pj} = F_{jk}\vec{q}_{Ik} \tag{2.57}$$

The formulation given in Equation (2.38) needed to be converted to discrete form. By comparison to the single fracture case, it was clear that there would be multiple transformation matrices $\mathbf{H_{jk}}$, that were analogous to the **H** matrix for the single fracture case. The one difference was that each row was multiplied by the corresponding factor, $w_{jk}(t)$. Then, all the transformation matrices were grouped into one:

$$\mathbf{H}_j = [\mathbf{H}_{j1}...\mathbf{H}_{jN_I}] \tag{2.58}$$

Similarly the kernels referring to producer *Pj* were written as a large vector:

$$\vec{\kappa}_j = [\vec{\kappa}_{j1}...\vec{\kappa}_{jN_I}] \tag{2.59}$$

So for each producer the kernels were estimated by solving the system:

$$\min_{\vec{\kappa}_j} \underbrace{\frac{1}{2}\left(\vec{C}_{Pj} - \mathbf{H}_j\vec{\kappa}_j\right)^T\left(\vec{C}_{Pj} - \mathbf{H}_j\vec{\kappa}_j\right)}_{data misfit} + \underbrace{\frac{1}{2}\vec{\kappa}_j{}^T R_j\vec{\kappa}_j}_{roughness penalty} \tag{2.60}$$

The resulting kernel estimates, based on the first 70 days of production are shown in Figure 1.17.

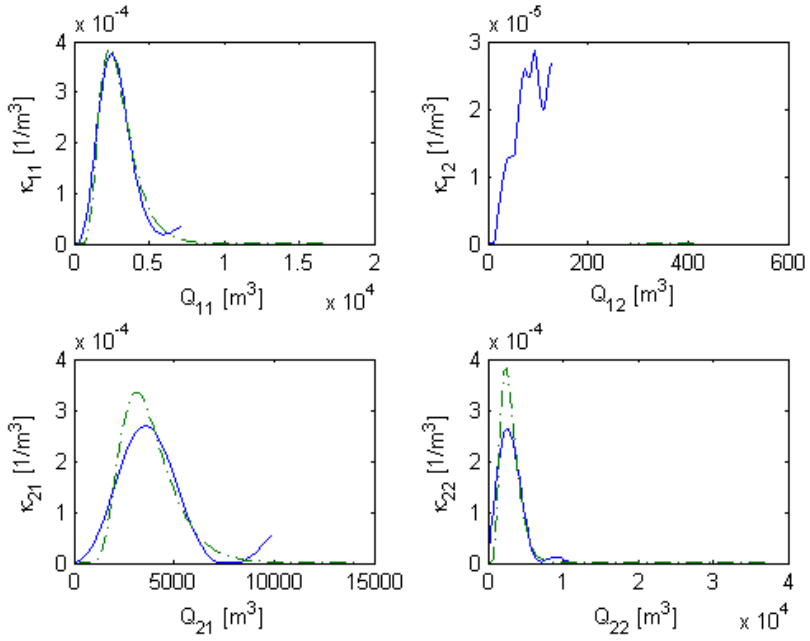

Figure 1.17: Kernel estimates for each of the injector-producer pairs. The estimates have blue solid lines, the true kernels have green dashed lines.

The kernel for pair *I1-P1* was the most accurate as there was very limited interference from the injection at *I2*. In contrast, the kernel for *I2-P1* was rather poorly determined, although it was determined to be very small, in terms of the magnitude of *Q*, making its influence negligible. This was consistent with the fact that there was no fracture connection between *I2* and *P1*. The kernels for *I1-P2* and *I2-P2* were relatively well determined. The predictive performance of the model was tested by cross-validation, i.e. using the kernel estimates to predict the concentration during the last 30 days of the production period. As shown in Figure 1.18, the variable rate kernels work well for prediction.

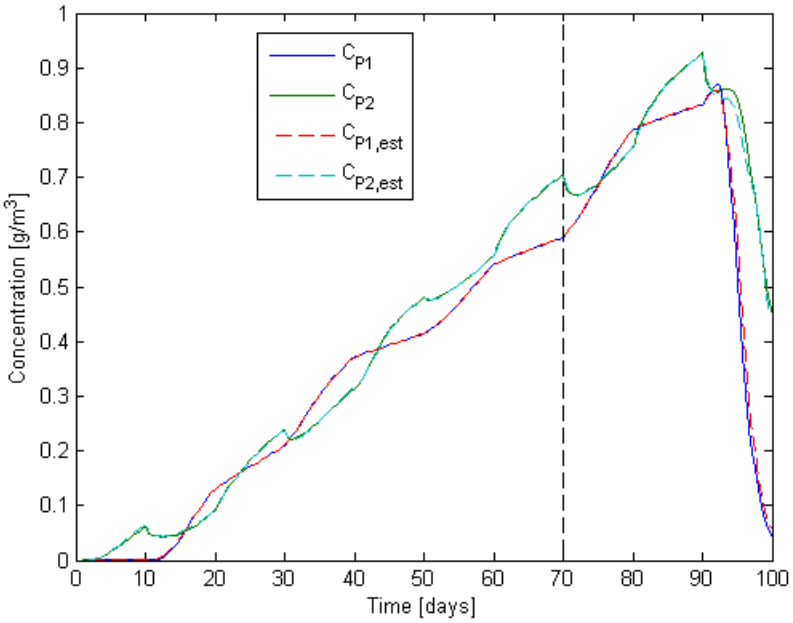

Figure 1.18: Prediction of tracer concentration in each producer, based on the kernel estimates shown in Figure 1.17. The first 70 days were used for estimation and the last 30 days were predicted.

1.6.2.1 More complex fracture patterns

Cases of more complex fracture patterns, i.e. where the dominant flow paths would intersect in the reservoir, were considered. An example of such a fracture pattern is shown in Figure 1.19. This fracture pattern is more challenging to analyze using the kernel method because it involves six kernels (*κ1-κ6*) and three mixing cells (*m1-m3*). To be able to estimate each kernel, the flow rate in each of the six fracture segments would need to be estimated, but that cannot be done using the MARX method (nor by any other method we know of). Moreover, the signal coming through the diagonal fractures will have gone through four different stages of smoothing, i.e. two kernels and two mixing cells, before it is recorded. This means that the input signal has lost a great deal of its original character and trying to infer two separate kernels from such a signal seems practically impossible.

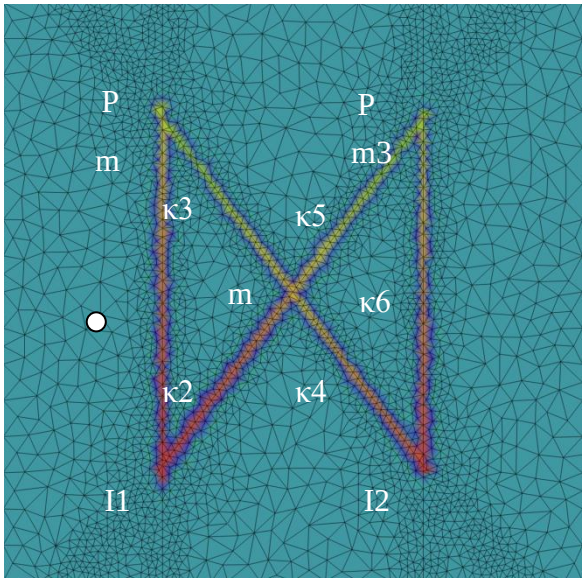

Figure 1.19: Fracture pattern with fractures intersecting in the reservoir.

Apart from the previously stated complications, we have obviously not yet begun to consider the fact that in practice one would not know the layout of the fracture network and thus how many kernels to search for in the first place. Additional complications would arise if there were more wells in the reservoir.

Instead of considering the complex case of six kernels and three mixing cells, one could assume that a representative kernel could be estimated for each of the injector-producer pairs. This is not rigorously correct since the kernels are functions of flow rate and the flow rates for say κ2 and κ5 will generally not be the same. However, defining the flow rate according to Equation (2.38) gave the kernel estimates shown in Figure 1.20.

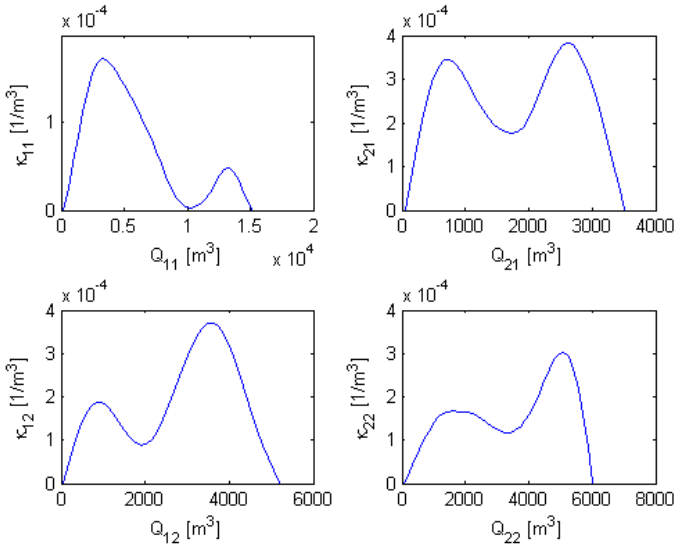

Figure 1.20: Effective kernel estimates for each injector-producer pair shown in Figure 1.19.

The predictive power of these kernels was examined by cross-validation. Data from the first 70 days were used to obtain the kernel estimates and then the concentration for the next 30 days was predicted, based on those estimates. The results are shown in Figure 1.21.

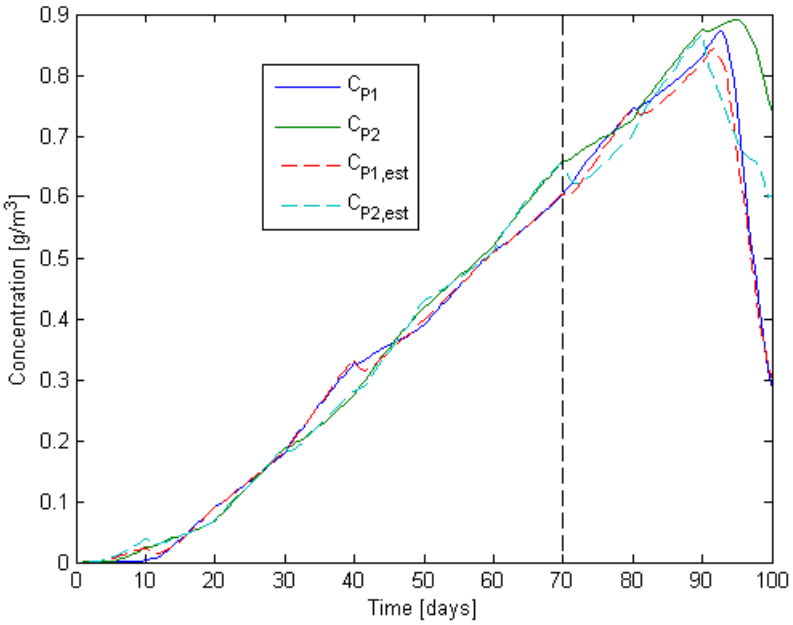

Figure 1.21 Prediction of tracer concentration in each producer, based on the kernel estimates shown in Figure 1.17. The black dashed line divides the estimation and the prediction periods.

Although the predictions in this case are not as good as those seen in Figure 1.18, they do seem reasonably accurate. This might be explained by the fact that the kernel model does capture both the fact that the injected tracer returns in a distributed manner over time, and that this time is measured in terms of the cumulative flow, which accounts for the variation in transport velocity to some extent.

As a final example, we examined a case where a three-dimensional fracture network was created using the FRACMAN software. The fracture network had 500 fractures which were drawn from a fractal size distribution (Figure 1.22). The fracture aperture and hydraulic conductivity were correlated to the fracture size. Some qualitative analysis of the fracture network revealed that producer P2 was relatively poorly connected to the bulk of the fractures, and especially injector I1.

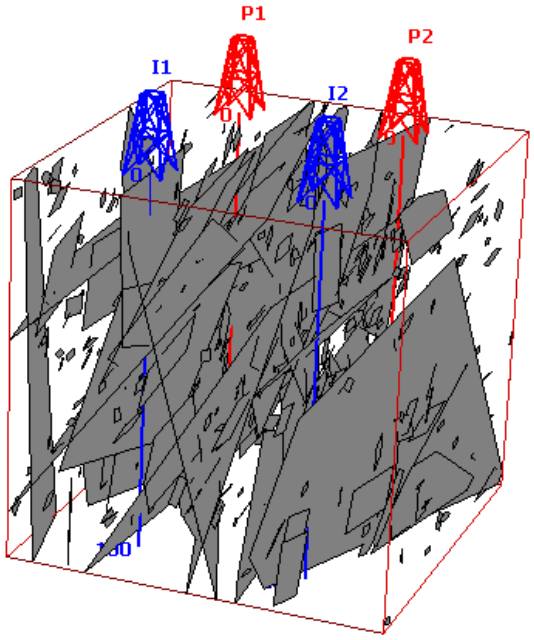

Figure 1.22: Three-dimensional fracture network generated in FRACMAN.

The fracture network was upscaled to a grid of 100 by 100 by 50 blocks, making each block 1 by 1 by 2 meters in size. The hydraulic conductivity of the blocks ranged from 10^{-5} to 12 m/s after the upscaling had been performed. Similarly the porosity ranged from 0.003 to 0.3. The upscaled data were imported into FEFLOW for flow simulation.

Four flow simulations were run, to find reference values, against which we could evaluate the kernels in this case. In each of these simulations, slugs of two different tracers were injected, one into each of the injectors. The flow rate was kept constant for the duration of each simulation, but how much was allocated to each well varied between each of the four simulations, as shown in Table 1.1.

Table 1.1: Injection rates for tracer slug simulations in the fractured reservoir shown in Figure 1.22.

	q_{I1} [m^3/day]	q_{I2} [m^3/day]
Simulation 1	200	800
Simulation 2	400	600
Simulation 3	600	400
Simulation 4	800	200

The simulated returns were normalized to account for variations in mass injected and the mixing of fluid streams, as shown by Equation (1.31).

$$\kappa_{jk}(Q_{jk}) = \frac{q_{Pj}}{q_{PjIk} F_{jk} m_{Ik}} C_{PjIk}(Q_{jk}) \tag{2.61}$$

The resulting simulated kernels are shown in Figure 1.23. The average of all four kernels is shown by the wider blue dashed line.

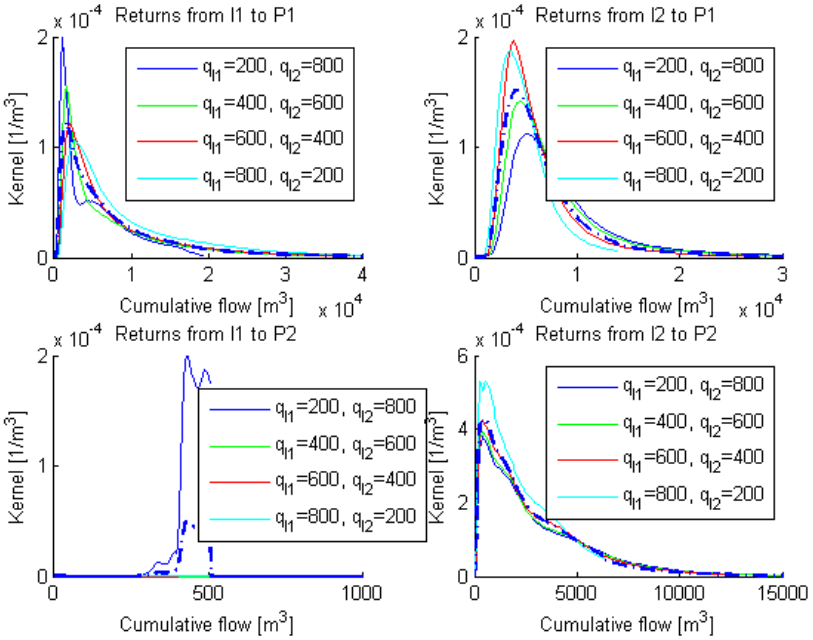

Figure 1.23: Tracer kernels as obtained from simulations of tracer tests at various flow conditions. The average of all four simulations is overlain in the blue dashed line.

Now to generate production data more similar to that found in practice, we used the injection histories shown in Figure 1.24. The simulated production rates (also in Figure 1.24) clearly show how *P1* produced considerably more than *P2*, since *P1* was connected to more of the large fractures in the reservoir. A similar observation could not as easily be made based on the tracer returns. This was because, even though a relatively small fraction of the total tracer injected went to *P2*, most of the water produced from there came from *I2*, and the fracture connections were relatively short and small. This led to fast tracer recovery.

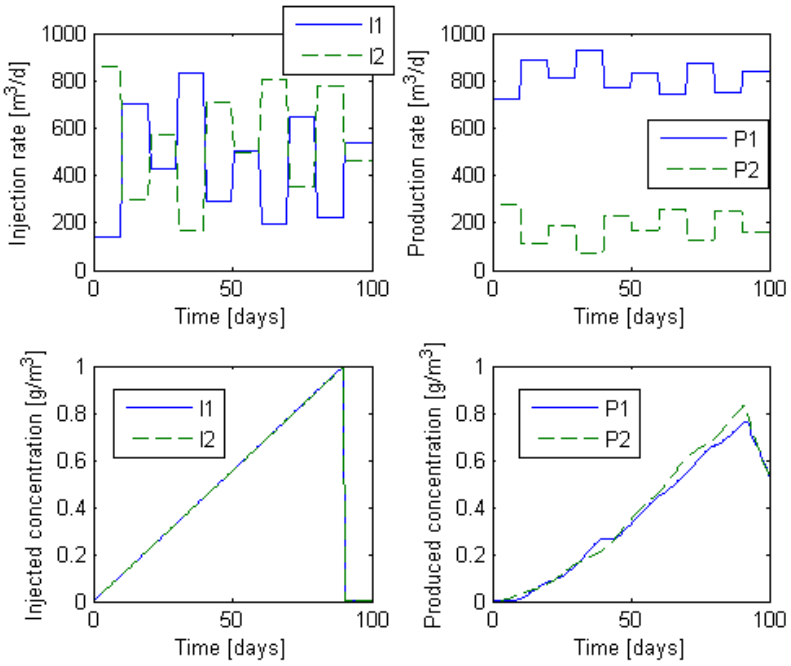

Figure 1.24: Simulated injection and production data for the three-dimensional fracture network presented in Figure 1.22.

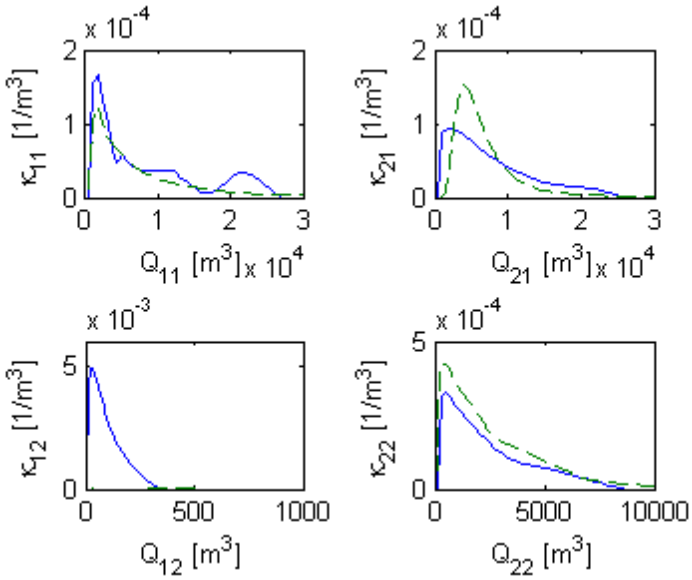

Figure 1.25: Kernel estimates obtained from production data (blue whole lines) contrasted with computed average of kernels from simulations at four different flow rate conditions (green dashed lines).

Data from the first 70 days of the simulated data set, shown in Figure 1.24, were used to estimate the kernels for each injector-producer pair. In Figure 1.25, these kernel estimates (blue whole lines) are contrasted with the average simulated kernels (green dashed lines).

The kernel estimates were finally used to predict the tracer concentration over the last thirty days. The results were quite accurate as shown in Figure 1.26.

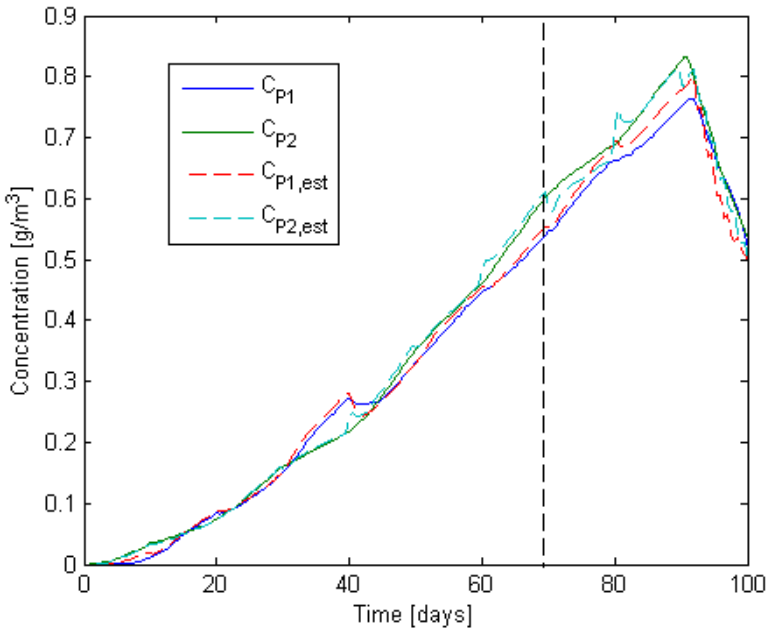

Figure 1.26: Cross-validation of tracer returns for the three-dimensional fracture network models shown in Figure 1.22. The black dashed line divides the estimation and the prediction periods.

1.7 OPTIMIZATION OF REINJECTION SCHEDULING

Utilizing tracer data to optimize reinjection strategies in geothermal reservoirs was discussed by Lovekin and Horne (1989). Several publications by Shook (2001; 2003; 2004) also discuss the potential application of tracer data to infer reservoir properties that could be used to optimize reinjection schedules. Methods for predicting thermal breakthrough in fractured reservoirs based on information interpretable from tracer tests have also been discussed by Lauwerier (1955), Gringarten and Witherspoon (1975), Bodvarsson and Pruess (1984), Kocabas (2005), and Wu et al. (2008). In this section we build on the work of these authors to develop a method for optimizing reinjection schedules.

In developing the optimization problem we considered three possible objective functions. The three formulations involved are covered briefly, and followed by short examples of their application in the quarterly report from winter 2011. One of these methods, the one focused on maximizing the net present value of operations, was deemed the most effective, and that is the only one of the three methods that will be discussed here.

For the net present value maximization model we used an empirical correlation between injection and production temperature and power output. The correlation, found by Bennett (2011), was based on results presented in the MIT report (Tester et al., 2006, Figure 7.3). The specific power output was defined as:

$$z_j(T_{Pj},T_I) = 3.854\times10^{-5}(T_{Pj}-\zeta)^2 - 1.268\times10^{-3}(T_{Pj}-\zeta) - 2.123\times10^{-2} \tag{2.62}$$

Here z_j is the specific power output of producer j [kW/(m^3/day)], and

$$\zeta = 0.563T_I - 14.51 \tag{2.63}$$

The temperatures are in degrees Celcius. Water density was assumed to be 900 kg/m^3.

The net present value of producing from the reservoir was then comptuted as

$$O(\bar{q}_I) = \sum_{j=1}^{N_P}\int_0^{t_f} P(t)z_j\left(T_{Pj}(t,\bar{q}_I),T_I\right)q_{Pj}(t,\bar{q}_I)e^{-rt}dt \tag{2.64}$$

where $P(t)$ denotes the unit price of energy and r denotes the chosen discount rate for the investment. T_{Pj} was computed using a thermal transport model:

$$T_{Pj}(t,\bar{q}_I) = \sum_{i=1}^{N_I} w_{ij}T_{ij}(t,\bar{q}_I) = \sum_{i=1}^{N_I} w_{ij}\left(T_0 - (T_0 - T_I)T_{D,ij}(t,q_{I_i})\right) \tag{2.65}$$

where T_0 is the initial temperature in the reservoir and $T_{D,ij}$ represents the a function of dimensionless temperature change as reported by most of the previously mentioned authors that have discussed thermal breakthrough in fractured reserovirs. For example, using Lauwerier's (1955) formulation

$$T_{D,ij}(t,q_{I_i}) = erfc\left\{\left(\frac{(\rho_a c_a)^2}{K_r\rho_r c_r}\left(\frac{\phi b q_{ij}}{V_{x,ij}}\right)^2\left(t - \frac{\rho_a c_a}{\rho_w c_w}\frac{V_{x,ij}}{\phi q_{ij}}\right)\right)^{-0.5}\right\} \tag{2.66}$$

where b denotes the fracture aperture, ϕ is the fracture porosity, K_r is the thermal conductivity of the rock and the group

$$\rho_a c_a = \phi\rho_w c_w + (1-\phi)\rho_r c_r \tag{2.67}$$

where the subscript r refers to the rock properties. The parameter w_{ij} denotes the mixing weight given by Equation (1.52).

Most of the thermodynamic parameters in Equation (1.65) can be estimated fairly accurately based on existing knowledge of the geology and reservoir fluid. The largest uncertainties are related to the geometry of the flow paths. The pore volume $V_{x,ij}$ and flow rate q_{ij} can be estimated from the tracer methods discussed in section 1.6, but methods to determine the group ϕb have not

been well established. Moreover, the Lauwerier solution assumes flow through a single fracture surrounded by a matrix of infinite size.

1.7.1 Maximizing net present value for a simple reservoir

An example with two injection wells and two production wells was used to test the application of the method. A reservoir model, with x and y dimensions of 1000 m and a height (in the z dimension) of 500 m, was created. Three vertical fractures were placed in the model, connecting the wells as shown in Figure 1.27. Each fracture was given an aperture of 1 m, height 500 m and porosity 5%. The distance between wells I1 and P1 (or I2 and P2) was 600 m and between I1 and P2 was 750 m.

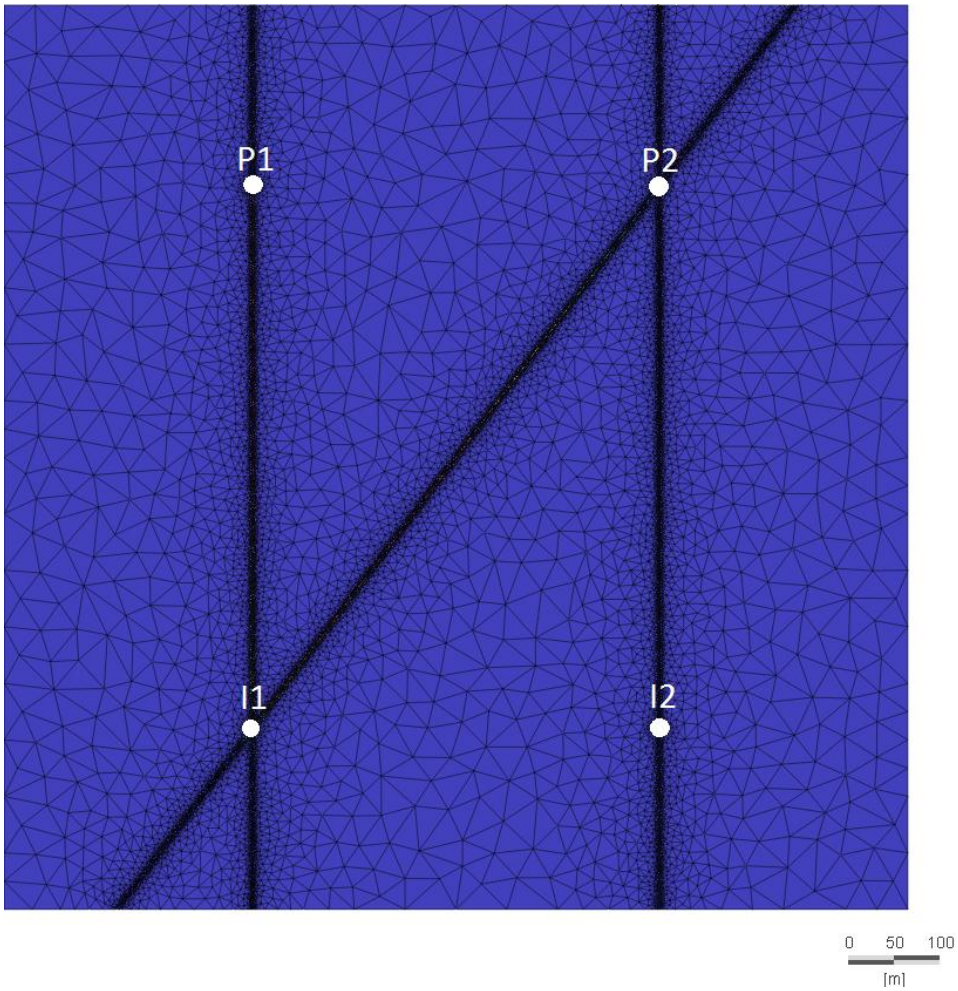

Figure 1.27: The configuration of wells and fractures in a test case used to investigate the possibility of optimizing reinjection scheduling based on tracer returns.

Simulations of continuous tracer injection were performed, with an injection rate of 2500 m^3/day into each well. The smallest grid blocks were around 2 m in the direction of flow, and the largest flow velocity was around 100 m/day. To limit numerical dispersion we limited the time step to 0.02 days and used the shock capturing flow transport option in FEFLOW. We also used a

dispersion coefficient of 50 m in the longitudinal direction and 5 m in the transverse direction. The resulting tracer returns were used to compute the tracer kernels shown in Figure 1.28.

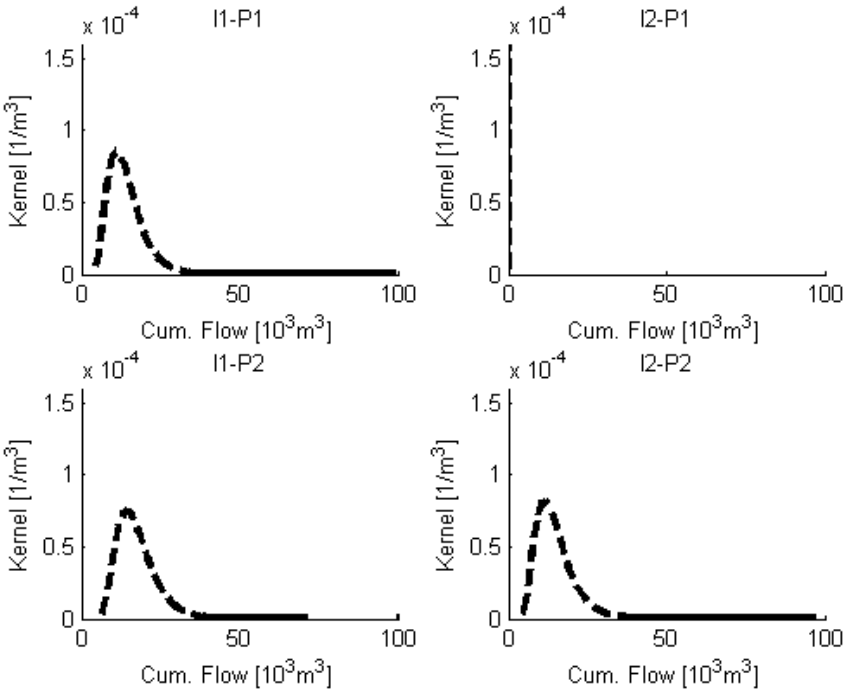

Figure 1.28: Tracer kernels derived from the flow model presented in Figure 1.27. Note that the kernel representing the connection between I2 and P1 is virtually zero because no tracer was delivered along that path. A kernel derived from an analytical equation with a very large volume was used to account for this anomaly when running the optimization algorithm.

The pore volumes estimated from the tracer kernels are shown in Table 1.2. A zero volume estimate was found for the I2-P1 connection because no tracer was transported from injector 2 to producer 1. This was accounted for in the optimization by assuming there was a very large volume separating the two wells, thereby leaving the optimization problem indifferent to this connection.

Table 1.2: Estimated pore volume of flow paths connecting wells in the model shown in Figure 1.27. The estimates are based on tracer tests. The estimate for the I2-P1 connection is poor because no tracer was transported along that connection.

Vx	I1	I2
P1	14,122	0
P2	17,522	14,881

Using this method to find the optimal injection rate allocation yielded an injection rate of 1646 m^3/day (64%) into well I1 and 909 m^3/day (36%) in I2. The objective function and constraints are shown in Figure 1.29. The increase in the objective function from the initial guess

(where all injection rates were equal to 2500 m^3/day) was quite significant, or about 79%. That does not include the savings that could be made by building a smaller power plant, if one knew that a smaller total flow rate would be required to sustain economic production over a 30 year period. This result was obtained assuming an interest rate r=8% per year and an energy price, increasing over a 30 year period in real terms, from 60 to 120 $/kWh with an added 2% inflation.

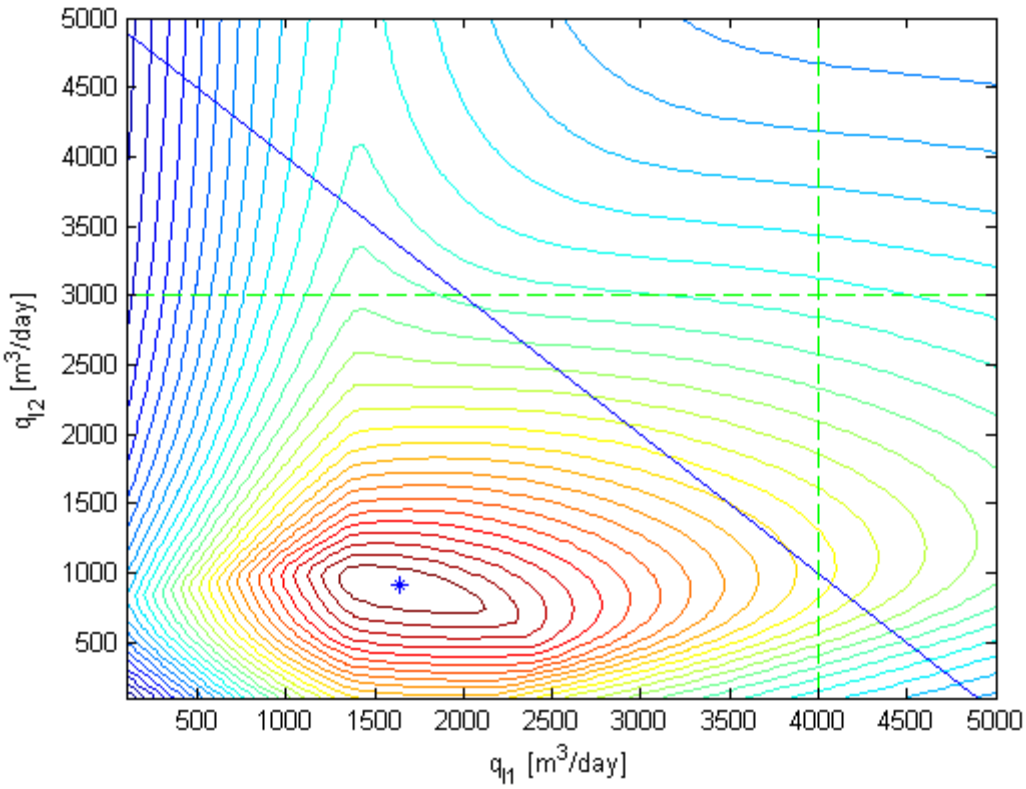

Figure 1.29: A contour plot of the objective function based on net present value of production. A constant total injection constraint of 5000 m^3/day is illustrated by the blue diagonal line. Maximum injection constraints of 4000 and 3000 m^3/day for injectors I1 and I2, respectively, are shown by the green dashed lines. The optimum feasible point is shown by the blue star.

The optimal solution in this case was well below the maximum allowable injection rate. This was because the power output would drop significantly if the production temperature fell below 120 C. Figure 1.30 shows how the predicted temperature would converge to a value close to 120 C near at the end of the production period. We see, by comparison to the simulated thermal returns, that the actual decline in production would occur earlier than predicted by the analytical model.

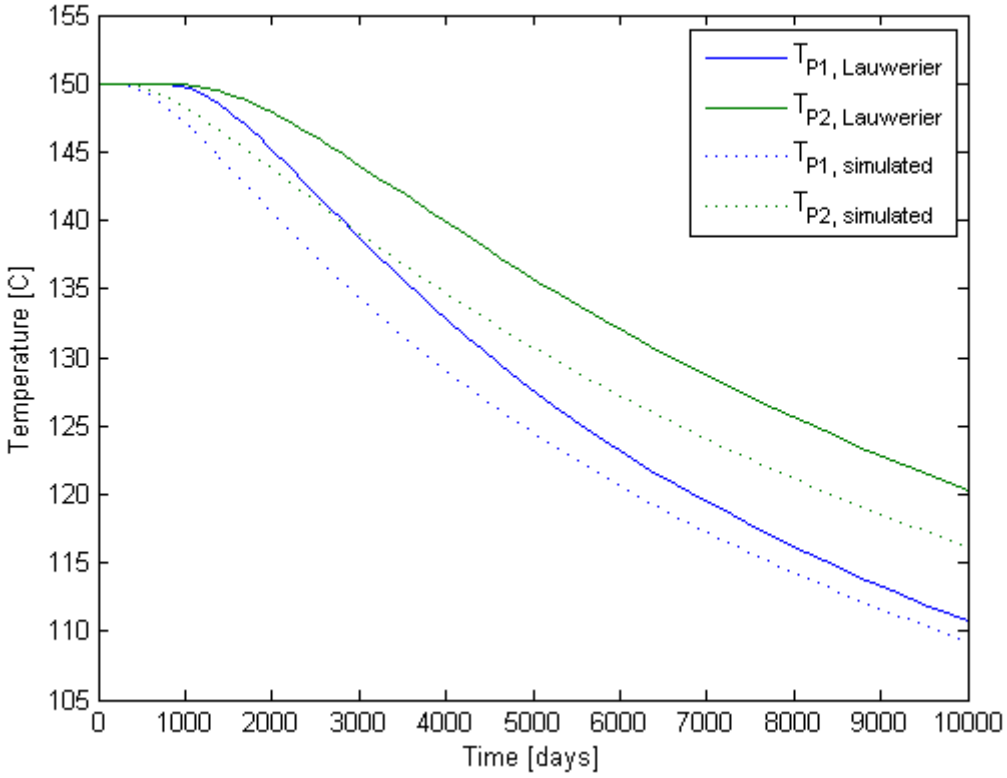

Figure 1.30: Simulated thermal breakthrough and thermal breakthrough as predicted by the Lauwerier (1955) analytical model. For this case water at 50 C was injected at the optimal allocation of 1646 m^3/day into injector I1 and 909 m^3/day into I2. The optimal solution sought to end at a temperature near 120 C since the specific power output would decline rapidly at lower temperatures.

1.7.2 Maximizing net present value with a larger scale reservoir model

In this section, we describe the development of a flow model based on data obtained from the Soultz-sous-Forêts enhanced geothermal system in France. The model included four injection wells and three production wells. Tracer flow simulations were run under various flow conditions to investigate the variability in tracer returns with flow rate. These flow rate and tracer data were then used to predict thermal breakthrough and optimize the injection strategy for the field. We also assumed that some porosity estimates and wellbore imaging data would be available as is the case for the Soultz reservoir. Any additional reservoir information from the underlying model was ignored. Hence, this was a test of how well an optimization would perform based on data that could be measured in the field using well established methods, without the use of a traditional reservoir simulator.

1.7.2.1 Reservoir model

A model based on the Soultz reservoir was chosen because it has been investigated extensively and observations have been reported in dozens of publications. Some of the more recent interpretations from seismic data were provided to us by Place et al. (2011). These data were

imported into the discrete fracture software FRACMAN. Seven of the largest fractures are shown in Figure 1.31.

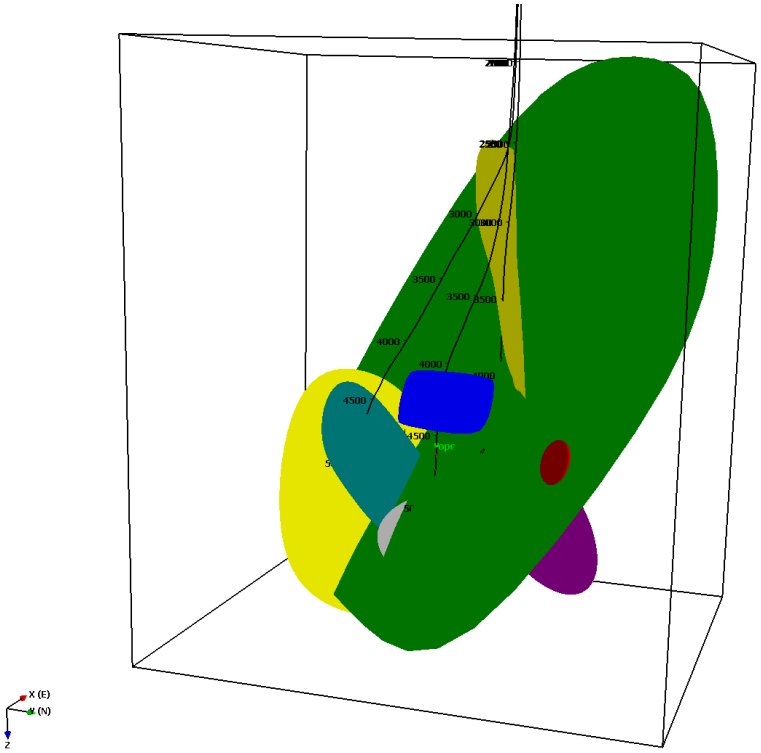

Figure 1.31: Seven of the fractures (or faults) found in the Soultz reservoir by Place et al. (2011).

Additional fractures were created in the model based on statistical correlations reported by Massart et al. (2010). The additional fractures were created in four sets. The sets had a mean North-South direction with East and West dips, forming conjugate sets. First a few relatively large East and West dipping fractures were created at random locations in the region of interest. Then 500 additional fractures of smaller size were generated in clusters around the preexisting fractures. One such stochastic fracture set is shown in Figure 1.32. Note that the Fisher dispersion recorded for the trend and dip was relatively low, indicating that the fracture orientations varied quite significantly.

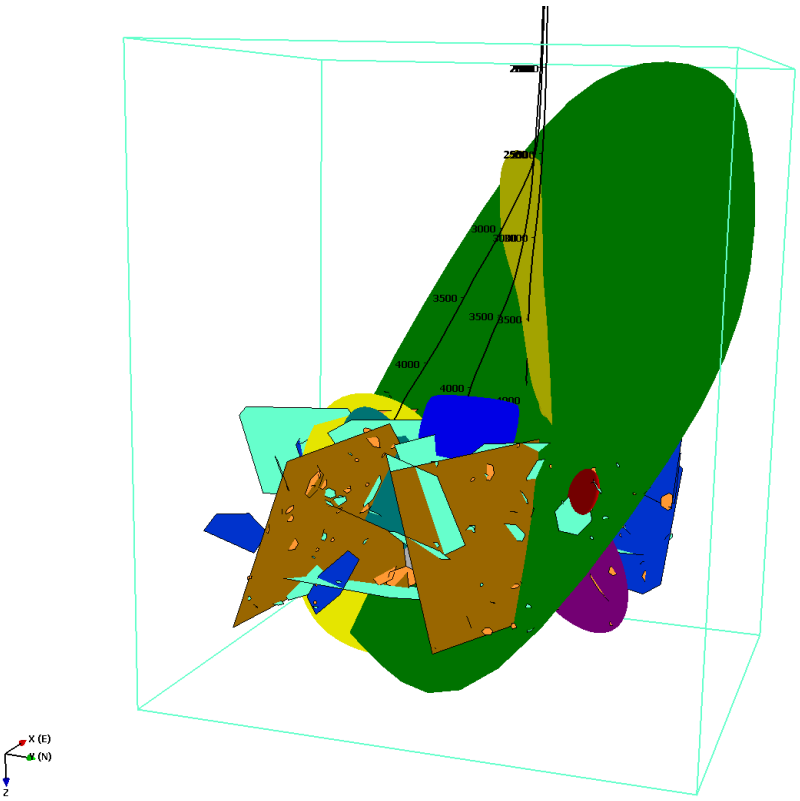

Figure 1.32: A number of stochastically generated fractures were added to the model. The spatial distribution of the fractures was based on the findings of Massart et al. (2010).

Moving from fracture generation to three-dimensional flow simulations proved challenging. We needed to create a model capable of handling pressure, solute and thermal transport. To be able to capture the effects of the high permeability fractures, we wanted to use discrete fracture simulations, but creating three-dimensional grids for such models and finding a simulator that can work with those grids seemed to be overly complicated at this point. Therefore, we decided to start by assuming that the fractures were all vertical. A trace map from one of the stochastic three-dimensional fracture models, taken at 4500 m depth, was used as a template for the layout of the vertical fractures. A grid conforming to the main fractures was generated using the Triangle mesh generator, and simulations with discrete fracture elements were run using FEFLOW.

Massart et al. (2010) suggested the following correlations between fracture size and aperture:

$$L = k_1(2b)^{D_1} \tag{2.68}$$

where L is the effective fracture radius and $2b$ is the fracture aperture. The parameter D_1 is the fractal dimension which Massart et al. determined to be 1.04 and k_1 is a correlation parameter which is relatively hard to quantify (Massart et al. suggested k_1=400). A similar correlation was assumed to exist between the hydraulic conductivity of the fractures and the fracture aperture:

$$K = \left(\frac{2b}{k_2}\right)^{D_2} \tag{2.69}$$

where K is the hydraulic conductivity and k_2 and D_2 were to be determined by history matching. The reservoir thickness was assumed to be 500 m and the height of each of the fractures was taken to be the minimum of the fracture length and 500 m. The porosity of the fractures was assumed to be 4%. The matrix porosity and permeability were much smaller than the corresponding fracture properties and therefore the matrix had negligible effect on the solute transport. A dispersion coefficient of 50 m was used for the longitudinal flow direction and 5 m for the transverse flow direction.

Gentier et al. (2010) reported the results of a tracer test carried out in Soultz in 2005. Tracer was injected into well *GPK3* (fluid injection rate $15\text{x}10^{-3}$ m^3/s) and produced from wells *GPK2* (fluid production rate $12\text{x}10^{-3}$ m^3/s) and *GPK4* (fluid production rate $3\text{x}10^{-3}$ m^3/s). No pumps were used for the production and therefore the wells in the simulation were designed to produce at a constant bottomhole pressure. We attempted to adjust the values of the fracture lengths and connections, and the parameters k_1, k_2, and D_2, until the model results gave an approximate match to the measured data. The history match shown in Figure 1.33 was obtained from the flow model illustrated in Figure 1.34 with k_1=1000, k_2=50, and D_2=1.8. There was some inconsistency in the amount of tracer retrieved in our simulation and the actual observations. In our model most of the tracer had been recovered (>95%) at 160 days, but the actual observations indicated that only about 25% of the tracer was retrieved. Therefore we scaled our simulated concentration values to match the measured concentrations shown in Figure 1.33. Thus, the history match could probably have been improved, e.g. by adding a larger secondary flow path between *GPK2* and *GPK3* or by starting with an over pressurized system. However, we let this match suffice because the main goal was to create a reservoir model with somewhat realistic dimensions, fracture connections and parameter distributions. This seemed to be accomplished with the current model.

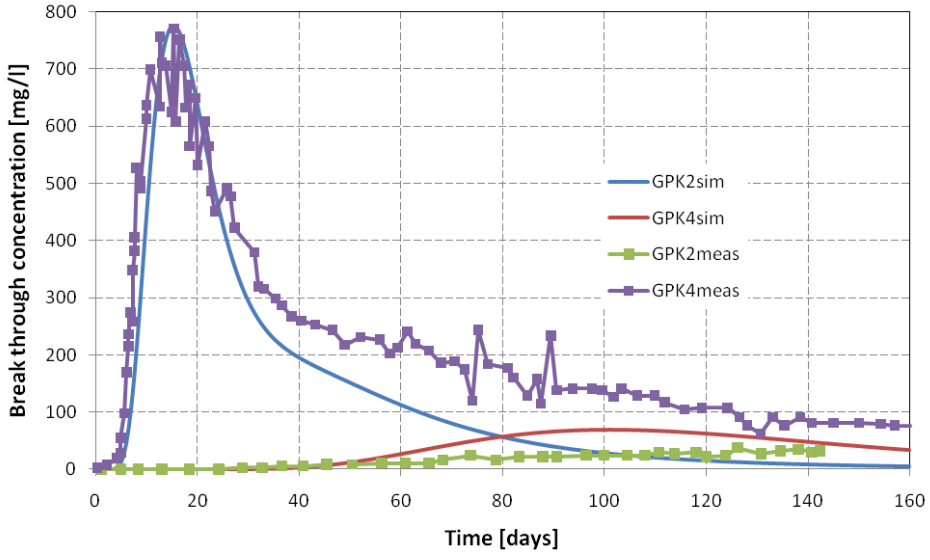

Figure 1.33: Match between simulated and measured breakthrough concentration for the tracer test performed in the Soultz reservoir.

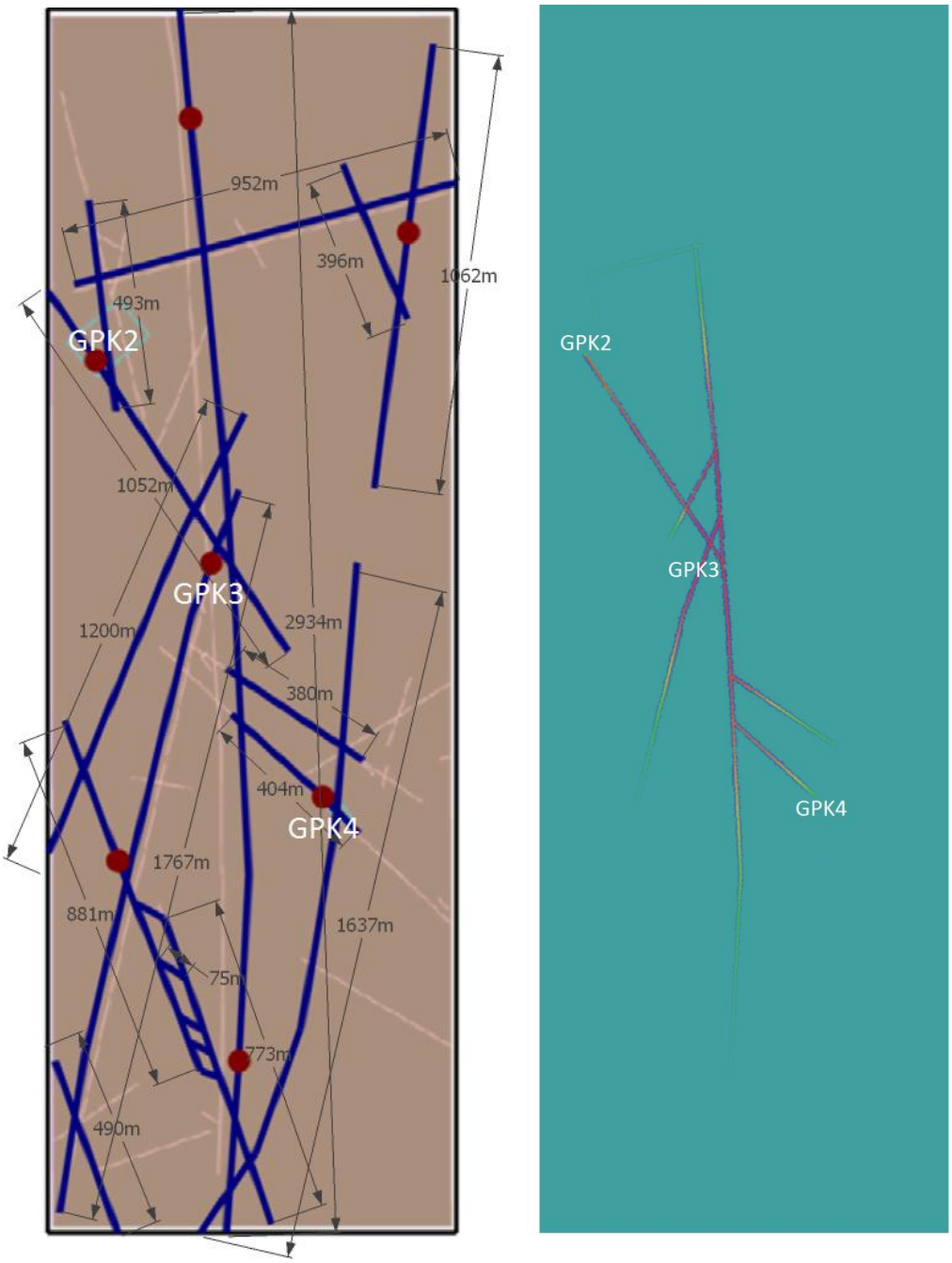

Figure 1.34: The left part of this figure shows the layout and approximate lengths of the fractures (blue lines) used in the Soultz model. The background shows the traces of fractures, at 4500 m depth, in one of the stochastic three-dimensional fracture models. The right part shows the tracer distribution in the reservoir at the end of the 160 day tracer test simulation. The existing wells are labeled GPK2, GPK3 and GPK4. The additional red dots in the left part of the figure represent four wells that were added to the model for further testing.

1.7.2.2 Tracer returns at various flow configurations

The two-dimensional Soultz flow model was used to investigate the expected variability in tracer returns under various injection rate configurations. Four additional wells were added to the model, such that there were four designated injection wells and three production wells (Figure 1.35).

Table 1.3 lists simulation runs which involved seven different injection rate configurations. A continuous concentration of tracer was injected into each of the injectors, one at a time, and the produced concentration was recorded over a period of 300 days. A total of 28 simulations were run.

Table 1.3: List of simulations run with various injection rate configurations and tracer allocations.

	Run #	I1 [m3/	I2 [m3/d]	I3 [m3/d]	I4 [m3/d]	I1 [mg/l]	I2 [mg/l]	I3 [mg/l]	I4 [mg/l]
Config. 1	1	1200	1200	4800	4800	1	0	0	0
	2	1200	1200	4800	4800	0	1	0	0
	3	1200	1200	4800	4800	0	0	1	0
	4	1200	1200	4800	4800	0	0	0	1
Config. 2	5	1200	4800	1200	4800	1	0	0	0
	6	1200	4800	1200	4800	0	1	0	0
	7	1200	4800	1200	4800	0	0	1	0
	8	1200	4800	1200	4800	0	0	0	1
Config. 3	9	1200	4800	4800	1200	1	0	0	0
	10	1200	4800	4800	1200	0	1	0	0
	11	1200	4800	4800	1200	0	0	1	0
	12	1200	4800	4800	1200	0	0	0	1
Config. 4	13	4800	1200	1200	4800	1	0	0	0
	14	4800	1200	1200	4800	0	1	0	0
	15	4800	1200	1200	4800	0	0	1	0
	16	4800	1200	1200	4800	0	0	0	1
Config. 5	17	4800	4800	1200	1200	1	0	0	0
	18	4800	4800	1200	1200	0	1	0	0
	19	4800	4800	1200	1200	0	0	1	0
	20	4800	4800	1200	1200	0	0	0	1
Config. 6	21	4800	1200	4800	1200	1	0	0	0
	22	4800	1200	4800	1200	0	1	0	0
	23	4800	1200	4800	1200	0	0	1	0
	24	4800	1200	4800	1200	0	0	0	1
Config. 7	25	3000	3000	3000	3000	1	0	0	0
	26	3000	3000	3000	3000	0	1	0	0
	27	3000	3000	3000	3000	0	0	1	0
	28	3000	3000	3000	3000	0	0	0	1

Figure 1.35 shows the distribution of tracer in the reservoir when 3000 m^3/day had been injected into each injector over a period of 300 days (i.e. runs 25-28).

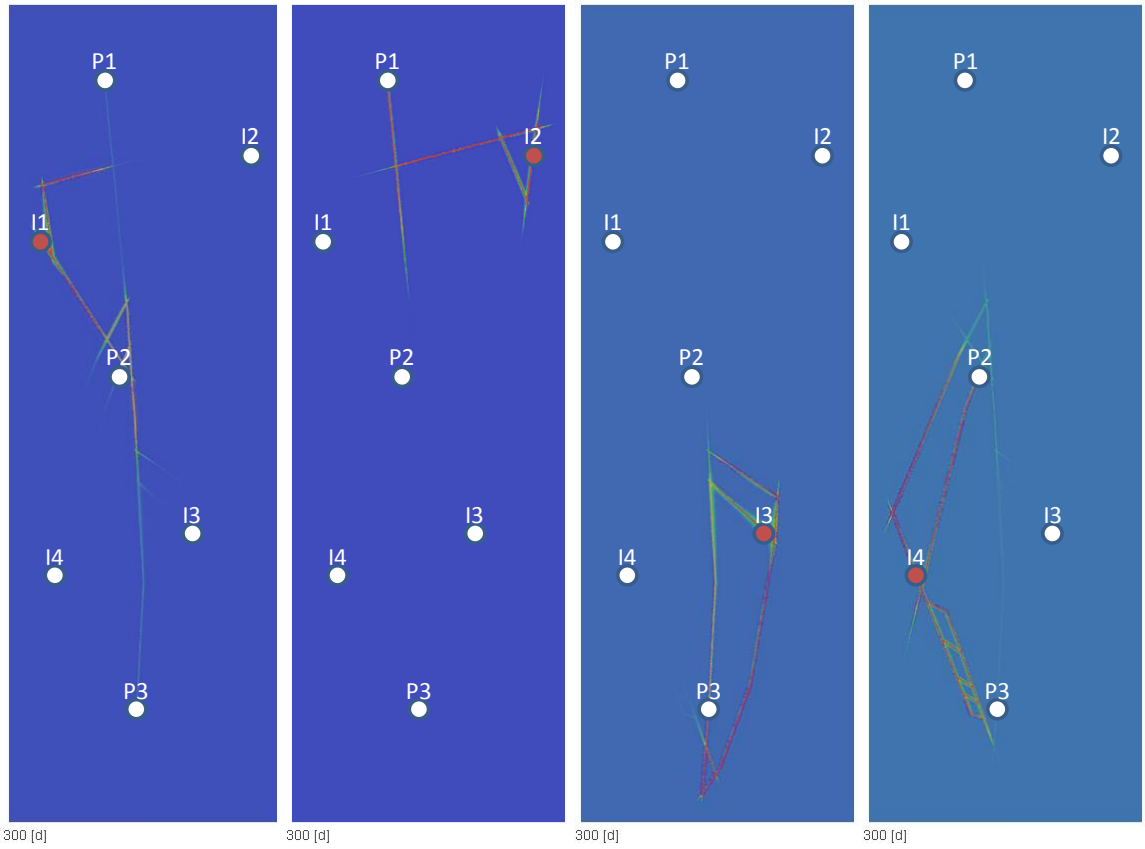

Figure 1.35: The tracer distribution in the reservoir after 300 days of tracer injection, into wells I1 through I4, going from left to right. The injection rate was 3000 m^3/day for each injector (i.e. configuration 7).

There were 12 possible injector-producer connections. The tracer returns for each connection, at each of the seven flow configurations, are shown in Figure 1.36. It was clear from these results that the tracer returns could vary significantly as a function of the injection rate configuration. The variation could occur in terms of the mean arrival time, the tracer dispersion, and the fraction of the initial concentration recovered. The variation in dispersion and arrival time could be reduced by viewing the responses in terms of the cumulative flow going from each injector to each producer.

To be able to compute the cumulative flow between well pairs we needed an estimate of the flow rate going from each injector to each producer. One way to estimate this quantity was to use variations in flow rate signals, as discussed by Lee et al. (2010) and Juliusson and Horne (2011). One could also compute the relative concentration of injectate eventually arriving at each producer, and equate that to the fraction of injection water arriving at the producer. That is:

$$\frac{C_{IiPj}(t_f)}{C_{Ii}} = w_{ij} = \tilde{F}_{ij}\frac{q_{Ij}}{q_{Pj}} \tag{70}$$

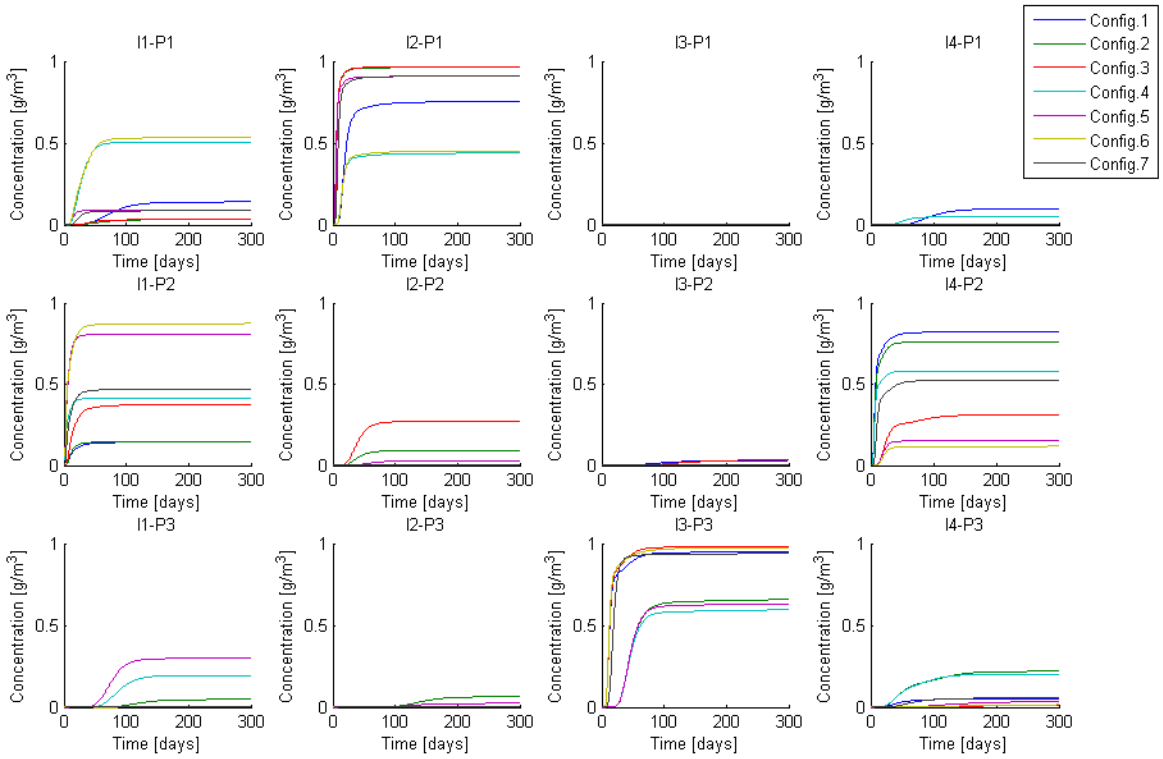

Figure 1.36: An illustration of the tracer returns coming from each injector to each producer under various injection rate configurations.

Here $\tilde{F}_{ij}$ is the fraction of water injected into injector *Ii* flowing towards producer *Pj*. It is the equivalent of F_{ij} in Equation (2.34), only computed based on tracer returns. $\tilde{F}_{ij}$ will be referred to as the tracer-based interwell connectivity (IWC). Note that the value of $\tilde{F}_{ij}$ may vary depending on the injection rate configuration. The cumulative flow for each injector producer pair would then be estimated as:

$$Q_{ij} = \tilde{F}_{ij} q_{Ii} t \tag{2.71}$$

where *t* was time from the beginning of tracer injection.

The tracer-based IWC was compared to the flow rate-based IWC. An additional simulation with step wise varying flow rates had to be run to compute the flow rate-based connectivity. The flow rate-based and tracer-based IWCs are compared in Figure 1.37. From this comparison it is apparent that the tracer-based IWC is generally more extreme than the flow rate-based IWC. We suppose that this is because the flow rates are affected more by the pressure (or diffusion) equation while the tracer travels mostly in an advective manner, i.e. along the main flow paths. A relatively large variability in the tracer-based IWC as a function of the injection rate configuration was observed (Figure 1.37). This variability was partially attributable to insufficient simulation time and numerical inaccuracy in the simulations; otherwise, it was caused by changes in the flow paths taken between each injector-producer pair.

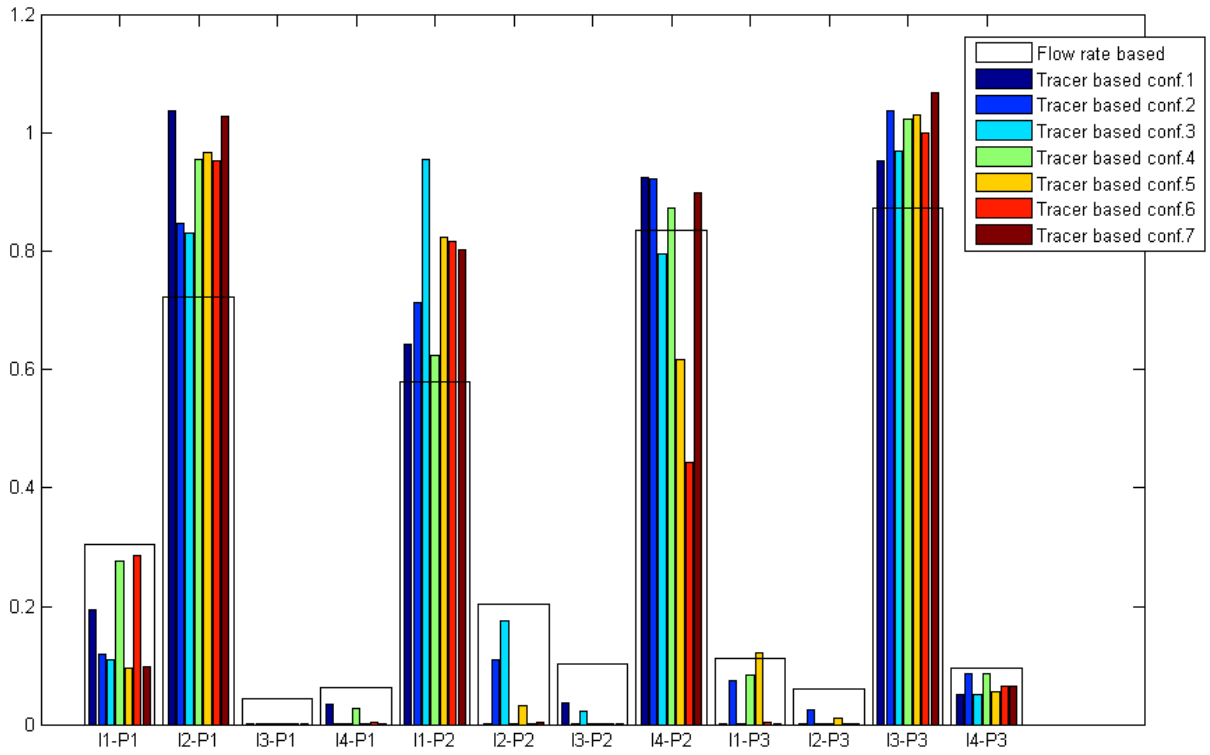

Figure 1.37: A comparison of the flow rate-based IWC and the tracer-based IWC.

The variability, from well to well, in the stabilized concentration of tracer recovery occurred because of dilution by flow streams coming from the other injectors or the reservoir itself. To account for this, we normalized the concentration by the last measured concentration value, i.e.:

$$C^N_{IiPj}(t) = \frac{C_{IiPj}(t)}{C_{IiPj}(t_f)} \tag{2.72}$$

These normalized concentration values are plotted in Figure 1.38 as a function of the cumulative flow computed from Equation (2.71), with $\tilde{F}$ estimated from the configuration 7 simulation results. It was noticeable that the return curves for the stronger well connections (e.g. *I2-P1*, *I1-P2*, *I4-P2* and *I3-P3*) coincided more accurately after this normalization, than did those that had weak connections (e.g. *I1-P3* and *I2-P3*). The proposed explanation for this was that the interaction between these wells was dominated by one (or possibly two) flow paths, and therefore, the one-dimensional advection-dispersion would provide a relatively good approximation of the tracer returns (see further discussion in Juliusson and Horne, 2011). This was important because it indicated that by performing a tracer test at one set of injection rates, one might expect to be able to predict what the tracer returns would be at another set of injection rates. This was especially true for the strongest well-to-well connections, which were the most important ones when it came to utilizing this information for injection scheduling.

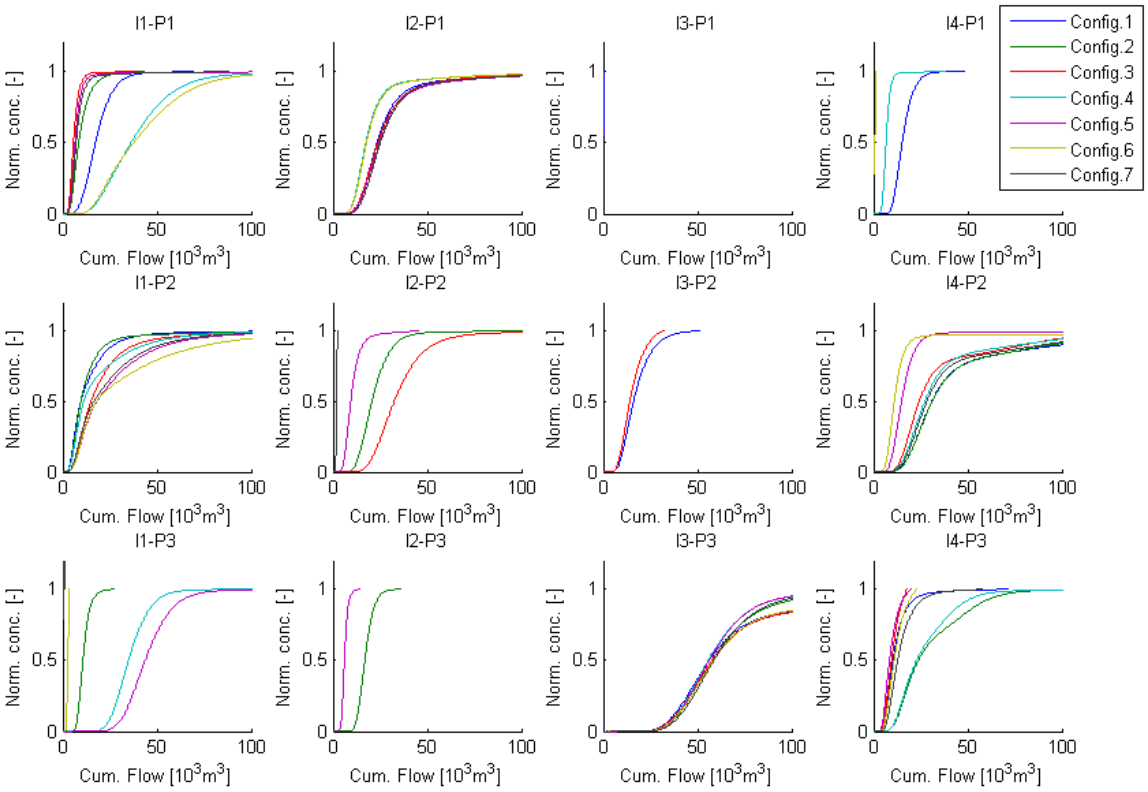

Figure 1.38: Normalized tracer returns as a function of an estimate of the cumulative flow passed between an injector-producer pair. The cumulative flow is based on an IWC estimate computed from each tracer return.

The tracer kernels were computed from the normalized step responses as:

$$\kappa_{ij}(Q_{ij}) = \frac{\partial C^N_{IiPj}}{\partial Q_{ij}} \tag{2.73}$$

The tracer kernels are shown in Figure 1.39. An average of the tracer kernels is shown by a blue dashed line. This can be compared to the response with all injection rates equal, shown by a black dashed line. Each one of these average responses was used to estimate the average pore volume for each connection. The volume was computed from Equation (2.38).

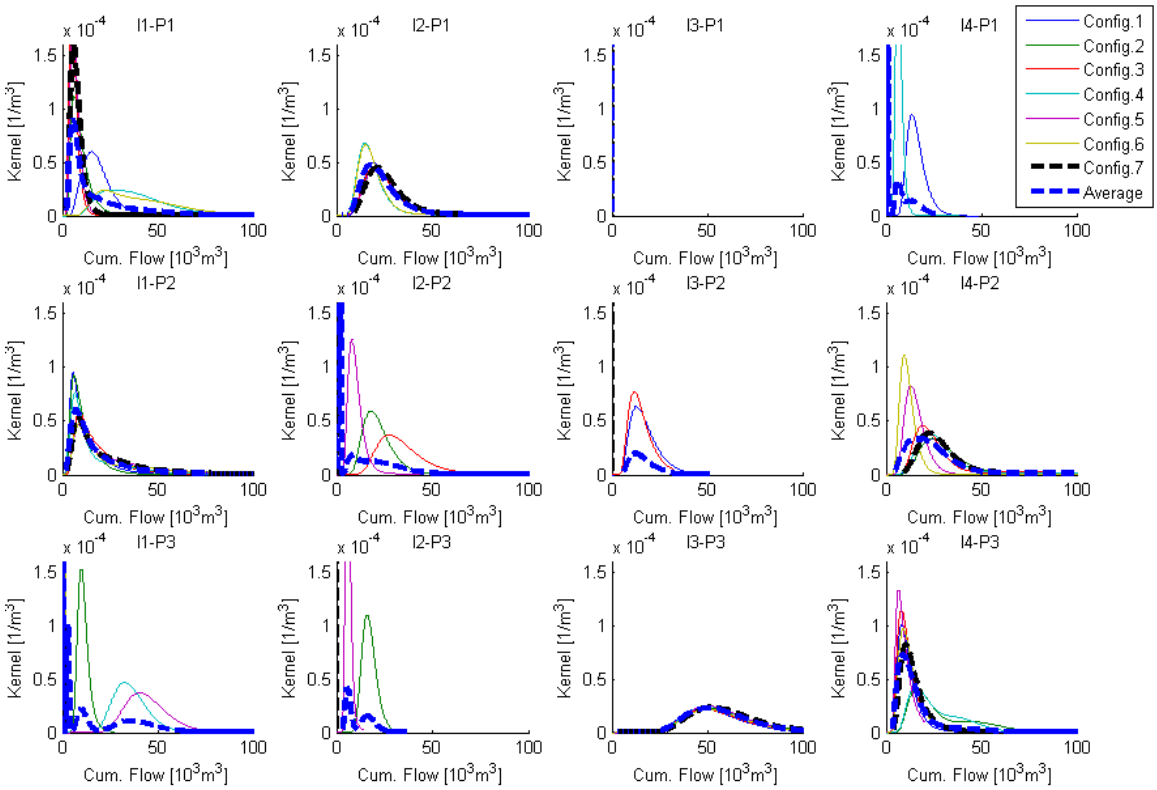

Figure 1.39: Tracer kernels computed for each of the injector-producer connections based on continuous injection tracer test at various injection rate configurations.

The resulting volume estimates are shown in Table 1.4 and Table 1.5. Note that when there was poor connectivity between the wells, the volume between the wells tended to be under estimated. This was because, in those cases, very little tracer had been delivered along the connection over the 300 day testing period. This problem was partially accounted for by averaging the responses, which is why more reasonable estimates were found using that method than just the tracer returns from configuration 7. Nevertheless, it was obvious (observe Figure 1.34) that there was a fracture connection of large volume between I3 and P1, for example. Erroneous estimates of this kind needed to be corrected manually. In practice, one might guess that if a very small fraction of tracer was returned, that probably means there was a very large pore volume separating the two wells or that there was a very small flow rate running between the wells in question. A small flow rate should correspond to a small IWC which could be confirmed by comparison to the flow rate-based connectivity parameters, F.

Table 1.4: Estimated pore volume of each injector-producer connection, as computed from the average response of all simulated injection rate configurations. The color coding refers to the presumed quality of the estimates; red is poor, yellow is medium and green is good. Volume estimates are in m^3.

Vx [m^3]	I1	I2	I3	I4
P1	19,052	28,920	405	7,972
P2	22,018	17,719	16,413	34,272
P3	18,864	11,796	71,227	16,432

Table 1.5: Estimated pore volume of each injector-producer connection, as computed from the response with all injection rates equal (Config. 7). The color coding refers to the presumed quality of the estimates; red is poor, yellow is medium and green is good. Volume estimates are in m^3.

Vx [m^3]	I1	I2	I3	I4
P1	8,367	32,691	0	1
P2	24,903	1,848	17	41,235
P3	241	1	65,371	14,676

1.7.2.3 Optimization of injection strategy

An optimal injection strategy was designed for the Soultz-based reservoir model. It was assumed that flow rate-based IWCs were available, along with tracer returns obtained with all injection rates equal to 3000 m^3/day (Config. 7, Table 1.3). We also assumed that some core samples were available, along with wellbore imaging logs that would give an idea about the aperture and porosity of the fractures we were looking at. Otherwise, we tried to ignore any additional knowledge we had about the reservoir.

The average of the flow rate and tracer-based IWCs was used to compute the injector-producer flow rates (Table 1.6).

Table 1.6: Interwell connectivity (IWC) parameters used for optimization. These are the average values of those parameters estimated by flow rate variations and tracer returns.

IWC≡F	I1	I2	I3	I4
P1	0.201	0.876	0.022	0.031
P2	0.692	0.103	0.052	0.869
P3	0.056	0.030	0.971	0.080

The direct estimation of the pore volumes using these IWCs gave the volume estimates shown in Table 1.7.

Table 1.7: Estimated pore volume using IWC parameters from Table 1.6 and tracer returns from flow configuration 7. Inadequate estimates are labeled in yellow.

Vx [m^3]	I1	I2	I3	I4
P1	17,116	27,807	8,263	5,776
P2	21,419	75,070	17,086	39,768
P3	10,423	24,325	59,393	18,229

The inadequate pore volume estimates corresponded to cases where relatively little tracer had been recovered. As explained earlier, this did not necessarily mean that there was no fracture connection between the wells in question. It could have been that the measurement time was not long enough, because the flow rate was low, as indicated by the IWC estimates. Thus, we used the good connections to compute an average pore volume per distance between wells. This yielded $\frac{V_x}{L} \approx 48$ m^2, which lead to the estimated pore volumes shown in Table 1.8.

Table 1.8: Estimated pore volumes used for optimization.

Vx [m3]	I1	I2	I3	I4
P1	17,116	27,807	79,572	85,899
P2	21,419	43,908	29,001	39,768
P3	82,304	97,164	59,393	18,229

The ratio of the pore volume to the IWC could be used as an indicator of the time until thermal breakthrough (Table 1.9). This can be seen by writing out Lauwerier's (1955) solution in the form:

$$T_{D,ij}(t, q_{Ii}) \approx erfc\left(\frac{\xi_{ij}}{2\sqrt{\theta\tau_{ij}}}\right) = erfc\left(\frac{V_{x,ij}}{F_{ij}q_{Ii}R\phi_f 2b_{ij}}\sqrt{\frac{K_r\rho_{am}c_{am}}{(\rho_w c_w)^2 t}}\right) \quad (2.74)$$

The pore volume to IWC ratio indicated that the largest interaction would be between well pairs *P1-I2*, *P2-I1*, *P2-I4*, and *P3-I3*.

Table 1.9: Ratio of pore volume to IWC estimated for the optimization problem.

Vx/F	I1	I2	I3	I4
P1	85,015	31,733	3,595,986	2,735,735
P2	30,949	428,119	561,737	45,775
P3	1,464,266	3,230,772	61,180	227,084

Equation (2.74) shows that the principal remaining uncertainty is with the group $R\phi_f b_{ij}$. In practice, some average estimate for the fracture and matrix porosity might be obtainable from

core sampling, but determining the effective aperture, b_{ij}, would be challenging. For lack of a better method we simply took b_{ij} =1 m, as that value would seem to be at the right order of magnitude based on well bore imaging. Assuming that the core data had given ϕ_m =0.001 and ϕ_f =0.04, we then had all the parameters required for Equation (2.74).

The optimization was performed using the IWCs and pore volumes given in Table 1.6 and Table 1.8, respectively. The net present value objective function was chosen, with a 4500 m^3/day upper bound constraint on the individual injection rates, and a 12000 m^3/day total injection constraint. As before, the interest rate was r=8% and the energy price was increasing over a 30 year period in real terms, from 60 to 120 $/MWh with an added 2% inflation. The optimal injection rates, based on these assumptions, are shown in
Table 1.10.

Table 1.10: Optimal injection rates.

Well	[m3/day]	
I1	1,225	20%
I2	1,244	20%
I3	2,145	35%
I4	1,516	25%
ΣIi	6,130	100%

The objective function could not be plotted in this case, as it was four-dimensional. We could, however, view slices of the objective function with two of the decision variables fixed at the optimal values. Figure 1.40 shows a $q_{I1} - q_{I2}$ slice of the objective function with q_{I3} and q_{I4} fixed at the optimal values. These plots were useful to verify that the optimization algorithm had at least found a local maximum.

Based on the analytical temperature estimates, the value of the objective function increased by 37% compared to the initial allocation of 3000 m^3/day per well. However, it is more meaningful to look at the improvement based on the simulations, since they were meant to represent the actual outcome of the injection strategy. The simulation based NPV for the initial allocation was 19.7 M$, while the optimized allocation yielded 25.2 M$. Thus, a 27% increase was obtained over the initial allocation.

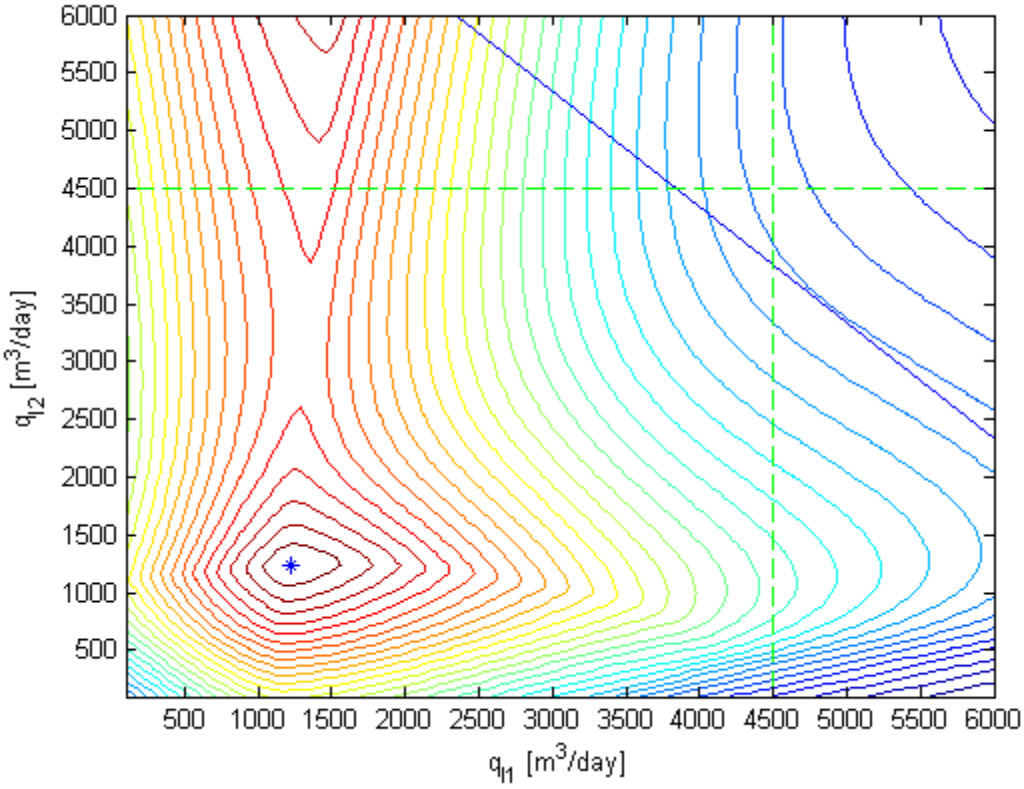

Figure 1.40: A contour plot of a slice through the objective function based on net present value of production. The slice is taken with q_{I3} =2145 m^3/day and q_{I4} =1516 m^3/day, which are the optimum values. A maximum total injection constraint of 12000 m^3/day is illustrated by the blue diagonal line. Maximum injection constraints of 4500 m^3/day for injectors I1 and I2 are shown by the green dashed lines. The optimum feasible point is shown by the blue star.

The predicted and simulated thermal breakthrough curves are shown in Figure 1.41 for the case when the flow was distributed evenly at 3000 m^3/day to each injector. The same curves for the optimal injection rates are shown in Figure 1.42.

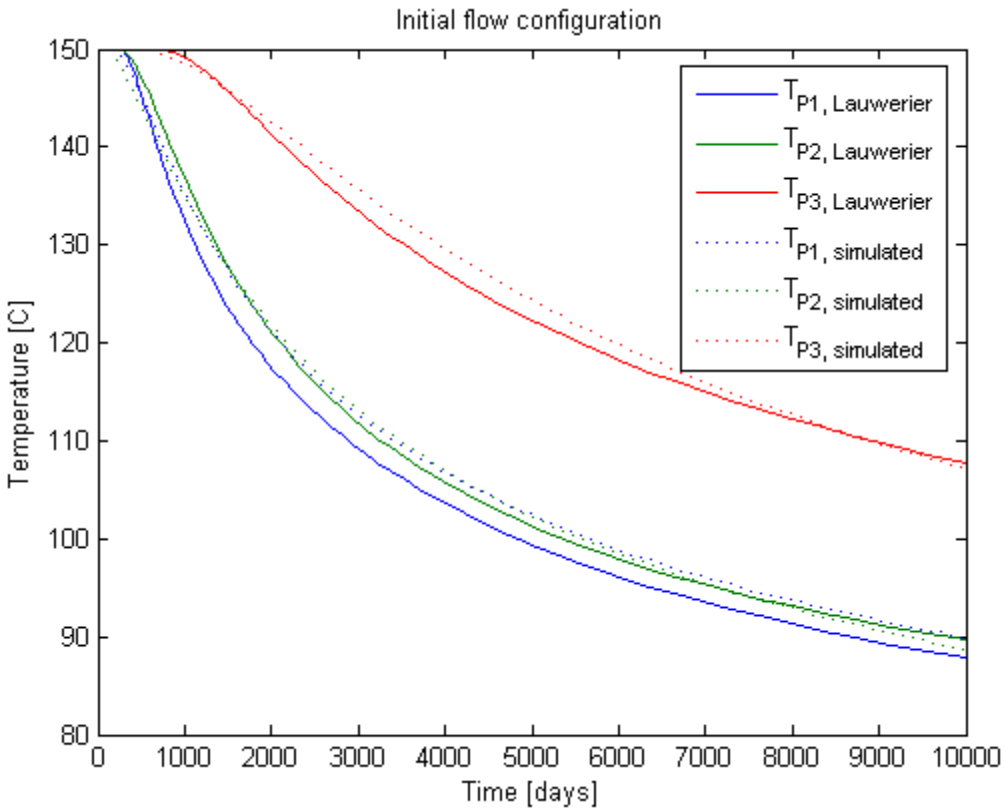

Figure 1.41: Comparison of simulated thermal breakthrough and thermal breakthrough as predicted by the Lauwerier (1955) analytical model. For this case water at 50 C was injected at 3000 m^3/day into each of the four injectors.

The predicted and simulated breakthrough curves matched surprisingly well, especially for the even injection case. This good match was probably somewhat coincidental because the aperture value was chosen rather arbitrarily. Better ways to characterize the fracture aperture are needed but not easy to find.

An alternative to finding the fracture aperture would be to estimate the effective heat transfer area of the flow path. For example, Equation (2.74) can be approximated in terms of the effective heat transfer area, $A_{x,ij}$, as follows:

$$T_{D,ij}(t, q_{Ii}) \approx erfc\left(\frac{A_{x,ij}}{F_{ij} q_{Ii}} \sqrt{\frac{K_r \rho_{am} c_{am}}{(\rho_w c_w)^2 t}}\right) \tag{75}$$

This way one could avoid having to determine the fracture volume and aperture and focus on ways to determine the size of the fracture surface, e.g., based on seismic imaging or functional tracers.

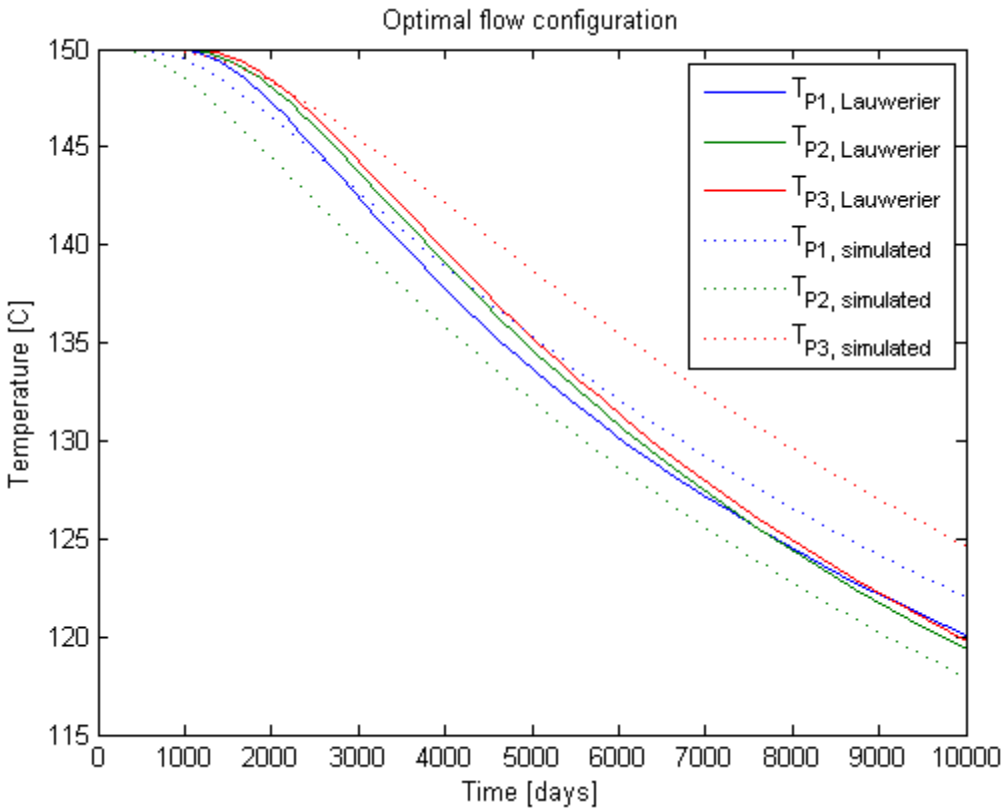

Figure 1.42: Comparison of simulated thermal breakthrough and thermal breakthrough as predicted by the Lauwerier (1955) analytical model. For this case water at 50 C was injected at the optimal flow rates given in Table 1.10.

1.8 CONCLUSIONS

This annual report summarizes a number of advances that have been made in characterizing fracture networks with production data, and utilizing that information to optimize reservoir performance.

The first section provided a relatively abstract overview of the regression models that have been used so far in relation to this research project. The section builds incrementally from relatively simple multiple input linear regression models to nonlinear nonparametric regression models with multiple inputs and multiple time lags (i.e. ACE). We also tried to analyze the advantages and disadvantages of each method, and point out how more free parameters may lead to better data fits but poorer predictive capabilities.

A solution to the one-dimensional advection-dispersion equation with time-varying coefficients was presented. This solution had not been presented in the solute transport literature to our knowledge, although a similar conclusion in discrete and rather convoluted form was derived by Carlier (2008). The solution is based on a change of parameters from time to cumulative injection. With this transformation a number of solutions can be written out based on known

solutions to the advection-dispersion equation for different boundary conditions and in multiple dimensions. Some simplifying assumptions had to be made about the relationship between dispersivity and flow rate.

The third part of this report gave a brief overview of models that have been used to describe rate-pressure, pressure-pressure and rate-rate interactions between wells. We attempted to give the most general form of the equations used in each case, along with the key tricks and assumptions used. The development of the rate-rate models was followed a bit more closely than the others. This was done mostly for the benefit of our understanding of how they work, and the fact that they seem particularly practical for large scale estimation and prediction.

The cumulative flow based solution to the advection-dispersion equation was used to estimate tracer kernels (or transfer functions) at multiwell variable flow rate conditions in Section 1.6. A nonparametric method for estimating the kernels was developed. The method performed very well for special cases of strongly fracture-dominated flow. For more complex fracture networks, rigorous application of the method becomes overly cumbersome, and it seems infeasible to estimate all the convolution kernels that need to be involved.

Nonetheless, reasonably good predictions were obtained by assuming that one convolution kernel could be found for each injector-producer pair. Although this method does not follow the physical model rigorously, it may work well in practice. The method has the advantage of capturing the delayed diffusive nature of tracer returns, and the delay is measured in terms of cumulative flow as opposed to time. Hence the method can be useful to characterize the fracture connections between wells, which is one of our primary objectives.

The final chapter was on scheduling of injection rates so as to maximize the net present value (NPV) of production from the reservoir. This model was based on an analytical thermal transport model, as well as a correlation between the specific power output and temperature. The specific power output function provided a natural way to incorporate a penalty for falling below a certain minimum design temperature. This made it possible to determine the absolute optimal values of the injection rates for each well.

All NPV method was tested with a relatively simple flow model with two injectors and two producers. The method was also tested on a larger scale model which was based on observations from the Soultz-sous-Forêts enhanced geothermal system in France. The results looked promising for those cases tested.

As for any modeling problem, the success of each of these optimization methods relies on the quality of the available data, and the extent to which the modeling assumptions apply to the system under investigation. These methods are most applicable in fractured reservoirs where there are relatively few dominant flow paths connecting the wells. Some of the required data can be obtained by standard methods, while others are relatively hard to obtain. Good estimates of the effective fracture aperture or the heat transfer area for each injector-producer pair seem to be particularly elusive.

2. FRACTURE CHARACTERIZATION OF ENHANCED GEOTHERMAL SYSTEMS USING NANOPARTICLES

This research project is being conducted by Research Associates Mohammed Alaskar and Morgan Ames, Senior Research Engineer Kewen Li and Professor Roland Horne. The objective of this study is to develop in-situ multifunction nanosensors for the characterization of Enhanced Geothermal Systems (EGS).

2.1 SUMMARY

The transport behaviors of both inert and sensitive nanoparticles of different shapes, sizes, and compositions were investigated in various porous and fractured media. Specifically, we performed injections of coated iron oxide nanoparticles into a slim tube packed with glass beads, spherical silver nanoparticles into Berea sandstone, tin-bismuth nanoparticles into Berea sandstone, silica nanoparticles into fractured greywacke, and fluorescent silica microspheres into both fractured greywacke and a glass fracture model. Several attempts were made to synthesize small diameter (< 200 nm), monodisperse tin-bismuth alloy nanoparticles using a sonochemical synthesis route. A preliminary experiment was performed to investigate the magnetic collection of nanoparticles. Finally, a preliminary study of using return curve analysis to determine the measurement geolocation of temperature measurements was performed.

The injection of iron oxide (Fe_2O_3) nanoparticles coated with surfactant polyvinylpyrrolidone (PVP) was conducted to explore the nanoparticles mobility through slim tube packed with glass beads. Surfactant coating of iron oxide nanoparticles modified their surface charge. Both the nanoparticles and flow medium have negative charge. Coated iron oxide nanoparticles were identified in the effluent using scanning electron microscopy (SEM) imaging. The concentrations were determined by measuring their absorption using UV-vis spectrophotometry. The return curve showed that about 23% of injected nanoparticles were recovered.

Spherical silver nanoparticles were injected into Berea sandstone. The silver nanoparticles were identified in the effluent samples and only 25% of injected nanoparticles were recovered. Post-injection of pure water at higher injection rates and backflushing of the core sample did not result in additional recovery of the silver nanoparticles and all effluents were nanoparticles free.

Tin-bismuth nanoparticles were injected into Berea sandstone and into a tube packed with glass beads. It was found that tin-bismuth nanoparticles can be recovered following their injection into the tube packed with glass beads without being trapped within the flow conduits, but not through the pore network of the Berea sandstone. During the core injection, the tin-bismuth nanoparticles were identified in a few effluent samples at low concentrations. It was observed that smaller nanoparticles (200 nm and smaller) were transported through the pore spaces of the rock. Backflushing showed that there was entrapment of nanoparticles, including sizes greater than 200 nm. This might be attributed to an affinity of these nanoparticles to the sandstone rock matrix or high nanoparticle concentration imposing constraints to their flow. Mobility of the tin-bismuth nanoparticles in the absence of rock material was tested by their injection into the tube packed with glass beads. It was found that the tin-bismuth nanoparticles of all sizes flowed through the slim tube.

The injection of silica (SiO_2) nanoparticles was conducted to explore the nanoparticle mobility through the fractured greywacke core from The Geysers. The silica nanoparticle size was 350 nm with negative 73 mV surface charge. The nanoparticles were identified in the effluent using scanning electron microscopy (SEM) imaging and dynamic light scattering (DLS). The return curve of the nanoparticles was not determined because the concentration of injected nanofluid or effluents were not known. The permeability of the core sample dropped significantly following the injection of the nanoparticles.

Preliminary investigation of the flow mechanism of nanoparticles through a naturally fractured greywacke core was conducted by injecting fluorescent silica microspheres. We found that silica microspheres of different sizes (smaller than fracture opening) could be transported through the fracture. We demonstrated the possibility of using microspheres to estimate fracture aperture by injecting a polydisperse microsphere sample. It was observed that only spheres of 20 μm and smaller were transported. This result agreed reasonably well with the measurement of hydraulic fracture aperture (27 μm) as determined by the cubic law.

We investigated the flow of fluorescent silica microparticles in a glass fracture model. The experimental apparatus setup and standard measurements of fracture hydraulic aperture and permeability were completed. The fracture aperture was found to be around 57 µm, with corresponding average permeability of 272 darcy. Silica microspheres were injected into the glass fracture model, and it was found that 2 µm microspheres of could be transported through the fracture, with a cumulative recovery of about 76%. This injection serves as a baseline experiment for future injections using the glass fracture model.

The sonochemical synthesis of tin-bismuth nanoparticles was repeated in less viscous oil in an attempt to achieve a more uniform particle size distribution, and the sample was characterized using SEM imaging and DLS. A monodisperse sample should allow more conclusive demonstration of the size change sensing mechanism and may even aid their transport through rock. While this sample had a narrower size distribution than was achieved previously, the size distribution is still wider than desired. In an attempt to obtain a sample with a narrower size distribution and particles smaller than 200 nm, centrifugations of this sample were performed at several centrifugation speeds. DLS measurements were performed on the resulting samples, and it was found that while narrower size distributions were achieved, particles larger than the 200 nm threshold were still present. Also, the resulting sample was very dilute. For these reasons, the sonochemical synthesis of tin-bismuth nanoparticles was repeated at the highest possible sonication power with the expectation of obtaining a sample with a greater number of small (<200 nm) nanoparticles. This sample was also centrifuged to separate large particles. The original and centrifuged samples were characterized using DLS.

An experiment was conducted to evaluate the feasibility of magnetic collection of nanoparticles from produced fluid. A magnetic trap was constructed using permanent neodymium magnets, and iron oxide nanoparticles coated with silica (magnetic silica nanoparticles) were injected into an open tube over which the magnetic trap was placed. It was estimated using uv-vis spectroscopy that 3% of the injected nanoparticles were recovered in a prototype magnetic collection device.

Finally, a preliminary investigation of the estimation of measurement geolocation was carried out. A simple analytical model was developed for a dye-releasing nanosensor and a conservative solute tracer. Synthetic return curve data was generated for two hypothetical tracer tests, and reasonably good estimates of measurement geolocation were realized, indicating that dye-releasing nanosensors could potentially be used to map the temperature distribution of geothermal reservoirs.

2.2 INTRODUCTION

Geothermal applications require materials that are suitable for harsh environments of high pressures and temperatures. Extraordinary properties of materials made at nanoscale can provide these requirements. Therefore, it is proposed to explore the possibility of utilizing nanoparticles as sensors to characterize fracture systems. The main idea is based on the fact that certain types of nanosensors have the ability to record data such as pressure and temperature within the reservoir. Actually, temperature-sensitive nanomaterials have been already used in biomedical industry for drug delivery to particular type of body cell. For geothermal field applications, it is envisioned that the nanoparticles of different sizes and shapes can accompany the injected fluids at one well and recovered from another within the same reservoir. The nanoparticles that made their way to the producing well will be analyzed and correlated with the fracture properties.

In the development of enhanced geothermal systems, the characterization of the size, shape and conductivity of fractures is crucial. Unlike conventional geothermal systems, enhanced geothermal systems do not require natural convective hydrothermal resources, but rather can be created in a hot, dry and impermeable volume of rock. Hydraulic stimulation of fractures is the primary means of creating functional geothermal reservoirs at such sites to allow economical heat recovery. The energy extraction rate is significantly dependent on the creation of fractured area within the targeted hot rock volume. Mapping fractured area is of equal importance. However, existing fracture characterization tools and analysis approaches are inadequate, especially at higher temperature and greater depth. Pressure and temperature are measured only at the wellbore, and it is not possible to determine the conditions out in the reservoir. There are no effective means to measure such properties far in the rock formations. Thus, the objectives of this research are to provide a new tool (nanosensors) and to develop reservoir engineering approach to estimate reservoir parameters and characterize fracture networks based on the measurements from these tools.

In order to investigate the feasibility of utilizing nanosensors in illuminating reservoir properties in general and fracture network properties in particular, it was essential to verify their transport mechanism through typical formation rock core samples. Initial testing with nanoparticles was also required to develop the understanding of their optimum injection procedures, sampling strategies and characterization techniques. Accordingly, various laboratory injection experiments were carried with inert and sensitive nanoparticle suspensions in a variety of porous and fractured media: injections of coated iron oxide nanoparticles into a slim tube packed with glass beads, spherical silver nanoparticles into Berea sandstone, tin-bismuth nanoparticles into Berea sandstone, silica nanoparticles into fractured greywacke, and fluorescent silica microspheres into both fractured greywacke and a glass fracture model. Temperature-sensitive tin-bismuth

nanoparticles were synthesized using a sonochemical synthesis route, and centrifugation was used to separate size fractions in an attempt to achieve a relatively monodisperse suspension with particle diameters less than 200 nm. Preliminary investigations were performed to investigate the magnetic collection of nanoparticles and the use of return curve analysis to determine the measurement geolocation of temperature measurements.

2.3 CHARACTERIZATION OF POROUS AND FRACTURED MEDIA

The measurements of the porosity, permeability and pore volume of the Berea sandstone core, slim tube packed with glass beads, fractured greywacke core, and glass fracture model are described in this section. Hydraulic fracture aperture measurements of the fractured greywacke core and glass fracture model are also described.

2.3.1 Berea Core Characterization

The core sample tested during tin-bismuth injection was a Berea sandstone of 3.8 cm diameter and 5.1 cm length. The porosity and liquid permeability were determined. Porosity and permeability results are summarized in Table 2.1. The pore volume was found to be of order 10 ml. The characterization of the Berea sandstone used in the silver nanoparticle injection can be found in the last quarterly report (July-September, 2010). The porosity, permeability and pore volume were found to be 17.1% , 60.7 md and 8 ml, respectively.

Table 2.1: Porosity and permeability measurements of Berea sandstone used in tin-bismuth injection experiment.

Property	Measurement method	Value
Porosity (%)	Saturation with deionized water	17.5
Permeability (md)	Liquid permeability	125.4
Pore volume (ml)	By resaturation	10

A schematic of the apparatus used in the measurement of liquid permeability is shown in Figure 2.1.

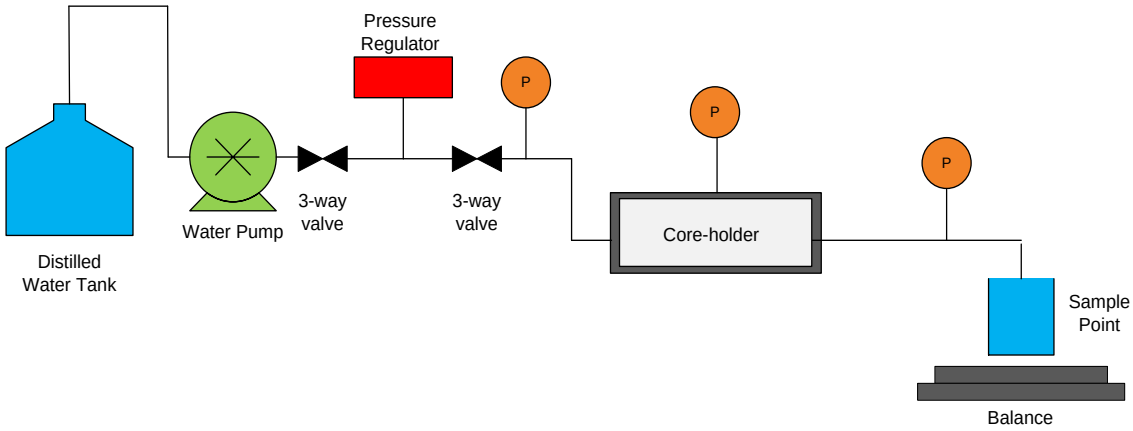

Figure 2.1: Schematic of apparatus for liquid permeability measurement.

The core sample was first saturated with water outside the core-holder. The core and related system were evacuated using a Welch Vacuum Pump for 4 hours at a vacuum pressure of about 20 millitorr to remove moisture. Pure water was introduced to submerge the sample completely. The core was then left submerged overnight and the remaining vacuum released to aid the process of saturation. After that the core was removed and wiped dry to remove excessive water on the surface. Finally, the core was weighed and hence its porosity was calculated. The core turned out to have a porosity of around 17.5 % and a pore volume of 10 cm^3. The porosity calculation is as follows:

$$\phi = \frac{V_p}{V_B} * 100 \tag{2.1}$$

$$V_p = W_s - W_d \tag{2.2}$$

$$V_B = \pi r^2 l \tag{2.3}$$

where ϕ is the porosity in percentage, V_p and V_B are pore and bulk volumes in cubic centimeter, respectively. W_s and W_d are the weight of core after and before saturation, in gram, respectively. r and l are the radius and length of the core in centimeter, respectively.

The average liquid permeability was found to be around 125.4 millidarcy. Darcy's law for horizontal flow was utilized to compute the permeability. Darcy's law for horizontal flow is given by:

$$k_{liq} = \frac{q\mu L}{A\Delta p} \tag{2.4}$$

where q is the volumetric flow rate in milliliter per second, μ is the viscosity in centipoise, L and A are the length and the cross-sectional area of the core in centimeter and square centimeter, respectively. Δp is the differential pressure across the core sample in atmospheres.

2.3.2 Polypropylene slim tube packed with glass beads

To investigate the mobility of nanoparticles in the absence of the rock materials (such as clays), iron oxides and tin-bismuth nanoparticles were injected into two separate slim tubes packed with glass beads. The 30 cm long polypropylene tubes were packed with glass beads (Glasperlen 1 mm in diameter from B. Braun Biotech International) and fitted with screens and valves at each end. A polypropylene slim tube is pictured in Figure 2.2.

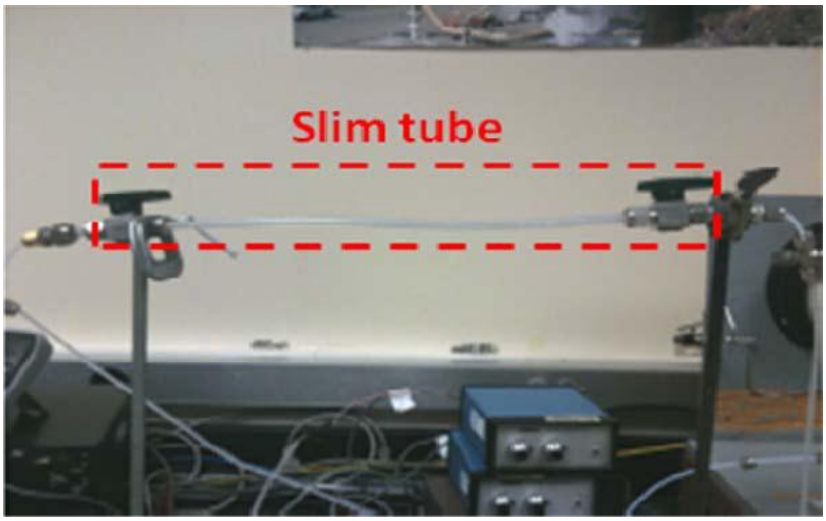

Figure 2.2: Polypropylene slim tube packed with glass beads. Two tubes were constructed: one for iron oxide and the other for tin-bismuth nanoparticle injection.

The porosity was measured by the saturation method. The porosity and pore volume of the slim tubes are summarized in Table 2.2

Table 2.2: Porosity and permeability measurements of slim tubes packed with glass beads used iron oxide and in tin-bismuth injection experiments.

Property	Iron oxide injection	Tin-bismuth injection
Porosity (%)	48	58
Permeability (darcy)	19	18.1
Pore volume (ml)	2.6	2.6

2.3.3 Fractured Greywacke Core

The core sample tested was a fractured greywacke from The Geysers geothermal field, with 5.08 cm diameter and 3.01 cm length (Figure 2.3). The core sample was fitted between the two end-pieces and wrapped with Teflon shrink tube. An electric heating gun was used to bond the assembly together. To achieve proper sealing, the heat was applied evenly starting bottom up in round motion. The assembly was positioned horizontally and polyethylene tubes (0.3175 cm in diameter) and fittings were used to connect the water pump and pressure manometer to the core assembly (Figure 2.4). Since only a very low differential pressure was required to flow fluid through the fractured core, the inlet pressure was measured using a manometer tube rather than a transducer. The flow rate was measured using a balance and stop watch. The hydraulic aperture of the fracture was determined using the cubic law. The average of the hydraulic aperture of the fracture was found to be approximately 27 μm. The average permeability of the rock was found to be 60 darcy.

Figure 2.3: Fractured greywacke core sample.

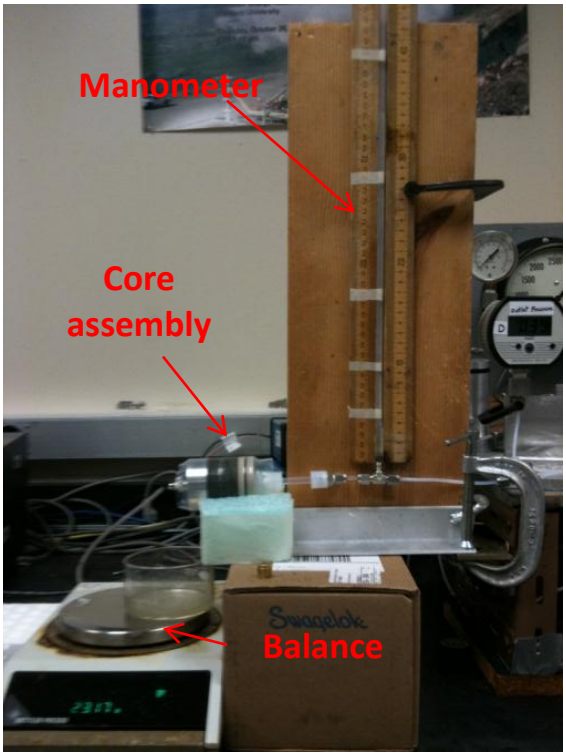

Figure 2.4: experimental setup for hydraulic aperture and permeability measurements of fractured greywacke rock sample.

Prior to saturation, the core was dried at 75°C under vacuum pressure of 0.09 MPa for about 3 days, using a vacuum oven. Then, the core and related system were saturated with dionized water. Initially, the system was evacuated using a vacuum pump under vacuum pressure of about 13 millitorr for about 4 hours. The vacuum pump was connected to the system from the inlet side of the core. A water column used to saturate the system was attached at the outlet side of the core assembly. The water column was positioned on a scale to observe the weight change and hence the water volume entered the system (Figure 2.5).

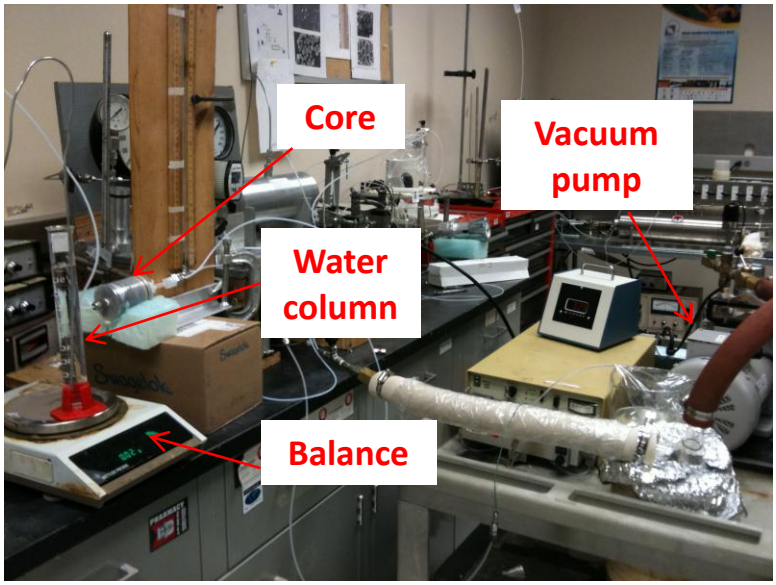

Figure 2.5: Experimental setup during saturation of the fractured greywacke core sample.

The pore volume of the fractured core sample was determined by subtracting the dead volume of connecting tubes, fittings and end pieces from the total volume displaced from the saturation water column. The dead volume of tubes and pore volume were calculated as follows:

$$V_p = V_{total} - V_d \tag{2.5}$$

$$V_{total} = \frac{W_{total}}{\rho_w} \tag{2.6}$$

$$V_d = \pi r^2 l \tag{2.7}$$

Where V_p and V_d are the pore and dead volumes in cubic centimeters, respectively. V_{total} is the total volume of water entering the system in cubic centimeters, W_{total} is the total weight of water entering the system in grams, ρ_w is the density of water in grams per cubic centimeters, l and r are the length and inner radius of tubes, respectively, in centimeters.

Based on the pore volume estimation, the porosity of the core sample was calculated as the ratio of the pore volume to the core bulk volume.

$$\phi = \frac{V_p}{V_B} * 100 \tag{2.8}$$

$$V_B = \pi r^2 l \tag{2.9}$$

where ϕ is the porosity in percentage, V_B is the bulk volume in cubic centimeter, r and l are the radius and length of the core in centimeter, respectively. The core sample was found to have a pore volume of 1.8 cm^3 and porosity of 2.9%. The total volume of water entering the system,

dead volume of tubes, dead volume of end pieces, pore volume and porosity are summarized in Table 2.3.

Table 2.3: summary of bulk, pore, dead volumes and porosity of fractured greywacke core

Measurement	*Value (cm^3)*
Dead volume of tubes	4.2
Dead volume of end pieces	1.75
Total water volume displaced	7.76
Pore volume	1.8
Bulk volume	61.1
Porosity	2.9%

The hydraulic aperture of the fracture was determined using the cubic law. The cubic law is given as

$$Q = \frac{b^2}{12}\frac{bD\Delta p}{\mu L} \tag{2.10}$$

$$k = \frac{b^2}{12} \tag{2.11}$$

Where Q is the flow rate in cubic meters per second, b is the fracture aperture in meter, D is the fracture width in meter, Δp is the pressure drop across the core sample in Pascal, L is the length of the fracture in meter, μ is the test fluid viscosity in Pascal second and k is the permeability in square meters. The permeability can be expressed in Darcy units using the following conversion

$$1darcy = 9.869 \times 10^{-13} m^2 \tag{2.8}$$

The average of the hydraulic aperture of the fracture was found to be approximately 27 μm. The average permeability of the rock was found to be 60 darcy.

2.3.4 Glass Fracture Model

The glass fracture model is being used to investigate the feasibility of using microspheres to estimate fracture aperture (fracture caliper) by injecting a polydisperse microsphere sample into fracture with a predetermined hydraulic aperture. The fracture apparatus used was originally designed to study the multiphase flow of gas and liquid phases through fractures. The apparatus was entirely designed and fabricated by previous researcher Gracel Diomampo during her Master's degree research at Stanford University (Gracel Diomampo, MS Thesis 2001).

The fracture model consists mainly of a smooth glass plate placed on top of an aluminum flat surface. The seal was achieved by placing an o-ring (Viton 1/8" thick #2-272) between the glass (top) and aluminum (bottom) plates. A metal frame was bolted to the bottom plate to improve the seal. The metal frame was designed with supporting beams to prevent glass deformation due to system pressure. The spacing between these two surfaces is the simulated fracture of predetermined width and length (4 by 12 inches). The fracture model is pictured in Figure 2.6.

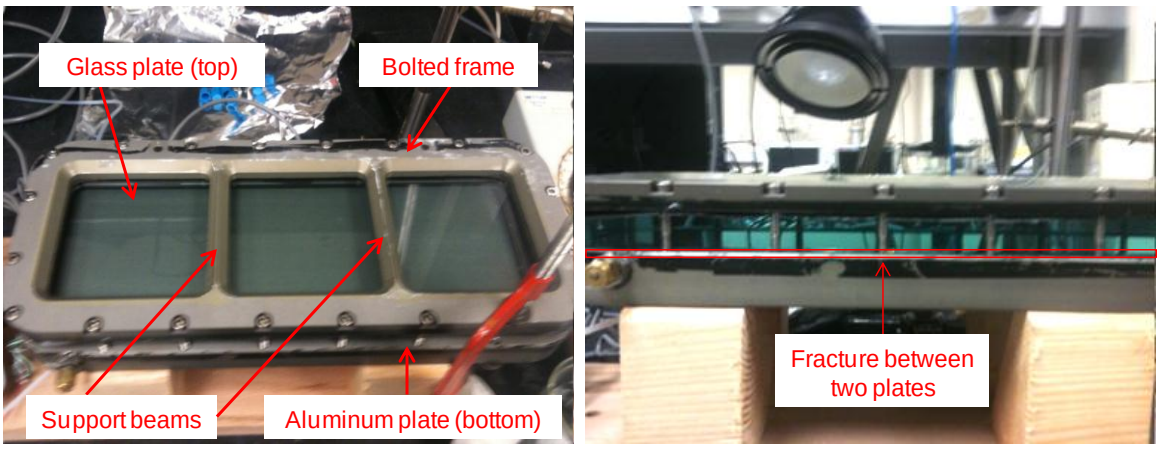

Figure 2.6: Picture of glass fracture apparatus. It shows the bolted frame, top and bottom plates and fracture location.

Since the fracture apparatus was originally designed to study two-phase flow, each fluid enters the fracture through two separate inlet ports, a total of 123 capillary ports, each 0.51 mm in diameter. These ports were aligned to the fracture surface alternately. Four pressure ports with a diameter of 0.51 mm were drilled at certain location throughout the fracture area. Temperature ports were also drilled, but not used during particles injection experiments. Ports were drilled with such a needle-size to minimize surface discontinuity. The fluids exit the fracture through a single outlet. A schematic diagram of the fracture apparatus is depicted in Figure 2.7.

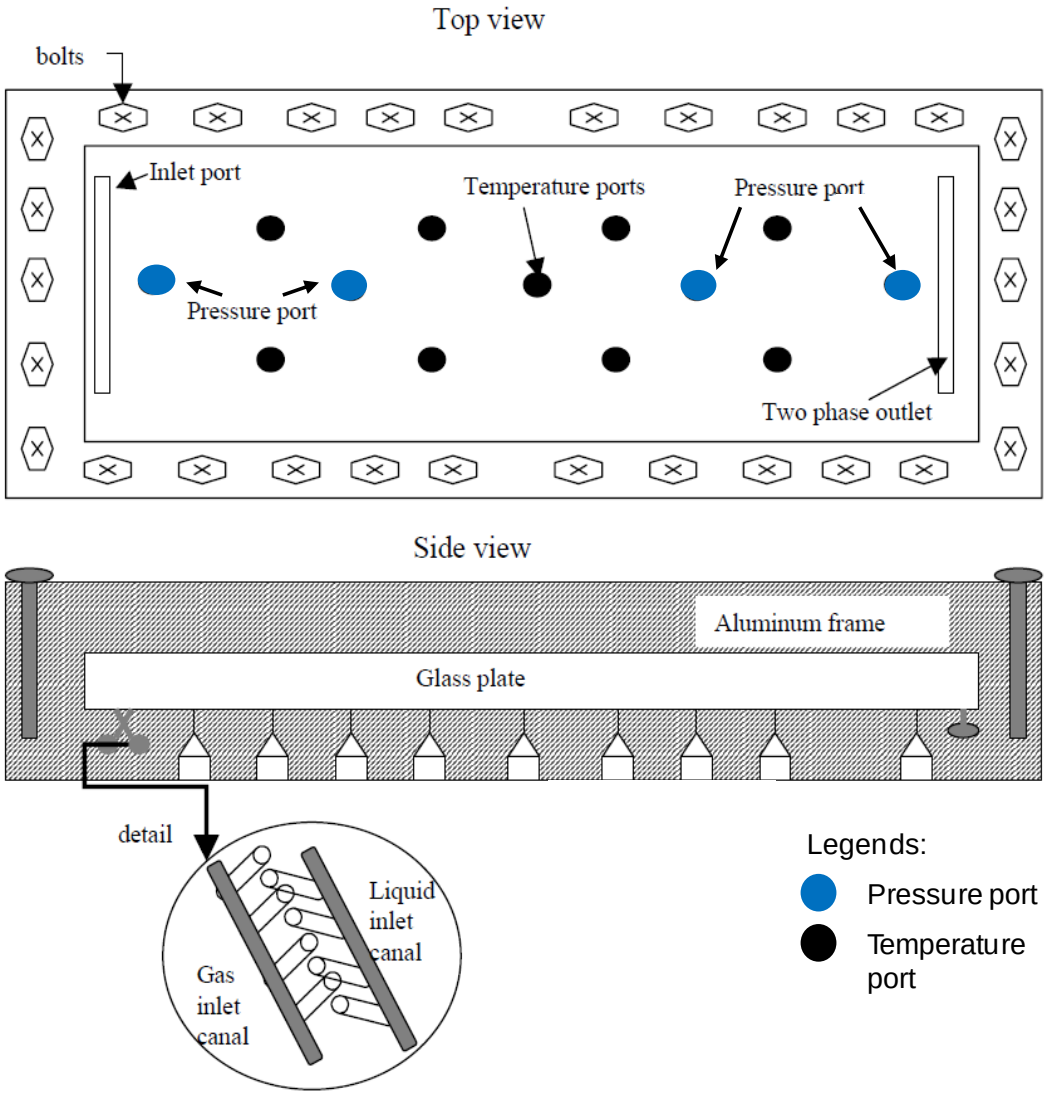

Figure 2.7: Schematic of the fracture apparatus (adopted from Gracel MS thesis).

The pressure difference through the fracture was obtained using low capacity differential transducers. Two liquid filled differential transducers (Validyne Transducer, model DP-215, range 0-1.5 psi and 0-5 psi) were attached to inlet and outlet pressure ports. Both differential pressure transducers were calibrated using a standard pressure gauge with an accuracy of 0.1 psi. The pressure transducer calibration curves are depicted in Figures 2.8 and 2.9. The pressure calibration curves indicate a good agreement between the standard pressure gauge and the differential pressure transducers.

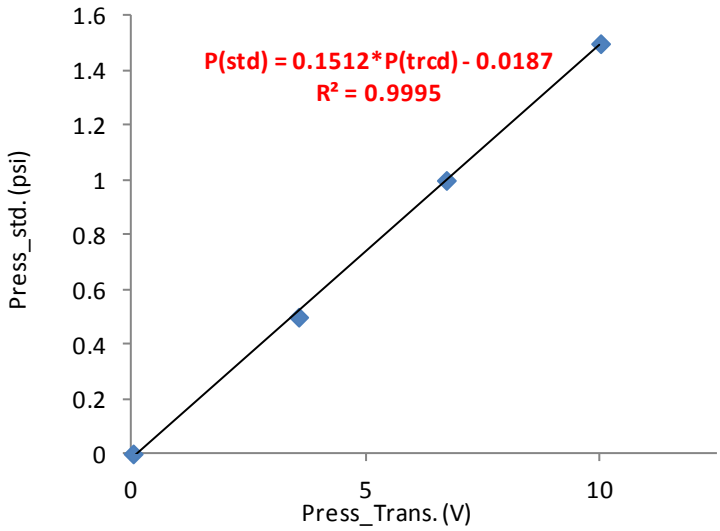

Figure 2.8: Calibration curve of the inlet pressure transducer.

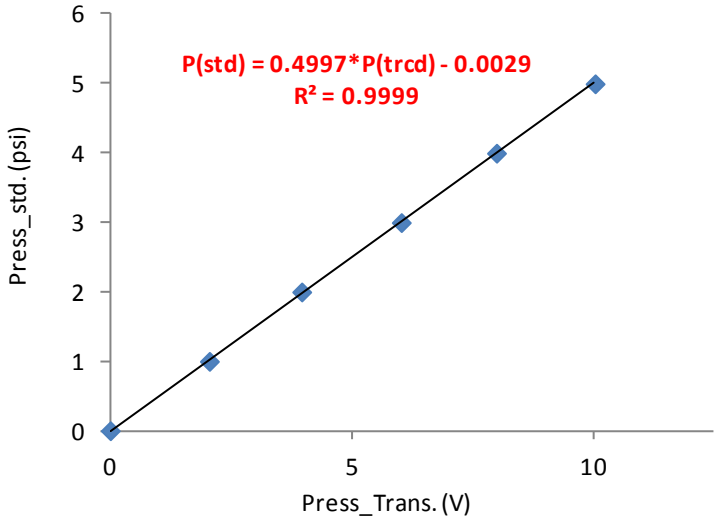

Figure 2.9: Calibration curve of the outlet pressure transducer.

A water pump (Dynamax, Model SD-200) manufactured by RAININ Instrument Company was used to inject the deionized water. The minimum pumping rate of the pump is 0.2 mL/min with an accuracy of 0.01 mL/min. This pump is an automated constant-rate pump. The flow rates of the water pump were calibrated before the experiment using a stop-watch and a Mettler balance (Model PE 300). The accuracy of the balance is 0.01g and the range is from 0 to 300 g. The calibration curve for this pump at room temperature is shown in Figure 2.10. The measured flow rates were consistent with those specified on the pump.

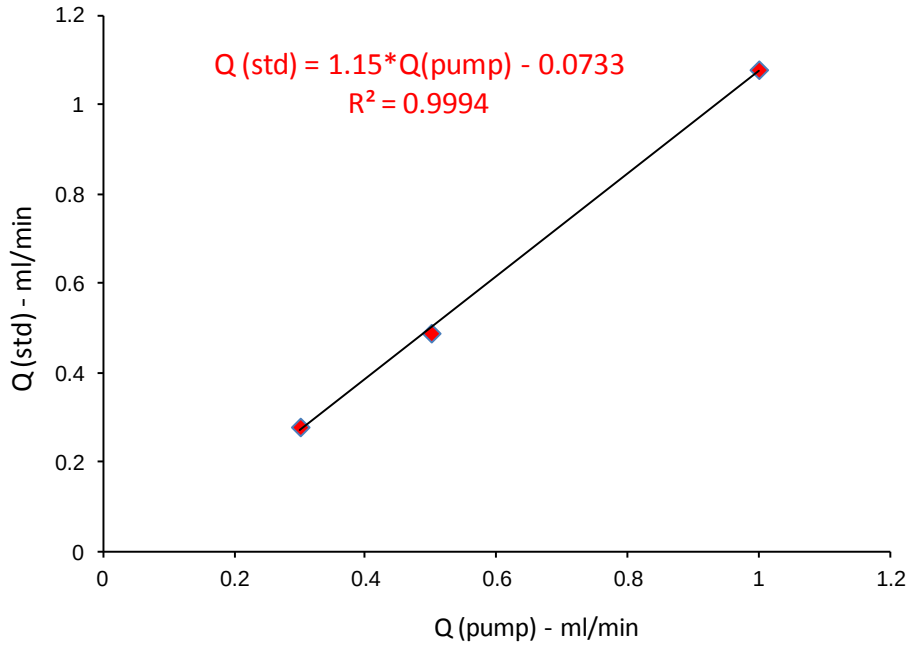

Figure 2.10: Water pump calibration curve.

Prior to permeability or hydraulic aperture measurements, the fracture was saturated with the testing fluid (i.e. deionized water). Air removal via vacuum and resaturation with water was not possible because the system was not designed to withstand vacuum. Instead, the saturation was achieved by first saturating the system with CO_2 then deionized water, as CO_2 dissolve easier in water than air. The fracture apparatus was also tilted by 45 degrees for gravity to aid the saturation process.

The determination of the fracture hydraulic aperture was essential for testing the fracture caliper concept. The hydraulic aperture of the fracture was determined using the cubic law. The cubic law is given as

$$Q = \frac{b^3}{12}\frac{bD\Delta p}{\mu L} \tag{2.12}$$

$$k = \frac{b^2}{12} \tag{2.13}$$

where Q is the flow rate in cubic meters per second, b is the fracture aperture in meter, D is the fracture width in meter, Δp is the pressure drop across the core sample in Pascal, L is the length of the fracture in meter, μ is the test fluid viscosity in Pascal second and k is the permeability in square meters. The permeability can be expressed in Darcy units using the following conversion

$$1 darcy = 9.869 \times 10^{-13} m^2 \tag{2.14}$$

The aperture of the fracture was set by installing stainless steel shims with certain thickness as the fracture spacer. Initially, shims with thickness of 51 µm and 102 µm were used. For both cases, the hydraulic aperture measurements were found to be around 185 µm, indicating that the

aperture measurements were insensitive to shims size of 102 µm or smaller. For example, fracture aperture and permeability measurements with the shims installed can be depicted in Figures 2.11.

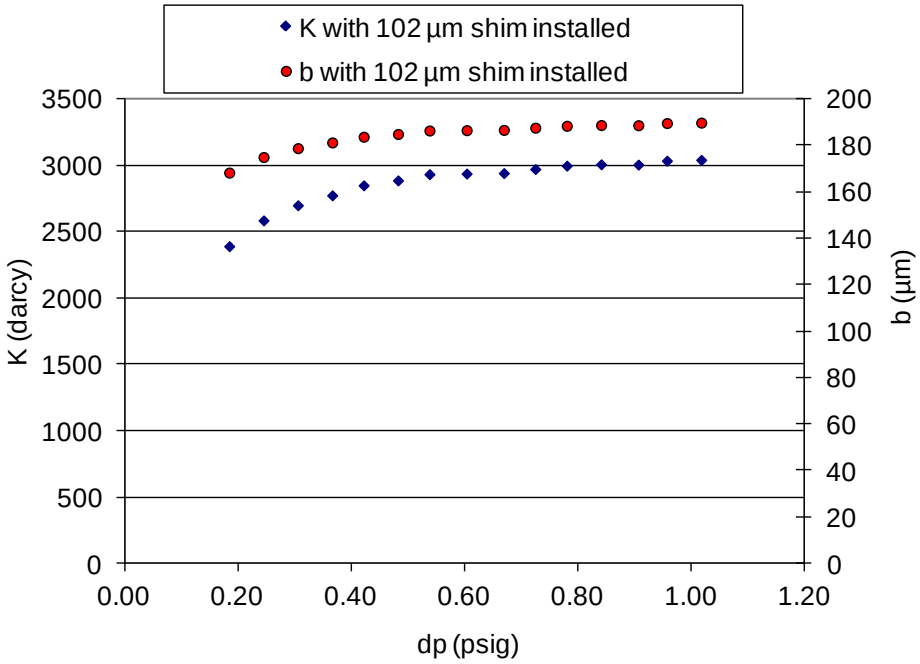

Figure 2.11: Aperture and permeability measurements as function of fracture pressure when 102 µm shims installed.

It was observed that the absolute permeability was changing with flow rate for fracture pressures below about 0.5 psig. It was implied that the fluid was lifting the glass as it flowed through the fracture. At pressures greater than 0.5psi, the glass was lifted to its maximum height defined by the confinement of the metal frame. At this pressure range, the absolute permeability was constant and found to be around 3100 darcy. To confirm the validity of Darcy's law (i.e. flow in fracture is laminar and that inertia effect is negligible), we examine the linearity between single-phase pressure drop and flow rate. Figure 2.12 shows a linear relationship between the pressure drop and flow rate, indicating the negligible effect of inertia of the flow within the fracture.

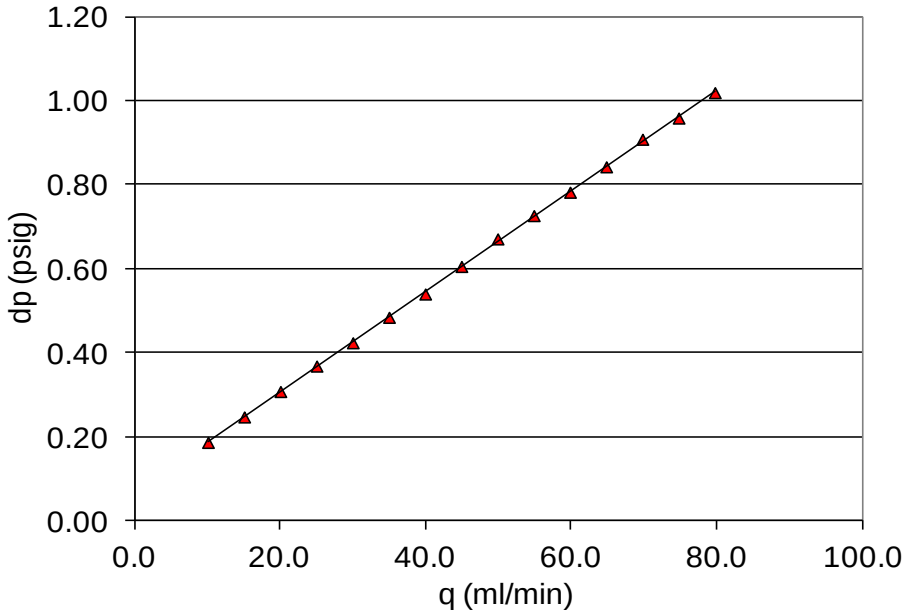

Figure 2.12: Steady-state, single-phase pressure drop versus flow rates during aperture measurements with 102 µm shims installed. Linearity between pressure drop and flow rate confirmed, hence, Darcy's law holds.

Due to the inconsistency between the measured fracture hydraulic aperture (185 µm) and shim size (102 µm), further investigation was carried out. The hydraulic aperture was measured after the removal of the shims. In this case, only the o-ring exists between the glass and aluminum plates. It was found that the hydraulic aperture of the fracture to be around 57 µm with an average permeability of 272 darcy. This has implied that the o-ring was compressed to a minimum height of about 57 µm. When shims were installed, the additional thickness of shims was added. If fracture surfaces were perfectly flat, the measured fracture aperture should be the sum of the o-ring and shim thicknesses (i.e. 102 µm plus 57 µm or total of 159 µm). The difference between measured aperture and expected value (about 26 µm) was believed to be a result of irregularities of flat surfaces. The fracture aperture and permeability measurements without shims can be depicted in Figures 3.3. To avoid uncertainty of aperture measurements, it was decided to use the model without shims during injection of microparticles. That is to design the influent sample to have particles smaller and bigger than 57 µm.

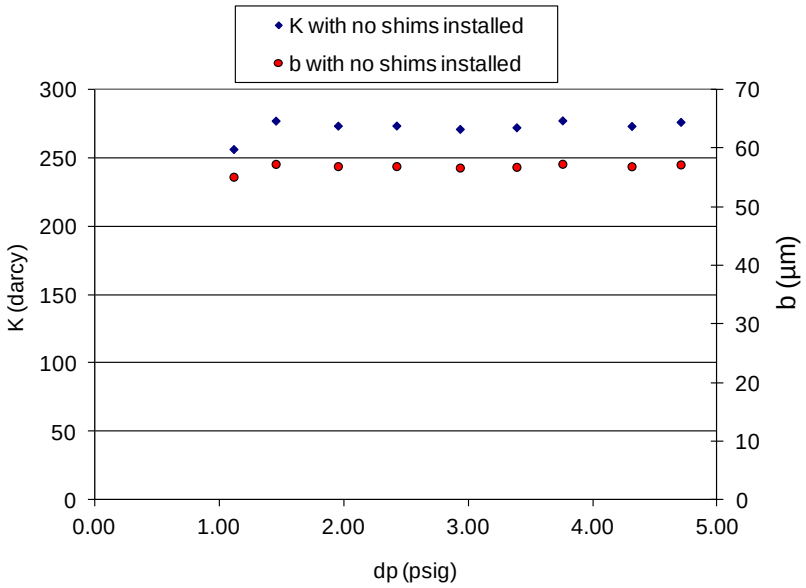

Figure 2.13: Aperture and permeability measurements as function of fracture pressure when 102 µm shims installed.

2.4 NANOPARTICLE AND MICROPARTICLE INJECTION EXPERIMENTS

The transport behaviors of both inert and sensitive nanoparticles of different shapes and sizes were investigated in various porous and fractured media. In this section, we describe injections of coated iron oxide nanoparticles into a slim tube packed with glass beads, spherical silver nanoparticles into Berea sandstone, tin-bismuth nanoparticles into Berea sandstone, silica nanoparticles into fractured greywacke, and fluorescent silica microspheres into both fractured greywacke and a glass fracture model.

2.4.1 Coated iron oxide characterization and injection experiment

In a previous quarter (July-September, 2010), iron oxide (Fe_2O_3) nanoparticles were coated with silica (SiO_2), the surfactants polyvinylpyrrolidone (PVP) and triethanolamine (TEA). The uncoated iron oxide nanoparticles exhibited very low mobility during their injection through the slim tube packed with glass beads (April-June 2010) which was attributed to their geometry and/or surface characteristics. To further investigate if the surface charge is limiting their flow, the iron oxide nanoparticles were coated with surfactants or silica to modify their surface charge. First, iron oxides coated with PVP were injected. However, they were neither detected at the effluent samples nor on the surfaces of the glass beads. It was speculated that the concentration of coated iron oxides in the injected sample was too low to be detected at effluent, and thus a more concentrated sample was prepared and the injection experiment was repeated.

2.4.1.1 Characterization of coated iron oxide (Fe_2O_3)

Coated iron oxides were characterized in terms of size, surface charge (zeta potential) and light absorption using SEM imaging, zeta potential analysis and UV-vis spectrophotometry, respectively. The original iron oxide nanoparticles were 500 nm in length and 100 nm in diameter (Figure 2.14). Surface charge measurements are summarized in Table 2.4. The reported

zeta potentials are the average of three sets of measurements with standard deviation less than 1 mV.

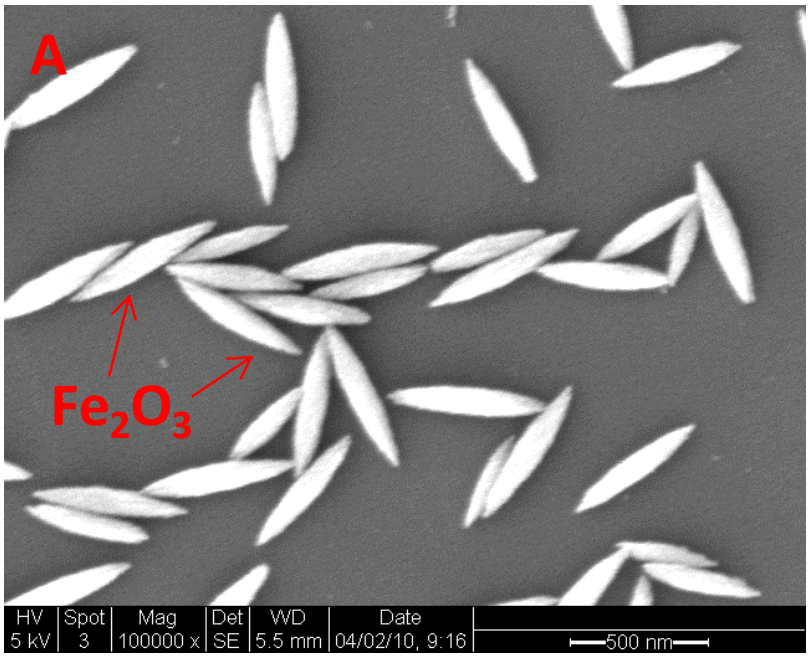

Figure 2.14: SEM image of iron oxide nanoparticles.

Table 2.4: Zeta potential and pH level for original and PVP coated iron oxide nanoparticles.

Sample	Average zeta potential (mV)	pH
Original Iron oxide	+59.3	3.3
Iron oxide-PVP	-1.06	N/A

It was evident from the surface charge measurements that the PVP coating had altered the surface charge of the original iron oxide nanorice. The original (uncoated) nanorice carries a high positive charge of 59.3 mV with low pH of 3.3 compared to the samples coated with PVP surfactant (negative 1.06 mV). The zeta potential distribution of uncoated and PVP coated iron oxide nanoparticles is depicted in Figure 2.15.

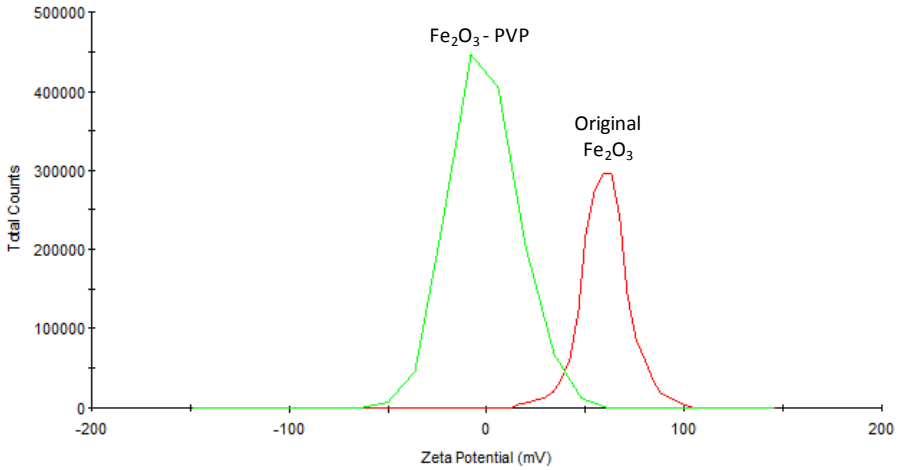

Figure 2.15: Zeta potential distribution of coated and uncoated iron oxide nanoparticles.

UV-visible spectrophotometry was used to measure the absorption of the iron oxide nanoparticles in effluent samples and hence their concentrations. This is an essential step as it enables us to construct the tracer return curve of concentrations versus volume injected. UV-visible spectrophotometry involves the spectroscopy of photons in the UV-visible region, which means that it deals with light in the visible, near-ultraviolet and near-infrared ranges. The spectrophotometer is the instrument used to measure the light intensity as a function of wavelength of light. Beer's Law is used to quantify the concentrations of absorbing species in solution (Wittung et al., 1994). The law states that the absorbance of a solution is directly proportional to the path length through the sample and the concentration of absorbing species in solution. Beer's Law is given by

$$A = -\log_{10}\left(I / I_o\right) = \varepsilon c L \tag{2.15}$$

where A is the measured absorbance, I is the intensity of light passing through the sample, I_o is the intensity of light before it passes through the sample, L is path length through the sample, c is the concentration of absorbing species and ε is the molar absorptivity constant which is specific for each species and wavelength at particular temperature and pressure and has units of $AU / M * cm$.

Therefore, measuring the absorbance of the substance in solution and knowing the path length of the sample along with the absorptivity constant, the concentration of that substance can be calculated. Due to the difficulty in obtaining the absorptivity constant, it is common to determine the concentrations by constructing a calibration curve. By doing so, there is no need to rely on a value of the absorptivity or the reliability of Beer's Law. This is accomplished by making few dilutions, each with accurately known concentration. It is important to ensure that those concentrations bracket the unknown concentrations under investigation. For each dilution, the absorbance is measured and plotted against the sample concentration. This is the calibration curve.

The concentration of the iron oxide nanoparticles in the fluid sample was 0.25 g/cm^3. The nanofluid was diluted 1 part of nanofluid to 2, 4, 9, 17, and 35 parts of ethanol. Dilutions were made using very accurate balance and pipette. The absorbance spectra were measured at room temperature using a Shimadzu UV-1700 double beam spectrophotometer with a 12 mm square polystyrene cuvette. All samples had been sonicated prior to analysis to disperse the particles. The optical (absorbance) signatures of the diluted silver nanofluid samples are shown in Figure 2.16.

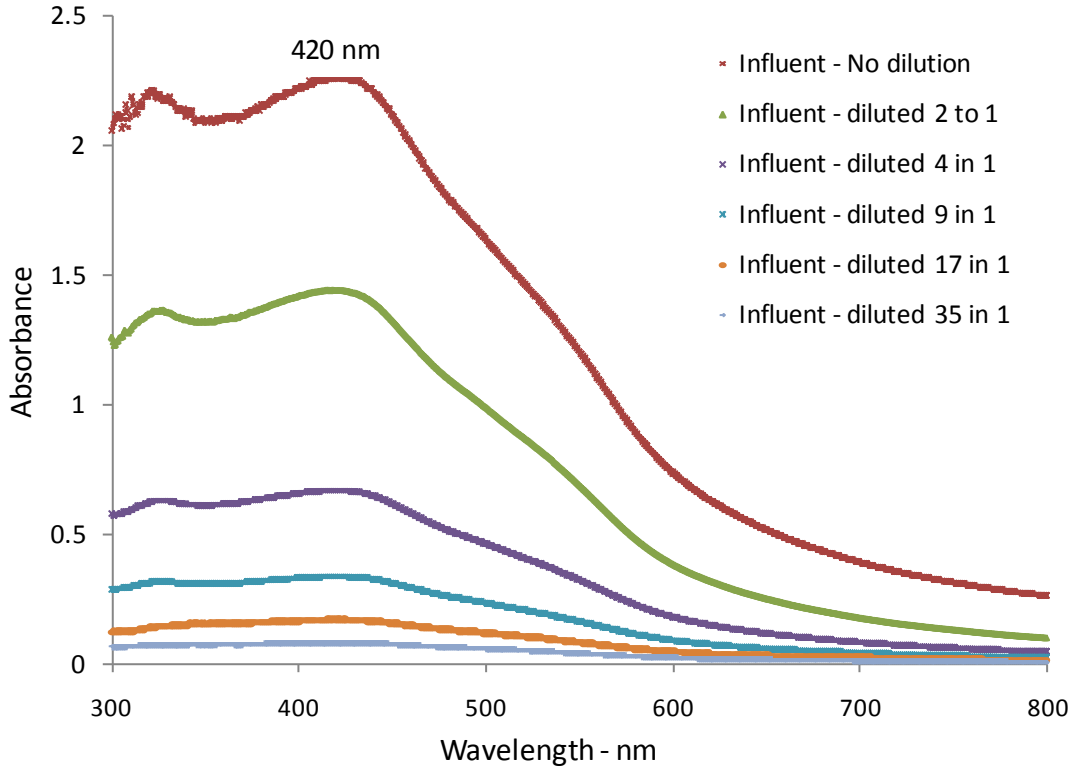

Figure 2.16: Absorbance of diluted iron oxide nanofluids of known concentrations.

The absorbance readings were all taken at a wavelength of 420 nm, as this is the wavelength at which the strongest (maximum) absorption occurs. The diluted sample concentrations and corresponding absorbance values were used to construct the calibration curve (Figure 2.17). The calibration curve was used to determine the concentration of effluent samples during the subsequent experiments.

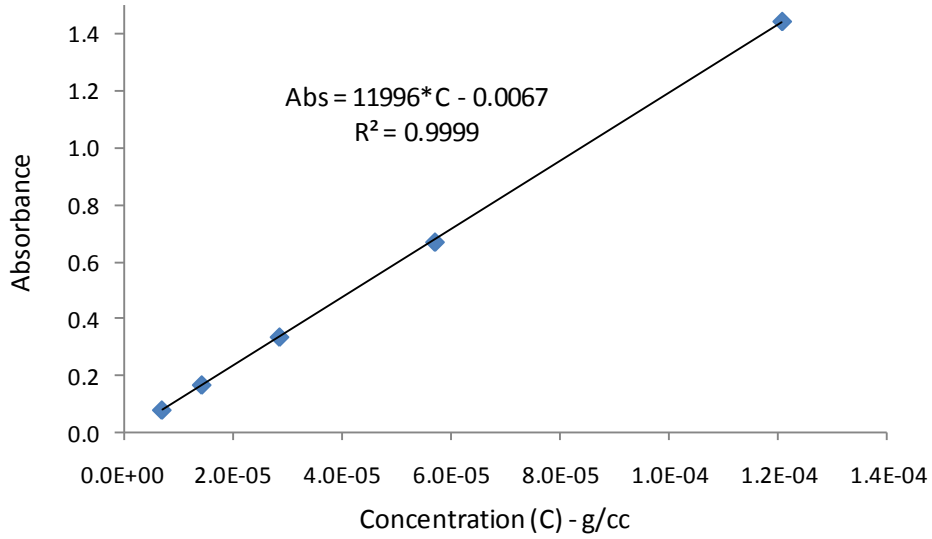

Figure 2.17: Calibration curve of iron oxide nanofluid.

2.4.1.2 Iron oxide (Fe_2O_3) nanoparticle coated with surfactant (PVP) injection into slim tube packed with glass beads

The iron oxide nanoparticles coated with PVP surfactant were injected into the slim tube packed with glass beads. A schematic of the apparatus used in the flow experiment is depicted in Figure 2.18.

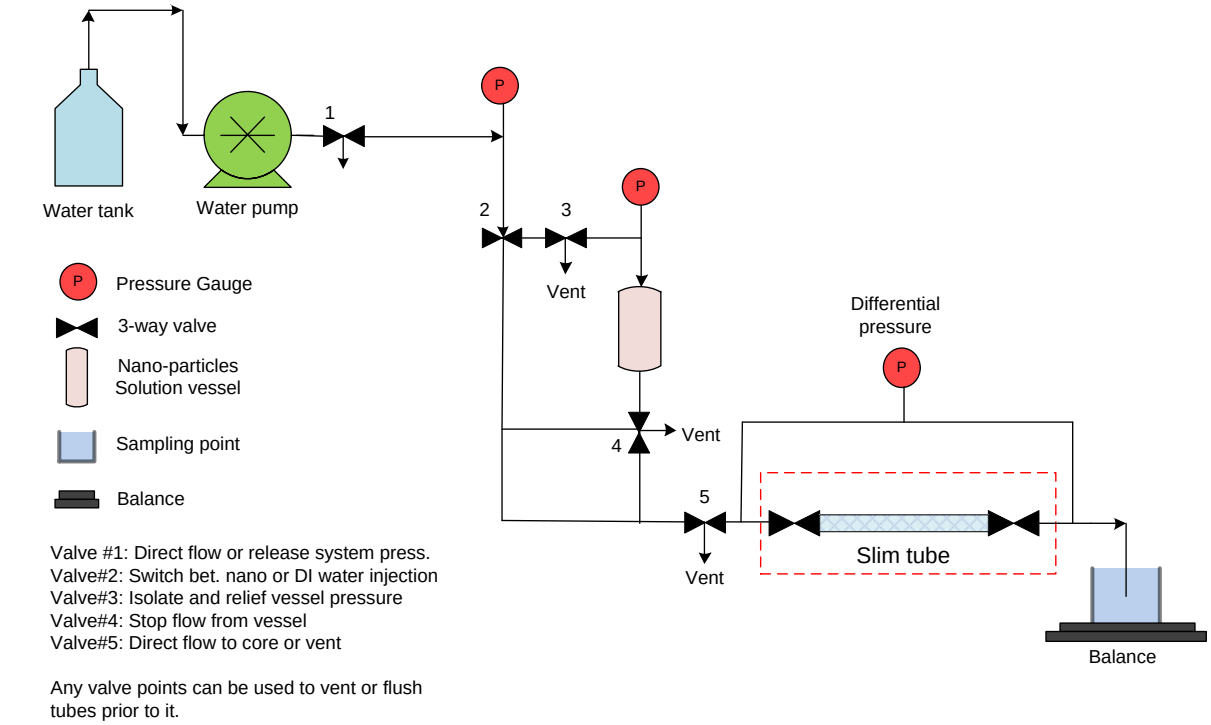

Figure 2.18: Experimental apparatus for nanofluid injection into tube packed with glass beads.

Initially, the slim tube was preflushed with several pore volumes of pure water. Then, 1 pore volume of the iron oxide nanofluid was injected at differential pressure of about 0.1 atm. Following the nanofluid injection, 14 pore volumes of pure water was injected at a rate of 0.5 ml/min and 40 effluent samples were collected. The permeability was not found to be altered during or after the injection.

2.4.2 Spherical silver nanoparticle characterization and injection experiment

The objective of this experiment was to investigate the transport and recovery of metal nanoparticles through the pores of Berea sandstone, initially using spherical silver nanoparticles. Initial testing began in earlier quarters with the injection of silver nanowires into Berea sandstone. The goal was to investigate the transport of a wire-like nanoparticle and determine if shape would introduce any complication to the nanoparticle flow. The silver nanowires were not detected in the effluent and were found trapped at the inlet face within the pore spaces of the core rock. The details can be found in an earlier quarterly report (July-September 2009). The injection of spherical silver nanoparticles also serves as preliminary testing of injecting spherical metal alloy (tin-bismuth) particles which might be used as temperature sensors in geothermal reservoirs.

Silver nanoparticles were characterized in terms of size, surface charge (zeta potential), light absorption and pH levels. The particle size was around 40 nm ±10 (Figure 2.19). Further details can be found in the last quarterly report (July-September, 2010).

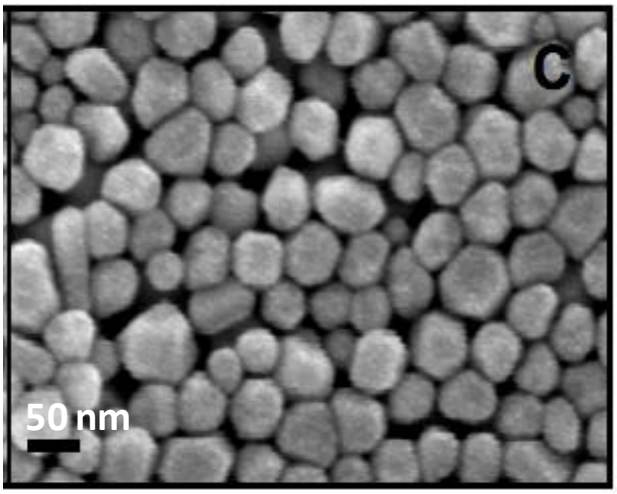

Figure 2.19: SEM image of the silver nanoparticles.(Levard, personal communication)

Last quarter (July-September, 2010), the spherical silver nanoparticles were injected and identified in the effluent samples using SEM imaging. The concentrations were determined by measuring their absorption using UV-vis spectrophotometry. The return curve showed that less than 25% of injected nanoparticles were recovered. During this quarter, we attempted to enhance the recovery of the sliver nanoparticles. These attempts included post-injecting pure water at higher rate and then backflushing the core rock. The flow rate of post-injected pure water was increased from 1 to 5 cm^3/min. Three pore volumes of pure water were injected. A total of nine

effluent samples were collected at the rate of 2.5 cm^3 per sample. After that, the core sample was backflushed with pure water at the same injection rate and nine effluent samples were collected. The permeability was measured during all injections. Some effluent samples were selected for SEM analysis.

2.4.3 Injection of tin-bismuth nanoparticles into Berea sandstone

Tin-bismuth nanoparticles have a melting point that is tunable across a wide range of geothermal temperatures, so they have potential to be used as geothermal temperature sensors. For this reason, the transport of these particles through porous media was investigated. Nanoparticle suspensions were injected into a slim tube packed with glass beads and into a Berea sandstone core.

First, tin-bismuth nanoparticles were injected into Berea sandstone. A schematic of the apparatus is shown in Figure 2.20. Nanofluid solution was contained in a pressure vessel downstream of the water pump. The tin-bismuth nanoparticles were injected with the aid of nitrogen gas. The configuration also allows for injection of particle-free water, without interrupting the flow.

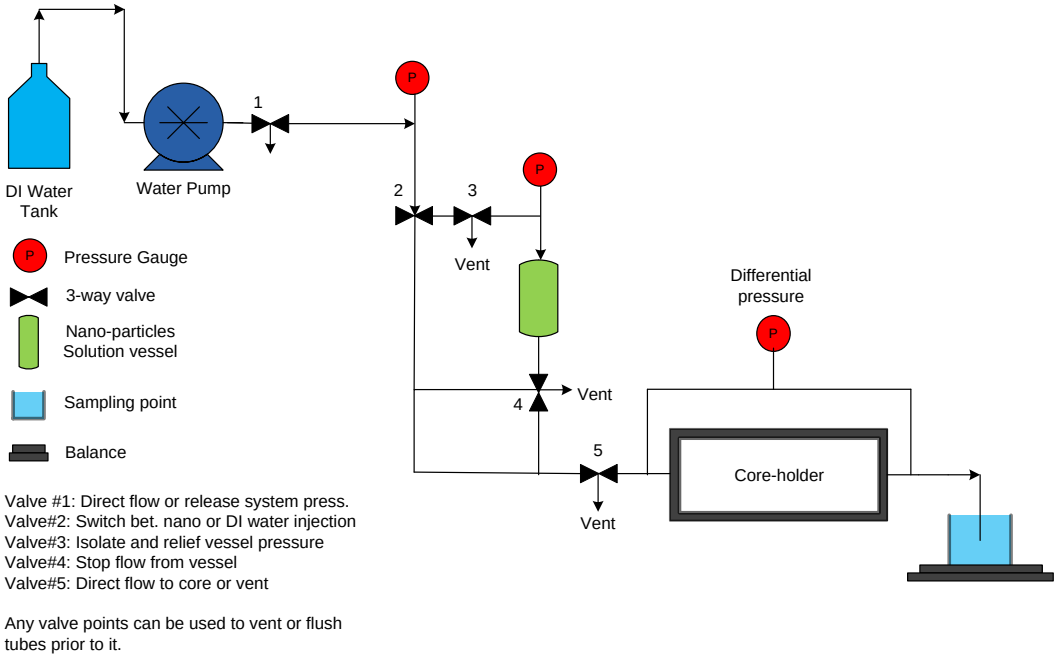

Figure 2.20: Schematic of the apparatus for tin-bismuth nanofluid injection into Berea sandstone.

Initially, the core was preflushed with pure water to displace rock fines and debris. About 30% of the pore volume (3 cm^3 of nanofluid) was then injected. Subsequent to the injection of the nanofluid, a post-injection of 13 pore volumes of pure water was introduced. In addition, the core was backflushed with 5 pore volumes in attempt to mobilize nanoparticles that might be trapped at the inlet of the core. The injection was at the rate of 1cm^3/min. A total of 40 effluent samples were collected at the rate of 2 cm^3 per sample. The effluent sample volume was increased to 6 cm^3 for the last six pore volumes. During the backflushing of the core, the flow rate was varied

between 1 to 5 cm^3/min. The higher flow rates were used to investigate their effect on the mobility of the nanoparticles. SEM imaging was used to analyze the selected effluent samples.

2.4.4 Injection of silica nanoparticles into fractured greywacke

This was a baseline experiment for the transport and recovery of fluorescent silica microspheres through the fracture of the greywacke core sample and study the relationship between the size of recovered microparticles and fracture aperture (section 2.4.5). Initial testing was conducted with injection of silica (SiO_2) nanoparticles which we had earlier shown to be transported successfully through Berea sandstone. Silica nanoparticles flowed through Berea sandstone core and were not trapped in the pore spaces by hydraulic, chemical or electrostatic effects. Given that the silica nanoparticles had been transported successfully through Berea sandstone, our first step in the fracture experiments was to test their delivery through the fractured greywacke core sample. The purpose was to determine whether the greywacke core material would impose any constraint on the recovery of silica based nanoparticles, prior to the injection of the fluorescent silica microspheres.

2.4.4.1 Characterization of silica nanoparticles

The silica (SiO_2) nanoparticles were characterized in terms of size, size distribution and zeta potential using SEM, Dynamic Light Scattering (DLS) and Zetasizer, respectively. The SiO_2 had average size of about 350 nm as shown in the SEM image in Figure 2.21.

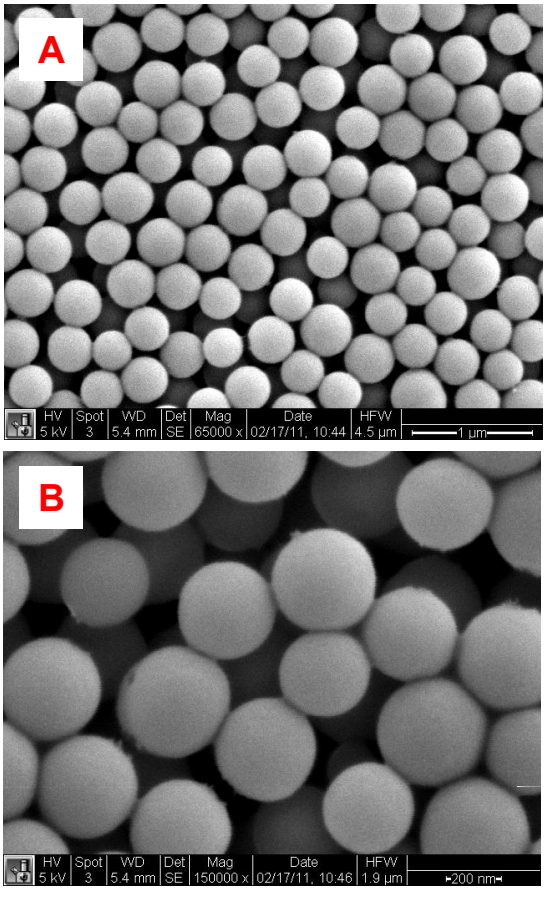

Figure 2.21: SEM image of the silica nanoparticles in the influent.

The size distribution of the silica nanofluid sample (Figure 2.22) obtained from DLS also showed that the sample has an average particle size of about 350 nm.

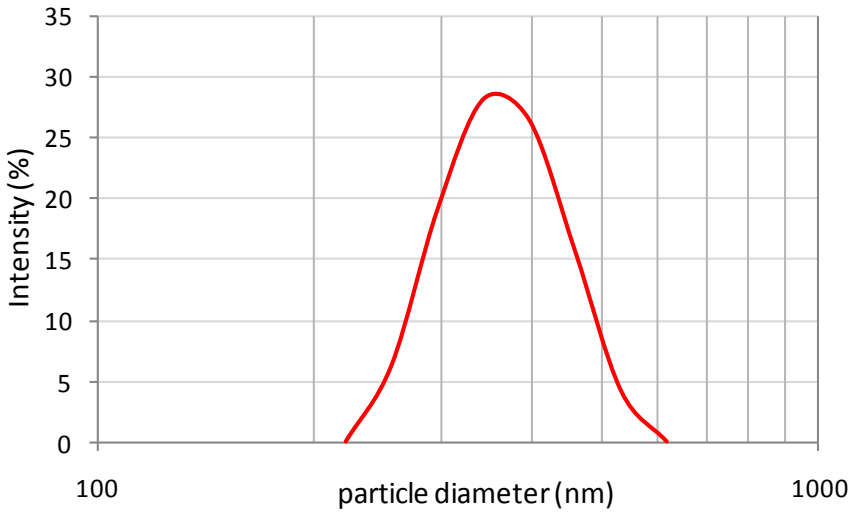

Figure 2.22: Particle size distribution by light intensity percentage of the influent.

The zeta potential of the silica nanoparticle sample was measured and the average of two sets of measurement was found to be negative 73.4 mV with standard deviation of 1.77. The zeta potential distribution of both measurements is shown in Figure 2.23. The fractured greywacke core sample carries a negative charge. So it is of interest to inject particles that carry the same type of charge (i.e. negative charge), as similar charges repel and should prevent particle attachment to the core.

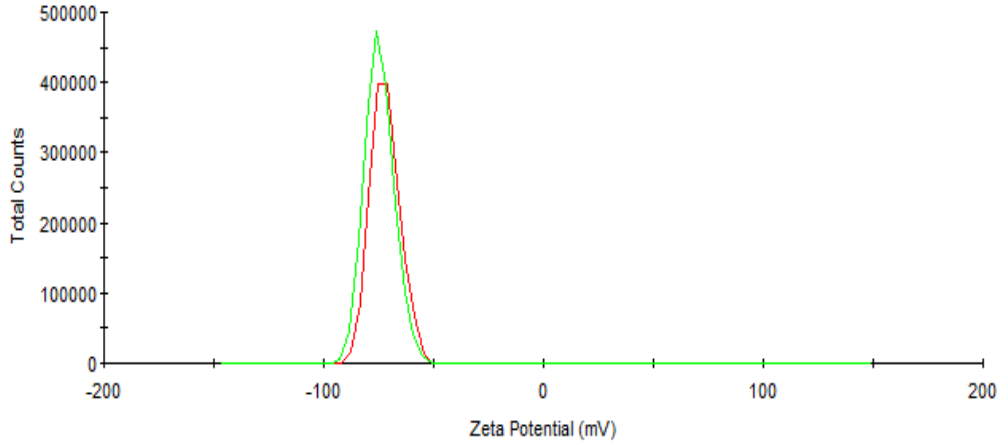

Figure 2.23: Zeta potential distribution of silica nanoparticles.

2.4.4.2 Silica nanoparticle injection into fractured greywacke

The silica nanoparticles injection was conducted to investigate their flow through the fractured greywacke core sample. The testing apparatus was similar to the permeability measurement experiment, but modified slightly to allow for the injection of nanoparticles. The configuration also allows for injection of particle-free deionized water, without interrupting the flow. The modified apparatus can be seen in Figure 2.24.

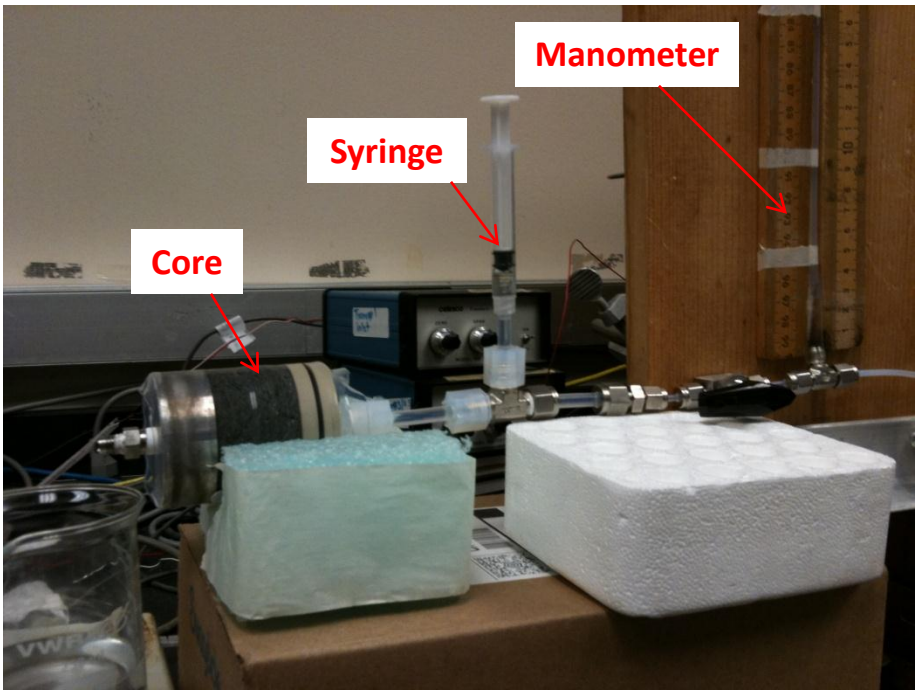

Figure 2.24: A picture of the silica nanoparticle injection apparatus.

The nanofluid was contained in a syringe downstream the water pump. The silica nanoparticles were injected using the syringe. The nanofluid of unknown concentration was diluted one part to 50 parts of deionized water. The volume injected into the core sample is one cubic centimeter. Prior to the injection of the nanofluid, the core was preflushed with several pore volumes of deionized water to displace rock fines and debris. Following the injection of the nanofluid (1 cm^3), a continuous flow of deionized water was introduced. Specifically, eight pore volumes of water were injected. The core was then backflushed with three pore volumes to flush any trapped particles at the inlet side of the core. The average flow rate during the injection was about 0.1 cm^3/min at an inlet pressure of about 0.1 atm. A total of ten effluent samples was collected and analyzed using SEM and DLS.

2.4.5 Fluorescent Silica Microspheres: Characterization and Injection Experiment

The objectives of this experiment were to investigate the transport and recovery of fluorescent silica microspheres through fractures, by using a greywacke core sample and study the relationship between the size of recovered microparticles and fracture aperture. As a base-line experiment, initial testing was conducted with injection of silica (SiO_2) nanoparticles which we had earlier shown to be transported successfully through Berea sandstone. Given that the silica

nanoparticles had been transported successfully through Berea sandstone, our first step in the fracture experiments was to test their delivery through the fractured greywacke core sample. The purpose was to verify if greywacke core material would impose any constraint on the recovery of silica based nanoparticles, prior to the injection of the fluorescent silica microspheres.

2.4.5.1 Characterization of fluorescent silica microspheres

Fluorescent silica microspheres were characterized in terms of size and shape, zeta potential and light emission (fluorescence). The zeta potential measurement was not possible because of the quick settlement of the silica microparticles at the bottom of the measurement cell (due to their size) during the analysis, leading to erroneous measurements. The size and shape of the microspheres were characterized using an optical microscope and scanning electron microscope (SEM). The emission spectrum was obtained using a Fluorescent Spectrometer.

Optical and scanning electron imaging of the microspheres samples are shown in Figure 2.1. The blue and green samples were shown to have uniformly shaped spheres with an average particle size of about 2 and 5 μm, respectively. The red silica spheres were polydisperse or polysized. The sample has spheres with diameters ranging from 5 to 31 μm.

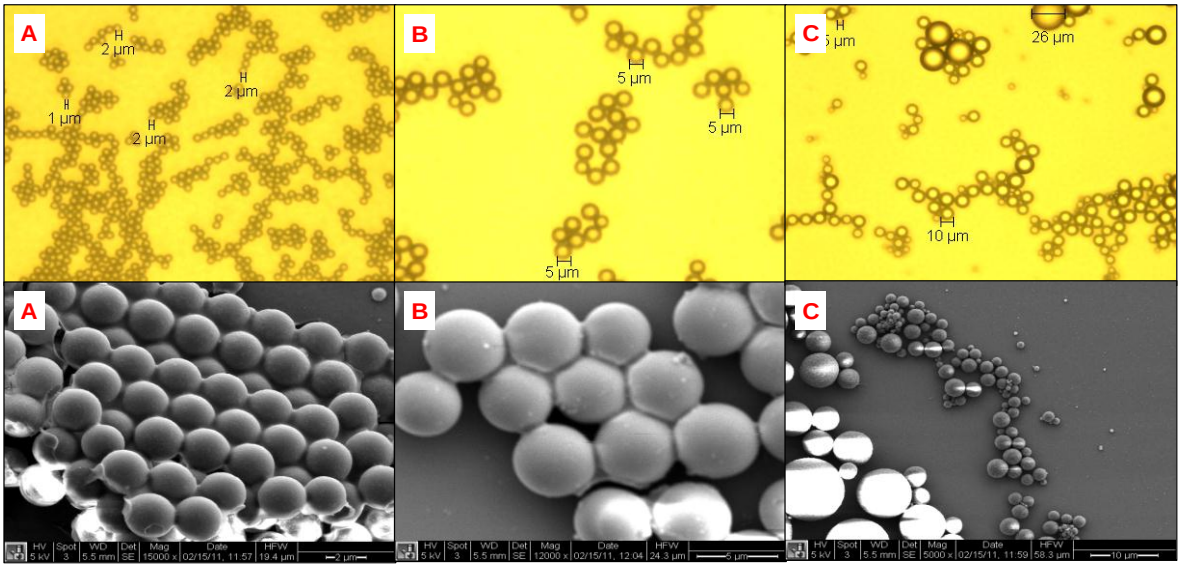

Figure 2.25: Optical and SEM images of (A) blue, (B) green and (C) red silica microspheres.

The volume of blue, green and red fluorescent silica samples was five cubic centimeters with concentration of five percent. The density of the sample was measured in the laboratory at temperature of 24.5ºC. An accurate pipette was used to obtain one cubic centimeter of microfluid at original concentration. The weight of the one cubic centimeter sample was measured using a balance with one milligram accuracy. It was found that the density of the blue, green and red fluorescence silica microfluid sample was about 4.995×10^{-2}, 4.93×10^{-2} and 4.95×10^{-2} grams per cubic centimeter, respectively.

2.4.5.2 Experimental method used in the fractured greywacke injections

The silica nanoparticles and fluorescent silica microspheres injections were conducted to investigate their flow through the fractured greywacke core sample. The testing apparatus was similar to the permeability measurement experiment, but modified slightly to allow for the injection of nanoparticles. The configuration also allows for injection of particle-free deionized water, without interrupting the flow. The modified apparatus can be seen in Figure 2.26.

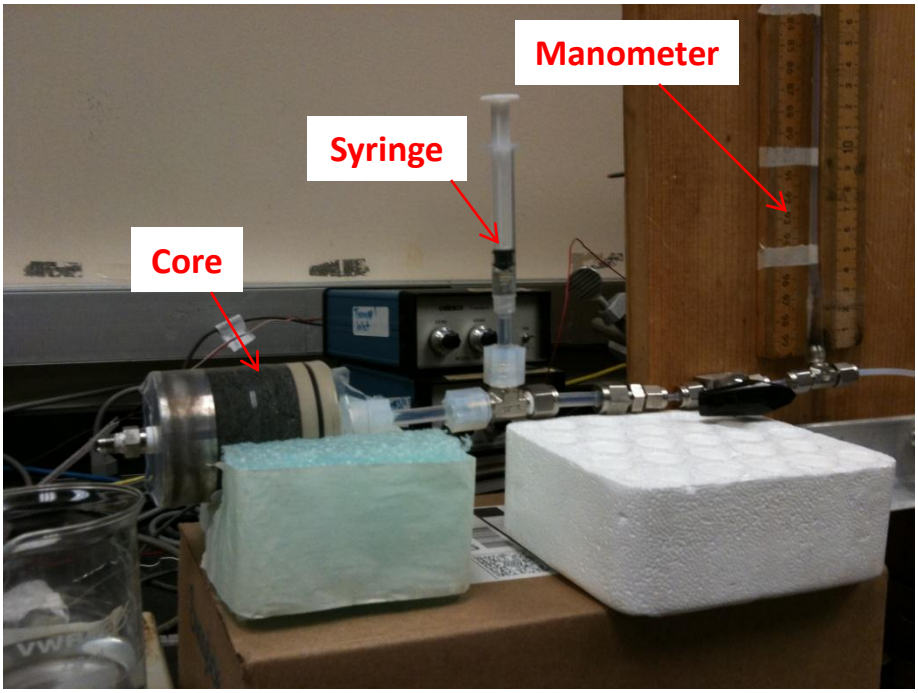

Figure 2.26: A picture of the silica nanoparticle injection apparatus.

The nanofluid was contained in a syringe downstream the water pump. The nanoparticles were injected using the syringe. The silica nanoparticle sample of unknown concentration was diluted one part to 50 parts of deionized water. The silica microsphere influent samples of two concentrations, one part to 50 and 100 parts of deionized water, were prepared, resulting in six influent samples (two blue, two green and two red samples). The new concentrations of diluted samples are summarized in Table 2.5. The volume injected into the core sample was one cubic centimeter. Prior to the injection of the nanofluid, the core was preflushed with several pore volumes of water to displace rock fines and debris. Following the injection of the nanoparticles or microspheres (1 cm^3), a continuous flow of water was introduced. The core was then backflushed with several pore volumes to flush any trapped particles at the inlet side of the core. A total of twenty effluent samples including backflushing was collected and analyzed for each injection experiment (total of 120 samples).

Table 2.5: Summary of diluted samples concentration of blue, green and red fluorescent silica samples.

Sample	*Microfluid volume*	*Original concentration*	*Water volume*	*Diluted sample volume*	*Diluted sample concentration*
	cm^3	g/cm^3	cm^3	cm^3	g/cm^3

Blue silica spheres					
1 to 100	0.02	4.99×10^{-2}	1.98	2	4.99×10^{-4}
1 to 50	0.04	4.99×10^{-2}	1.96	2	9.99×10^{-4}
Green silica spheres					
1 to 100	0.02	4.93×10^{-2}	1.98	2	4.93×10^{-4}
1 to 50	0.04	4.93×10^{-2}	1.96	2	9.86×10^{-4}
Red silica spheres					
1 to 100	0.02	4.95×10^{-2}	1.98	2	4.95×10^{-4}
1 to 50	0.04	4.95×10^{-2}	1.96	2	9.90×10^{-44}

The sequence by which the transport of the silica microspheres through the fractured greywacke core was investigated is as follows. Initially, the silica nanoparticles were injected and the core was then backflushed. The (1:100) diluted blue and green samples were then injected, followed by the injection of the (1:50) diluted blue and green samples. Effluent samples during injection and backflushing were collected following each injection. Due to the polydisperse nature of the red silica microspheres and concerns regarding plugging of the fracture by large spheres, both diluted samples of the red silica spheres (1:100 and 1:50) were injected at the end.

2.4.6 Injection of fluorescent silica microspheres into glass fracture model

The objectives of this experiment were to investigate the transport and recovery of fluorescent silica microspheres through fractures, by using a glass fracture model and study the relationship between the size of recovered microparticles and fracture aperture. Several injections were conducted with silica microspheres through a fractured greywacke core. We intended to further explore the possibility of measuring the fracture aperture by using the size of the largest recovered particles. As a baseline experiment, we injected silica microspheres (2 μm) of the size about 4% of fracture aperture. The goal of this injection was to verify that the silica microspheres were not trapped within the fracture due to chemical or electrostatic forces. The next step will be to inject a polydisperse sample with microparticles bigger and smaller than fracture aperture.

This section provides the silica microsphere injection experiment details. The characterization of the blue fluorescent silica microspheres can be found in a previous quarterly report (April-June, 2011).

The fluorescent silica microspheres injection was conducted to investigate their flow through the glass fracture model. The testing apparatus was similar to the hydraulic aperture and permeability measurements experiment, but modified slightly to allow for the injection of microparticles. The configuration also allows for injection of particle-free deionized water, without interrupting the flow. The modified apparatus can be seen in Figure 2.27.

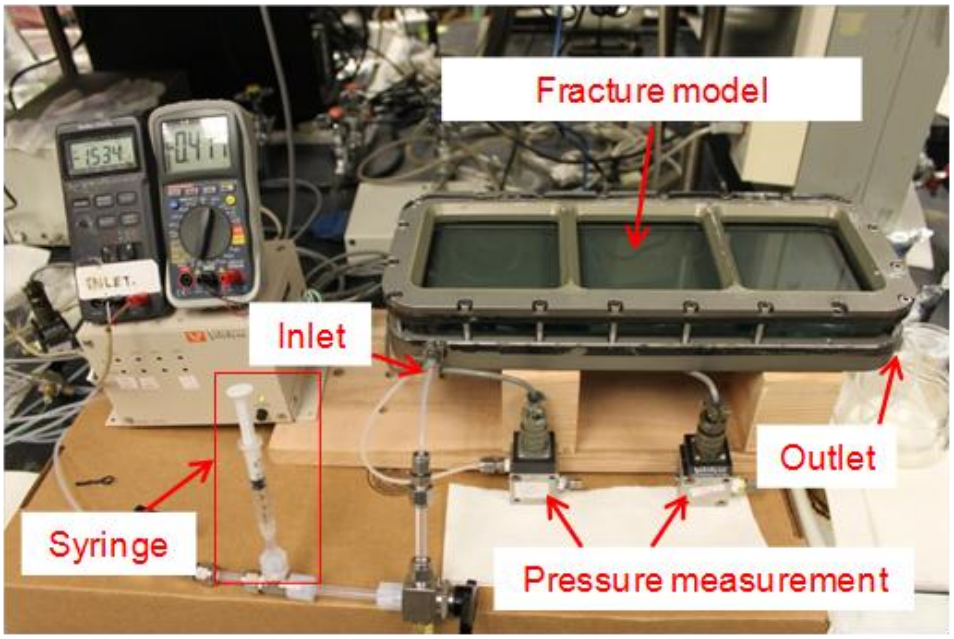

Figure 2.27: A picture of the fluorescent silica microsphere injection apparatus.

The nanofluid was contained in a syringe downstream the water pump. The microparticles were injected using the syringe. The silica microspheres sample of original concentration of 4.99×10^{-2} g/cm^3 was diluted by a factor of 100 using deionized water. The new concentration of injected silica microsphere influent was 4.99×10^{-4} g/cm^3. Prior to the injection of the microfluid, the fracture model was preflushed with several pore volumes of water. Following the injection of the microparticles (1 cm^3), a continuous flow of water was introduced. Effluent samples were then collected, and fluorescence spectrometry was used to determine the concentration of the silica microspheres in effluent samples.

2.5 SYNTHESIS, CHARACTERIZATION, AND CENTRIFUGATION OF TIN-BISMUTH NANOPARTICLES

In this section, various attempts to synthesize monodisperse tin-bismuth nanospheres are described. Characterization of the tin-bismuth nanoparticles and attempts to separate size fractions using centrifugation are also described.

2.5.1 Synthesis of tin-bismuth nanoparticles in low viscosity paraffin oil

The synthesis of the tin-bismuth nanoparticles used in the injection experiment described in Section 2.5 was performed in a previous quarter not detailed in this report. It was concluded from this experiment that a more monodisperse sample of tin-bismuth nanoparticles with smaller diameters may aid particle transport through rock. For this reason, the synthesis was repeated using less viscous oil in order to obtain a narrower distribution of particle size.

To perform the synthesis, Sn and Bi were melted together at the eutectic composition (~60 wt % Bi and ~40 wt % Sn). After the alloy was cooled to room temperature, two 1 g samples were sonicated in 120 ml of light paraffin oil, a slight variation of the sonochemical method suggested by Chen (2005). To investigate whether the time of sonication had any impact on the particle

size distribution, Sample 1 was sonicated for 2 hours, and Sample 2 was sonicated for 4 hours. It was believed that using less viscous paraffin oil would allow more uniform energy distribution in the oil, resulting in more monodisperse particles. The VC-750 ultrasonic processor manufactured by Sonics & Materials, Inc. with a 0.75 in. diameter high gain solid probe was used. The sonicator was operated at 60% amplitude for both samples, resulting in 70.5 and 70.2 W average ultrasonic powers for Samples 1 and 2, respectively. The mixture was cooled to room temperature. The alloy particles were washed and centrifuged several times with a 1:1 mixture of hexane and acetone, rinsed in a solution of 0.1 M polyvinyl pyrrolidone (PVP) in ethanol, and finally suspended in ethanol. The centrifuge setting was 6000 rpm for 15 minutes each time.

2.5.2 Characterization and size separation of tin-bismuth nanoparticles

First, the tin-bismuth nanoparticles were characterized in terms of size and shape using SEM imaging (Figures 2.28 – 2.31).

Visually, it was estimated from Figures 2.28 – 2.31 that the particles are predominantly spherical with sizes range from about 50 nm to larger than 500 nm. It seems that the particle size distribution resulting from using less viscous oil may be somewhat narrower than the previous synthesis, but the distribution is still too wide. It can also be inferred that sonication time had little impact on the particle size distribution. It is therefore hypothesized that using a high sonication power is the best route to obtaining the monodisperse particles reported by Chen et al. (2006). Particle size separation by centrifugation is another possible route.

Particle aggregation was observed in Figures 2.28 – 2.31, which may be attributed to aggregation on the substrate. The particles also have a blackberry-like texture (most visible in Figure 2.31). This may be attributed to the smaller particles aggregating onto the surface of larger ones in order to reduce their surface energy.

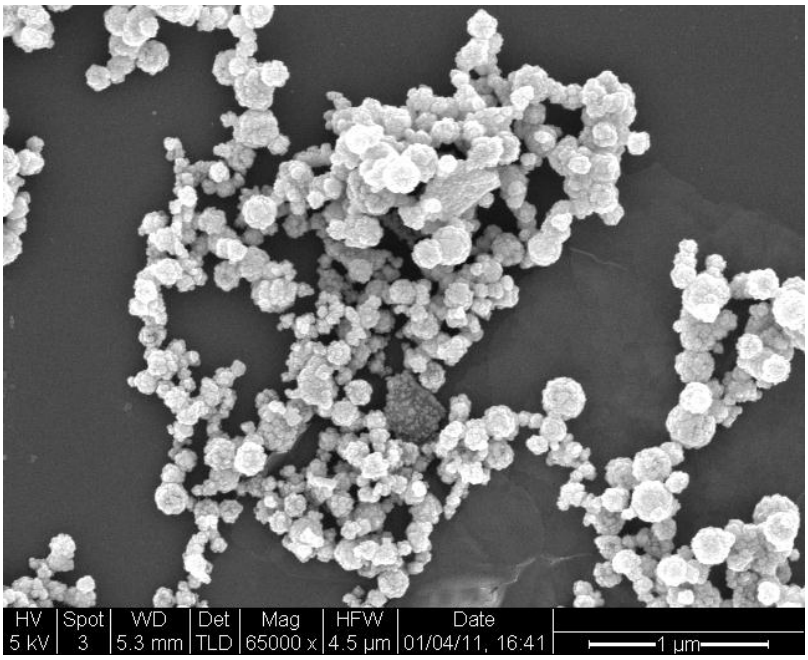

Figure 2.28: SEM image of Sample 1 at 65,000× magnification.

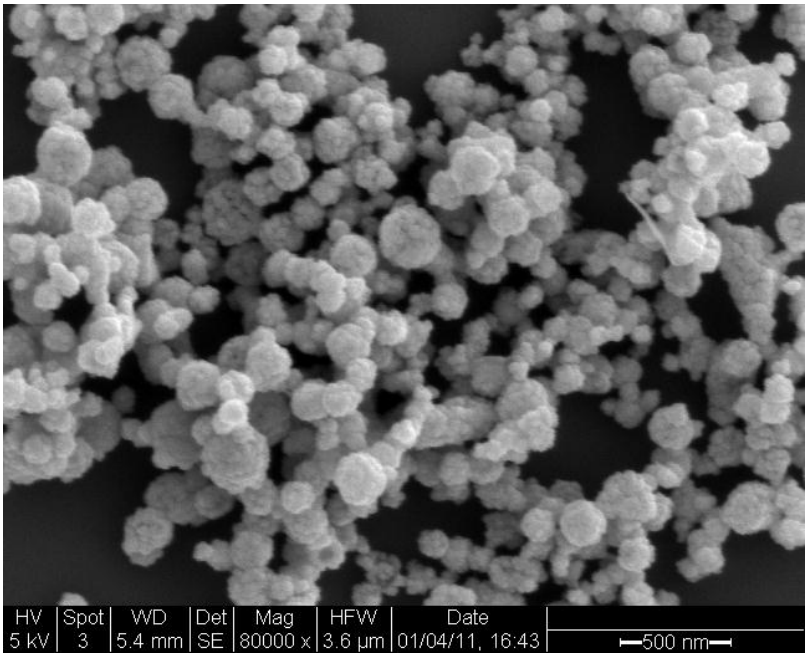

Figure 2.29: SEM image of Sample 1 at 80,000× magnification.

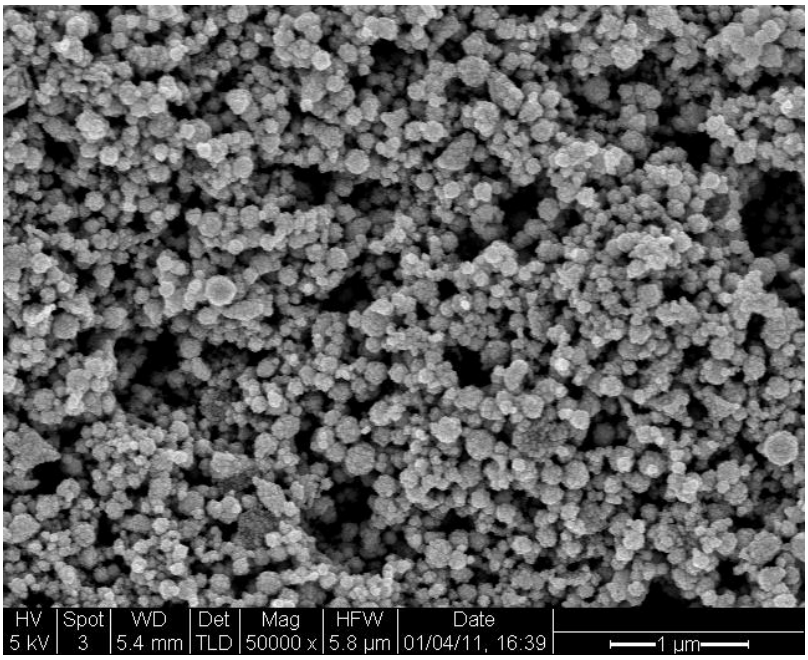

Figure 2.30: SEM image of Sample 2 at 50,000× magnification.

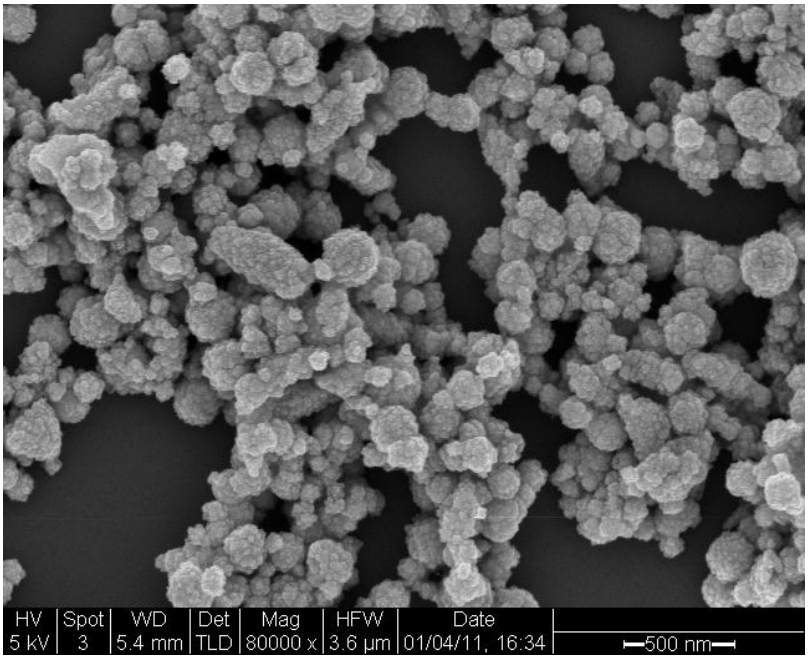

Figure 2.31: SEM image of Sample 2 at 80,000× magnification.

The tin-bismuth nanoparticles were characterized in terms of size using DLS (Figure 2.32). It was found that these nanoparticles had unsatisfactorily large size and a wide particle size distribution. For this reason, the sample was centrifuged at 1000 rpm for 15 minutes, and the supernatant was characterized using DLS (Figure 2.32). Subsequently, the supernatant from the

first centrifugation was centrifuged at 2500 rpm for 20 minutes, and the supernatant from this second centrifugation was characterized using DLS (Figure 2.32).

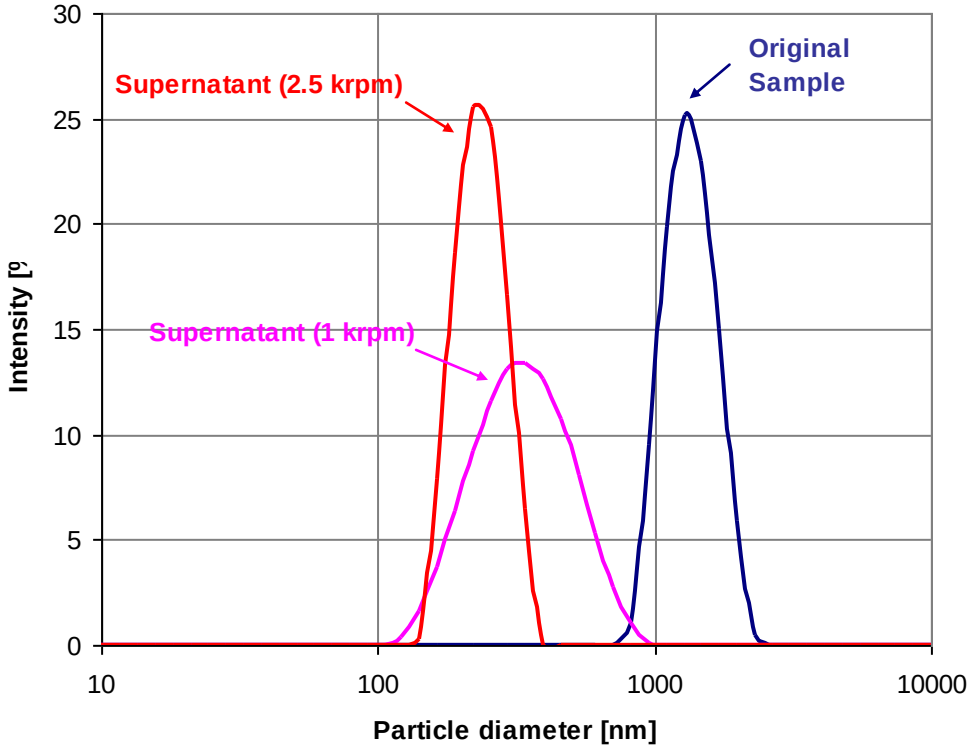

Figure 2.32: Particle size distribution by light intensity percentage of original sample and supernatant samples of tin-bismuth nanoparticles

It is shown in Figure 2.32 that the size distribution was narrowed significantly by centrifugation, and the peak particle diameter was lowered from to 1370 nm (original sample) to 360 nm (1000 rpm), and, subsequently, 239 nm (2500 rpm). However, the final sample after centrifuging at 2500 rpm appeared by visual inspection to be very dilute. Also, judging from these DLS results, there are still particles larger than 200 nm in the sample. Chen et al. (2005) reported that higher sonication power used during synthesis leads to smaller diameter particles and tighter size distributions. Thus, it was decided to repeat the synthesis at higher sonication power.

2.5.3 High-power synthesis, centrifugation, and characterization of tin-bismuth nanoparticles

While encouraging results were obtained, the resulting sample still contained particles larger than 200 nm and was very dilute. For this reason, the sonochemical synthesis and subsequent cleaning of tin-bismuth nanoparticles was repeated at the highest possible sonication power for the type of mineral oil used. This sample was centrifuged, and the original and resulting samples were characterized using DLS.

In the tin-bismuth injection experiment performed last quarter (Oct. – Dec., 2010), it was found that only particles with diameters of 200 nm and smaller were transported successfully through the pore spaces of the Berea sandstone core. Thus, it is desired to obtain a sample of tin-bismuth nanoparticles that has a narrow size distribution and contains particles smaller than 200 nm. This would allow a more conclusive demonstration of the particle growth temperature-sensing mechanism and may aid particle transport through rock.

To perform the synthesis, Sn and Bi were melted together at the eutectic composition (~60 wt % Bi and ~40 wt % Sn). After the alloy was cooled to room temperature, a 0.98 g sample was sonicated in 120 ml of light paraffin oil, a slight variation of the sonochemical method suggested by Chen et al. (2005). The VC-750 ultrasonic processor manufactured by Sonics & Materials, Inc. with a 0.75 in. diameter high gain solid probe was used. The sonicator was operated at 90% amplitude (with a splash guard constructed of Teflon tape to prevent loss of the sample), resulting in an average ultrasonic power of 145 W. The mixture was cooled to room temperature. The alloy particles were washed and centrifuged twice with a 1:1 mixture of acetone and hexane, once with a 3:1 mixture of acetone and hexane, once in a solution of 0.1 M polyvinyl pyrrolidone (PVP) in ethanol, and once in ethanol. After this final wash and centrifuge, the nanoparticles were suspended in water. The centrifuge setting was 6000 rpm for 15 minutes each time.

This latest sample of tin-bismuth nanoparticles was characterized in terms of size using DLS (Figure 2.33). This sample was centrifuged at 2500 rpm for 30 minutes, and both the supernatant and infranatant were characterized using DLS (Figure 2.33).

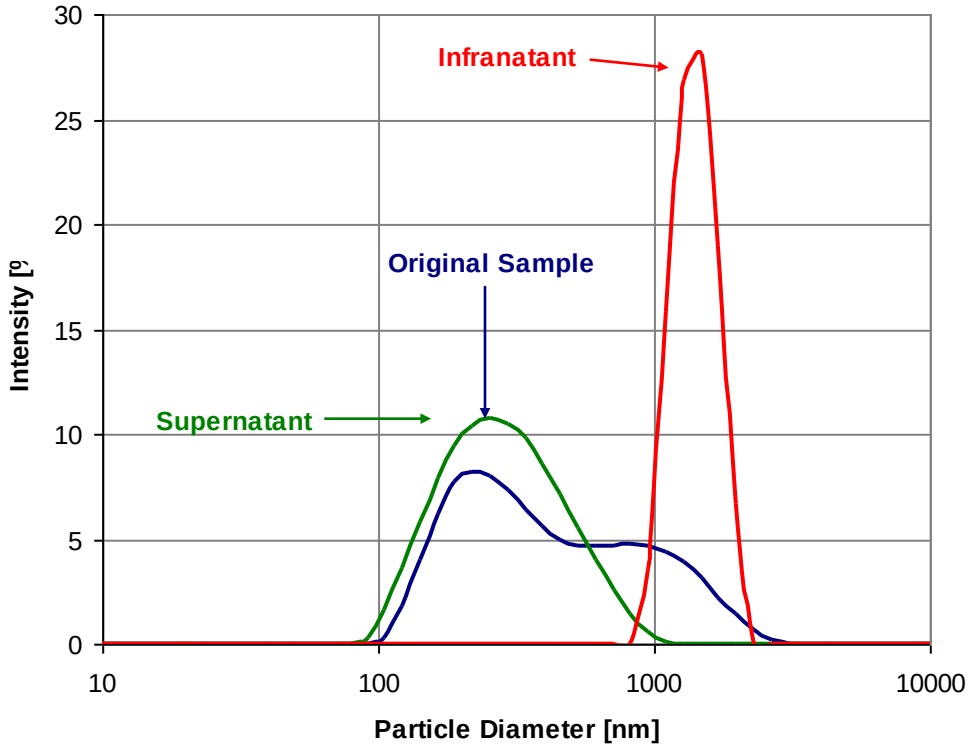

Figure 2.33: Particle size distribution by light intensity percentage of original tin-bismuth nanoparticles and separated samples after centrifugation at 2500 rpm for 30 min.

By comparison of Figures 2.32 and 2.33, it can be seen that the original sample of this latest synthesis had a higher fraction of smaller particles, as predicted. This sample was found to have a bimodal distribution with peaks at 306 nm and 1087 nm. After centrifugation, this sample was separated into a supernatant with a peak at 318 nm and an infranatant with a peak at 1430 nm. These results suggest that the incremental centrifugation performed with the previous sample was a more effective method of separation.

2.6 EXPERIMENTAL INVESTIGATION OF MAGNETIC COLLECTION OF NANOSENSORS

For nanosensors to provide information about temperature distribution in a geothermal reservoir, they must be successfully collected from produced fluid. Since this is not a trivial task, an experiment was performed to investigate the concept of magnetic collection of paramagnetic nanoparticles from flowing fluid. In order for a magnetic collection scheme to be successful, the magnetic force on the particles must dominate inertial, drag, gravitational, and diffusional forces acting on the particles (Moeser et al., 2004). In geothermal applications, it is likely that the two main competing forces will be the magnetic and inertial forces on the particles. Gerber and Birss (1983) define the magnetic force on a particle in a magnetic field as:

$$F_m = \mu_0 V_p M_p * \nabla \mathrm{H} \qquad (2.16)$$

where F_m is the magnetic force, μ_0 is the constant permeability of free space, V_p is the volume of the paramagnetic particle, M_p is the magnetization of the particle, and ∇H is the magnetic field gradient. It is clear from Equation 2.16 that there are three parameters that can be tuned in order to increase the magnetic force on the particles: particle size, magnetization (which can be tuned by changing particle composition), and applied magnetic field gradient. It seems as if the applied magnetic field gradient may have the most potential as a tuning knob, since particle size and composition are constrained by other factors (e.g. mobility in the reservoir).

In this proof of concept experiment, it was decided to use low flowrates (i.e. low pressure gradient and inertial forces) were used in order to increase the likelihood of successful collection. The results of this experiment will be used to help design future experiments.

The experimental apparatus used for magnetic nanoparticle collection is illustrated in Figure 2.34.

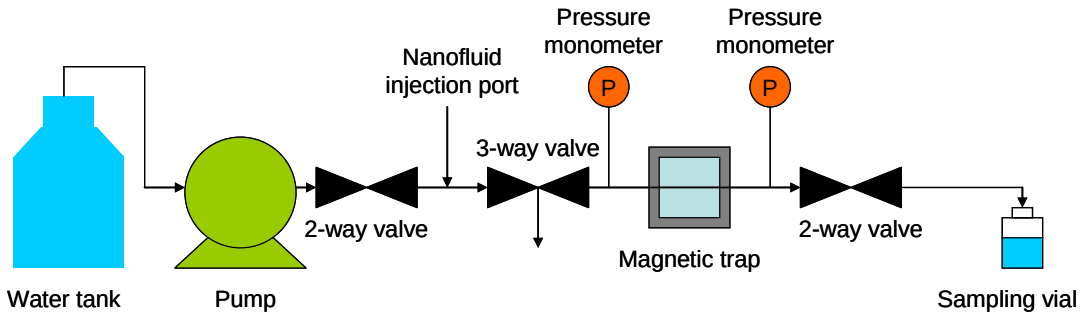

Figure 2.34: Schematic of experimental apparatus used in the magnetic collection experiment

A Dynamax solvent delivery system (Model SD-200) was used to pump water through the apparatus. Four BX084 neodymium block magnets manufactured by K&J magnetics were used in the magnetic trap, with two magnets affixed to each side of the tube. This configuration was chosen in order to expose the injected nanoparticles to the strongest part of the magnetic field, which is illustrated in Figure 2.35. The proximity of the magnets is critical to the success of the collection scheme because magnetic force is a strong function of distance, as shown in Figure 2.36 for the particular magnets used.

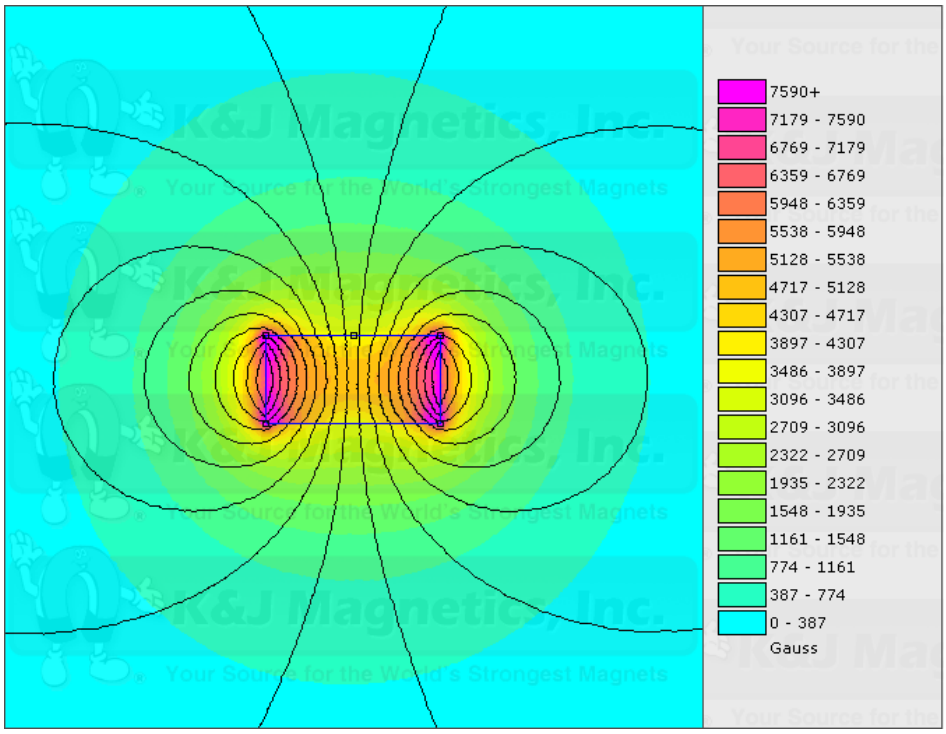

Figure 0: Magnetic field of neodymium block magnets. Reproduced from K&J Magnetics.

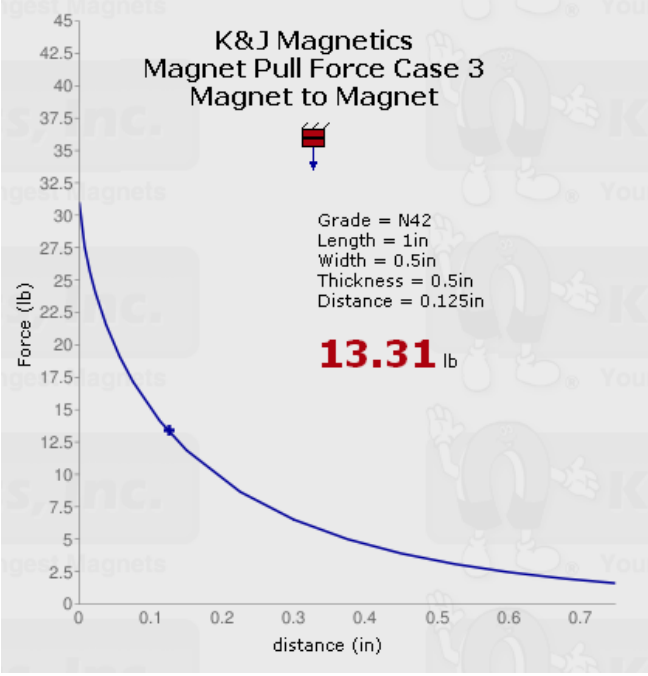

Figure 2.36: Magnetic pull force between two neodymium magnets as a function of distance. The point on the curve corresponds to 13.31 lb_f at a distance of 0.125 in., or the radius of the collection tube used. Reproduced from K&J Magnetics.

A 5 wt % suspension of paramagnetic iron oxide nanoparticles coated with silica in water were purchased from Corpuscular, Inc. These particles were characterized using SEM imaging, as shown in Figure 2.37.

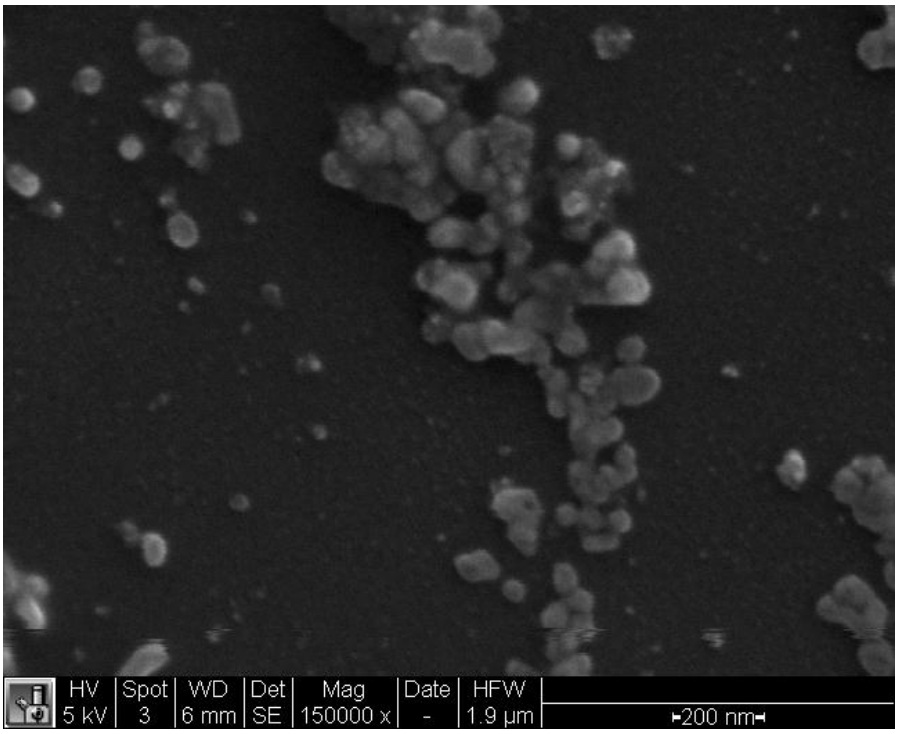

Figure 2.37: SEM image of iron oxide nanoparticles coated with silica.

The pump was used to fill the apparatus with water, the first valve was closed, the 3-way valve was turned to allow water to be flushed out, and 1 mL of iron oxide nanofluid was injected. The valves were turned to their initial settings, water was through the apparatus at a flowrate of 0.1 mL/min for 6.5 hours to push the nanofluid through the magnetic trap. All effluent was collected. Pressure remained constant throughout the experiment at 0.023 psig and 0.018 psig at the inlet and outlet of the collection tube, respectively. Most of the nanofluid was observed visually passing through the magnetic trap without being trapped. After flushing the apparatus with about 39 mL of water, the effluent was very dilute, and a small static cloud of nanofluid was observed at the outlet of the magnetic trap.

At this point, the flowrate was increased to 2.0 mL/min, and tendrils of previously static nanofluid were observed exiting the magnetic trap. The apparatus was flushed at this flowrate for about 50 min, at which point the effluent was visually indistinguishable from water. The pump was turned off, the valves were closed, and the magnetic trap was removed, revealing a cloud of nanoparticles that had been trapped by the magnet, as shown in Figure 2.38.

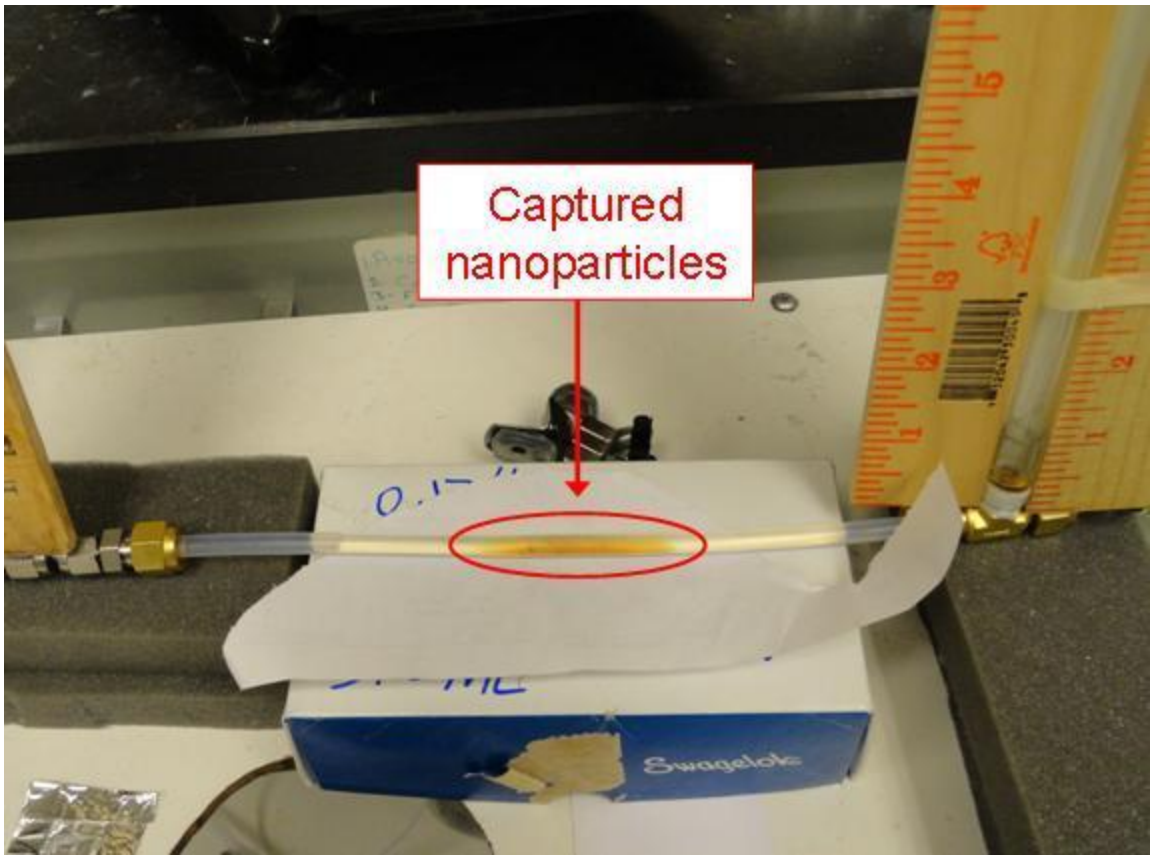

Figure 2.38: Photograph of trapped nanoparticles after the removal of the magnetic trap.

The outlet side of the collection tube was disconnected, and the previously trapped nanoparticles were collected. The volume of the collected fluid was measured to be 3.7 mL. In order to calculate a collection efficiency, the concentration of the nanoparticles in the trapped sample had to be estimated. This was done by using uv-vis spectroscopy to measure the absorbance spectra of the trapped sample and of dilutions prepared from the original nanofluid with known concentrations. The absorbance at a specific wavelength was found to scale linearly with concentration, and the resulting correlation was used estimate the concentration of the collected sample. The baseline concentration of nanoparticles was calculated to be 0.08 g/mL using the 5 wt % specified by the manufacturers and the measured nanofluid density of 1.6 g/mL.

2.7 ANALYSIS OF TRACER RETURN CURVES TO ESTIMATE MEASUREMENT GEOLOCATION

It has been shown that silica nanoparticles with covalently attached dye have potential to measure temperature in geothermal reservoirs (Alaskar et al., 2011). However, simply knowing that some region of the reservoir has a certain temperature without knowing the geolocation of the measurement is of limited use to reservoir engineers. If this geolocation could be estimated accurately, the reservoir temperature distribution could be mapped. This could make it possible to predict thermal breakthrough in a reservoir and would allow reservoir engineers to make more informed decisions. The potential capability of nanosensors with a dye-release sensing

mechanism (e.g. dye-attached silica nanoparticles) to estimate measurement geolocation via analysis of the return curve of released dye is addressed in this chapter.

2.7.1 Simple analytical model for return curve analysis to estimate geolocation

A thought experiment was performed consisting of two hypothetical tracer tests performed in a well doublet: one with a conservative solute tracer and one with dye-releasing nanosensors. Synthetic tracer return curves for these hypothetical tests were generated using an analytical solution to the advection-dispersion equation, which is often used to describe subsurface tracer flow. Juliusson and Horne (2011) expressed the one-dimensional form of this equation as:

$$R\frac{\partial C}{\partial t} = \alpha u \frac{\partial^2 C}{\partial x^2} - u\frac{\partial C}{\partial x} \tag{2.17}$$

where C is tracer concentration, x is the spatial coordinate, t is time, u is the flux velocity, and α is the dispersion length, and R is the tracer retardation factor, which accounts for the retardation of tracer transport caused by the reversible adsorption of tracer to rock interfaces. For this initial investigation, the simple case with a constant flux velocity v (i.e. constant flow rate) was considered, and it was assumed that R is constant with respect to t, x, and C for both the solute tracer and the nanosensors. It may be more realistic to assume that R varies spatially, as is suggested by Chrysikopoulos (1993), and that nanoparticle flow likely requires even more complex treatment. With these caveats in mind, it was decided to first examine the simplest possible case.

Kreft and Zuber (1978) provided a solution to the advection-dispersion equation with flux injection and detection boundary conditions, and Juliusson and Horne (2011) rewrote this solution to include the retardation factor R:

$$C = \frac{mV_x}{qt\sqrt{4\pi V_\alpha qt}} \exp\left(-\frac{\left(qt - V_x\right)^2}{4V_\alpha qt}\right) \tag{2.18}$$

$$V_x = RA\phi x \tag{2.19}$$

$$V_\alpha = RA\phi\alpha \tag{2.20}$$

where m is the mass injected, q is the volumetric flowrate, t is time, V_x is the pore volume modified by the retardation factor R, V_α is the dispersion volume modified by R, A is cross-sectional area, φ is porosity, and α is the dispersion length.

Consider a flow-path in a geothermal reservoir between a well doublet that consists of a single fracture with length L, cross-sectional area A, and porosity φ. Before extraction, the reservoir had a uniform temperature distribution with a temperature of T_1. Some years after the onset of extraction, the thermal front has advanced to the position x_f, and the portion of the reservoir behind the front has cooled to temperature T_2, as shown in Figure 4-1. Suppose a nanosensor has been designed to release a fluorescent dye at the threshold temperature T_1, and assume that this release occurs instantaneously upon exposure to this threshold.

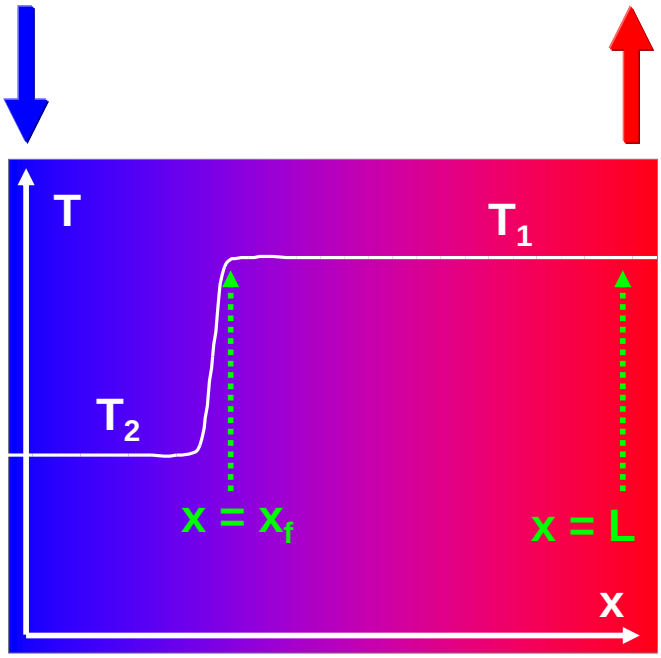

Figure 2.39: Cartoon of temperature distribution in a geothermal reservoir with a thermal front at position x_f.

Two tracer tests are performed. In one test, a mass m_c of a conservative tracer with a retardation factor R_c is injected into the reservoir. The tracer is sampled at the production well (i.e. $x = L$), and the return curve can be described by:

$$C_c = \frac{m_c V_{x,c}}{qt\sqrt{4\pi V_{\alpha,c} qt}} \exp\left(-\frac{\left(qt - V_{x,c}\right)^2}{4V_{\alpha,c} qt}\right) \tag{2.21}$$

$$V_{x,c} = R_c A\phi L \tag{2.22}$$

$$V_{\alpha,c} = R_c A\phi\alpha \tag{2.23}$$

where the subscript c denotes the conservative solute tracer.

In the second test, a slug of the dye-releasing nanosensors with retardation factor R_n is injected into the reservoir. Upon reaching exposure to the threshold temperature T_1 at position x_f, the nanosensors release a mass m_r of the attached dye, which itself behaves like the conservative solute tracer in the previous tracer test, and has a retardation factor R_c. The released dye is sampled at the production well. The return curve of the released dye is influenced by both R_n and R_c, because it travels with the nanosensor retardation factor R_n from $x = 0$ to $x = x_f$ and the retardation factor R_c from $x = x_f$ to $x = L$. Thus, the return curve of the released dye can be described by convolution:

$$C_r = \int_0^t \frac{m_r V_{x,n}}{qt\sqrt{4\pi V_{\alpha,n} q(t-\tau)}} \exp\left(-\frac{\left(q(t-\tau) - V_{x,n}\right)^2}{4V_{\alpha,n} q(t-\tau)}\right) \bullet \frac{qV_{x,r}}{qt\sqrt{4\pi V_{\alpha,c} q\tau}} \exp\left(-\frac{\left(q\tau - V_{x,r}\right)^2}{4V_{\alpha,c} q\tau}\right) \partial\tau \tag{2.24}$$

$$V_{x,n} = R_n A\phi x_f \tag{2.25}$$

$$V_{\alpha,n} = R_n A\phi\alpha \tag{2.26}$$

$$V_{x,r} = R_c A\phi\left(L - x_f\right) \tag{2.27}$$

where the subscript *n* denotes the nanosensors and the subscript *r* denotes the released dye. Note that $V_{x,r}$ can be rewritten as:

$$V_{x,r} = V_{x,c} - \frac{V_{\alpha,c}}{V_{\alpha,n}} V_{x,n} \tag{2.28}$$

Thus, the return curves for the conservative tracer can be fit to Equation 2.21 by adjusting the values of unknowns $V_{x,c}$ and $V_{\alpha,c}$ (i.e. minimizing the norm of the differences between the return curve data and the model with the unknowns as decision variables). Subsequently, the return curves for the released dye can be fit to Equation 2.24 by adjusting the values unknowns $V_{x,n}$ and $V_{\alpha,n}$. Note that $V_{x,r}$ is not explicitly adjusted here because it can be expressed in terms of the other unknowns. Once the values of the unknowns have been determined, one can calculate the geolocation of the thermal front as:

$$x_{f,d} = \frac{x_f}{L} = \frac{V_{x,c} - V_{x,r}}{V_{x,c}} \tag{2.29}$$

where $x_{f,d}$ is the dimensionless position of the thermal front.

2.7.2 Example problem for estimating geolocation of temperature measurements

This analysis was demonstrated successfully in an example problem with the parameter values shown in Table 2.6.

Table 2.6: Parameter Values Used In Return Curve Analysis Demonstration Problem

Parameter	**Value**
R_c	2
R_n	1
A	200 m^2
φ	0.10
L	1000 m
α	25 m
$Pe = L / \alpha$	40
m_c	123.75 kg
m_r	123.75 kg
q	43.2 m^3/hr

These values were chosen somewhat arbitrarily for the purposes of this demonstration. However, values of R_c and R_n were used such that the nanosensors experience no retardation and the solute tracer does experience retardation. This is based on studies of colloid transport in fractures which showed that non-adsorbing colloids exhibit breakthrough more rapidly than solute tracers because they tend to stay in fluid streamlines and do not experience matrix diffusion (Reimus 1995). Also, the volumetric flow rate q and the masses of the tracer slugs m_c and m_r were based on values reported by Gentier et al. (2010) for the 2005 tracer test performed in the Soultz-sous-Forets reservoir.

Synthetic return curve data for the conservative tracer and the nanosensors were generated for various values of x_f using Equations 2.21 and 2.24, and Gaussian noise was added for the sake of realism. An optimization solver was then used to find the best fit to Equations 2.21 and 2.24 by adjusting the unknowns. The results are tabulated in Table 2.7, and select return curves are plotted in Figure 2.40.

Table 2.7: Estimates of Temperature Measurement Geolocations In Demonstration Problem For Various True Values of $x_{f,d}$

$x_{f,d}$ **true**	$x_{f,d}$ **estimate**	**Error**
0.05	0.037	26%
0.15	0.155	3.2%
0.25	0.248	0.8%
0.35	0.382	9.1%
0.45	0.431	4.3%
0.55	0.517	5.9%
0.65	0.632	2.7%
0.75	0.746	0.6%
0.85	0.852	0.2%
0.95	0.925	2.7%

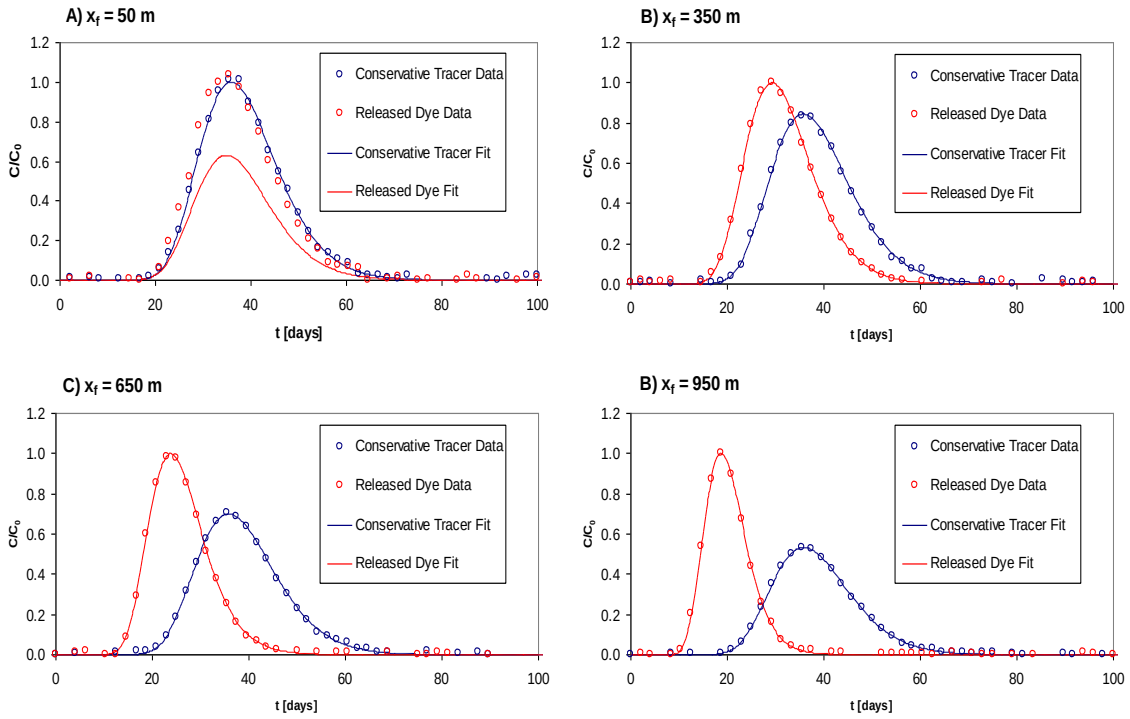

Figure 2.40: Return curve data and fits for A) x_f = 50 m, B) x_f = 350 m, C) x_f = 650 m, and D) x_f = 950 m. Note that released dye experiences breakthrough first because it is carried a distance x_f by the nanosensor, which has a retardation factor of 1, while the conservative tracer has a retardation factor of 2.

Reasonably good estimates of the geolocation of the thermal front were obtained for all scenarios except for x_f = 0.05. This is physically intuitive, because the return curves for the conservative tracer and the released dye are almost identical when the thermal front is still close to the injection well, making it difficult to estimate the front geolocation quantitatively. The poor fit of the return curve of the released dye can be attributed mathematically to the problematic nature of the optimization surface for this scenario, which is shown in Figures 2.41 and 2.42.

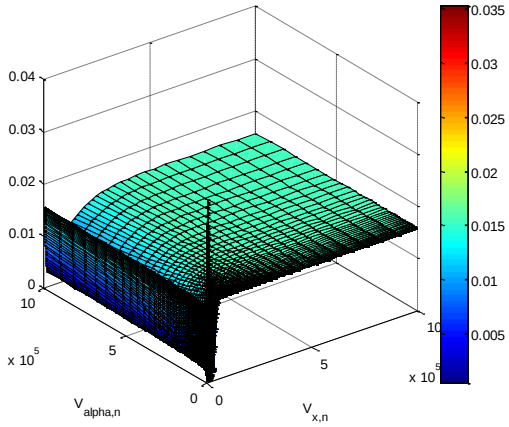

Figure 2.41: Objective function surface for fitting the return curve of the reactive tracer when x_f = 50 m.

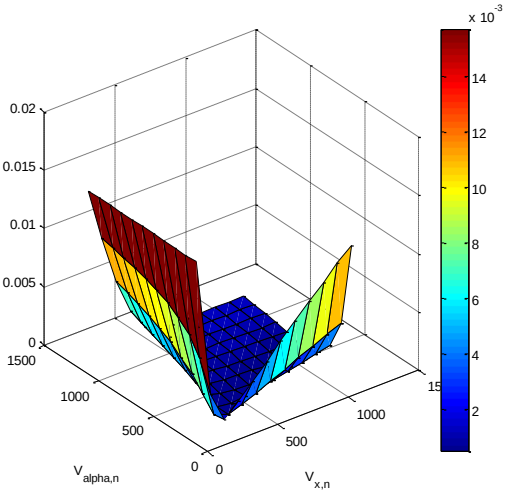

Figure 2.42: Objective function surface for fitting the return curve of the reactive tracer when x_f = 50 m, zoomed in near the minimum of ($V_{x,n}$ = 1000 m^3, $V_{\alpha,n}$ = 500 m^3). Note that the point chosen by the solver was ($V_{x,n}$ = 268.3 m^3, $V_{\alpha,n}$ = 180.8 m^3).

The large trough along the $V_{\alpha,n}$ axis in Figure 2.41 indicates that for large initial guesses of $V_{\alpha,n}$, the solver might get stuck far from the minimum (since change in the objective function is the termination criteria). Moreover, the values of the objective function vary very little near the minimum, as shown in Figure 2.42. This explains why the solver terminated at the point ($V_{x,n}$ = 268.3 m^3, $V_{\alpha,n}$ = 180.8 m^3) and resulted in a poor fit.

2.8 RESULTS

This section contains the results of a number of flow experiments conducted in the past year: the injections of coated iron oxide nanoparticles into a slim tube packed with glass beads, spherical silver nanoparticles into Berea sandstone, tin-bismuth nanoparticles into Berea sandstone, silica nanoparticles into fractured greywacke, and fluorescent silica microspheres into both fractured greywacke and a glass fracture model. The results of a preliminary magnetic nanoparticle collection experiment are also discussed.

2.8.1 Iron oxide coated with surfactant (PVP) injection experiment results

To determine whether the transport of iron oxide nanoparticles was limited by their surface characteristics, iron oxide was coated with SiO_2 and the surfactants TEA and PVP to modify its surface properties. Among these three, iron oxide coated with PVP was selected for injection (July-September, 2010). The iron oxide nanoparticles were transported through the tube packed with glass beads and were detected in the effluents. SEM imaging confirmed the transport of the nanoparticles as shown in Figure 2.43.

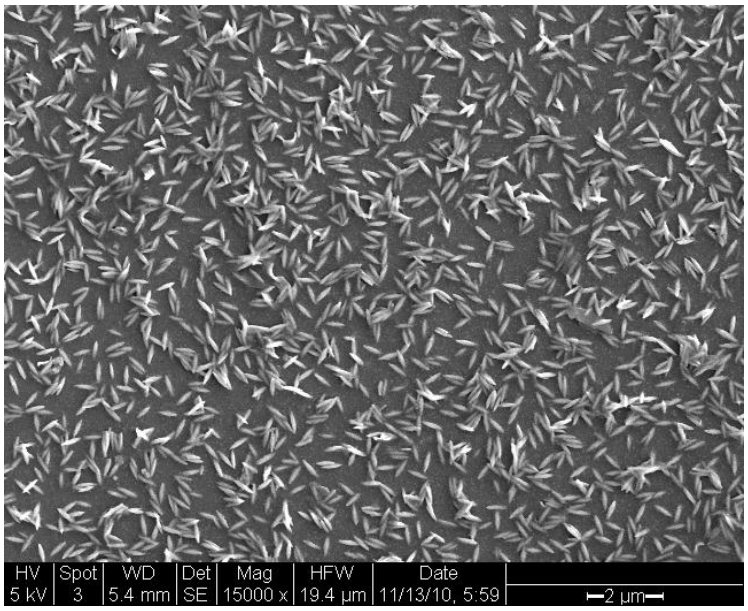

Figure 2.43: SEM image of effluent sample taken from the third post-injected pore volume.

The recovery of the iron oxide nanoparticles was also confirmed by dynamic light scattering (DLS). The size reported by DLS was the average size obtained when the light struck the particles from different angles. These iron oxide nanoparticles were 500 nm in the longitudinal direction and 100 nm in traverse direction. During the measurement, the light hits the nanoparticles from all directions and the reported size is an average size between 100 to 500 nm, depending of the sample concentration. Figure 2.44 shows the dependency of the nonspherical nanoparticle size measurements on sample concentration. Several dilutions of iron oxide nanofluid were prepared and DLS measurements were performed. The average size of the nanoparticles represented by the peak of the distribution changed with any change in sample concentration. There was a shift of about 300 nm of the peak of the distribution between the original and the most diluted nanofluid sample. DLS measurements performed on effluent samples at the fourth and fifth post-injected pore volumes were found to match the size distribution of dilutions (1 to 32) and (1 to 256), respectively (Figures 2.45 and 2.46)

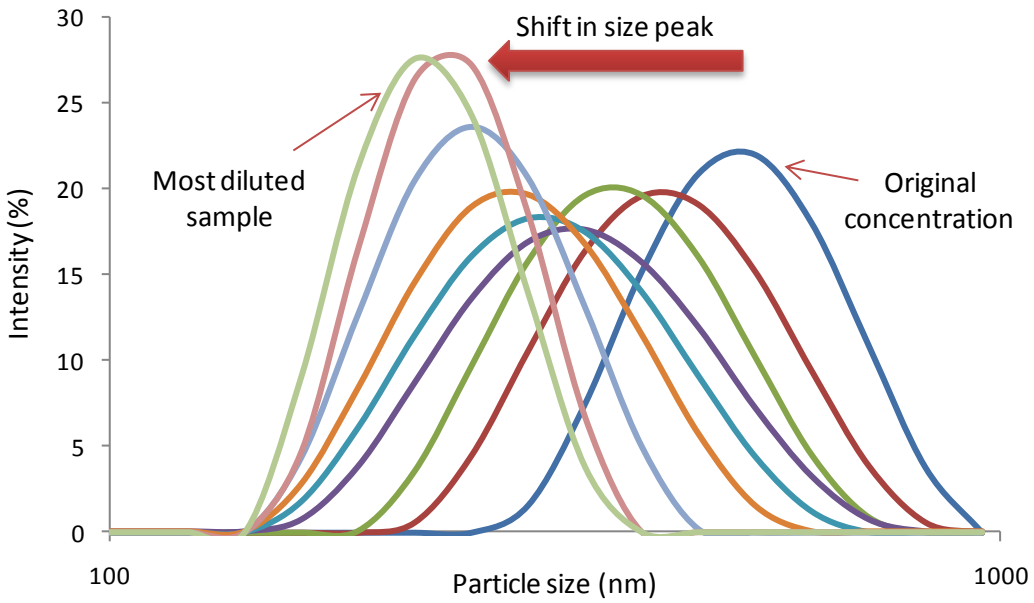

Figure 2.44: DLS measurements of size distribution of iron oxide nanofluids at various concentrations. The graph shows the shift in the peak of the distribution as concentration changes.

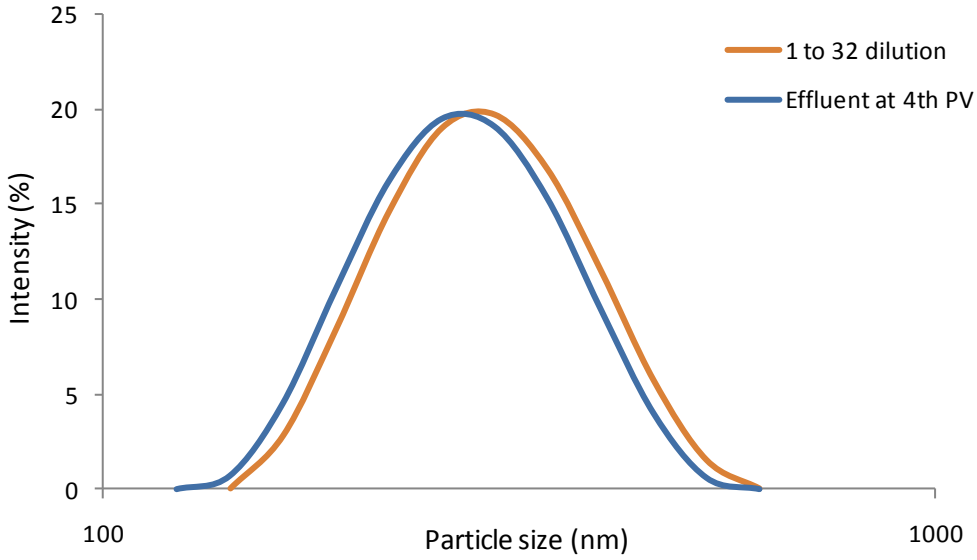

Figure 2.45: Size distribution of effluent sample at the fourth post-injected pore volume. This matches the size distribution of a diluted sample.

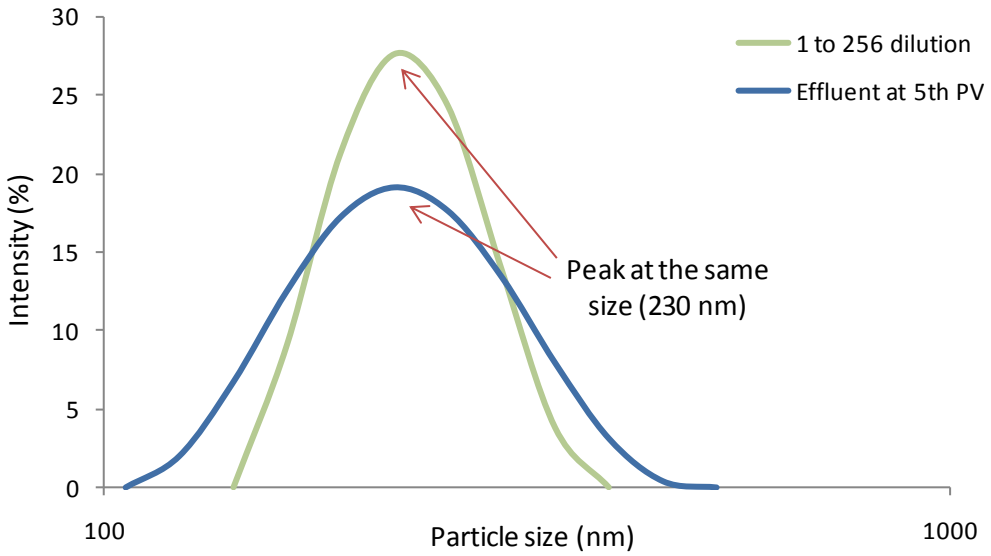

Figure 2.46: Size distribution of effluent sample at the fifth post-injected pore volume. This matches the size distribution of a diluted sample.

The concentration of the effluent samples was determined by measuring their absorbance using the UV-vis spectrophotometry. The absorption spectra for all effluent samples are depicted in Figure 2.47.

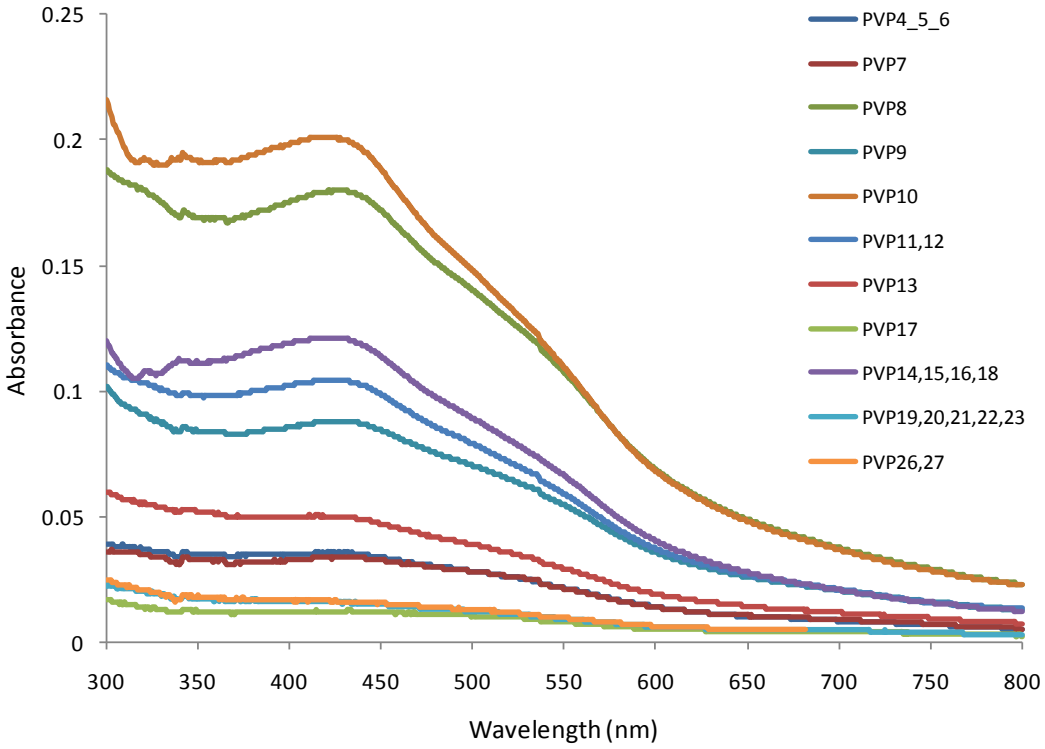

Figure 2.47: Absorbance of all effluent samples collected during iron oxide nanoparticles injection experiment.

Most absorbance spectra had identical signature. The absorbance spectra of samples PVP 4, 5 and 6 could not be measured separately, perhaps due to their low concentration, and thus they were mixed together and one absorbance spectrum was obtained. The same approach was applied to samples PVP 11-12, PVP 14-18, PVP 19-23 and PVP 26-27 at the third, fourth, fifth and sixth post-injected pore volumes, respectively. Dilution was carried out wherever required.

The calibration curve was then used to obtain the corresponding concentrations for all samples. Diluted sample concentrations were calculated using the following linear relationship.

$$C_1V_1 = C_2V_2 \tag{2.6}$$

where C_1 and C_2 are concentrations before and after dilution, respectively. V_1 and V_2 are sample volumes before and after dilutions, respectively.

Following the determination of the effluent samples concentration, the production history curve of the iron oxide nanoparticles coated with PVP was estimated (Figure 2.48).

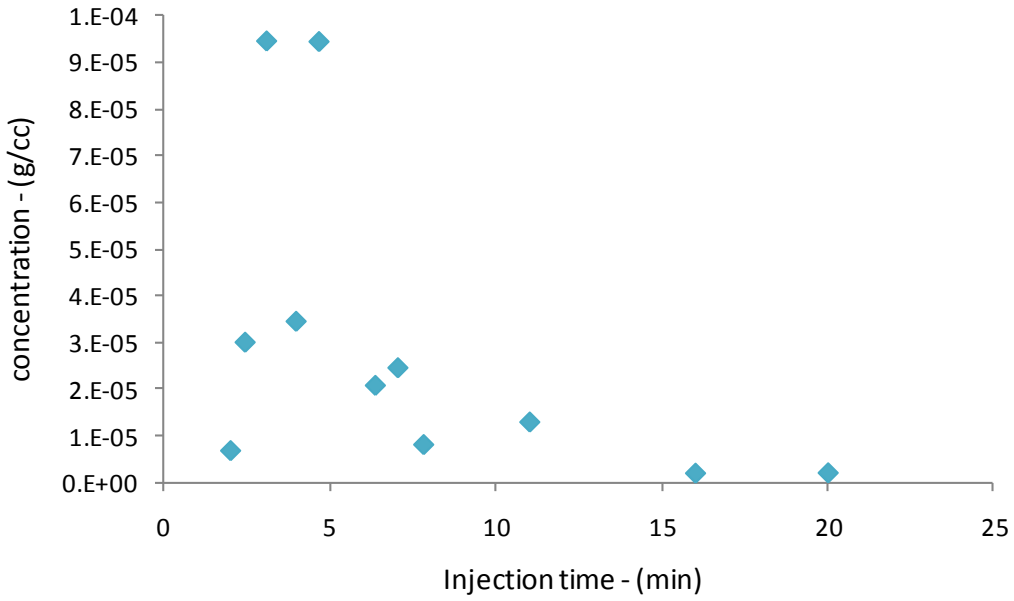

Figure 2.48: Production history (return curve) of coated iron oxide nanoparticles surfactant (PVP).

The number of nanoparticles recovered can be calculated by integrating the area under the return curve. A rough estimate has indicated that less than 23% of injected nanoparticles were recovered.

2.8.2 Spherical silver nanoparticles injection experiment results

Spherical silver nanoparticles were detected in the effluent samples and about 25% of injected nanoparticles were recovered as reported in last quarterly report (July-September, 2010). This quarter, post-injection of pure water was performed at higher flow rate to investigate if larger flow rates would improve the recovery. The rock was also backflushed at the same rate in an attempt to mobilize nanoparticles trapped at the inlet of the core. The silver nanoparticles were not detected in any of the effluent samples collected during high flow rate injection or backflushing. During backflushing, the permeability was improved by about 25 md as depicted in Figure 2.49.

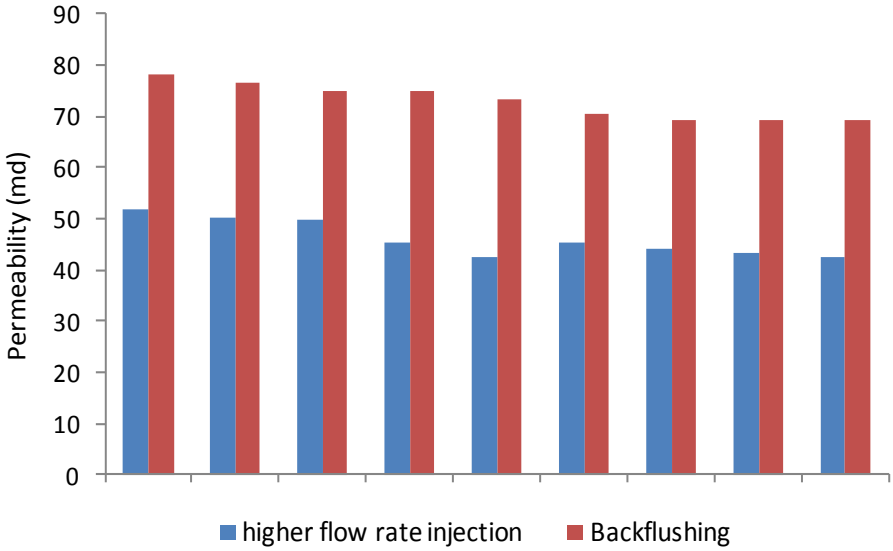

Figure 2.49: Comparison of permeability measurements during backflushing and injecting at higher flow rates. There was about 25 md difference.

Despite the permeability improvement during backflushing, silver nanoparticles were still not detected in the effluents. UV-vis analysis was conducted and optical density spectra were obtained. All effluent samples (from backflushing and injecting at higher flow rates) exhibited the behavior of pure water as shown in Figure 2.50. Effluents were examined by SEM imaging in which no images showed any sign of silver nanoparticles.

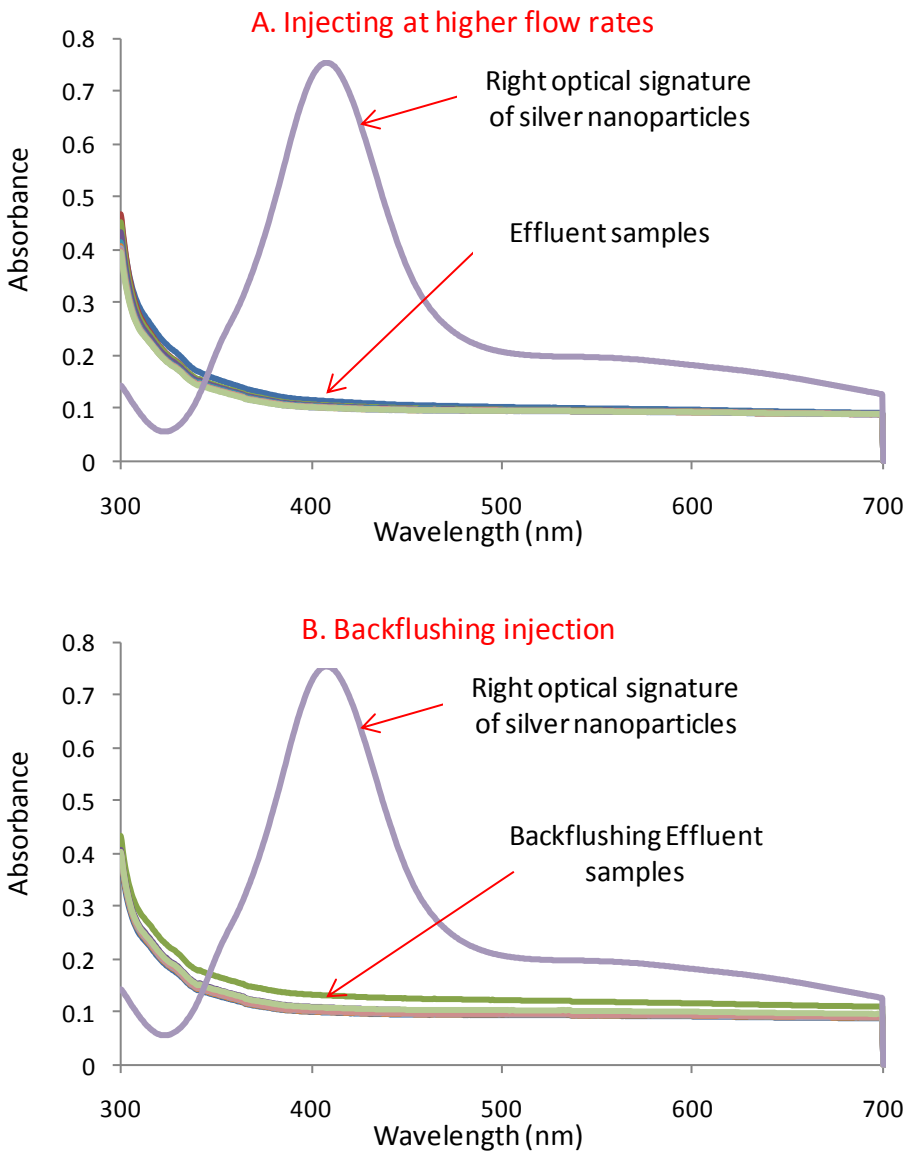

Figure 2.50: Optical density spectra of effluents collected during (A) post-injection at higher flow rate and (B) backflushing at the same rate.

2.8.3 Tin-bismuth injection results

Tin-bismuth nanoparticles were identified in a few effluent samples in low concentrations. It was observed that only nanoparticles with diameters 200 nm and smaller were transported within the pore spaces of the rock, as shown in the SEM image in Figure 2.51A. Note that the influent sample contained nanoparticles as large as 600 nm. It was speculated that larger particles (greater than 200 nm) were trapped at the inlet of the core. In fact, SEM imaging of the backflushing effluents showed that there was entrapment and remobilization of various nanoparticle sizes, including the sizes greater than 200 nm (Figure 2.51B). The rock filtered the injected nanofluid,

allowing only certain particle sizes to flow through. It should be noted that this is a qualitative analysis in which the determination of the relative numbers of particles recovered was not possible.

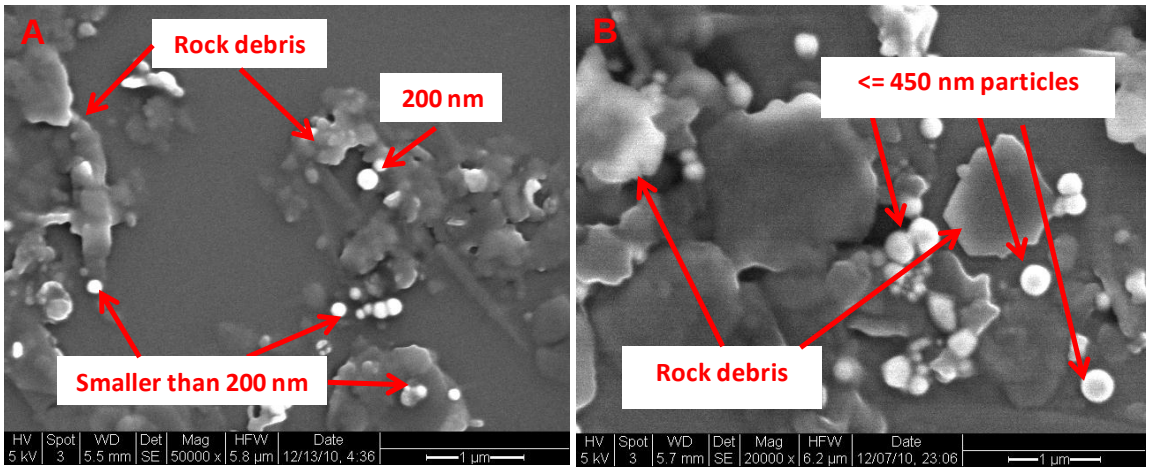

Figure 2.51: SEM imaging showing the tin-bismuth nanoparticles at the effluent during (A) injection and (B) backflushing of the Berea sandstone. Only particles smaller than 200 nm were transported through the pore spaces while larger particles were trapped at the inlet of the core and remobilized during backflushing.

The permeability measurements during the injection agree with this finding. The permeability as a function of the injected volume is depicted in Figure 2.52. There was a drop in permeability to about 56% of the original value, after which the permeability remained at that level during the first post-injected pore volume, indicating the partial plugging of the pores. Then, permeability started to increase until reaching a plateau at approximately 82% of its value prior to the nanofluid injection. At this time, only nanoparticles of 200 nm and smaller were observed in the effluent, using SEM (Figure 2.51A). As mentioned earlier, the backflushing of the core remobilized some particles and as a result the permeability of the rock improved slightly by 8% (i.e. back to 90% of its original value). However, permeability improvement (from 56% to 90% of original value) does not imply a good recovery of the injected nanoparticles. If the injected nanofluid has a visible color, it is possible to observe the nanoparticles in the effluent visually. In the case of the tin-bismuth injection, the influent had a dark gray color. All effluent samples appeared colorless and transparent, so it was hypothesized that many of the nanoparticles had been trapped within the rock pores, most likely at the inlet of the core. Examining the pore spaces of the rock itself confirmed that considerable numbers of the tin-bismuth nanoparticles were trapped (Figure 2.53).

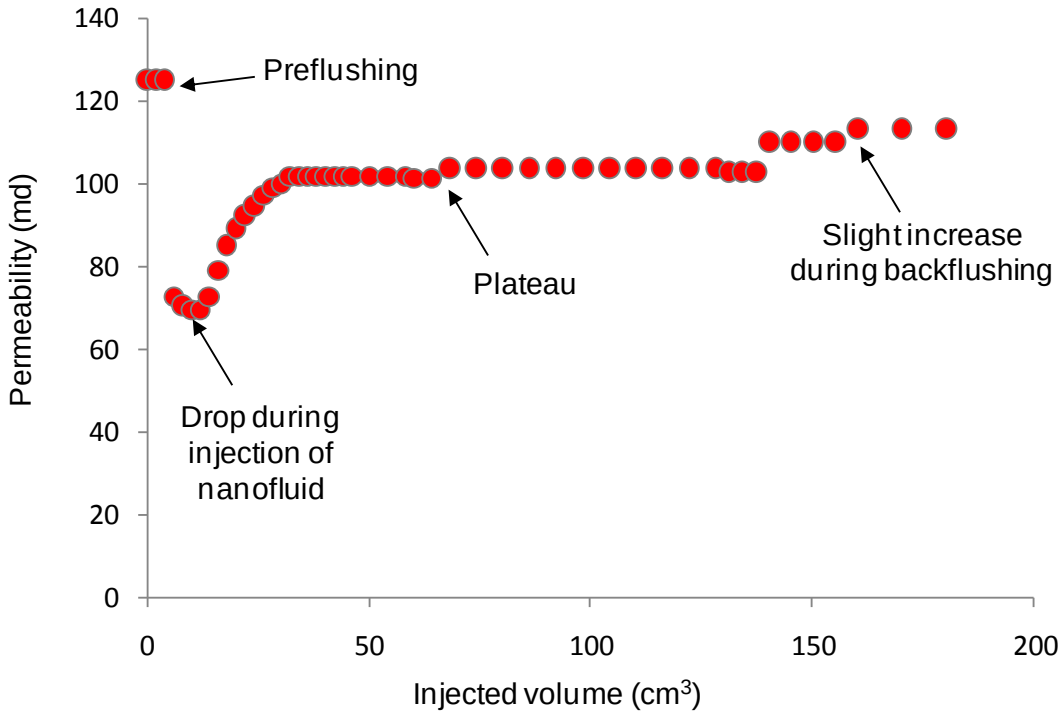

Figure 2.52: Permeability measurements during the injection of the tin-bismuth nanoparticles.

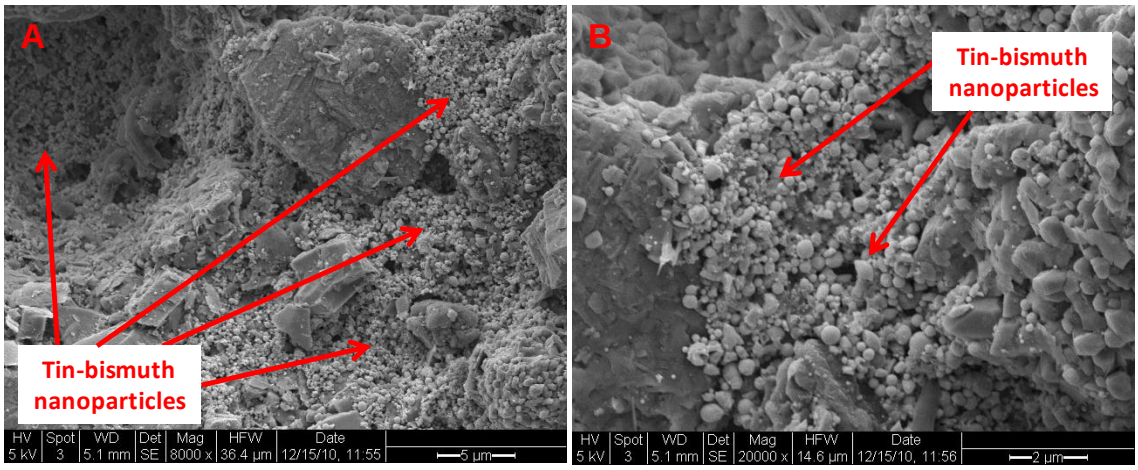

Figure 2.53: SEM image of (A) the pore space at the inlet of Berea sandstone used during the tin-bismuth injection, (B) at higher magnification. Nanoparticle entrapment is apparent.

Further evaluation of the rock pore spaces using SEM imaging (Figure 2.54) demonstrated the bridging and plugging of the tin-bismuth nanoparticles in the pore throat entry. Kanj et al. (2009) explained that high concentrations of small particles might bridge across the pore throats. The authors also added that larger particles could result in direct plugging of the pore entry. Both

phenomena would impact the rock permeability negatively. Particles shown in Figure 2.53 could not be mobilized either by increasing the injection flow rate or by backflushing and were probably responsible for the permanent reduction in the rock permeability.

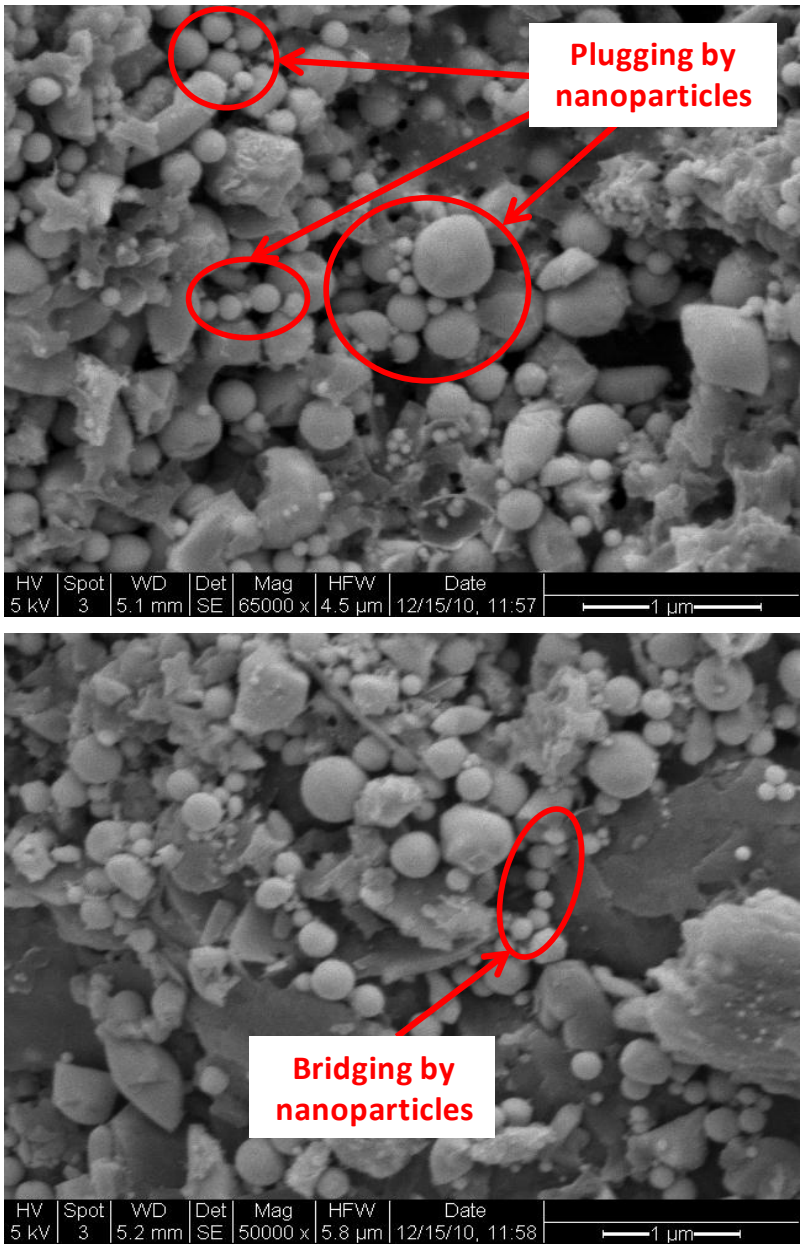

Figure 2.54: SEM images from within the pore spaces of the Berea sandstone, demonstrating the bridging and plugging phenomena.

The SEM analysis did not provide conclusive evidence of the mechanism of particle entrapment. Alaskar et al. (2010) reported that the nanoparticle shape and surface characteristics play a major role in their transport through a porous medium. They also reported that the spherical silica (SiO_2) nanoparticles with narrow size distribution and surface charge compatible with that of the

rock were transported successfully through the pore spaces of Berea sandstone. SiO_2 nanoparticles were not trapped in the pore spaces by hydraulic, chemical or electrostatic effects. The tin-bismuth nanoparticles exhibit similar properties in terms of shape and surface charge (negatively charged), except that the tin-bismuth nanoparticles had a wider distribution of sizes between 50 to 600 nm. Thus, particle shape and surface charge should not have imposed flow constraints. The optimized testing program suggested by Kanj et al. (2009) emphasizes particle size, influent concentration and affinity of particles to rock matrix. In the case of tin-bismuth injection, although the influent sample had wide distribution of particle sizes, they were all within the size range of the pore network. Therefore, it was concluded that the tin-bismuth nanoparticles affinity and/or concentration may have caused their entrapment.

Further investigation of particle affinity to Berea sandstone was carried out by injecting the same influent sample with identical concentration into a slim tube packed with glass beads. This allowed testing the transport of the tin-bismuth nanoparticles in the absence of the rock core material. One pore volume of the nanofluid was injected at the rate of 0.5 cm^3/min followed by continuous injection of pure water at the same rate. Several effluent samples were collected and analyzed by SEM imaging. It was found that the tin-bismuth nanoparticles of all sizes flowed through the slim tube. The increasing concentration of the nanoparticles was observed visually through the injection of the first post-injected pore volume as illustrated in Figure 2.55. SEM imaging confirmed this finding as depicted in Figure 2.56.

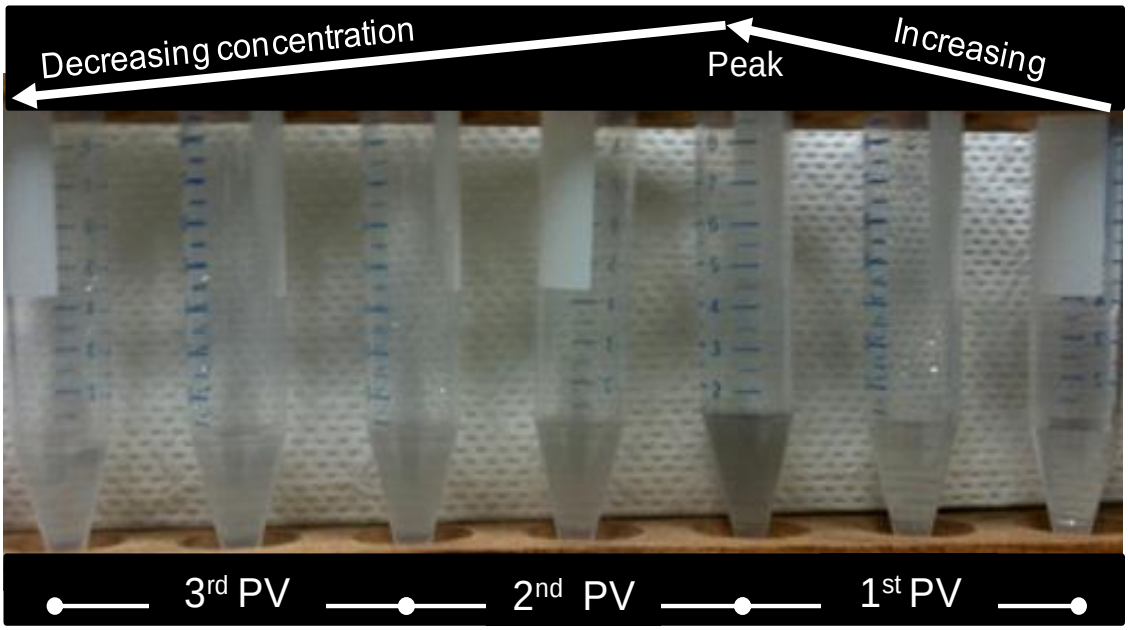

Figure 2.55: Visual characterization of effluent samples for their tin-bismuth nanoparticles content based on color.

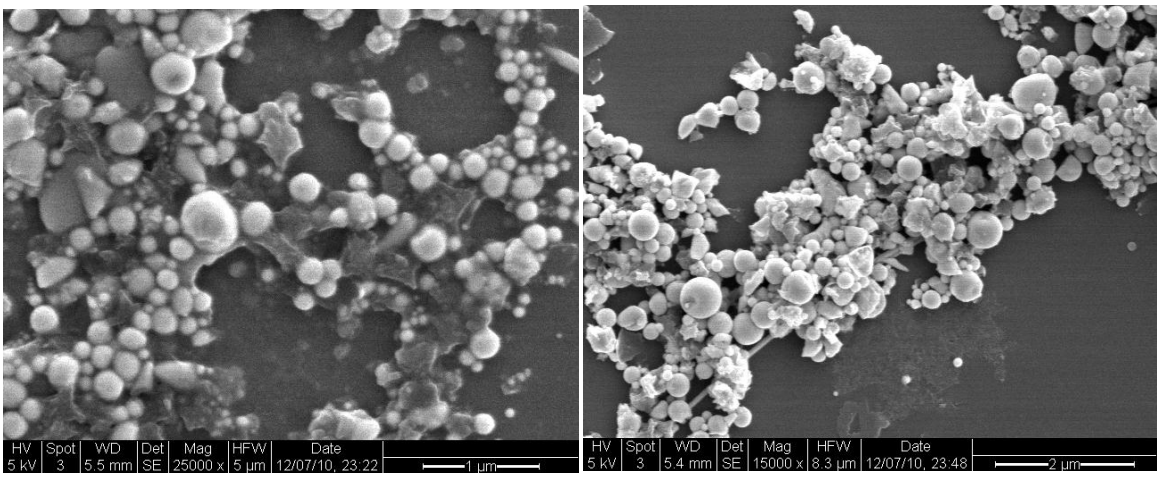

Figure 2.56: SEM images of the effluent collected during the injection of tin-bismuth nanoparticles into the slim tube packed with glass beads.

Thus, it has been demonstrated that the spherically shaped tin-bismuth nanoparticles can be recovered following their injection into tube packed with glass beads without being trapped within the flow conduits, but not through the pore network of the rock (which has much smaller pores). This might be attributed to an affinity of these nanoparticles to the sandstone rock matrix or high nanoparticle concentration imposing constraints to their flow. The complexity of the rock pore network compared the large pores between the glass beads was not taken into consideration during this analysis.

2.8.4 Silica nanoparticle injection results

This section provides the results of the injection of silica nanoparticles into the fractured greywacke core. The objective of this experiment was to investigate the transport of silica nanoparticles through fractured greywacke core, providing a baseline for subsequent injections of the fluorescent silica microspheres.

The silica (SiO_2) nanoparticles flowed through the fractured greywacke core successfully. The nanoparticles had a relatively narrow distribution of size between 350 – 420 nm. The nanoparticles were easily distinguishable from the core fines and debris due to their size and spherical shape, even though all are made of same material as the rock itself (silica). The effluent samples were examined for the presence of the nanoparticles using the DLS technique. For instance, the effluent samples at the second and third post-injected pore volumes of deionized water showed particle size distributions that were identical to the particle size distribution of the injected influent. The particle size distributions of these effluent samples is shown in Figure 2.57.

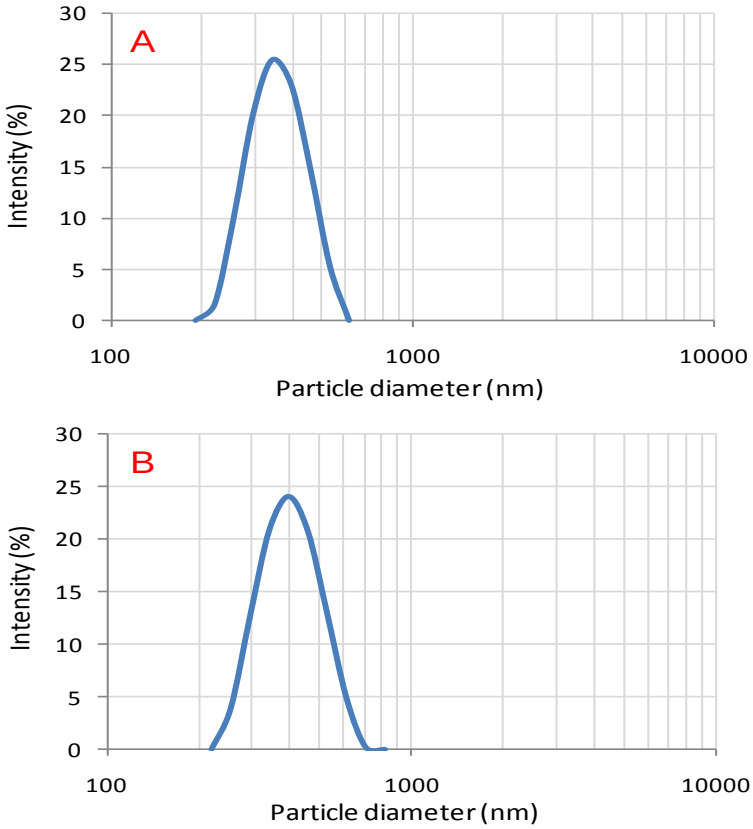

Figure 2.57: Particle size distribution by intensity percentage of effluent samples at (A) second and (B) third post-injected pore volume of deionized water.

The more precise approach using SEM imaging of the effluent confirmed this finding (Figure 2.58). The average nanoparticle size in Figure 2.58 is around 350 nanometers.

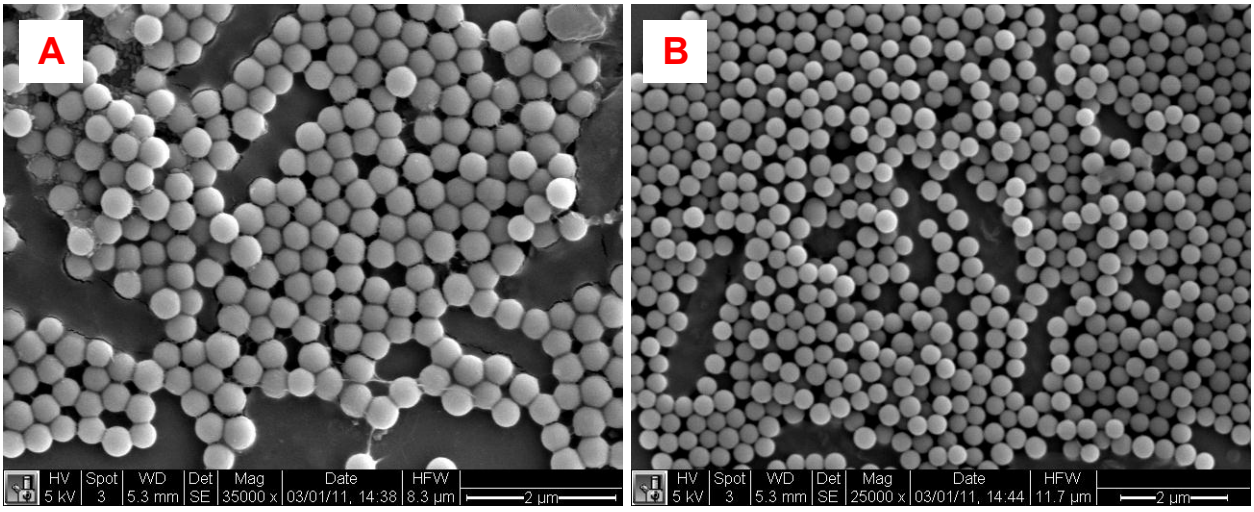

Figure 2.58: SEM image showing SiO_2 nanoparticles in the effluent samples at (A) second and (B) third post-injected pore volume of deionized water.

SEM imaging of an effluent sample at the seventh post-injected pore volume showed the decrease in the silica nanoparticles as more water was injected (Figure 2.59). Only few nanoparticles were identified in the later effluent sample.

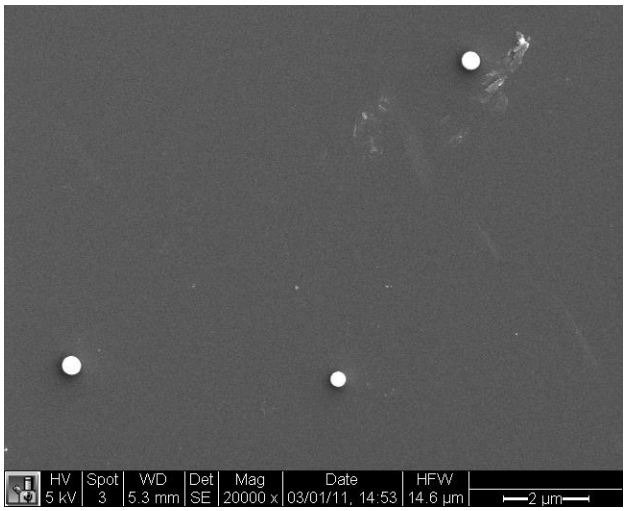

Figure 2.59: SEM image showing few SiO_2 nanoparticles in the effluent sample at later post-injected pore volume of deionized water.

The permeability measurement (Figure 2.60) during and after the injection of the SiO_2 nanofluid was relatively constant with minimal change of about ± 3 darcy. Note that the permeability during the post-injection was about 47 darcy, 22% less than the permeability values measured right after saturation of the core sample. This was believed to be caused by the swelling of the clays of core. A significant reduction in permeability during the backflushing of the core sample was observed. There was approximately 86% reduction in the permeability from 47 to 7 darcy. It is worth mentioning that the backflushing of the sample was conducted a few weeks after the injection of the nanoparticles. By that time, the core had been saturated for about 2 months. It is not unexpected that the clays in the core could be swelling, especially as greywacke is known to

have a high content of clay materials. Consequently, the injection of the fluorescent silica microsphere was postponed. The core will be dried and resaturated with deionized water. The injection of silica nanoparticles will be repeated, followed immediately by the fluorescent silica microspheres. This should reduce the possibility of clay swelling at least prior to the injection of the silica microspheres.

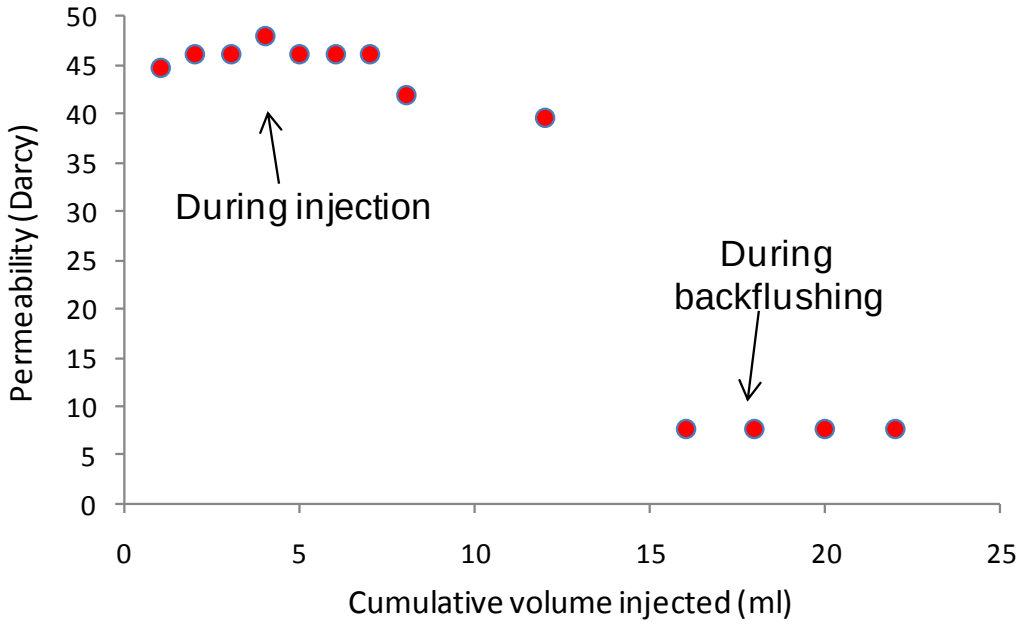

Figure 2.60: Permeability measurements during injection and backflushing of the fractured greywacke core sample.

2.8.5 Results of fluorescent silica injection into fractured greywacke

This section provides the results of the injection of fluorescent silica microspheres into the fractured greywacke core. prior to the injection of the silica spheres, silica nanoparticles were injected. The objective of this experiment was to investigate the transport of silica nanoparticles through fractured greywacke core, providing a baseline for subsequent injections of the fluorescent silica microspheres.

The silica (SiO_2) nanoparticles flowed through the fractured greywacke core successfully. The results were fully discussed in a previous quarterly report (January-March, 2011)

The fluorescent silica microspheres were also transported through the fractured greywacke core successfully. As mentioned earlier, the silica microspheres influent samples of the same concentration (but different size) were consecutively injected. That is the injection of the blue silica microspheres diluted (1:100) was followed by the (1:100) diluted green silica microspheres. Following that, the blue silica microspheres influent with doubled concentration (1:50 dilution) was injected, followed by the green silica microspheres influent of the same concentration.

The silica microspheres were identified in the effluent samples using optical microscopy and fluorescence spectroscopy, confirming their delivery through the fracture. Example of the optical imaging performed on collected effluent samples post the injection of the (1:100) diluted blue and (1:50) green silica microspheres can be depicted in Figure 2.61. Similar images were obtained for effluents resulted from the other injections (i.e. the (1:50) blue and (1:100) green injections experiments).

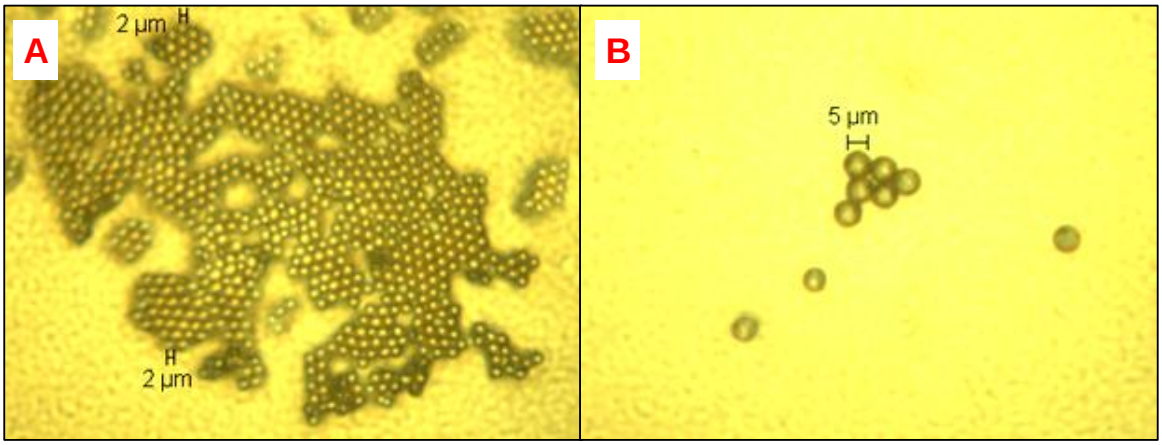

Figure 2.61: Optical images of the effluent during the (A) blue and (B) green silica microsphere injections.

The recovery of the silica microspheres was determined by measuring the emission spectrum and correlating it to the effluent concentration using a calibration curve. The fluorescence emission spectra of all effluent and backflushing samples collected during the blue silica microsphere injection (1:100 and 1:50) are shown in Figure 2.62. The samples were excited at a wavelength of 350 *nm* and the emission spectrum was measured between 350 to 600 *nm*, with a peak or maximum emission at a wavelength of about 434 *nm*. To construct the calibration curve, the emission spectra of a few samples of known concentrations were acquired. The concentrations of effluent samples were determined based on the maximum emission intensity at the peak. The return curves of the blue microspheres were then estimated as depicted in Figure 2.63. It was found that about 54% of the injected (1:100) diluted blue spheres influent was recovered. The microspheres were produced throughout the post injection at roughly constant level ($\pm 1.5 \times 10^{-5}$ g/cm^3), with no clear or identifiable peak. On the other hand, only 19% of the (1:50) blue spheres influent was recovered, mostly during the post injection of the first five pore volumes. Note that this injection followed the injection of the (1:100) green spheres. The green silica spheres were more than twice the size of the blue spheres. It was hypothesized that part of the fracture might have been plugged causing the microparticles to accumulate at plugged sections and hence cause entrapment of subsequently injected spheres (i.e. 1:50 blue spheres).

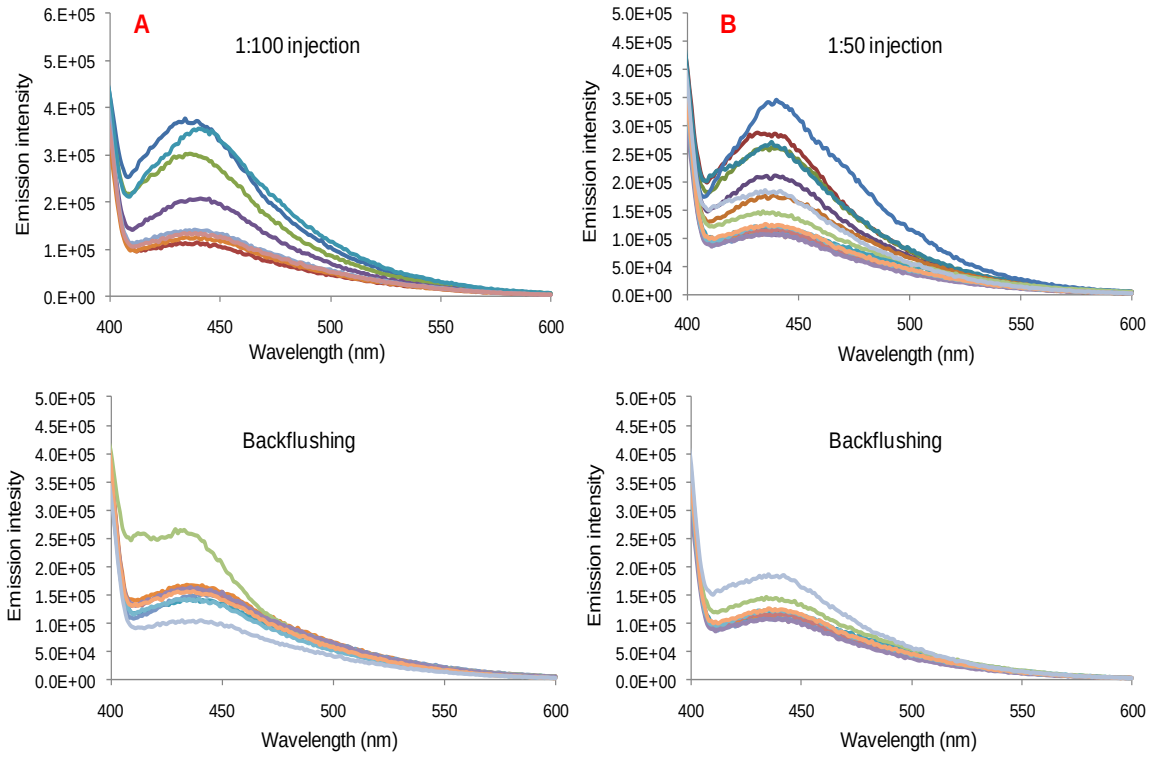

Figure 2.62: Emission spectra of effluent and backflushing samples during (A) 1:100 and (B) 1:50 dilutions of the blue silica spheres.

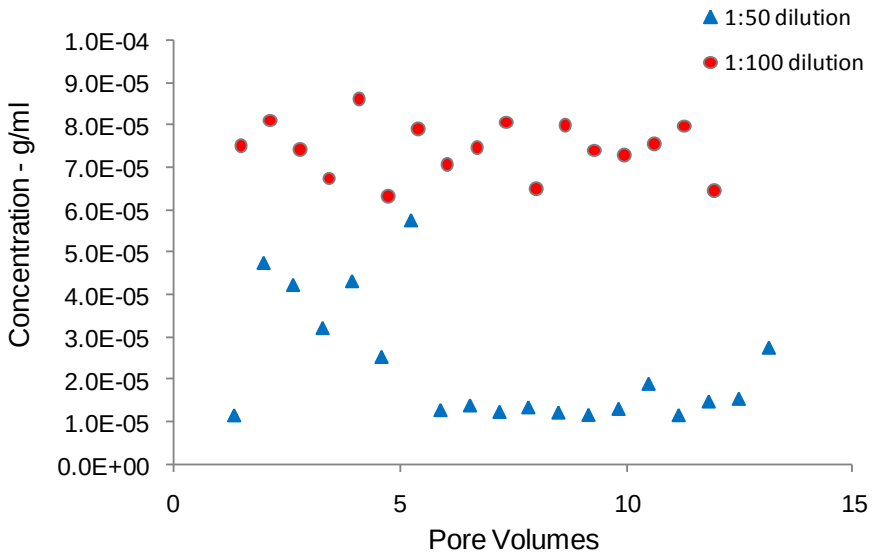

Figure 2.63: Blue silica microspheres return curves.

To support this finding, we attempted to estimate the recovery of the green silica microspheres. The (1:100) and (1:50) green spheres influents followed the injection of the (1:100) and (1:50)

blue spheres samples. The construction of the calibration curve of the green silica microspheres was not feasible due to discrepancies in the fluorescence emission spectra measurements of diluted samples. However, we attempt to estimate the average recovery of the green spheres by calculating the cumulative ratio of emission intensity of effluent (E_e) to emission intensity of influent (E_i). The fluorescence emission spectra of effluent and backflushing samples of the green silica microsphere injection (1:100 and 1:50) are shown in Figure 2.64. The effluent and backflushing samples were excited at wavelength 480 *nm* and the emission spectrum was acquired between 480 to 700 *nm*, with maximum emission at wavelength of about 525 *nm*.

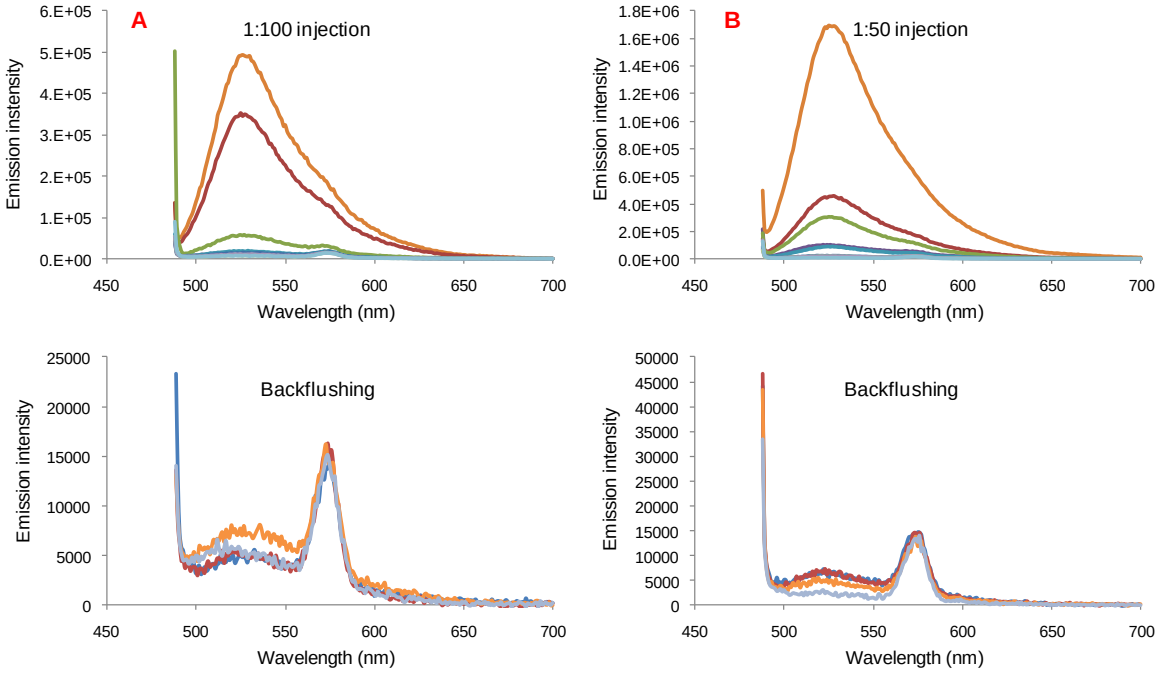

Figure 2.64: Emission spectra of effluent and backflushing samples during (A) 1:100 and (B) 1:50 dilutions of the green silica spheres.

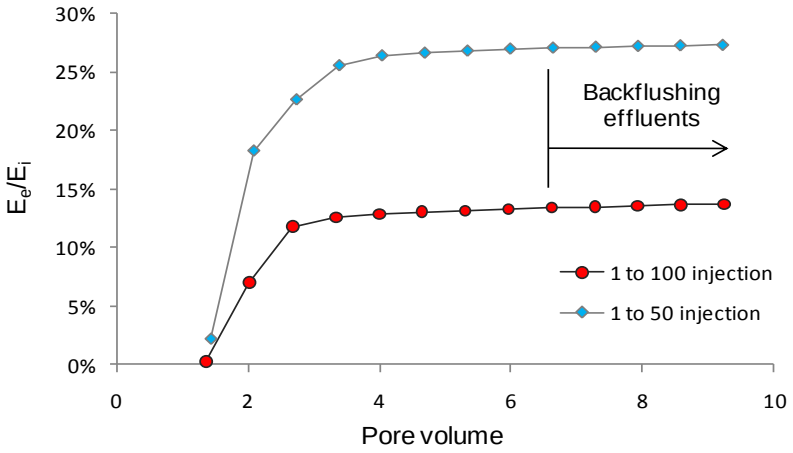

Figure 2.65: Green silica spheres cumulative ratio of emission intensity of effluent (E_e) to influent (E_i) as function of pore volumes injection.

Figure 2.65 shows the cumulative ratio of emission intensity of effluent to that of the influent. In the case of the 1:100 green spheres injection, the cumulative emission intensity ratio reached a plateau at around 13.7%, indicating a poor recovery of the microspheres. Many spheres were trapped within the fractured core. This injection preceded the (1:50) blue spheres injection. The plugging of the green spheres may have resulted in the poor recovery (19%) during the injection of the (1:50) blue spheres. In the case of the 1:50 green sphere injection, the recovery of particles was about 27.3%, double the value observed in the 1:100 injection.

We have demonstrated the feasibility of transporting nanoparticles and/or microparticles through a fractured greywacke core. In terms of characterizing the fractures in the rock, which is a primary objective of the project, the preliminary experiments showed promise. Figure 2.66 is an SEM image from within the pore spaces of Berea sandstone following the injection of silica (SiO_2) nanoparticles. This shows that the nanoparticles passed through pores of sizes larger than themselves, but were unable to pass into the tinier natural fracture that existed within the rock structure. A smaller nanoparticle could have entered the fracture providing a direct correlation between the recovered particle size and fracture aperture. Therefore, it might be possible to use nanoparticles as fracture aperture caliper.

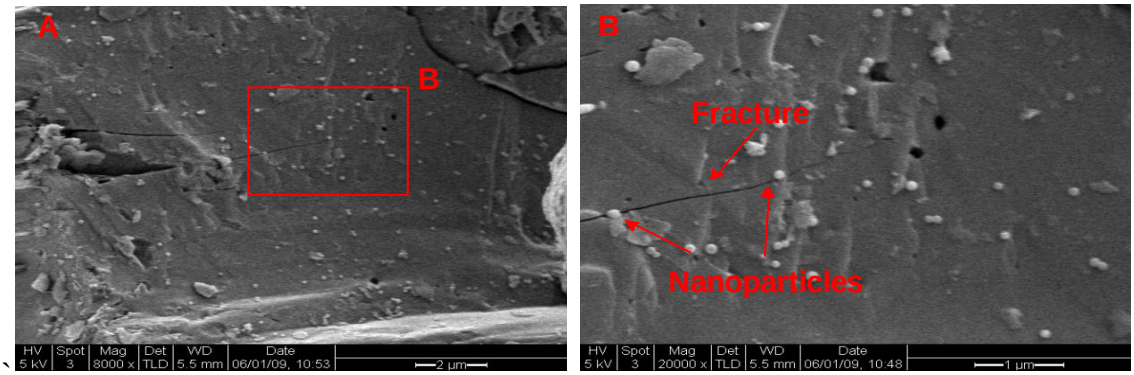

Figure 2.66: (A) Natural fracture with two nanoparticles at its entry, (B) close-up image. Smaller nanoparticles would enter the fracture providing direct fracture aperture measurement based on recovered particle size.

Investigation into the idea of using particles to measure the fracture aperture was carried out by injecting the polydisperse (diameter ranging from 5 to 31 μm) red silica microsphere influent (Figure 2.67A) into the fractured greywacke core. It was found that only microspheres with diameters smaller than 20 μm were transported through the fracture (Figure 2.67B). This suggested that the fracture has an aperture of at least 20 μm, but not as large as 31 μm. This result was in agreement with the hydraulic fracture aperture measurement (i.e. 27 μm as determined by cubic law), and demonstrates the possibility of using particles to estimate the size of the fracture opening. Another interesting finding was that the particle size did not need to be three times smaller than the space available for its flow (the rule of thumb commonly used to size membrane filters).

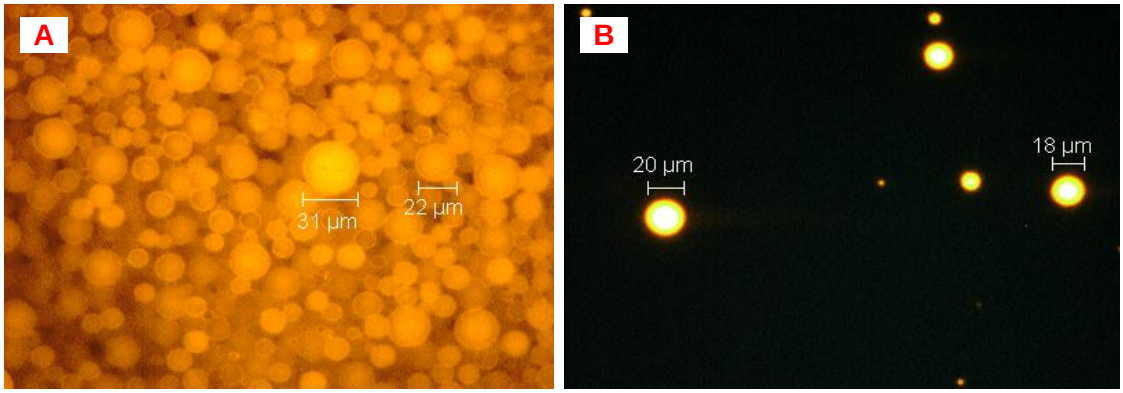

Figure 2.67: Optical images for red fluorescent silica microspheres of (A) influent, (B) effluent samples. Only spheres of about 20 µm *flowed through the fracture of predetermined aperture of 27* µm.

The recovery of the red silica microspheres was determined by calculating the ratio of fluorescence emission intensity of effluent to that of the influent. Two diluted influent samples (1:100) and (1:50) of red spheres were injected one after the other. Note that the fractured core was flushed with many pore volumes prior to the injection of the red spheres; in attempt to mobilize remaining microspheres from previous injections (blue and green silica spheres). The core was also dried and resaturated again. The cumulative emission intensity ratio as function of pore volume injected is shown in Figure 2.68. The recovery following the (1:100) influent injection was around 15.7%. Acquiring the emission spectrum of some effluent and backflushing samples was not possible, because fluorescence levels in these samples were below detection limit of the instrument. The recovery was improved to 47.5% when the concentration of influent was doubled (i.e. 1:50 dilution).

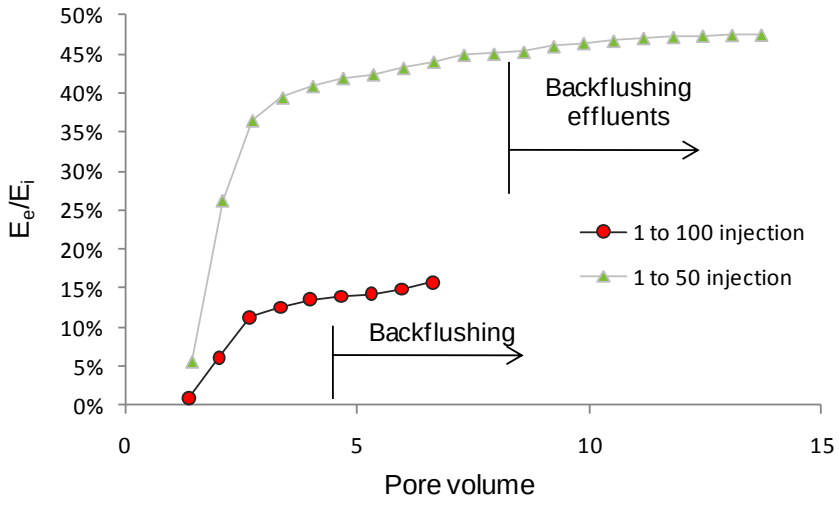

Figure 2.68: Red silica spheres cumulative ratio of emission intensity of effluent (E_e) to influent (E_i) as function of pore volumes injection.

2.8.6 Results of fluorescent silica injection into glass fracture model

This section provides the results of the injection of fluorescent silica microspheres into the glass fracture model. The fluorescent silica microspheres were transported through the fracture model successfully.

The recovery of the silica microspheres was estimated by measuring the emission spectra and correlating it to the effluent concentration using a calibration curve. The fluorescence emission spectra of all effluent samples collected during the blue silica microsphere injection are shown in Figure 2.69. The samples were excited at a wavelength of 350 *nm* and the emission spectra were measured between 350 to 600 *nm*, with a peak or maximum emission at a wavelength of about 430 *nm*. Note that the emission peaks of samples B3 and B4 were not clearly shown because of the low content of silica particles, compared to the concentration of sample B2 that contains the bulk of the silica microspheres. Despite the fact that the effluent samples volume was 0.5 mL, this is significantly higher than the pore volume of the fracture and therefore the majority of particles was captured on one sample (B2). To construct the calibration curve, the emission spectra of a few samples of known concentrations were acquired. The concentrations of effluent samples were determined based on the maximum emission intensity at the peak (Figure 2.70).

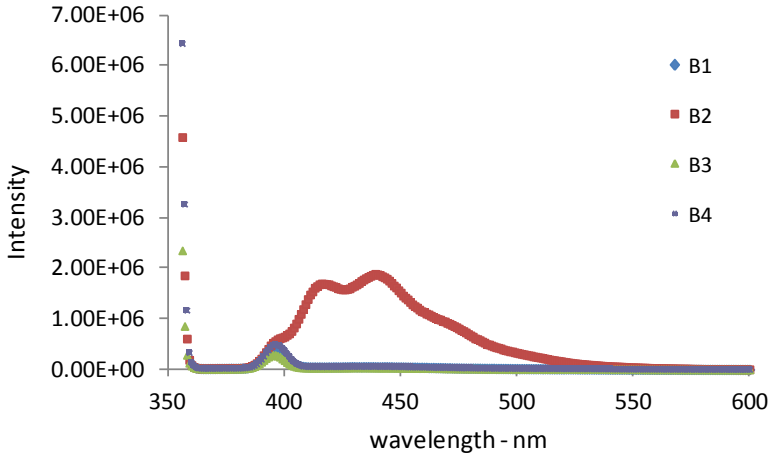

Figure 2.69: Emission spectra of effluent samples during injection of the blue silica spheres.

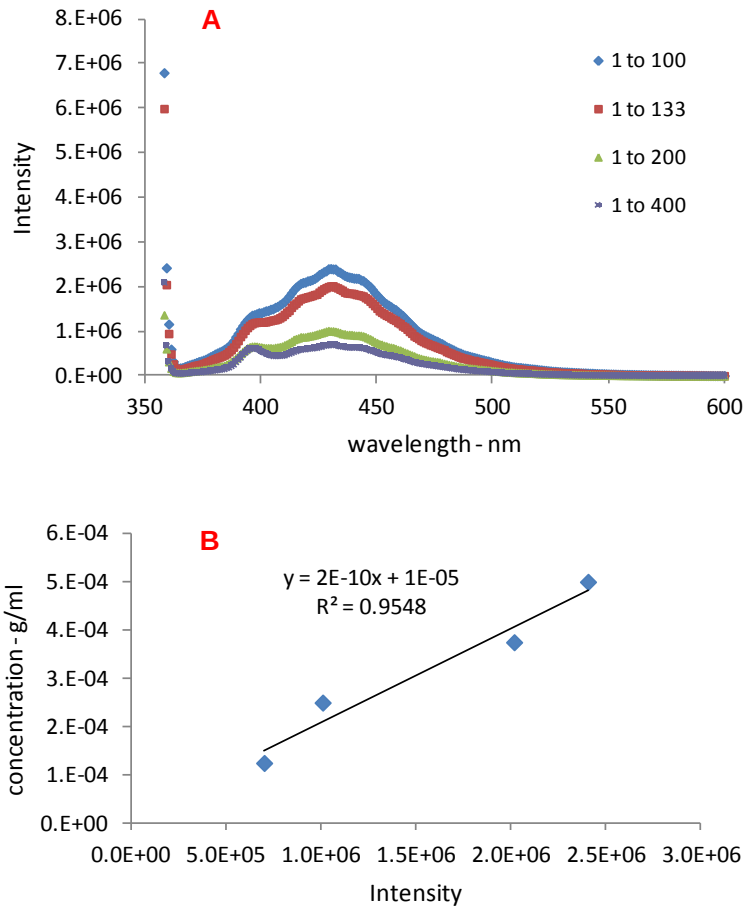

Figure 2.70: (A) Emission spectra of diluted silica samples of known concentrations, (B) calibration curve.

The return curves of the blue microspheres were then estimated as depicted in Figure 2.71. It was found that cumulative recovery of injected blue silica microspheres was about 70%. Estimation of the cumulative recovery of the silica spheres was also attempted by calculating the cumulative ratio of emission intensity of effluent (I) to emission intensity of influent (I_o). Based on the intensity ratio, the cumulative recovery was about 76%. Both recovery values were reasonably in agreement. The slight difference may be attributed to error introduced during the construction of the calibration curve. The unrecovered silica microspheres were believed to be trapped within fittings and/or valves used for their injection.

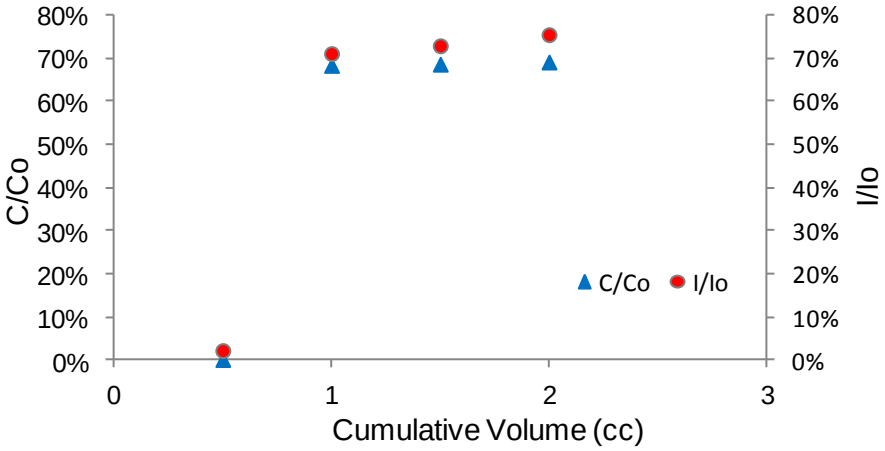

Figure 2.71: Cumulative recovery of silica microspheres calculated based on concentration and intensity ratios.

2.8.7 Magnetic Collection Experimental Results

In order to calculate the collection efficiency, or the percentage of injected nanoparticles that were remained in the magnetic trap at the end of the experiment, dilutions of the original nanofluid with known concentrations. The dilution with the closest visual match to the trapped nanofluid is shown in Figure 2.72.

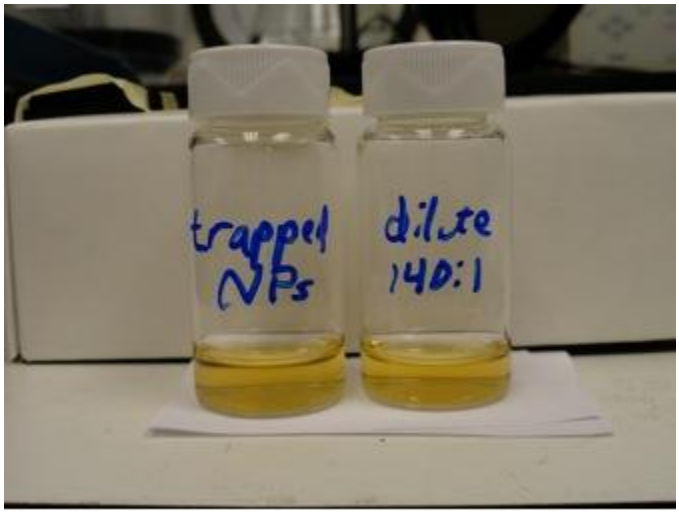

Figure 2.72: Visual comparison of trapped nanofluid sample and 142.5 to 1 dilution of original nanofluid.

The absorbance spectra of the trapped nanofluid and the prepared dilutions were measured using uv-vis spectroscopy, and are shown in Figure 2.73. As is predicted by Beer's Law, concentration was found to scale linearly with absorbance. This is shown in Figure 3-8. For this correlation, the absorbance was read at a wavelength of 460 nm, because the spectra have an inflection point at this wavelength.

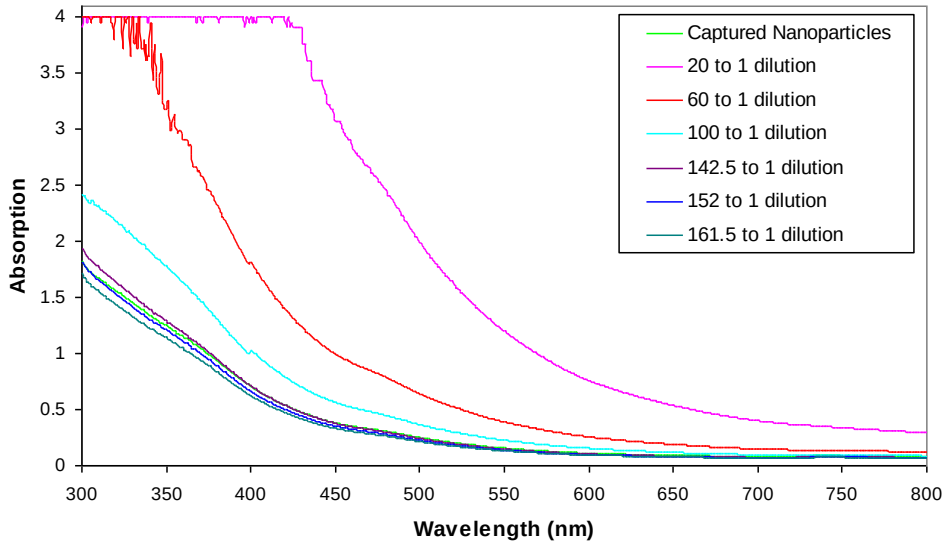

Figure 2.73: Absorbance spectra of suspensions of iron oxide nanoparticles coated with silica.

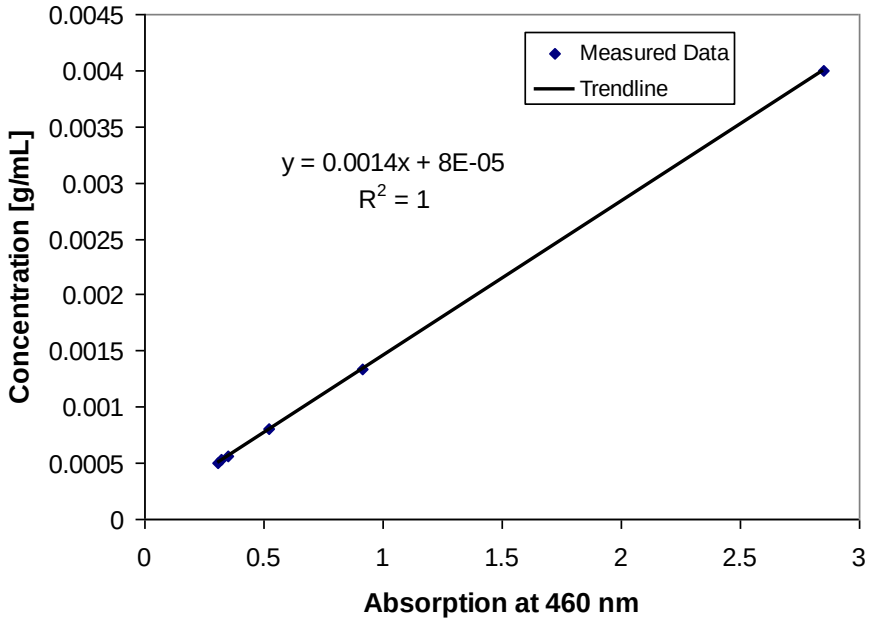

Figure 2.74: Correlation of concentration to absorbance for dilutions of iron oxide nanofluid with known concentrations.

Using the correlation shown in Figure 2.74, the concentration of the trapped nanofluid was estimated to be 0.00057 g/ml. The collection efficiency was calculated using Equation 2.30.

$$\eta_{collection} = \frac{m_{collected}}{m_{injected}} * 100\% = \frac{C_{collected} V_{collected}}{C_{injected} V_{injected}} * 100\% \qquad (2.30)$$

where $\eta_{collection}$ is collection efficiency, m denotes mass, C denotes concentration, and V denotes volume. The collection efficiency for this experiment was estimated to be 3%.

2.9 FUTURE WORK

It is planned to continue our investigation of the flow of particles through fractured rock cores. Several core samples will be saw-cut to create fracture of predetermined aperture. Further magnetic collection experiments will also be performed using different magnets and configurations in order to increase collection efficiency.

We will continue our investigation of the flow of particles through the glass fracture model. We plan to inject a polydisperse sample with particles bigger and smaller than predetermined hydraulic aperture, to further investigate the fracture caliper concept. Since the model allows for visual study of particle flow, we also plan to visually investigate the diffusion of particles during flow.

It is also planned to synthesize tin-bismuth nanoparticles using an emulsion synthesis route to yield a monodisperse sample of nanoparticles with diameters of ~100 nm. This will enable more conclusive flow experiments and heating experiments to be conducted using these temperature sensitive particles.

3. FRACTURE CHARACTERIZATION USING RESISTIVITY

This research project is being conducted by Research Assistant Lilja Magnusdottir, Senior Research Engineer Kewen Li and Professor Roland Horne. The objective of this project is to investigate ways to use resistivity to infer fracture properties in geothermal reservoirs.

3.1 SUMMARY

In this project, the aim is to use Electrical Resistivity Tomography (ERT) to characterize fracture properties in geothermal fields. The resistivity distribution of a field can be estimated by measuring potential differences between various points while injecting an electric current into the ground and resistivity data can be used to infer fracture properties due to the large contrast in resistivity between water and rock. The contrast between rock and fractures can be increased further by injecting a conductive tracer into the reservoir, thereby decreasing the resistivity of the fractures. In this project, the potential difference has been calculated between two points (an injector and a producer) as conductive fluid flows through fracture networks. The time history of the potential field depends on the fracture network and can therefore be used to estimate where fractures are located and the character of their distribution.

The analogy between Ohm's law that describes electrical flow and Darcy's law describing fluid flow makes it possible to use flow simulator TOUGH2 to calculate electric fields. This annual report illustrates how EOS1 module in TOUGH2 has been used to calculate the potential fields as conductive fluid is injected into different types of reservoirs and how the time history of the potential field depends on the fracture networks. The report also discusses how EOS9 module in TOUGH2 can be used instead of EOS1 to get accurate results of the electric field. In EOS9 the density and viscosity can be defined as constants instead of being pressure dependent, allowing for a simulation of an electric field without the resistivity becoming dependent on the electric potential. A few simple simulations were performed and results compared to the resistivity model described in the preceding annual report. The advantage of using TOUGH2 to solve the electrical field instead of the resistivity model is that the same grid can be used for both electric and fluid flow models. TOUGH2 also allows use of nonrectangular elements making the simulation faster and more efficient.

3.2 INTRODUCTION

Characterizing the dimensions and topology of fractures in geothermal reservoirs is crucial for optimal designing of production and to find feasible drilling locations. Fractures carry most of the fluid in the reservoir so fracture configuration is central to the performance of a geothermal system both in fractured reservoirs as well as in Enhanced Geothermal System (EGS) applications. The knowledge of fluid-flow patterns is necessary to ensure adequate supply of geothermal fluids and efficient operation of geothermal wells and to prevent short-circuiting flow paths from injector to producer that would lead to premature thermal breakthrough. Fracture characterization therefore increases the reliability of geothermal wells and the overall productivity of geothermal power plants.

The goal of this study is to find ways to use Electrical Resistivity Tomography (ERT) to characterize fractures in geothermal reservoirs. ERT is a technique for imaging the resistivity of a subsurface from electrical measurements. Pritchett (2004) concluded based on a theoretical

study that hidden geothermal resources can be explored by electrical resistivity surveys because geothermal reservoirs are usually characterized by substantially reduced electrical resistivity relative to their surroundings. Electrical current moving through the reservoir passes mainly through fluid-filled fractures and pore spaces because the rock itself is normally a good insulator. In these surveys, a direct current is sent into the ground through electrodes and the voltage differences between them are recorded. The input current and measured voltage difference give information about the subsurface resistivity, which can then be used to infer fracture locations.

Resistivity measurements have been used in the medical industry to image the internal conductivity of the human body, for example to monitor epilepsy, strokes and lung functions as discussed by Holder (2004). In Iceland, ERT methods have been used to map geothermal reservoirs. Arnarson (2001) describes how different resistivity measurements have been used effectively to locate high temperature fields by using electrodes located on the ground's surface. Stacey et al. (2006) investigated the feasibility of using resistivity to measure saturation in a rock core. A direct current pulse was applied through electrodes attached in rings around a sandstone core and it resulted in data that could be used to infer the resistivity distribution and thereby the saturation distribution in the core. It was also concluded by Wang and Horne (2000) that resistivity data have high resolution power in the depth direction and are capable of sensing the areal heterogeneity.

In the approach considered in this project so far, electrodes would be placed inside two geothermal wells and the potential differences between them studied to locate fractures and infer their properties. Due to the limited number of measurement points, the study is investigating ways to enhance the process of characterizing fractures from sparse resistivity data. For example, in order to enhance the contrast in resistivity between the rock and fracture zones, a conductive tracer would be injected into the reservoir and the time-dependent voltage difference measured as the tracer distributes through the fracture network.

Slater et al. (2000) have shown a possible way of using ERT with a tracer injection by observing tracer migration through a sand/clay sequence in an experimental $10 \times 10 \times 3$ m^3 tank with cross-borehole electrical imaging. Singha and Gorelick (2005) also used cross-well electrical imaging to monitor migration of a saline tracer in a $10 \times 14 \times 35$ m^3 tank. In previous work, usually many electrodes were used to obtain the resistivity distribution for the whole field at each time step. The resistivity distribution was then compared to the background distribution (without any tracer) to see resistivity changes in each block visually, to locate the saline tracer and thereby the fractures. Using this method for a whole reservoir would require a gigantic parameter space, and the inverse problem would not likely be solvable, except at very low resolution. However, in the method considered in this study, the potential difference between the wells would be measured and plotted as a function of time while the conductive tracer flows through the fracture network. Future work will involve using that response, i.e. potential difference vs. time, in an inverse modeling process to characterize the fracture pattern.

First, the analogy between water flow and electrical flow is defined and the possibility of using TOUGH2 flow simulator to solve an electric field is investigated. Next, electric field time histories, calculated using EOS1 module in TOUGH2 for three different fracture networks are

illustrated. The possibility of using EOS9 module instead of EOS1 to get accurate results for the electric potential is investigated by calculating the electric field for three simple cases and comparing the analytical solution to the results from EOS9, EOS1 and the resistivity model described in the preceding annual report.

3.3 WATER FLOW ANALOGY OF ELECTRICAL FLOW

The steady-state flow of an electric current through a conducting medium due to differences in energy potential is analogous to the steady-state flow of a fluid through porous medium. Darcy's law is an empirical relationship similar to Ohm's law,

$$J = -\sigma \nabla \phi \tag{3.1}$$

where J is current density [A/m^2], σ is the conductivity of the medium [Ωm] and ϕ is the electric potential [V] but instead of describing electrical flow Darcy's law describes fluid flow through a porous medium,

$$q = -\frac{k}{\mu} \nabla p \tag{3.2}$$

where q is the flow rate [m/s], k is permeability [m^2], μ is viscosity of the fluid [kg/ms] and p is pressure [Pa]. Table 3.1 presents the correspondence between the variables and relations of water flow (Darcy's law) and electric current flow (Ohm's law).

Table 3.1: Correspondence between electric current flow and water flow.

	Darcy's law: $q = -\frac{k}{\mu} \nabla p$	Ohm's law: $J = -\sigma \nabla \phi$
Flux of:	Water q [m/s]	Charge J [A/m^3]
Potential:	Pressure p [Pa]	Voltage ϕ [V]
Medium property:	Hydraulic conductivity $\frac{k}{\mu}$ [m^2/Pa·s]	Electrical conductivity σ [1/Ωm]

The similarities between these two equations imply that it is possible to use flow simulator like TOUGH2 to solve electric field due to flow of electric current. Then, the pressure results from TOUGH2 would correspond to the electric voltage, the current density to the flow of water and the electrical conductivity would correspond to the hydraulic conductivity, i.e.

$$\sigma = \frac{k}{\mu} \tag{3.3}$$

However, it must be taken into account that viscosity depends on pressure while conductivity of a reservoir does not depend on the electric voltage used. Figure 3.1 shows how viscosity of water at 150°C changes with pressure.

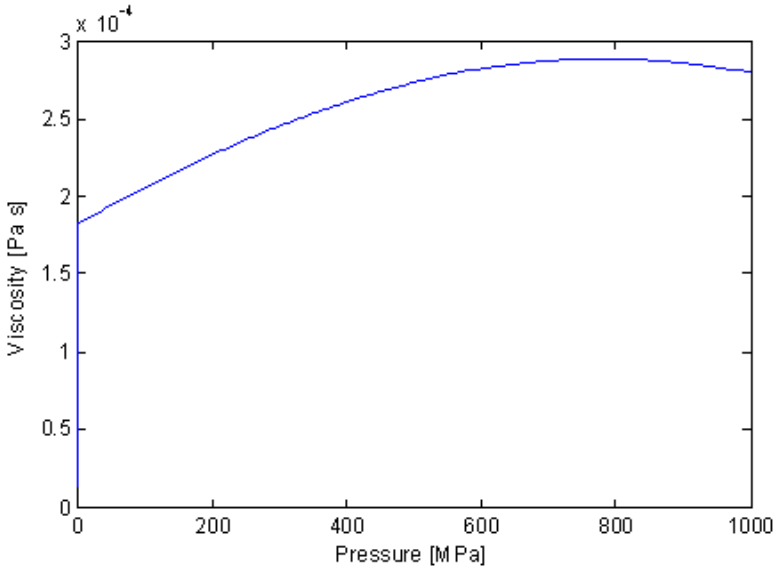

Figure 3.1: Viscosity [Pa·s] as a function of pressure [MPa].

In order to take the pressure dependence into account EOS9 module in TOUGH2 was studied. It considers flow of a single aqueous phase consisting of a single water component. The conditions are assumed to be isothermal so only a single water mass balance equation is solved for each grid block and the thermal properties of water can be overwritten. Therefore, liquid viscosity, density and compressibility can be defined constant and reference pressure and temperature can be overwritten, making the imitation of electric flow possible.

In TOUGH2, Darcy's law is solved using the following discretization,

$$F_{nm} = \rho u_{nm} = -k_{nm}\left[\frac{k_r \rho}{\mu}\right]_{nm}\left[\frac{P_n - P_m}{D_{nm}} - \rho_{nm} g_{nm}\right] \tag{3.4}$$

where ρ is density and g_{nm} is gravity in direction from m to n. Suitable averaging are used at the interface between grid blocks n and m, and D_{nm} is the distance between the nodal points n and m (see Figure 3.2).

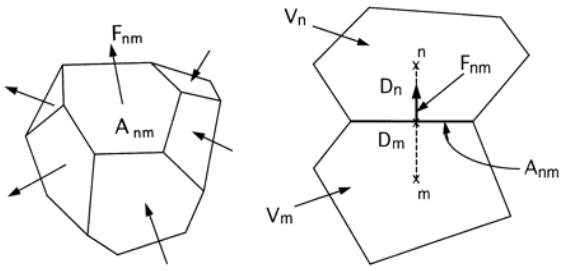

Figure 3.2: Space discretization, grid blocks n and m.

In order to calculate the flow simulation the following equation is solved using Newton/Raphson iteration

$$R_n^{K,K+1} = M_n^{K,K+1} - M_n^{K,K} - \frac{\Delta t}{V_n}\left[\sum_m A_{nm} F_{nm}^{K,K+1} + V_n q_n^{K,K+1}\right] \qquad (3.5)$$

Where $R_n^{K,K+1}$ are residuals between time step t^k and $t^{k+1} = t^k + \Delta t$, M is mass accumulation, A is the surface area of the grid block, V is the volume and q denotes sinks and sources.

The pressure solved in a flow simulation is of higher magnitude then the voltage in the electric case would ever be, so some of the electric parameters need to be scaled in order to solve the electric problem using a flow simulator. Table 3.2 shows the scaling of the electrical parameters for the flow simulation where the density of the fluid has been taken into account as well.

Table 3.2: Scaling of electric parameters.

Electric parameters:	Multiplied by:	Flow parameters:
ϕ [V]	10^6	P [Pa]
J [A/m^3]	10^9	q [m/s]
D [m]	10^6	D [m]
A [m^2]	10^{12}	A [m^2]
V [m^3]	10^{12}	V [m^3]

The initial pressure is set to 10^6 Pa so in order to get the electric potential results assuming initial voltage to be zero, the initial pressure is subtracted from the pressure results and the results are then multiplied by 10^{-6} to get the electric voltage results.

3.4 RESULTS

A flow simulation was performed using EOS1 module in TOUGH2 reservoir simulator to see how a tracer, which increases the conductivity of the fluid, distributes after being injected into the reservoir. The simulation was carried out on a two-dimensional grid with dimensions 1000 × 1000 × 10 m^3 with fractures first modeled as a cross in the upper left corner (green blocks) as shown in Figure 3.3, then as a larger cross in the upper left corner as Figure 3.4 shows and finally with no fractures.

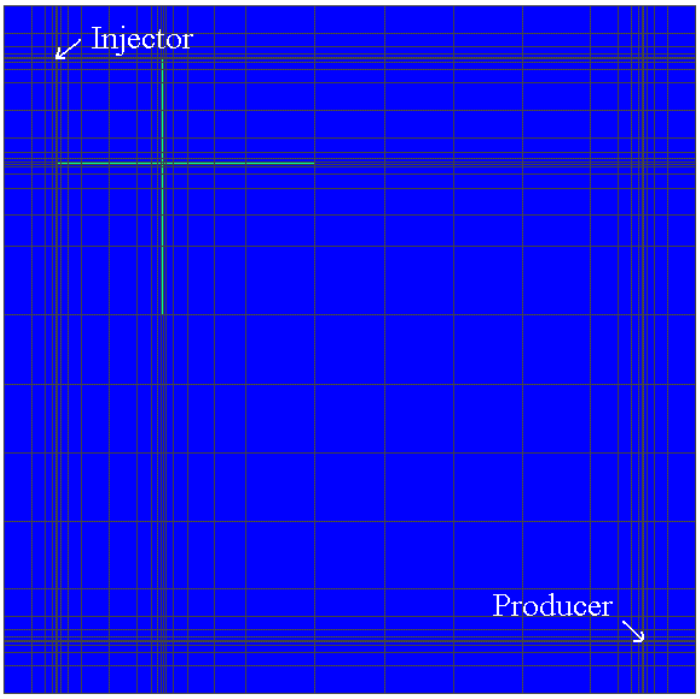

Figure 3.3: Fractures (green blocks) modeled as a small cross in the upper left corner of the reservoir.

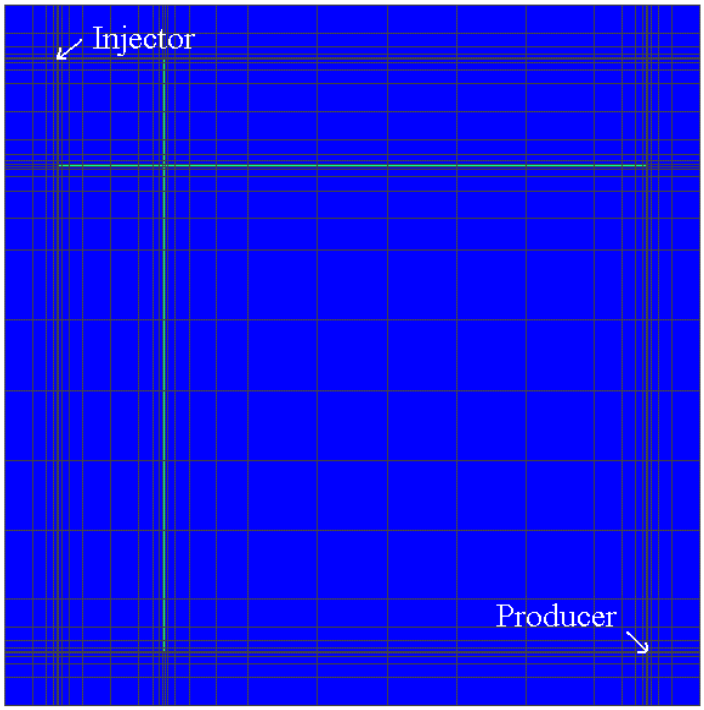

Figure 3.4: Fractures (green blocks) modeled as a larger cross in the upper left corner of the reservoir.

The goal was to study the difference in potential field between these three cases as conductive fluid is injected into the reservoir. The reservoir is modeled with porosity 0.2 and permeability 10^5 md (10^{-10} m^2) while the fractures have permeability 5×10^9 md (5×10^{-4} m^2). No-flow

boundary conditions were used and 100 kg/s of water was injected in the upper left corner with enthalpy 100 kJ/kg, and 0.1 kg/s of tracer with enthalpy 100 kJ/kg. The initial pressure was set to 10 atm, temperature to 150°C and initial tracer mass fraction to 10^{-9} because the simulator could not solve the problem with zero initial tracer mass fraction.

The tracer injected into the reservoir is a NaCl solution which resistivity changes with temperature and concentration. Ucok et al. (1980) have established experimentally the resistivity of saline fluids over the temperature range 20-350°C and their results for resistivity of NaCl solution calculated using a three-dimensional regression formula is shown in Figure 3.5.

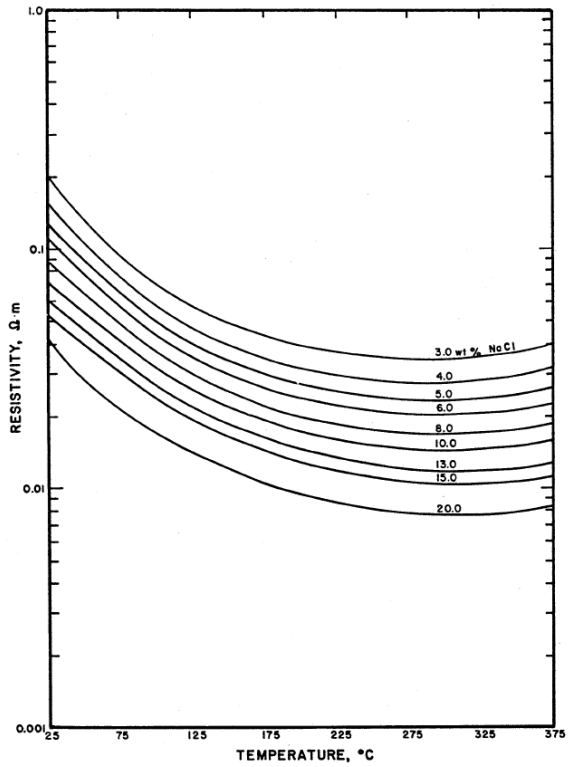

Figure 3.5: Resistivity of NaCl solution as a function of temperature and concentration (Ucok et al., 1980).

They calculated that the dependence of resistivity is best represented by the formula

$$\rho_w = b_0 + b_1 T^{-1} + b_2 T + b_3 T^2 + b_4 T^3 \tag{3.6}$$

where T is temperature and b are coefficients found empirically. The best fit for the concentration dependence was found to be

$$\rho_w = 10/(\Lambda c) \tag{3.7}$$

where

$$\Lambda = B_0 - B_1 c^{1/2} + B_2 c \ln c + higher\ \ order\ \ terms \tag{3.8}$$

Coefficients B depend on the solution chemistry and c is the molar concentration.

In this project, the tracer concentration resulting from the flow simulation is changed into molar concentration and the following B coefficient matrix for the three-dimensional regression

analysis of the data studied by Ucok et al. (1980) is used to calculate the resistivity of the NaCl solution,

$$B = \begin{matrix} 3.470 & -6.650 & 2.633 \\ -59.23 & 198.1 & -64.80 \\ 0.4551 & -0.2058 & 0.005799 \\ -0.346E\text{-}5 & 7.368E\text{-}5 & 6.741E\text{-}5 \\ -1.766E\text{-}6 & 8.787E\text{-}7 & -2.136E\text{-}7 \end{matrix}$$

Therefore, the resistivity value of each block depends on the tracer concentration in that block and the value decreases as more tracer flows into the block.

The EOS1 module in TOUGH2 was used to calculate the electric potential distribution for the reservoirs. A current is set equal to 1 A at a point in the upper left corner, and as -1 A at the lower right corner and the potential field calculated based on the resistivity of the field at each time step. Figures 3.6 and 3.7 show how the potential difference between the injector and the producer changes with time for the reservoirs shown in Figure 3.3 and 3.4 and Figure 3.8 shows the potential difference time history for the reservoir with no fractures.

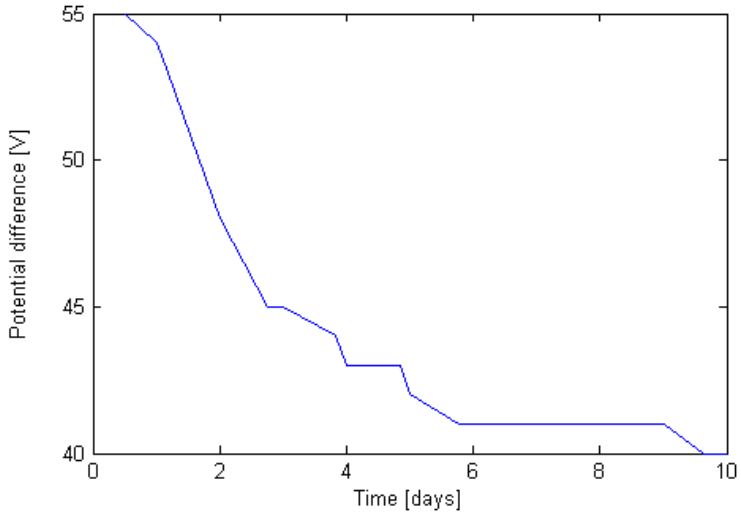

Figure 3.6: Potential difference between injection and production wells for reservoir in Figure 3.3.

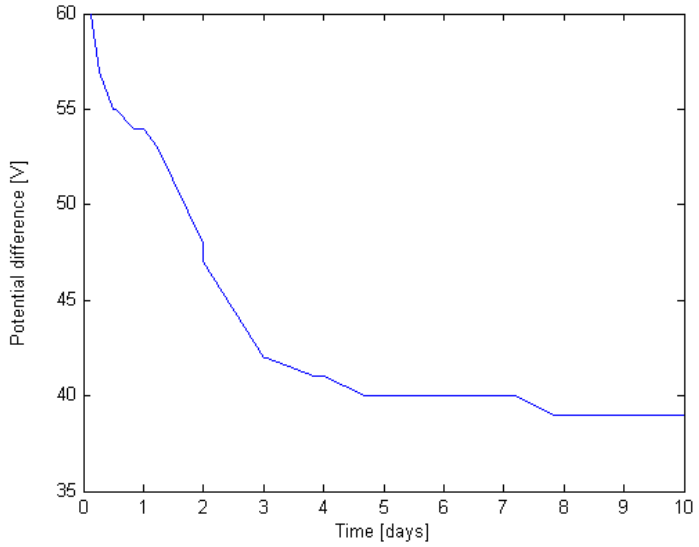

Figure 3.7: Potential difference between injection and production wells for reservoir in Figure 3.4.

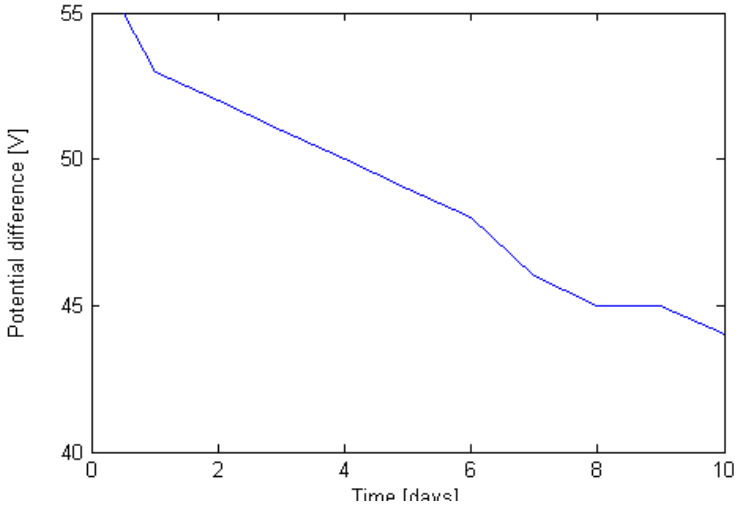

Figure 3.8: Potential difference between injection and production wells for the reservoir with no fractures.

The potential difference in the graph in Figure 3.7 drops faster than the difference in Figure 3.6 because of larger fractures enabling conductive fluid to flow faster through the reservoir. Figure 3.8 shows a much slower decline in potential difference since the reservoir has no fractures. The potential difference after 10 days of injection is 39 V for the larger fractured reservoir, 40 V for the smaller fractured reservoir and 44 V for the reservoir with no fractures. The results also indicate that different fracture properties give different potential difference histories between two wells, and could therefore be used to indicate fracture characteristics.

The results showed how EOS1 module in TOUGH2 was used to solve both tracer flow and electric potential for fracture networks. By using TOUGH2 and the same grid for both

simulations, nonrectangular elements could be used making the simulation faster and more efficient. However, since the density and viscosity of the fluid is pressure dependent while the electric conductivity does not depend on the electric potential, the EOS1 module might not give accurate results even though the viscosity does not change drastically within the pressure range used (see Figure 3.1). Therefore, an analytical solution was calculated for a simple flow model, shown in Figure 3.9, to studied whether EOS1 module in TOUGH2 would give similar results as when EOS9 is used with density and viscosity defined constant.

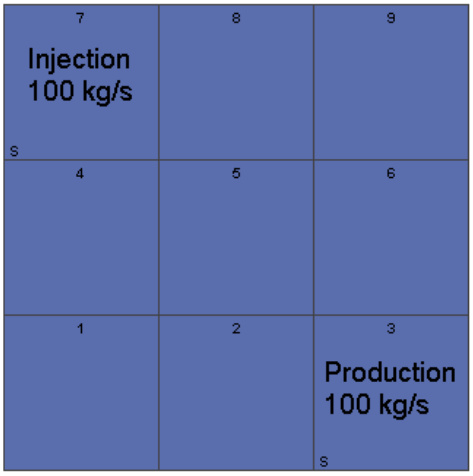

Figure 3.9: A simple flow model with injection and production in opposite corners.

The homogeneous reservoir was modeled with permeability 10^7 md (10^{-8} m^2) and when analytical solution was calculated as well as when EOS9 module of TOUGH2 was used the reservoir was modeled with a constant liquid density of 1000 kg/m^3 and a constant viscosity of 1.7×10^{-4} Pa·s. No-flow boundary conditions were used and 100 kg/s of water was injected in the upper left corner and 100 kg/s produced in the lower right corner. Initial pressure was set to 10^6 Pa. Table 3.3 shows the analytical solution of the pressure which is the same as when EOS9 was used and Table 3.4 shows the pressure calculated using EOS1 module of TOUGH2. The rows of the tables represent the rows of blocks shown in Figure 3.9.

Table 3.3: Pressure [Pa] from analytical solution as well as from using EOS9 module.

1.0013×10^6	1.0004×10^6	1.0000×10^6
1.0004×10^6	1.0000×10^6	9.9958×10^5
1.0000×10^6	9.9958×10^5	9.9873×10^5

Table 3.4: Pressure [Pa] calculated using EOS1 module.

1.0015×10^6	1.0005×10^6	1.0000×10^6
1.0005×10^6	1.0000×10^6	9.9951×10^5
1.0000×10^6	9.9951×10^5	9.9852×10^5

The results when EOS9 module is used are the same as the analytical solution but the results calculated using EOS1 module are a little bit different since the water density and viscosity is pressure dependent.

Next, the electric field was calculated for a similar 3x3 block matrix using EOS9 and the results compared to the resistivity model previously used for electric field calculations (described in quarterly report January-March 2011).

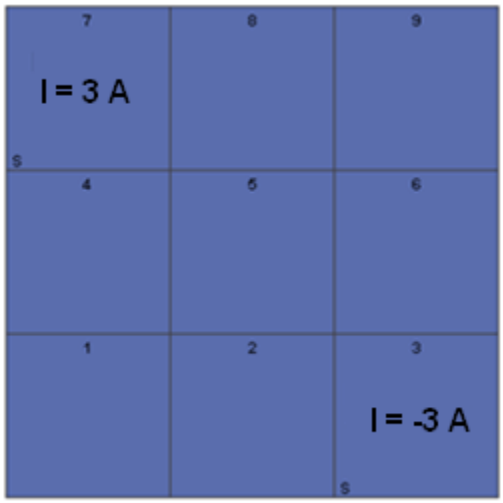

Figure 3.10: Homogeneous electric model with the current set as 3 A in the upper left corner and as -3 A in the lower right corner.

The resistivity was set as 0.1 Ωm and the initial electric potential was set as zero. The electric parameters were scaled as showed in Table 3.2 when EOS9 module was used to solve the electric field. The analytical solution and the solution from the resistivity model were the same as when EOS9 was used. Results are shown in Table 3.5.

Table 3.5: Electric potential calculated using the resistivity model and EOS9 module in TOUGH2 as well as when using the analytical solution.

0.225 V	0.075 V	0 V
0.075 V	0 V	-0.075 V
0 V	-0.075 V	-0.025 V

The matrix shown in Figure 3.11 was studied as well to verify that the scaling used for EOS9 would also work for an inhomogeneous case. The blue blocks have resistivity set as 0.005 Ωm and the green block has the resistivity set as 0.0025 Ωm.

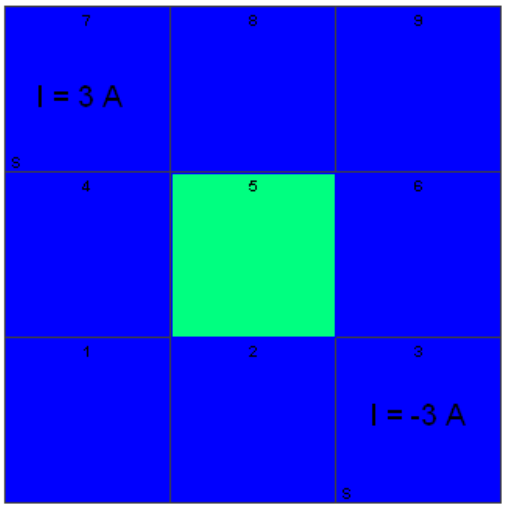

Figure 3.11: Inhomogeneous electric model with the current set as 3 A in the upper left corner and as -3 A in the lower right corner.

The results from using EOS9, see Table 3.6, were the same as the results from the resistivity model and also the same as the analytical solution. Therefore, EOS9 module in TOUGH2 can be used to calculate the electric field accurately by defining the water density and viscosity constant.

Table 3.6: Electric potential calculated using the resistivity model, EOS9 module in TOUGH2 and the analytical solution.

0.0107 V	0.0032 V	0 V
0.0032 V	0 V	-0.0032 V
0 V	-0.0032 V	-0.0107 V

Currently, the model used to calculate the electric potential distribution for the reservoirs shown in Figures 3.3 and 3.4 is being modified so that the accurate electric potential distribution can be calculated for the same reservoirs using EOS9 module in TOUGH2.

4. REFERENCES

Alaskar, M., Ames, M., Horne, R.N., Li, K., Connor, S. and Cui, Y.: "Smart Nanosensors for In-situ Temperature Measurement in fractured geothermal reservoirs," GRC Annual Meeting, San Diego, USA, (2011).

Alaskar, M., Ames, M., Horne, R.N., Li, K., Connor, S. and Cui, Y.: "In-situ Multifunction Nanosensors for Fractured Reservoir Characterization," GRC Annual Meeting, Sacramento, USA, vol. 34 (2010).

Barker, J.: A generalized radial flow model for hydraulic tests in fractured rock. *Water Resources Research,* (1988).

Bear, J., *Dynamics of fluids in porous media*, (1972), Dover.

Bennett, K., and Horne, R.N.: Power Generation Potential from Coproduced Fluids in the Los Angeles Basin, *Geothermal Resources Council Transactions* (2011).

Bodvarsson, G., and Pruess, K.: Thermal effects of reinjection in geothermal reservoirs with major vertical fractures. *Journal of Petroleum Technology*, **36(9)**, 1567–1578, (1984).

Breiman, L., and Friedman, J. H.: Estimating optimal transformations for multiple regression and correlation. *Journal of the American Statistical Association*, ***80*(391)**, 580–598, (1985).

Carlier, E.: Analytical solutions of the advection-dispersion equation for transient groundwater flow. A numerical validation. *Hydrological Processes*, (2008).

Chen, Chih-Ying: Liquid-gas Relative Permeability in Fractures: Effects of Flow Structures, Phase Transformation and Surface Roughness, PhD thesis, Stanford University, Stanford, California (2005).

Chen, H., Li, Z., Wu, Z. and Zhang, Z.: "A novel route to prepare and characterize Sn-Bi nanoparticles," *Journal of Alloys and Compounds*. 2005, **394**, 282-285.

Chrysikopoulos, C. V. "Artificial Tracers for Geothermal Reservoir Studies." *Environmental Geology* 22.1 (1993): 60-70.

Deng, X., and Horne, R.: Well Test Analysis of Heterogeneous Reservoirs. *SPE Annual Technical Conference and Exibition, Houston, Texas, (1993).*

Diomampo, G.P.: Relative Permeability through Fractures, MS thesis, Stanford University, Stanford, California (2001).

Gentier, S., Rachez, X., Ngoc, T., Dung, T., Peter-Borie, M. and Souque, C.: 3D flow modelling of the medium-term circulation test performed in the deep geothermal site of Soultz-sous-Forêts (France) *World Geothermal Congress Proceedings*, (2010).

Gerber, Richard, and Robert R. Birss. High Gradient Magnetic Separation. Chichester: Research Studies, 1983.

Gringarten, A. C., and Witherspoon, P.:. Theory of heat extraction from fractured hot dry rock. *Journal of Geophysical Research*, **80(8)**, p. 1120-1124, (1975).

Holder, D.S.: Electrical Impedance Tomography: Methods, History and Applications, IOP, UK (2004).

Horne, R. N. and Szucs, P., Inferring Well-to-Well Connectivity Using Nonparametric Regression on Well Histories, *In Thirty-Second Workshop on Geothermal Reservoir Engineering, Stanford*, (2007) http://www.geothermal-energy.org/pdf/IGAstandard/SGW/2007/horne.pdf

Jensen, C., and Horne, R.: Matrix diffusion and its effect on the modeling of tracer returns from the fractured geothermal reservoir at Wairakei, New Zealand. *Proc. Ninth Workshop on Geothermal Reservoir Engineering, Stanford University, Stanford, California,* (1983).

Juliusson, E. and Horne, R. N., Characterization of Fractures in Geothermal Reservoirs, *In World Geothermal Congress. Bali*, (2010), http://www.geothermal-energy.org/pdf/IGAstandard/WGC/2010/2292.pdf

Juliusson, Egill, and Roland N. Horne. "Analyzing Tracer Tests During Variable Flow Rate Injection and Production." Proc. of Thirty-Sixth Workshop on Geothermal Reservoir Engineering, Stanford University, Stanford, CA.

Kanj, M., Funk, J., and Al-Yousif, Z.: "Nanofluid Coreflood Experiments in the Arab-D," SPE paper 126161, presented at the 2009 SPE Saudi Arabia Technical Symposium and Exhibition held in Saudi Arabia, Alkhobar, May 09-11.

Kocabas, I.: Geothermal reservoir characterization via thermal injection backflow and interwell tracer testing. *Geothermics,* **34(1)**, p. 27-46 (2005).

Kreft, A., and A. Zuber. "On The Physical Meaning Of the Dispersion Equation and Its Solutions For Different Initial and Boundary Conditions." *Chemical Engineering Science* 33 (1978): 1471-480.

"K&J Magnetics - Magnet Calculator." K&J Magnetics - Strong Neodymium Magnets, Rare Earth Magnets. 20 May 2011. <http://www.kjmagnetics.com/calculator.asp>.

Lauwerier, H. A.: The transport of heat in an oil layer caused by the injection of hot fluid. *Applied Scientific Research*, **5(2)**, p. 145-150, (1955).

Lovekin, J. and Horne, R. N., Optimization of injection scheduling in geothermal fields, *In DOE Research and Development for the Geothermal Marketplace, Proceedings of the Geothermal Program Review VII*, (1989), pp. 45-52.

Lee, K. H., Ortega, A., Jafroodi, N., Ershaghi, I., A Multivariate Autoregressive Model for Characterizing Producer Producer Relationships in Waterfloods from Injection/Production Rate Fluctuations, *In SPE 2010 Western Regional Meeting, paper number SPE 132625*., (2010).

Lee, K. H., Ortega, Antonio, Nejad, A., Jafroodi, Nelia, and Ershaghi, Iraj.: A Novel Method for Mapping Fractures and High Permeability Channels in Waterfloods Using Injection and Production Rates. *Proceedings of SPE Western Regional Meeting*. Society of Petroleum Engineers (2009).

Lee, W. J.: *Well testing*. Society of Petroleum Engineers. (1982).

Levard, Clement. <clevard@stanford.edu (2010, July 8)>. [Personal email].

Levitan, M.: Practical Application of Pressure/Rate Deconvolution to Analysis of Real Well Tests. *SPE Reservoir Evaluation and Engineering,* (2005), 8 (2): 113–121,

Levitan, M.: Deconvolution of multiwell test data. *SPE Annual Technical Conference and Exhibition,* (2006), 24-27.

Massart, B., Paillet M., Henrion V., Sausse J., Dezayes C. and Genter A.: Fracture Characterization and Stochastic Modeling of the Granitic Basement in the HDR Soultz Project (France), *World Geothermal Congress Proceedings*. (2010)

Nomura, M., and Horne, R.: Data processing and interpretation of well test data as a nonparametric regression problem. *SPE Western Regional Meeting* (2009).

Onur, M., Ayan, C., and Kuchuk, F.: Pressure-Pressure Deconvolution Analysis of Multiwell Interference and Interval Pressure Transient Tests. *Proceedings of International Petroleum Technology Conference*. Society of Petroleum Engineers, (2009).

Pimonov, E., Ayan, C., Onur, M., and Kuchuk, F.: A New Pressure Rate Deconvolution Algorithm to Analyze Wireline Formation Tester and Well-Test Data. *Proceedings of SPE Annual Technical Conference and Exhibition*, (2009), 1-23.

Place, J., Garzic, E.L.E., Geraud, Y., Diraison, M., and Sausse, J.: Characterization of the Structural Control on Fluid Flow Paths in Fractured Granites. *Thirty-Sixth Workshop on Geothermal Reservoir Engineering Proceedings* (2011)

Pritchett, J.W.: Finding Hidden Geothermal Resources in the Basin and Range Using Electrical Survey Techniques. A Computational Feasibility Study, report INEEL/EXT-04-02539 (2004).

Reimus, Paul W. *The Use of Synthetic Colloids in Tracer Transport Experiments in Saturated Rock Fractures*. Thesis. University of New Mexico, 1995.

Sayarpour, M., Zuluaga, E., Kabir, C. S., and Lake, L. W. The Use of Capacitance-Resistive Models for Rapid Estimation of Waterflood Performance and Optimization. *SPE Annual Technical Conference and Exhibition*. Society of Petroleum Engineers, (2006).

Schroeter, T. von, Hollaender, F., and Gringarten, A. C.: Deconvolution of Well-Test Data as a Nonlinear Total Least-Squares Problem. *SPE Journal*, *9*(4), (2004).

Schroeter, T. v., and Gringarten, A.: Superposition Principle and Reciprocity for Pressure-Rate Deconvolution of Data From Interfering Wells. *SPE Annual Technical Conference*, (2007).

Shook, G. M.: Predicting thermal breakthrough in heterogeneous media from tracer tests. *Geothermics*, **30(6)**, (2001)

Shook, G. M.: A simple, fast method of estimating fractured reservoir geometry from tracer tests, *Geothermal Resources Council Transactions*, **27**, (2003).

Shook, G. M.: Estimating Fracture Surface Areas from Tracer Tests: Mathematical Formulation, *Geothermal Resources Council Transactions*, **28**, p. 627-630, (2004)

Singha, K. and Gorelick, S.M. Saline Tracer Visualized with Three-dimensional Electrical Resistivity Tomography: Field-scale Spatial Moment Analysis. *Water Resources Research*, **41** (2005), W05023.

Slater, L., Binley, A.M., Daily, W. and Johnson, R. Cross-hole Electrical Imaging of a Controlled Saline Tracer Injection. *Journal of Applied Geophysics*, **44**, (2000), 85-102.

Stacey, R.W., Li, K. and Horne, R.N.: Electrical Impedance Tomography (EIT) Method for Saturation Determination, *Proceedings*, 31st Workshop on Geothermal Reservoir Engineering, Stanford University, Stanford, CA (2006).

Sullera, M. M., and Horne, R. N.: Inferring injection returns from chloride monitoring data. *Geothermics*, (2001), *30*(6), 591–616. Elsevier.

Tester, J., Anderson, B.,. Batchelor, A., Blackwell, D., DiPippo, R., Drake, E., et al.: The Future of Geothermal Energy: Impact of Enhanced Geothermal Systems on the United States in the 21st Century. *Massachusetts Institute of Technology*, (2006)

Ucok, H., Ershaghi, I. and Olhoeft, G.R.: Electrical Resistivity of Geothermal Brines, *Journal of Petroleum Technology*, **32**, (1980), 717-727.

Urbino, E. G., and Horne, R. N.: Optimizing reinjection strategy at Palinpinon, Philippines, based on chloride data. *Sixteenth Workshop on Geothermal Reservoir Engineering*. Stanford: Stanford University, (1991).

Villacorte, J. D., Malate, R. C. M. and Horne, R. N., Application of Nonparametric Regression on Well Histories of Geothermal Production Fields in the Philippines, *In World Geothermal Congress. Bali*, (2010), http://www.geothermal-energy.org/pdf/IGAstandard/WGC/2010/2311.pdf

Wang, P. and Horne, R.N.: Integrating Resistivity Data with Production Data for Improved Reservoir Modeling, SPE 59425, SPE Asia Pacific Conference, Yokohama, Japan (2000).

Wittung, P., Kajanus, J., Kubista, M., and Malmström, Bo G. (1994). "Absorption flattening in the optical spectra of liposome-entrapped substances," FEBS Letter 352, 37-40.

Wu, X., Pope, G., Shook, G.M., and Srinivasan, S.: Prediction of Enthalpy Production from Fractured Geothermal Reservoirs using Partitioning Tracers, *International Journal of Heat and Mass Transfer*, 51(5-6), p. 1453-1466 (2008).

Yousef, A., Gentil, P., Jensen, J., and Lake, L.: A capacitance model to infer interwell connectivity from production and injection rate fluctuations. *SPE Reservoir Evaluation & Engineering*. (2005).